

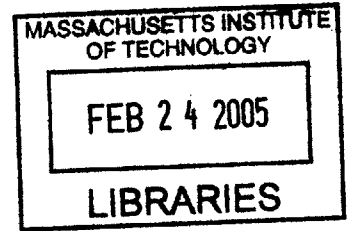
**Moisture Degradation in FRP Bonded Concrete Systems:
An Interface Fracture Approach**

by

Ching Au

Bachelor of Engineering, Civil & Structural
The Hong Kong Polytechnic University, 1999

S.M.
Massachusetts Institute of Technology, 2001



SUBMITTED TO THE DEPARTMENT OF CIVIL & ENVIRONMENTAL ENGINEERING
IN PARTIAL FULFILLMENT OF THE REQUIREMENTS FOR THE DEGREE OF

DOCTOR OF SCIENCE IN STRUCTURES AND MATERIALS
AT THE
MASSACHUSETTS INSTITUTE OF TECHNOLOGY

FEBRUARY 2005

© 2005 Massachusetts Institute of Technology. All rights reserved.

Signature of Author _____
Department of Civil and Environmental Engineering
November 22, 2004

Certified by _____
Oral Büyüköztürk
Professor of Civil and Environmental Engineering
Thesis Supervisor

Accepted by _____
Andrew Whittle
Chairman, Departmental Committee on Graduate Studies

BARKER

Moisture Degradation in FRP Bonded Concrete Systems: An Interface Fracture Approach

by

Ching Au

Submitted to the Department of Civil and Environmental Engineering
on November 22, 2004 in partial fulfillment of the
requirements for the degree of
Doctor of Science in Structures and Materials

ABSTRACT

The objective of this research is to develop new mechanistic understanding of moisture affected debonding failures in carbon fiber-reinforced plastic (FRP) bonded concrete systems by means of an interface fracture approach. Central to the investigation is the use of interface fracture toughness as the quantification parameter, which is considered a bond property, to analyze, compare, and correlate physical observations of FRP bonded concrete joints. Owing to the non-negligible epoxy bond line thickness found in real-world retrofitted systems, a new tri-layer fracture energy model is derived to facilitate the computation of interface fracture toughness values. Also, with this model, the five possible debonding scenarios in FRP bonded concrete that include interface separation and material decohesion, are quantitatively distinguished and precisely described for the first time. Debonding characterization is conducted using mesoscale peel and shear fracture models manufactured with full-scale bond lines. These models are subjected to accelerated moisture conditioning to achieve various levels of moisture content in the bond region. They are then mechanically tested at selected time intervals for capturing the change in bond property and debonding mode with respect to increasing moisture concentration, which is evaluated by means of 3-dimensional moisture diffusion simulations. Diffusion and mechanical properties of the constituent materials with respect to moisture uptake are physically determined to act as inputs in the diffusion simulation and in the computation of toughness values. The knowledge of computed toughness values, simulated diffusion behavior, and observed debonding modes, combined with finite element fracture computation, mode-mix characterization, and kink criterion implementation, form a synergistic analysis of the mechanistic debonding behavior affected by moisture. Results have shown that moisture affected debonding is a highly complex phenomenon that involves physical changes in the bond as well as in its constituent materials. In particular, moisture can initially enhance or reduce the interface fracture toughness, depending on the epoxy formulation being used. The toughness can, however, decrease by as much as 60% and become asymptotic upon reaching a certain moisture concentration threshold, which can be attained in as short as 2 weeks in case of peel fracture. While various debonding modes have been observed for dry specimens, epoxy/concrete interface separation, which has generally been considered an unlikely debonding mode, is observed consistently in all wet fracture specimens. Interface fracture analysis indicates that this newly discovered interfacial debonding mode is attributed to various interfacial material toughening or weakening mechanisms, and has also hinted on the possible interphase formation as a consequence of moisture diffusion. The new knowledge and results obtained from this research provide a basis for further analysis directions and for design of FRP bonded concrete systems against moisture affected debonding.

Thesis Supervisor: Oral Büyüköztürk

Title: Professor of Civil and Environmental Engineering

This thesis is dedicated to my love Joanne

ACKNOWLEDGEMENTS

I would like to express my sincere gratitude to my thesis supervisor Professor Oral Büyüköztürk for his guidance, friendship, encouragement, patience, and support during my years at MIT. I am particularly obliged to him for providing me with the opportunities to be actively involved in different research projects and in various scholarly activities beyond a traditional graduate training such that I have developed a range of skills that will benefit me significantly for the time to come.

I am deeply honored to have Professor John W. Hutchinson of Harvard University to serve on my committee. I would like to thank him for his time, encouragement, and insightful comments during the course of this research. I feel really lucky to have the opportunity to learn from him in person and I enjoyed every minute of our stimulating discussions on interface fracture mechanics. I am also honored to have Professor Frederick J. McGarry of the Department of Materials Science and Engineering to serve on my committee. In particular, I would like to thank him for introducing me to the fascinating world of fracture mechanics back in 2001 so that I became equipped to conduct this research. Thank is also due to Professor Eduardo Kausel for taking his time to serve on my committee and for his friendship and encouragement.

Gratitude is extended to Professor Subra Suresh, Professor David Roylance, and Professor Jerome J. Connor of MIT, Professor Christopher K.Y. Leung of the Hong Kong University of Science and Technology, Professor Urs Meier of the Swiss Federal Laboratories for Materials Testing and Research (EMPA), Professor Ferdinand Rostasy of the Technical University of Braunschweig, and Professor Zdenek P. Bazant of Northwestern University for their interest and advice.

This research was supported by the National Science Foundation (NSF) CMS Grant #0010126 and I am grateful to Dr. Perumalsamy N. Balaguru, the cognizant NSF official, for his interest and support in this work. Appreciation is also extended to Stephen W. Rudolph, the laboratory technician, for his help in the laboratories at MIT, Sean Fowler of Q-Panel Lab Products for technical support on the Q-Fog environmental chamber, Janet Z. Swaysland of ABAQUS for technical and administrative support that facilitated the finite element modeling activities, and various industrial collaborators for providing composite materials and related information.

I would like to thank all of my friends and colleagues for their friendship and support over the years, in particular: Dr. Michael Bockstaller, Dr. Joonsang Park, Dr. Dirk Mohr, Dr. Oguz Gunes, Erdem Karaca, Konstantinos Stamoulis, Dr. Peter Kan, Tzu-Yang Yu, and Jose Alberto Ortega. Also, I have enjoyed working with my UROP assistants Abraham Reyes, Vladimir Barzov, and Ian Jacobi, who have spent substantial amount of time and arduous efforts in making the experimental program successful.

I will always have my cordial appreciation and love to my parents, Francis and Landy Au, my uncle and aunt, Dr. Larry and Frances Lee, and my brother, Ned Au, who have been very supportive throughout the years.

Finally, I would like to give my deepest appreciation to the love of my life, Joanne Seto, for her unconditional love, support, and care. Without her sacrifice and tenacity, I would never have had such an enjoyable experience at MIT. I dedicate this thesis to her as a diminutive way of saying *thank you*.

TABLE OF CONTENT

CHAPTER 1	INTRODUCTION	14
1.1	Background	14
1.2	Research Motivation and Objective	16
1.3	Research Scope and Approach	17
1.4	Thesis Organization	18
CHAPTER 2	LITERATURE REVIEW	24
2.1	Material Systems	24
2.1.1	FRP Composites and Their Durability	24
	A. An Overview on FRP Composites	24
	B. Fiber Reinforcement	26
	C. Resin Matrix	27
	D. Mechanical & Other Properties	28
	E. Durability	31

2.1.2	Structural Adhesives and Their Durability	36
	A. Adhesive Classification	37
	B. Epoxy Base, Hardeners, and Additives	38
	C. Durability	39
	D. Adhesion Mechanism	41
2.1.3	Concrete Durability	42
2.2	Structural Systems	44
2.2.1	Debonding in FRP/Concrete Systems	44
	A. Definition of Debonding	44
	B. Experimental Observations	44
	C. Possible Causes of Debonding	45
	D. Debonding Models	45
2.2.2	Environmental Degradation of FRP Bonded Concrete	48
	A. Strength Approach Studies	49
	B. Fracture Approach Studies	49
2.3	Theoretical Background of Critical Phenomena	50
2.3.1	Moisture Diffusion	50
	A. Overview	50
	B. Types of Diffusion Behavior	51
	C. Diffusion Coefficient	52
	D. Estimation of Time to Saturation	53
2.3.2	Interface Fracture	54
	A. Overview	54
	B. Bi-material Elasticity	54
	C. Interface Fracture Energy Release Rate in a Bi-layer	55
	D. Crack Kinking	57
2.4	Summary Comments	58
 CHAPTER 3 QUANTIFICATION OF DEBONDING A TRI-LAYER FRACTURE TREATMENT		 69
3.1	Strength-Based Approach vs. Fracture-Based Approach	69

3.2	Need for a New Tri-Layer Interface Fracture Model	71
3.3	Energy Arguments	72
3.4	Interface Fracture Models and Solutions	73
3.5	Specialized Solutions for Debonding in Peel & Shear Fracture Specimens	81
3.5.1	Solutions for Debonding under Peel	81
3.5.2	Solutions for Debonding under Shear	82
3.5.3	Solutions for Debonding under Combined Peel and Shear	83
3.6	Verification Studies	84
 CHAPTER 4 MATERIAL CHARACTERIZATION & MOISTURE DIFFUSION SIMULATION		 94
4.1	Material Description	94
4.2	Epoxy Specimen Preparation	96
4.3	Conditioning and Test Environments	97
4.4	Choice of Water for Conditioning	97
4.5	Moisture Sorption Studies – Material Test Program Part 1	98
4.5.1	Moisture Uptake Behavior	99
4.5.2	Activation Energy of Moisture Diffusion	100
4.5.3	Discussions of Diffusion Behavior in Epoxies	101
4.6	Thermal Analysis of Epoxies – Material Test Program Part 2	102
4.6.1	Effect of Moisture on Glass Transition Temperature	106
4.6.2	Effect of Post-Curing at Elevated Temperature on Glass Transition Temperature	106
4.7	Mechanical Property Characterization – Material Test Program Part 3	107
4.7.1	Concrete Characterization	108
4.7.2	Epoxy Characterization	110
	A. Tensile Test	110
	B. Shear Test	113
4.8	3-D Moisture Diffusion Simulation	118
4.8.1	Solution Techniques	118
4.8.2	The Model	119

CHAPTER 5	INTERFACE FRACTURE TEST PROGRAM PEEL & SHEAR CHARACTERIZATION	138
5.1	Selection of Specimen Configurations	139
5.2	Specimens	140
5.2.1	Dimensions	140
5.2.2	Concrete Surface Preparation	141
5.2.3	Bond Length Determination Using Micro-Strain Profile Analysis	141
5.3	Fracture Test Program	143
5.4	Fracture Test Setup	144
5.4.1	Peel Fracture	144
5.4.2	Shear Fracture	144
5.5	Results	146
5.5.1	Failure Modes	146
	A. Peel Fracture Modes	146
	B. Shear Fracture Modes	147
5.5.2	Load-Displacement Behavior	148
	A. Peel Fracture Behavior	148
	B. Shear Fracture Behavior	149
5.5.3	Interface Fracture Toughness	150
	A. Peel Fracture Toughness	154
	B. Shear Fracture Toughness	155
CHAPTER 6	INTERFACE FRACTURE ANALYSIS OF FRP DEBONDING AFFECTED BY MOISTURE	178
6.1	Effect of Moisture on Debonding Resistance	179
6.1.1	Effect on Peel Fracture Toughness	179
6.1.2	Effect on Shear Fracture Toughness	181
6.2	Effect of Moisture on Locus of Fracture	182
6.2.1	Locus of Fracture for Dry Specimens	183
	A. Mode Separation Analysis by Finite Element Method	184
	B. Effect of Negative K_{II}^*	187

6.2.2	Locus of Fracture for Wet Specimens	188
A.	Possible Existence of Weak Interphase	189
B.	Possible Existence of Tough Interphase	190
C.	Possible Non-Existence of Interphase	190
6.3	Plasticity in the Debonding Process	190
 CHAPTER 7 SUMMARY, CONCLUSION, & FUTURE WORK		 200
7.1	Research Approach	201
7.2	Summary of Research Results	202
7.2.1	Tri-Layer Interface Fracture Model Development	202
7.2.2	Constituent Material Characterization	203
7.2.3	3-D Moisture Diffusion Simulation	204
7.2.4	Interface Fracture Characterization	205
7.3	Conclusion	207
7.4	Contributions	208
7.5	Future Work	209
 BIBLIOGRAPHY		 211
 APPENDIX		 236
1.	Finite Element (ABAQUS) Input File for 3-D Moisture Diffusion Simulation	237
2A.	Finite Element (ABAQUS) Input File for Global Peel Modeling	243
2B.	Finite Element (ABAQUS) Input File for Global Shear Modeling	247
3A.	Finite Element (ABAQUS) Input File for Computation of J -Integral and Mode Separation under Peel	251
3B.	Finite Element (ABAQUS) Input File for Computation of J -Integral and Mode Separation under Shear	253

LIST OF FIGURES

Figure 1.1	Flexural Strengthening Using carbon FRP Laminates	20
Figure 1.2	Anchorage Schemes at Laminate Ends	21
Figure 1.3	Differential Crack Mouth Movements Causing Debonding (Kaiser 1989)	22
Figure 1.4	Research Plan	23
Figure 2.1	Ductile and Non-Ductile Creep Behavior	60
Figure 2.2	Debonding Scenarios in the Vicinity of the Interface	60
Figure 2.3	Debonding Failure Under End Anchorage (Gunes 2004)	61
Figure 2.4	Common Causes of Debonding	62
Figure 2.5	Conceptual Illustration of Interfacial Stresses	63
Figure 2.6	Peel Test Setup (Karbhari et al 1996)	64
Figure 2.7	Illustration of Case I and Case III Diffusion Behavior (Crank 1975)	65
Figure 2.8	Typical Pseudo-Fickian Moisture Uptake Curve	65
Figure 2.9	Fracture of Isotropic Material versus Bi-material	66
Figure 2.10	Conventions and Geometry for an Interface Crack	66
Figure 2.11	Values of Dundurs Parameters for Selected Bi-material Combinations	67
Figure 2.12	Interface Crack in a Bi-Layer (Hutchinson and Suo 1992)	68
Figure 2.13	Substrate Crack in a Bi-Layer (Hutchinson and Suo 1992)	68
Figure 3.1	Possible Debonding Locations	86
Figure 3.2	Model Idealization and Definition of Debonding Between Layers 2 & 3	86
Figure 3.3	Idealization & Definition of All Debonding Scenarios	87
Figure 3.4	Resemblance of Local Debonding Region	89
Figure 3.5	Peel Fracture Model	90
Figure 3.6	Shear Fracture Model	90
Figure 3.7	Fracture Under Angular Load	91
Figure 3.8	Deformed Mesh in the Crack Tip Vicinity of the Peel Model	92
Figure 3.9	Deformed Mesh in the Crack Tip Vicinity of the Shear Model	93
Figure 4.1	Micrographs of Fracture Surfaces of Cured Epoxy 1 and Epoxy 2	120
Figure 4.2	Moisture Sorption Test Matrix	121

Figure 4.3	Mass Uptake Curves for Concrete	122
Figure 4.4	Mass Uptake Curves for CFRP	122
Figure 4.5	Mass Uptake Curves for Epoxy 1 and Epoxy 2	123
Figure 4.6	Loss of Transparency of Epoxy 2 after Moisture Conditioning	123
Figure 4.7	DMA 3-Point Bend Test Setup	124
Figure 4.8	Typical Plots from DMA and the Definition of T_g	124
Figure 4.9	T_g versus M_r for Epoxy 1 and Epoxy 2	125
Figure 4.10	Effect of Elevated Temperature Post Curing on Thermal Property Stability of Ambient-Cured Epoxies	126
Figure 4.11	Mechanical Test Matrix	127
Figure 4.12	Concrete Specimens & Mechanical Test Configurations	128
Figure 4.13	Concrete Compressive Properties vs. Moisture Uptake	129
Figure 4.14	Concrete Tensile Strength vs. Moisture Uptake	130
Figure 4.15	Concrete Mode I Fracture Toughness vs. Moisture Uptake	130
Figure 4.16	ASTM D638 Type I Dumbbell Shaped Epoxy Tensile Specimen	131
Figure 4.17	Epoxy Tensile Properties vs. Moisture Uptake	132
Figure 4.18	Crazing and Shear Banding Developed in the Gage Length of Epoxy 2 Tensile Specimen	133
Figure 4.19	ASTM D732 Punching Shear Tool	134
Figure 4.20	Epoxy Shear Strength vs. Moisture Uptake	135
Figure 4.21	3D Moisture Diffusion Finite Element Model	136
Figure 4.22	Snapshots of Moisture Concentration at the Epoxy/Concrete Interface	137
Figure 5.1	Traditional Interface Fracture Specimens	156
Figure 5.2	Example of a FRP Bonded Concrete Sandwiched Specimen	157
Figure 5.3	Chosen Interface Fracture Specimens	158
Figure 5.4	Dimensions of Specimens	159
Figure 5.5	Pneumatic Needle Scaler	160
Figure 5.6	Surface Strain Variation under Shear Load	161
Figure 5.7	Determination of Bond Length for Shear Fracture Specimens Using Micro-Strain Profile Analysis	161
Figure 5.8	Fracture Test Matrix	162

Figure 5.9	Fracture Specimens under Ambient Cure	162
Figure 5.10	Peel Fracture Test Setup	163
Figure 5.11	Shear Fracture Test Setup	164
Figure 5.12	Shear Slip Response Due to Different Target Locations	165
Figure 5.13	Typical Epoxy 1 Peel Fracture Modes	166
Figure 5.14	Typical Epoxy 2 Peel Fracture Modes	167
Figure 5.15	Typical Epoxy 1 Shear Fracture Modes	168
Figure 5.16	Typical Epoxy 2 Shear Fracture Modes	169
Figure 5.17	Typical Epoxy 1 Load-Deformation Curves under Peel	170
Figure 5.18	Typical Epoxy 2 Load-Deformation Curves under Peel	171
Figure 5.19	Typical Epoxy 1 Load-Deformation Curves under Shear	172
Figure 5.20	Typical Epoxy 2 Load-Deformation Curves under Shear	173
Figure 5.21	Peel Fracture Toughness Variation of Epoxy 1	174
Figure 5.22	Peel Fracture Toughness Variation of Epoxy 2	175
Figure 5.23	Shear Fracture Toughness Variation of Epoxy 1	176
Figure 5.24	Shear Fracture Toughness Variation of Epoxy 2	177
Figure 6.1	Correlation of Moisture Concentration in the Peel Fracture Region	192
Figure 6.2	Atypical Variation of Epoxy 1 Peel Fracture Toughness	193
Figure 6.3	Correlation of Moisture Concentration in the Shear Fracture (Bond) Region	194
Figure 6.4	Atypical Variation of Epoxy 1 Shear Fracture Toughness	195
Figure 6.5	Variations of Fracture Energy Release Rate Ratios with Phase Angle (Hutchinson and Suo 1992)	196
Figure 6.6	Effect of Negative K_{II}^*	197
Figure 6.7	Possible Existence of Interphase between Epoxy and Concrete	197
Figure 6.8	Correlation of the Peel G Model	198
Figure 6.9	Correlation of the Shear G Model	199

LIST OF TABLES

Table 3.1	Summary of G Model Cases	74
Table 3.2	Solutions of $A_{1,k}$ and $I_{1,k}$	79
Table 3.3	Solutions of $A_{2,k}$ and $I_{2,k}$	80
Table 3.4	Solutions of $A_{3,k}$ and $I_{3,k}$	80
Table 3.5	Eccentricities	83
Table 3.6	Model Parameters	85
Table 3.7	Result Comparison	85
Table 4.1	Moisture Diffusion Properties	99
Table 4.2	Activation Energy Parameters	101
Table 4.3	DMA Test Results of Epoxy 1	104
Table 4.4	DMA Test Results of Epoxy 2	105
Table 4.5	Initial Properties of Concrete	109
Table 4.6	Initial Tensile Properties of Epoxies	110
Table 4.7	ASTM D638 Test Results on Tensile Properties of Epoxy 1	111
Table 4.8	ASTM D638 Test Results on Tensile Properties of Epoxy 2	112
Table 4.9	ASTM D732 Test Results on Shear Strength of Epoxy 1	114
Table 4.10	ASTM D732 Test Results on Shear Strength of Epoxy 2	116
Table 5.1	Correspondence of Conditioning Duration & M_t/M_s	143
Table 5.2	Basic Parameters Used to Compute Interface Fracture Toughness	151
Table 5.3	Interface Peel Fracture Toughness	152
Table 5.4	Interface Shear Fracture Toughness	153
Table 6.1	Dry Fracture Toughness	183
Table 6.2	Mode Separation for Case 2	188
Table 6.3	Wet Fracture Toughness	189

CHAPTER 1

INTRODUCTION

1.1 Background

Fiber reinforced plastic (FRP) materials have become increasingly popular in civil infrastructure applications since the 1990s (Saadatmanesh and Ehsani 1990, Ritchie et al 1991). Existing applications include concrete internal reinforcements, pre- and post-stressing tendons, external strengthening and repair, as well as all-composite structural systems. In particular, FRP strengthening and repair of reinforced concrete (RC) elements such as beams, slabs, and bridge decks have been predominant owing to the increasing number of substandard structures as a result of design code revision, physical aging, environmental deterioration, and inadequate maintenance (Gunes 2004). FRP has become increasingly attractive due to its inherent advantageous mechanical properties, lightness, corrosion resistance, and decreasing cost of the composite materials. Carbon, glass, and aramid composites are most widely used nowadays.

For flexural strengthening, lightweight FRP laminates in the form of strips and sheets are often bonded to the soffits of the RC elements, such as those shown in Figure 1.1, using a thixotropic ambient-cured epoxy that is designed to possess relatively high

viscosity for in-situ overhead applications. These epoxy materials are thicker than most elevated-temperature cured epoxy commonly found in aerospace applications and they usually have a bond line thickness the same order as the FRP laminate itself. In some cases, the epoxy manufacturers pre-process the epoxy and hardener components into a solid base material to provide better troweling capability (Sika 2004).

Ample research can be found in the literature in regards to the analysis and design of such retrofitted systems. The level of understanding of the short-term mechanical behavior has reached a point that construction specifications were recently made available (ACI-440 2001, NCHRP 10-59 2004). Experimental investigations on large-scale retrofitted RC beams (Triantafillou and Plevris 1992, Buyukozturk and Hearing 1998, Gunes 2004) have indicated that failures usually take place through various possible mechanisms, depending on the concrete grade, rebar provision, and properties of FRP. Identified failure modes include: (1) concrete crushing before steel yielding; (2) steel yielding followed by concrete crushing; (3) steel yielding followed by FRP rupture; (4) shear failure; (5) concrete cover delamination; and (6) debonding in the vicinity of the FRP bond interface. Failure modes 1, 2, and 3 are considered flexural failures while 5 and 6 are considered debonding modes. From a structural design standpoint, failures 2 and 3 are the favorable modes as they exhibit ductile failures that demonstrate the best use of material limits. The rest are usually premature and of brittle nature.

Brittle debonding has been particularly observed at laminate ends due to high concentration of shear and peel stresses at discontinuities where shear cracks in concrete are likely to develop. Various methods of anchorage such as anchor bolts, L-shaped plates, and U-wraps, have been devised and proved effective to prevent FRP debonding from plate ends (Sharif et al 1994, Garden and Holloway 1998, Khalifa et al 1998, 2000, Smith and Teng 2001, Gunes 2004). Figure 1.2 illustrates some of such anchorage schemes.

Provision of end anchorages seems to have forced debonding failures to take place elsewhere such as within the retrofit span (Hassanen and Raof 2001). Unfortunately, debonding at such locations is considered more challenging to tackle as the beam soffit often already consists of anomalies and discontinuities such as shear and flexural cracks prior to bonding (Hearing 2000, Ali et al 2001). Debonding can be

initiated by crack widening and differential vertical movements of the crack mouths that are induced by external loading and the interface crack will propagate toward plate ends. Figure 1.3 shows a close-up illustration of such a phenomenon.

Furthermore, it has been recognized that debonding could affect the capacity of the retrofitted system to a great extent and is considered an undesirable premature failure mode (Kaiser 1989, Gunes 2004). Regardless of where debonding is initiated, concrete delamination has been the most observed debonding mode from both large-scale beam tests and mesoscale shear and peel tests (Smith and Teng 2001). The cause of such is generally pointed toward the fact that concrete is the weakest and most brittle material in the interfacial bond region. Other failures such as FRP delamination and adhesive decohesion have also been observed but do not appear as frequently. Interface separation modes such as FRP/adhesive separation and adhesive/concrete separation are believed to be highly unlikely to occur and have not been reported in short-term tests so far (Gdoutos et al 2000).

1.2 Research Motivation and Objective

While short-term mechanical and debonding behaviors of such retrofitted systems have been studied quite extensively, long-term performance and durability issues with respect to the effects of moisture ingress, thermal cycles, freeze-thaw actions, and coupling of environmental and mechanical loading remain largely uncertain and unanswered. In particular, little understanding has been developed regarding the effect of moisture on the stability and bond properties of these FRP retrofitted concrete systems which essentially govern the lifecycle and effectiveness of the retrofit itself. Realistically, moisture could diffuse into the interfacial bond region through the adjoining concrete, existing crack mouths, and around the bond lines. Once moisture is trapped in the region, it could be difficult to recover the dryness due to the nature of the materials and the bond configurations. The retained moisture could then lead to bond deterioration and might cause premature debonding at an even earlier stage.

This current research therefore attempts to investigate the effect of moisture on FRP bonded concrete systems by (1) quantifying debonding failures as affected by moisture, (2) determining the role of moisture as an external environmental agent in the

debonding process, and (3) understanding the mechanistic behavior of the associated debonding failure modes, in FRP bonded concrete that simulates the possible debonding behavior from within the retrofit span in a flexurally strengthened/repaired concrete system that is prone to moisture attack.

1.3 Research Scope and Approach

To achieve the research objectives, an interface fracture mechanics approach is adopted to examine the problem by means of a research plan that consists of both experimental and analytical studies, as shown in Figure 1.4. Central to the investigation is the interface fracture toughness being the quantification parameter of the debonding problem, which provides the means to compare, correlate, and analyze the observed behavior. Computation of the interface fracture toughness requires the development of a new tri-layer fracture model that contains parametrically the material and geometric information of the FRP bonded concrete system because conventional bi-layer fracture models (Hutchinson and Suo 1992) is not sufficient to handle this particular layered system as a consequence of the thick bond lines resulted from the viscous adhesives popularly used in the retrofit industry.

Debonding characterization is conducted using meso-level peel and shear fracture models that consist of real scale bond lines. These physical models undergo accelerated conditioning to achieve various levels of moisture diffusion in the interfacial bond region. The conditioned samples are then mechanically tested at selected time intervals in standard laboratory conditions so that the change in bond fracture toughness and debonding behavior with respect to time or moisture content can be captured. Moisture concentration in the bond region for the selected time intervals are assessed by means of three-dimensional finite element diffusion simulations, of which the required input of diffusion properties for each constituent materials are determined by moisture uptake tests. Also, mechanical properties of the respective constituent materials at the selected time intervals that correspond to a certain level of moisture concentration of the bonded system are needed as inputs to compute the interface fracture toughness of the bond. Material tests on samples that undergo identical accelerated conditioning environments

are thus performed accordingly to establish the trend of mechanical property changes with increasing moisture uptake.

With the experimentally determined fracture toughness values, moisture diffusion information from finite element simulations, and observed debonding failure modes, interface fracture analysis can then be conducted to determine the role of moisture in the debonding process, as well as to understand the associated mechanistic behavior. Crack kinking criterion is first implemented, using experimental data, to examine and correlate the observed debonding modes and theoretical predictions. Finite element fracture analysis and mode-mix characterization is then performed to understand the mechanics near the crack tip and interfacial region and as to how the crack propagates during the debonding process under peel and shear loading configurations. The role of moisture can then be determined by relating the analytical results and by comparing various observed debonding modes obtained from fracture tests.

1.4 Thesis Organization

This thesis consists of six subsequent chapters.

Chapter 2 reviews comprehensively state-of-the-art knowledge regarding moisture degradation in FRP bonded concrete systems. Discussions are approached from both the material and structural standpoints. Theoretical backgrounds on moisture diffusion and interface fracture, the two important phenomena central to this research, are also laid out.

Chapter 3 develops the tri-layer fracture energy model, which forms the foundation of this research. Derivation concepts and procedures are detailed and the full set of solutions that describe the possible distinct interface fracture scenarios with fairly general boundary conditions are presented. Specialized solutions that correspond to peel and shear loading configurations are also developed for use in subsequent chapters.

Chapter 4 presents the results from the extensive material testing that characterizes material properties with increasing moisture content. Results from gravimetric sorption tests, which lead to the determination of diffusion coefficients, are also presented. Finally, the three-dimensional moisture diffusion simulation will be

presented and discussed. This chapter forms the basis for subsequent fracture toughness evaluation, debonding mode interpretation, and interface fracture analysis.

Chapter 5 details the fracture test program that features both peel fracture and shear fracture characterizations of mesoscale FRP bonded concrete models. Sample preparation, experimental setup, loading and instrumentation are discussed. Results including load-displacement behavior, fracture toughness variations, and debonding modes are presented and summarized.

Chapter 6 analyzes the debonding problem by means of an interface fracture approach, which consists of finite element fracture computation, mode-mix characterization, and kink criterion implementation. The analysis represents a synergistic effort that integrates the knowledge developed in all prior chapters including material test results, interface fracture toughness values, three-dimensional moisture diffusion behavior, and observed failure modes into the interface fracture analytical interpretations. The role of moisture on the crack propagation behavior and debonding mode is extensively discussed from a fracture mechanics point of view.

Chapter 7 summarizes the thesis and draws conclusions from the work. Areas for future investigation are also presented.

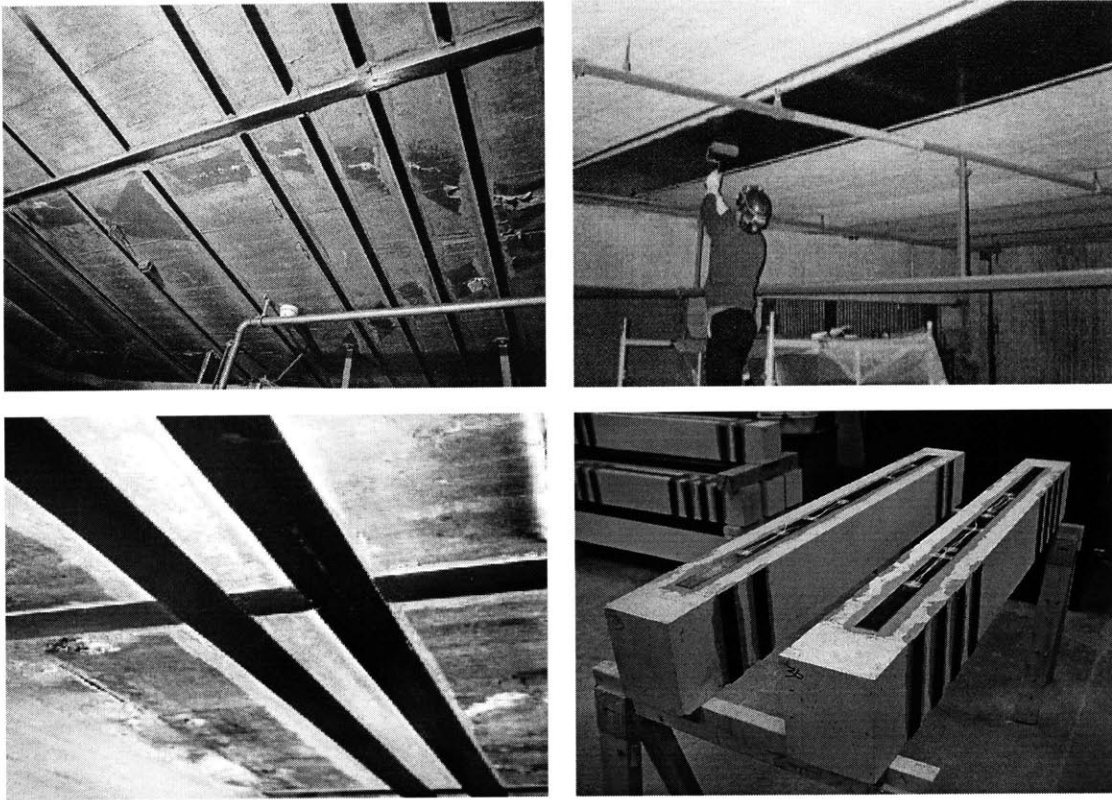


Figure 1.1 Flexural Strengthening Using carbon FRP Laminates

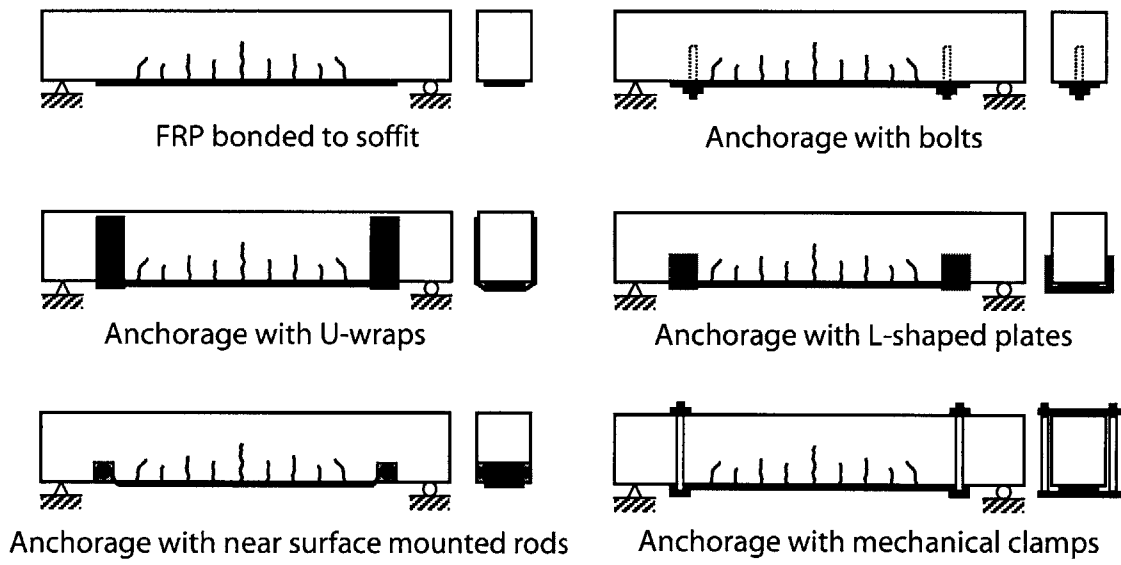
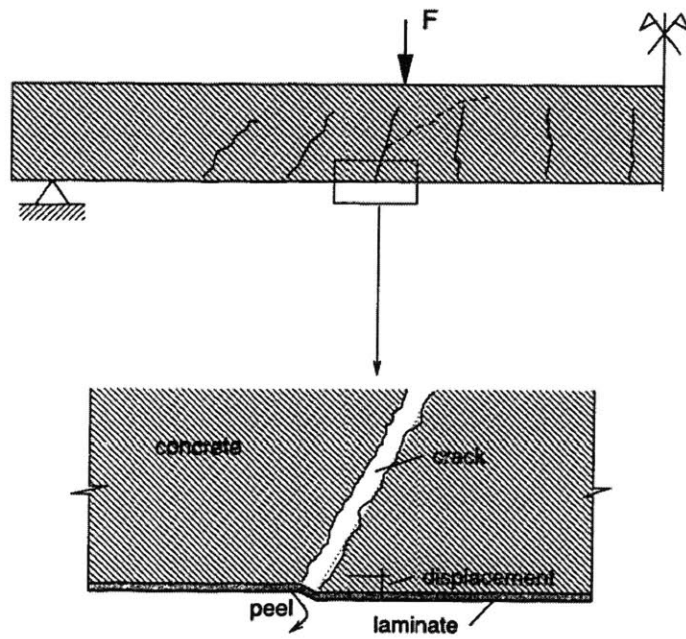


Figure 1.2 Anchorage Schemes at Laminate Ends



**Figure 1.3 Differential Crack Mouth Movements Causing Debonding
(Kaiser 1989)**

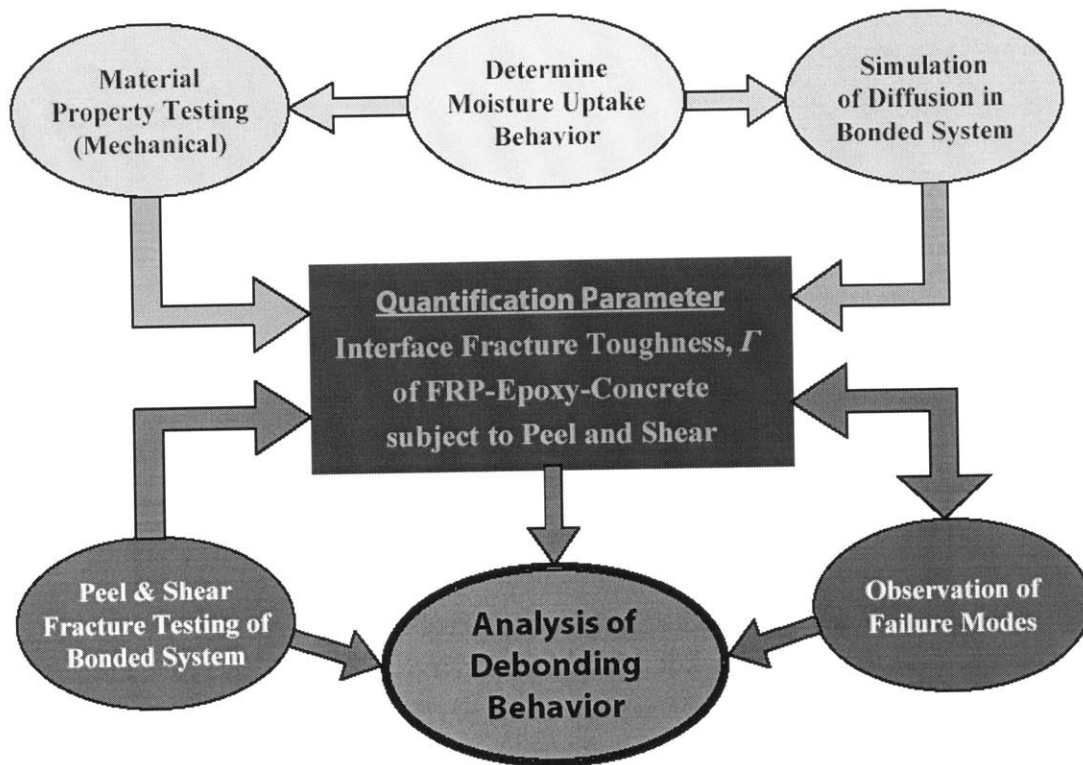


Figure 1.4 Research Plan

CHAPTER 2

LITERATURE REVIEW

Lifecycle of a FRP retrofitted flexural RC system that involves external adhesive bonding hinges upon the quality and stability of the bond as well as the durability of the constituent materials in the interfacial region. This Chapter provides a comprehensive overview of the state-of-the-art knowledge regarding moisture degradation in FRP bonded concrete systems and its related durability areas from both the material and structural standpoints. Theoretical backgrounds on moisture diffusion and interface fracture, the two important phenomena central to this research, are also laid out.

2.1 Material Systems

2.1.1 FRP Composites and Their Durability

A. An Overview on FRP Composites

FRP composites are defined as the materials that consist of fibers embedded in a resin matrix. The aim of combining fibers and resins that are different in nature is to take advantage of the distinctive material features of either component to result in an engineered material with desired overall composite action for specific applications.

Engineering properties of FRP composites for structural applications, in most cases, are dominated by fiber reinforcements. More fibers usually give rise to higher strength and stiffness. Excessively high fiber/matrix ratios may, however, lead to strength reduction or premature failure due to internal fracture. Fiber lengths and orientations can also affect the properties considerably.

Resin matrix is an adhesive that supports the fibers from buckling under compressive stress, binds the fibers together through cohesion and adhesion, protects the fibers from physical and chemical attacks and micro-cracking during service, and provides shearing strengths between FRP laminas. Shearing strength is essential to resist delamination, lap joint failure and impact forces.

Structural FRP composites are generally high strength, reasonably stiff, environmentally resistant, and significantly lighter than conventional construction materials such as concrete and steel. After more than 6 decades of development, FRP composites have started to penetrate into the construction industry to a larger extent as a result of lower material cost and higher commercial utilization in a wider spectrum with applications including vehicles, sporting goods, and electronic equipments. In the existing civil engineering sector, FRP composites have found their use mostly in repair and strengthening, and as internal reinforcement.

FRP composites can be manufactured using a variety of processes to produce different sizes and shapes to suit a particular application. Some of the existing structural forms include one-dimensional reinforcing bars, two-dimensional reinforcing grids, prestressing tendons, bridge cables, strengthening sheets and plates, three-dimensional weaved fabrics, confinement jackets, pultruded structural shapes, bridge decks, sandwich cores, and piles.

Choice of particular types of fibers and resins depends on the specific applications. Load-bearing capacity, level of exposure, wear resistance, temperature and frequency ranges, fire and water resistance, and costs are some of the important issues that need to be thoroughly considered. For instance, the choice of FRP composite materials for retrofitting a group of columns inside a parking lot would be different than that for building a FRP deck in an offshore structure due to different service environments and loading conditions.

B. Fiber Reinforcement

Reinforcing fibers can be manufactured with an abundance of materials, ranging from titanium to carbon, to polystyrene, and even to basalt. In the construction industry, however, glass, carbon, and aramid fibers are the most popular choices due to their distinctive properties. Each type will be briefly introduced below.

Glass Fiber

Glass fibers are mainly categorized into E-glass and S-glass. The “E” in E-glass is abbreviated from “Electrical”; the “S” in S-glass is abbreviated from “Structural”. In general, E-glass possesses excellent electrical insulation characteristics while S-glass has higher strength and greater corrosion resistance. Both types of glass fibers are calcium aluminoborosilicate formulations. They are inorganic and do not support combustion. E-glass fibers are considered the industry standard and cost less than the S-glass fibers. Typical tensile strength and stiffness of E-glass fibers are about 3.5 GPa (500 ksi) and 72.5 GPa (10.5×10^6 psi) respectively. S-glass fibers, however, have higher strengths due to their higher alumina content. In spite of their chemical resistance, fire resistance, and high tensile strength, glass fibers have a significant drawback. The fiber surface is prone to moisture attack under certain conditions of exposure and above certain stress levels. This attack normally lead to stress-rupture failure if no appropriate remedial measure is provided (Peters 1998, Kelly 1989, Weeton et al 1987).

Carbon Fiber

Carbon fibers are produced by the thermal decomposition of organic precursor fibers such as rayon or polyacrylonitrile (PAN), followed by a stabilization and carbonization procedure. Other alternative precursors are coal, petroleum, and synthetic pitches. The fabrication involves a spinning process. Tensile strength of PAN-based fibers has always been higher than the pitch-based fibers. Therefore, most carbon fibers today are PAN-based. The typical tensile strengths of carbon fibers are 4.1-5.2 GPa (600-750 ksi), at the higher end of the S-glass fiber strengths, or about 20 times that of A36 structural steel. Some even have strengths as high as 6.9 GPa (1000 ksi), which are less consumed in the industry because of their high production cost. Carbon fibers are in

general more brittle than glass fibers. But they show exceptional fatigue resistance. Stiffness ranges from lower than to exceedingly higher than structural steel and has a wide range from 120 GPa (17.5×10^6 psi) to more than 800 GPa (116.3×10^6 psi) (Peters 1998, Kelly 1989, Chung 1994, Weeton et al 1987).

Aramid Fiber

Aramid fibers are aromatic polyamide formulations that are organic in nature. They can be categorized into two main types – para-aramid and meta-aramid fibers. Para-aramid fibers have higher strength and are normally used in high performance applications. One well-known trade name for para-aramid fibers is the Kevlar fibers. Due to their highly aromatic and ordered structure, aramids have very high thermal resistance. They do not melt prior to decompositions and do not burn when the flame source is removed, although they can be ignited. Compared to inorganic fibers like carbon or glass, aramid fibers are superior in fire resistance because the fibers themselves do not readily conduct heat into the matrix. The typical decomposition temperature is around 450°C . The typical tensile strength and stiffness are 2.8 GPa (400 ksi) and 104 GPa (15×10^6 psi) respectively. Another advantage of aramid fibers is that they have very high fracture toughness and hence impact resistance. One major drawback, however, is their weak bending and compressive strengths. Aramid fibers easily buckle or kink under compression forces. Also, adhesion to most resin matrix is low and moisture absorption is high (Peters 1998, Kelly 1989, Shook 1986).

C. Resin Matrix

Resin matrix is broadly categorized as thermoplastics and thermosets. Thermoplastic resins can return to their original liquid state upon heat and pressure while thermoset resins cannot once they have been cured. So far, thermoset resins are dominant in structural applications due to their excellent mechanical properties, limited shrinkage upon curing, and good viscosity during processing temperatures (Eckold 1994, Barbero 1998, Peters 1998). They consist of three-dimensional polymer network that is cross-linked to form a stiff, strong, and brittle resin. Additives such as rubber particles in the micron scale are usually used to toughen the resin to prevent fracture failure. Epoxy,

vinyl ester, polyester, and phenolic resins are the most commonly used thermosets. In particular, epoxy and polyester resins are described below.

Epoxy Resin

Epoxy, which is a strong high performance resin, provides excellent adhesion to a wide variety of fibers due to its inherent polar nature. After curing, the material has a low level of shrinkage and releases no volatile by-product that can cause bubble or void formation. Yet, epoxy has a tendency to absorb moisture both in the cured and uncured stages. Its elongation-to-failure is also relatively low, which makes it only applicable to stiffness control structures that have small deformations. Room temperature and heat accelerated curing are possible (Peters 1998, U.S. Army 1997).

Polyester Resin

Polyester resin has generally excellent mechanical properties and very good environmental durability. Polyester resins have excellent UV resistance and can be formulated to be very chemical resistant. Compared to epoxy resin, polyester resin is less costly. However, it does not provide adequate adhesion to carbon and aramid fibers. Shrinkage due to curing is also relatively large. Owing to the adhesion problem, polyester resin usually goes with glass fibers. Use of polyester resin with carbon and aramid fibers is less common. Room temperature and heat accelerated curing are possible (Peters 1998, U.S. Army 1997).

D. Mechanical & Other Properties

Combining fibers and resins under different fabrication processes, distinctive FRP systems can be manufactured for different structural applications. For civil engineering retrofit applications, two-dimensional laminates remain dominant. Mechanical properties of FRP composites are the weighted average of those of fibers and resins. Rule of mixtures are normally applied to estimate strength and stiffness of a FRP composite material that is composed of a particular type of fiber and resin. Owing to the relative brittleness of FRP composites (in the fiber direction), strength values from experimental testing normally exhibit a higher variance than those of other construction materials like

steel. The use of the rule of mixtures or the micro-mechanics approach does not predict strength very well. Statistical approaches such as Weibull analysis are thus required for appropriate quantification (Military Handbooks, Dally and Riley 1991). On the contrary, stiffness values from testing are relatively uniform and can be predicted with high accuracy using micro-mechanics formulation (Jones 1999).

Density

Compared to steel and concrete, FRP composites are about 1.5 to 5 times lighter. For example, carbon/epoxy composites (AS-4/3501-6) has a density of 1.6 g/cm^3 compared to 7.9 g/cm^3 of steel and 2.4 g/cm^3 of concrete. This lightweight characteristic not only leads to very high specific strength and specific stiffness, hence high load-taking efficiency with decreased structural weight, but also has strong implication on reduced costs of transportation, handling, and construction.

Strength

Tensile strength of FRP composites ranges from about that of mild steel to more than that of prestressing steels, depending on the fiber types, arrangements, orientation, and production. While compressive strength of steel is identical to its tensile strength, the compressive strength of FRP composites is normally less than the tensile counterpart due to fiber buckling failure. Yet, the strengths of commercial FRP composites are tremendous compared to any conventional construction materials. In situations where high tensile and compressive strengths are considered assets, FRP composites offer strong incentive for use. Some of such situations include tensile and flexural members, as well as fatigue sensitive and small-deflection stiffness control designs.

Shear strength of all unidirectional laminates is relatively low since this parameter is mainly controlled by the strength of resin in such FRP systems. However, for a laminate that is made up of multiple plies, fibers can be designed to the particular orientation that matches with the maximum shear stress. In such case, shear strength is provided by the fibers, which act in tension, instead of the resin.

Stiffness

Stiffness of FRP composites ranges widely and has strong correlation with fiber content, continuity, and orientation. Glass FRP generally has lower stiffness than carbon FRP while the latter can have a magnitude from half of the stiffness of ordinary structural steel to higher than that of high strength steel. One unique feature about FRP composites is that the material exhibit linear or nearly linear stress-strain phenomenon throughout their load carrying range, meaning that the stiffness does not change over their load history. This behavior is significantly different from that of steel and concrete in which reduction of stiffness occurs even when the applied stress has not quite yet reached the ultimate material capacity.

Coefficient of Thermal Expansion

Unlike all other construction materials that civil engineers are acquainted with, many FRP composites (unidirectional laminates) shrink upon temperature increase. In particular, carbon and aramid FRP have negative coefficients of thermal expansion while that of glass FRP is positive (Barbero 1998, Jones 1999, Reddy and Murty 1992, Weeton et al 1987). Although resins expand upon heating, carbon and aramid fibers resist thermal expansion. The magnitude of thermal shrinkage of carbon fibers and thermal expansion of epoxy resins is about to cancel out each other and thus gives rise to an overall near-zero coefficient of thermal expansion for carbon/epoxy FRP. This property is of great significance in terms of residual stress development in the bond interface.

Electrical Conductivity

Electrical conductivity may be of great interest when provision of post-curing is desired for the bonding adhesives so as to boost higher the glass transition temperature to prevent viscoelastic responses during the service life. In fact, some companies who provide FRP retrofit materials have started to develop electrical heating systems that can be clamped onto the FRP plates to heat up the bond interface for further curing. As such, electrical conductivity of FRP composites is a parameter that is worth looking into.

For glass fibers, conductivity ranges from 10^{-10} to $10^{-14} (\Omega\cdot m)^{-1}$ while that of carbon fibers is 10^{-4} to $10^{-7} (\Omega\cdot m)^{-1}$, depending on the level of graphitization during the

manufacturing process. For comparison, AISI 304 stainless steel has a conductivity of $1.4 \times 10^6 \text{ } (\Omega \cdot \text{m})^{-1}$ and that of copper is $6.5 \times 10^7 \text{ } (\Omega \cdot \text{m})^{-1}$. In general, glass is classified as an insulator while carbon is in the semiconductor range (Kelly and Rabotnov 1985). In other words, post-curing of the bond line through electrical heating on carbon FRP composites systems is more feasible than that of glass. Nevertheless, electrical conductivity of FRP composites can be controlled by varying the ratio of mixtures and it has been reported that electrical conductivity of carbon FRP increases with fiber weight content up to 30%, beyond which poses no further reduction in resistivity (Kelly and Rabotnov 1985).

Delamination Strength

Delamination is a unique and major failure mode for FRP laminates. Delamination can occur, without through-thickness loading, at free edges and around a cut hole. Unloaded edge delamination is caused by inter-laminar normal stresses that peak at free edges. It has been observed that this kind of delamination could reduce static strength and fatigue life, but not stiffness (Jones 1999). Delamination failure can be mitigated by various means, including the use of toughened resin matrix, edge caps, interleaved adhesive layers at edges, and interlaced laminas to form a three-dimensional fiber network. The key is to provide enough strength to take inter-laminar normal stresses, either by the resin itself or by some fibers (Reddy and Murty 1992, Jones 1999). In FRP bonded concrete, delamination has also been observed as one of the failure modes, although not as frequent as concrete decohesion. This failure mode is often promoted by the lack of wetting of the adhesive being used.

E. Durability

To designers of FRP retrofitted systems, the main durability issues include but are not limited to thermal cycling, humidity, exposure to ultraviolet (UV) light, weathering, creep, and fatigue. Unlike other structural systems such as aircrafts, which have an average expected service life of less than 30 years (TPI Composites 2002), civil infrastructures and their retrofit systems are expected to last for 75 years and beyond (Volpe Center 2002). Durability is thus an extremely important topic of study.

Thermal Cycling

Thermal cycles such as that from freeze and thaw as well as from thermal extremes over seasonal changes can contribute to cyclic thermal fatigue. It has been observed that unless void content in the resin is high, freeze-thaw effect on strength within the normal civil engineering application temperature range of (+30 °C to -20 °C) is insignificant (U.S. Army 1997), although thermal aging at temperatures higher than 300 °C can degrade the mechanical properties due to oxidation of fibers and resins (Chung 1994). Resin systems that can resist very extreme temperatures for aerospace applications, however, have been developed and service conditions in civil engineering applications normally fall well within the comfort zone. Also, protective coating and special additives have been developed to tackle known problems of cyclic thermal fatigue and were found to be effective (Peters 1998).

Moisture Attack

Corrosion in the presence of moisture and oxygen is a well-known phenomenon in steel. Unlike steel, FRP is resistant to many chemicals and metal corrosive agents. Yet, moisture uptake could occur through the resin by nature, as will be discussed in more detail later. Moisture absorption is a function of void content, resin type, fiber type, temperature, applied stress, and presence of microcracks (U.S. Army 1997). Improperly manufactured FRP composites may result in high void content and development of microcracks upon curing. These will promote water ingress, which will cause swelling (in the transverse and out-of-plane directions) and property change of the resin. The water absorption phenomena may or may not be reversible, depending on the type of resin being used.

Glass fibers are prone to moisture attack upon prolonged contact due to the hygroscopic nature of the alkaline metallic oxides in the silica of glass. E-glass and S-glass, however, contain only trace amounts of such oxides and are relatively resistant to water damages. Aramid fibers can absorb large amount of water and can swell considerably. These fibers are, however, coated during fabrication, and thus are protected from moisture ingress in FRP laminates. Carbon fibers do not exhibit any degradation due to water (Mallick 1988). However, carbon FRP, when in direct contact with metals

(except platinum, gold, and titanium), will make metals corrode due to galvanic action (Chung 1994), although the rate needs to be determined experimentally for the specific metal at hand.

UV Radiation

Ultraviolet radiation (from sunlight) is known to harden and discolor (or chalk) polymeric resin matrix. Degradation, however, only takes place at the skin of the FRP laminates, as the material has a self-screening effect, although topcoat delamination may occur. For thicker composites, degradation effect on mechanical properties is minimal (U.S. Army 1997). Use of UV-resistant coating has been a popular tactic to substantially slow down or even eliminate the associated degradation. Coating ingredients may include UV screener, absorber, energy quencher, and light-stabilizing antioxidants (LSA). Each ingredient actively stabilizes each stage of the photo-degradation process (Calbo 1987).

UV screeners such as carbon black and titanium dioxide are the oldest form of UV protection materials for polymers. They have the ability to absorb light and increase photo-stability. UV absorbers (or UVA) such as 2-hydroxy-benzophenones, 2-cyano-3,3-diphenylacrylic acid and oxyanilides are colorless additives that can absorb light very intensely in the UV spectrum and safely dispose the absorbed energy as heat. Light-stabilizing oxidants such as hindered amine light stabilizers (or HALS) are used to terminate the free radicals resulted from the bond breaking due to unreleased energy absorbed, hence retarding thermal oxidation. The combination use of UVA and HALS is observed to provide the greatest UV protection effect.

It is found that a 40-micron coating containing 2% of UVA with the use of HALS can effectively protect a light-sensitive substrate from “seeing” UV light entirely. For maximum protection and minimum coating maintenance, UV resistant ingredients could be mixed into the polymer matrix during material processing as one of the additives. To fully characterize the resistance to UV radiation, accelerated testing must be performed in lieu of moisture and applied stress. The most common UV accelerated test is the Florida black box test (Calbo 1987).

Weathering

Weathering is the deteriorating action that alters the surface color, texture, and material properties of the structure. For FRP composites, resin matrix is responsible of protecting the structure from degrading upon prolonged exposure in outdoor environments. Degradation of the resin will not normally affect the mechanical properties of the FRP composites such as stiffness and strength in general, as long as the resin can still transfer and distribute external loads to the fibers and that they are not damaged. Also, weathering degradations mostly take place at the material surface. Degraded surface is usually shallow and it acts as a protective layer to the under layers from further degradation. (Wypych 1995)

Erosion weathering is seldom discussed in the open literature due to the lack of experience, although situations such as sandstorm erosion on an interstate highway structure may actually take place.

Creep

Creep is the time-dependent deformation under a constant load. Upon load removal, unrecoverable deformation occurs after some nominal recovery (besides elastic strain). Creep in FRP is a resin dominant behavior and is dependent on temperature, moisture, and the magnitude of applied stress. The behavior can either be ductile or non-ductile as shown in Figure 2.1 (Clarke 1996), depending upon the fiber contents. FRP laminates for structural applications normally have fiber contents as high as 60% and while the creep resistance is relatively high, the associated behavior is usually non-ductile. For this type of behavior, rate of creep diminishes with time until failure is reached. Non-ductile fast fracture occurs when the flaw grows to the critical size.

Thermosets such as epoxy resin are more creep resistant than thermoplastics due to their inherent cross-linking structures. Temperature intervenes by affecting molecular activities. More creep is usually observed at higher temperature. Moisture ingress due to high void contents, microcracks, fiber debonding or fracture, and ply delamination may lead to further weakening and damages of internal bonds and resin softening.

As inferred by the creep behavior, apparent material stiffness reduces with time. This apparent stiffness or creep modulus is less than the instantaneous modulus obtained

from short-term testing. For stiffness-control retrofitted structures, creep modulus of the FRP laminate must be used for design. Ideally, creep modulus should be obtained by direct experimentation on the FRP laminate in question. Such data are very scarce and application non-specific. Extrapolation of existing shorter-term creep data using a mathematical model like the Findley theory may thus be required (Jones 2001, Schapery and Sun 2000).

Besides using thermoset resins, high fiber content, and proper manufacturing technique to minimize defects in the matrix and the fiber-resin interface, the use of continuous and straight fibers with high stiffness and orientation that aligns with stress directions will also significantly increase creep resistance. High stiffness fibers attract more load and limit shear deformation in the matrix. Straight fibers also avoid the stress concentration that arise from crimps (for instance in weaved fabrics) and hence reduce creep strain. For unidirectional carbon FRP laminates with fiber content of 60% such as those carbon FRP plates most often used in beam retrofits, near zero creep can be resulted in the load direction (Clarke 1996). Yet, creep in the out-of-plane direction is still possible, if loads are applied normal to the plane (e.g. in the case of slab retrofit). Fibers or some kind of clamping must be provided in that direction to prevent creep from happening.

As a general rule of thumb, in the designs that minimize creep effects, it has been suggested that the material strains (in their own fiber directions) be limited to less than 0.1%. Where creep resistance is critical, fibers should be continuous, uncrimped, high strength and stiffness, and be provided with a volume fraction in excess of 50%. Also, the resin system should be selected to cater to temperature and moisture effects by allowing a conservative margin between the in-service temperature and the glass transition temperature (Clarke 1996).

Fatigue

Research to date indicates that FRP possess good fatigue resistance in tension-tension cycling (U.S. Army 1997), although the effects of moisture, temperature, reverse loading, long-term, and compressive load cycling have yet to be researched and documented. Long-fiber composites retain a high proportion of the short-term strength

after 10 million cycles. Amongst all FRP composites, carbon FRP exhibits the highest fatigue resistance. The stiff carbon fibers are able to bridge the cracks that occur across the matrix and hence reduce the stress intensity of the crack tip. With a high fiber content, between 50% and 70%, carbon FRP almost does not fatigue due to its high strength and stiffness, as fatigue is in essence a strain-induced phenomenon.

Fatigue behavior of carbon FRP is superior to that of steel (Chung 1994). Fatigue degradation occurs more substantially, however, in glass FRP. Glass fibers are comparatively less stiff and the stress transfer mechanism from the matrix to the fibers is less effective, making the matrix more prone to large stresses and strains, promoting crack development under fewer number of load cycles. Fatigue tests on glass FRP laminates indicated a deterioration of stiffness, especially at low cycle testing (Peters 1998). It was suggested that the deterioration was due to the creep behavior of the resin matrix. For all FRP composites, when the load direction and the fibers do not align, lower fatigue strength should be expected.

2.1.2 Structural Adhesives and Their Durability

An adhesive is a material which, when applied to surfaces, can join them together and resist their separation (Mays and Hutchinson 1992). Some of such materials include cement, glue, and paste. Structural adhesives, however, are mostly referred to as the monomer compositions that polymerize to yield fairly stiff and strong compounds that unite two similar or dissimilar adherends to form a stress transfer mechanism. For civil engineering applications, the choice and availability of structural adhesives are comparatively very limited as traditional mass-produce manufacturers have mostly tailored their products to suit the needs of other industries (e.g. aerospace and general manufacturing) that consume significantly of such materials. Recently, however, a handful of companies have started to develop dedicated adhesive materials for specific civil engineering applications such as FRP retrofitting.

Requirements of structural adhesives used in FRP retrofitting can be exceedingly demanding due to the stress transfer requirement, the need for in-situ curing, the long-term environmental effects that are being subjected to, and the expected long life cycle of the retrofitted structure. A design engineer must face the challenge of developing

understanding and integrating the knowledge regarding the choice of a suitable class of adhesive for the specific problem at hand, the durability of such materials under the practical service environments (e.g. moisture, extreme temperature and its cycling, sustained or cyclic loading), as well as the various adhesion mechanisms that governs proper bonding.

Thus, in this section, different classes of adhesives will first be introduced, followed by a specific review on the epoxy adhesive, which is most widely used in the construction industry (after Mays and Hutchinson 1992), and then a brief review of the durability studies performed within the civil engineering community on the structural adhesives used in FRP retrofit, and finally a discussion of the various known adhesion mechanisms that are critical to analyzing certain debonding phenomena in any bonded system characterization programs.

A. Adhesive Classification

Structural adhesives that form the bond line interface are often organic in nature and can be broadly classified as thermoplastic and thermosetting. These adhesives need not be and often are not the same as those used as resin materials in FRP composite products such as a carbon FRP laminate, although they may belong to the same class.

Thermoplastic adhesives, as inferred by its name, may be softened by heating and re-hardened upon cooling without undergoing chemical transformation. Thermoplastic adhesives can be derivatives of vinyl, polyester, nylon, and cyanoacrylate. Vinyl based adhesives such as PVA (poly vinyl acetate) often serve as general purpose adhesives, but are formulated in aqueous emulsions and thus are moisture sensitive. Cyanoacrylate based adhesives, on the other hand, set very quickly due to the low viscosity liquid monomers that polymerize very easily on contact with traces of moisture present on the surface of adherends. These adhesives are often found as bonding agents for strain gages often used in structural test programs, and are commercially formulated and known as “Super Glue”.

Thermosetting adhesives, on the other hand, undergo irreversible cross-linking during the curing process. Upon heating, they become viscous or “rubbery” and lose strength and stiffness significantly. Thermosetting adhesives can be formed by reaction

between urea, phenol, resorcinol, or melamine and formaldehyde. One more important adhesive from this class is the formation of epoxy and unsaturated polyester. Epoxy adhesives are the most widely known and used in this group as a structural adhesive due to its versatility of tailoring the properties by blending in various additives, including flexibilisers, tougheners, and fillers. Epoxies can be cured either at ambient temperature or at high temperature, depending on the formulations.

B. Epoxy Base, Hardeners, and Additives

Epoxy Base

Now that epoxies are the most used commercial adhesives in FRP retrofit applications, they will be discussed at greater lengths. The formal chemical structure of epoxy adhesive is often of a DGEBA (diglycidyl ether of bisphenol A) or a DGEBF (diglycidyl ether of bisphenol F) formulation. Thermal and mechanical properties are largely due to polymerization as a result of the addition of cross-linking agent or the hardener, forming a relatively tough three-dimensional polymer network.

Epoxy Hardeners

Hardeners for epoxy are of three main groups, namely, (1) aliphatic polyamines, (2) cycloaliphatic amines, and (3) aromatic amines.

Aliphatic polyamines are one of the most commonly used in room (or ambient) temperature curing epoxy adhesive systems. The hardened adhesives are rigid and are resistant to chemicals, solvents, and moisture. Some aliphatic amine compositions react with carbon dioxide and moisture in the air, causing a tacky surface layer on the cured product and thus do not provide a good bonding surface for additional epoxy.

Cycloaliphatic amines are usually employed to deal with low temperature and high humidity. Mechanical properties and their resistance to chemicals are similar to those of aliphatic amines.

Aromatic amines are developed to provide improved heat and chemical resistance. These hardeners, however, do not yield good curing at room temperature. The resulting epoxy adhesives are also rather brittle and of lower strength than the aliphatic amines

counterpart, as the benzene ring structure of aromatic amines results in a dense cross-linked network. Note that brittleness increases with cross-link density.

Epoxy Additives

Two most frequently used additives in epoxy adhesives are fillers and tougheners. Fillers such as sand (or silica) are, in general, inert materials that may be added to help reduce cost, fill gaps, reduce creep, reduce exothermal reaction, inhibit corrosion, act as fire retardants, and most interestingly, provide thixotropy, a shear rate dependency that improve troweling ability for overhead and vertical applications without dripping. Despite the advantages, fillers seem to cause negative impact on moisture ingress and chemical resistance (Comyn 1981).

Tougheners are becoming increasingly popular in adhesive systems designed for FRP retrofit purposes, due to the inherent brittle nature of unmodified epoxies under peel load. For instance, in FRP bonded flexural concrete systems, despite special efforts have been made to ensure proper shear transfer from the concrete beam to the FRP laminate, the elastic mismatch nature of the bond almost always promote a peeling action at the laminate end (or discontinuity). To improve resistance to peel fracture, rubber tougheners have thus been developed as an extra energy absorption mechanism. Shear banding, crazing, and failure of rubber particles provide the main energy absorption against peel fracture. A common toughening agent is CTBN (carboxyl-terminated butadiene acrylonitrile).

C. Durability

Durability of structural adhesives can be determined by testing bonded joints or conducting bulk material tests on specimens that have been subjected to the designed amount of desired environmental exposure. Although testing of the behavior of the overall bonded system is more realistic and critical, fundamental knowledge should also be gained toward the adhesive bulk properties to better understand some of the phenomena observed in the bond tests. So far, however, there is no standard procedure as to how these tests should be carried out in order to determine the durability of the adhesive bonded system and its bond line material and how bulk material test data is

applicable to analysis a bonded system, although it has been suggested that the bond line thickness will determine the extent to which bulk behavior is relevant (Lees and Hutchinson 1992). Only very limited experimental data is available in the civil engineering community (Mays and Hutchinson 1992, Lees and Hutchinson 1992, Tu and Kruger 1996, Frigione et al 1998, 2000, Chin et al 1999, Aiello et al 2002), especially when considering the large amount of possible environmental parameters and their synergistic effects, although work has been done on structural adhesives used in other industries as early as 20 years ago (Kinloch 1983).

Nevertheless, it has been recognized that, in response to the typical specifications for adhesive design in the construction industry, the following properties of the adhesive are worth characterizing in bulk material tests (Lees and Hutchinson 1992):

- Young's modulus
- Shear modulus
- Glass transition temperature
- Coefficient of thermal expansion
- Moisture resistance

Besides, the author believes that fracture toughness, creep, and fatigue properties should also be among the top priorities of characterization. Nonetheless, the said parameters are often quantified under the influence of moisture, which is found to be one of the most harmful environmental agents for both bonded joints and the adhesives. Considering the adhesives, moisture effect can be particularly difficult to handle because water can seep through bond line as well as from the adherends while the polar groups which confer adhesive properties make the adhesives inherently hydrophilic (Mays and Hutchinson 1992).

Effect of Moisture on Adhesives

It is generally believed that the influence of moisture on the adhesive is largely reversible (though not necessarily so for bonded joints) such that the degraded mechanical properties can be recovered upon drying. The extent of which depends, of course, upon the adhesive composition. When moisture is diffused into the adhesive material, it is in either one of two forms – free water (absorption) or bound water

(adsorption). Free water occupies the free volume of the epoxy resin and does not cause swelling while bound water chemically reacts with the polymer chain via hydrogen bonding, disrupting the chain, and enhances the chain mobility, causing swelling to occur. In other words, the effective cross-link density is reduced when adsorption takes place, but for a few mass percent of moisture uptake, the swelling is barely measurable.

One universal observation is that water depresses the glass transition temperature, for both ambient cured adhesives and for heat-cured adhesives. This could be particularly worry to the civil engineering community regarding the FRP retrofitted structures where ambient cured adhesives are almost always used. These cold-cured adhesives have a typical glass transition in the range of 40°C – 60°C, within the vicinity of upper bound service temperature. With further depression by moisture, it would mean that the adhesive materials behave viscoelastically under normal service conditions, reducing the stress transfer over time, and upsetting the purpose of the whole retrofit exercise.

The plasticization effect of moisture, on the other hand, enhances the fracture toughness of adhesives due to greater plastic deformation and enhanced crack-tip blunting mechanisms (Kinloch 1982). Cohesive strength may, however, be reduced (Antoon and Koenig 1980, Hutchinson 1986) to sufficiently offset the increased toughness.

D. Adhesion Mechanism

To understand the undertaking of external environmental agents at the interfaces and hence the FRP bonded concrete system property, the major adhesion mechanisms must first be identified. Adhesion is popularly believed to take place in one (or more) of four forms: (1) physical attraction (or adsorption), (2) chemical bonding, (3) mechanical interlock, and (4) mutual diffusion.

Adsorption involves surface forces that develop between atoms in the two bonding surfaces that are resulted from intimate intermolecular contact between the two materials. The most common surface forces being referred to are the van der Waals forces. Since intimate intermolecular contact is required for adsorption to be properly developed, good wetting from the adhesive is essential. Wetting is perceived as the

ability of the adhesive to spread spontaneously on the substrate when the joint is initially formed.

Chemical bonding, on the other hand, suggests the formation of primary chemical bonds across the interface. Chemical bonding is strong and often demands the use of coupling agents for proper formation.

Mechanical interlock involves the adhesive penetrating into the macroscopically profiled substrate surface and locking mechanically to the substrate when loaded. This mechanism is direction dependent and is considered only a secondary mechanism that adds resistance to adhesion failure as suggested by excellent adhesion achieved between smooth sound adherend surfaces in many studies. Peel fracture, for instance, should be less influenced by mechanical interlock than shear fracture.

Finally, mutual diffusion only occurs when both the adhesive and adherend are polymeric (e.g. adhesive and CFRP). This theory, however, has found limited application in materials with high cross-link density such as the epoxy being used in this study.

In view of the four adhesion mechanisms, physical attraction and mechanical interlock seem to be the two that are responsible for the adhesion at the epoxy/concrete interface while physical attraction, chemical bonding, and mutual diffusion might be the synergistic adhesion mechanisms responsible for the adhesion at the FRP/epoxy interface.

2.1.3 Concrete Durability

Concrete is a familiar material to civil engineers and thus will not be discussed in the herein context. However, concrete durability often involves complex phenomena and thus will be discussed in this subsection.

The American Concrete Institute (ACI) defines concrete durability as the resistance to weathering action, chemical attack, abrasion, and any other degradation processes. Some of the more important degradation mechanisms include the following (Bazant and Prat 1988, Mehta and Monteiro 1992, Konvalinka 2002):

- Freeze-thaw damage
- Alkali-aggregate reactions
- Sulfate attack
- Microbiological induced attack

- Corrosion of embedded rebar
- Abrasion
- High temperature
- High moisture

Of these, the effects of high moisture on mechanical properties are to be discussed, in view of the role of moisture in the interfacial region of a FRP bonded concrete system. Presence of moisture is believed to enhance the mechanical properties of concrete due to continued hydration. However, comparative mechanical tests on dry and wet specimens of the same concrete indicate that the presence of free water can lead to substantial reduction in strengths (Bazant and Prat 1988, Ross et al 1996, Neville 1997, Konvalinka 2002).

Two hypothetical explanations have been offered so far to explain this phenomenon. The first explanation approaches the problem from a viewpoint of volumetric change of the hardened cement paste (Konvalinka 2002). It is believed that drying of concrete decreases the volume of the hardened cement paste, reducing the average distance between the surfaces of the hardened cement gel. This reduction naturally leads to increase in secondary bonds between the surfaces, and hence increases the strength of the dry specimens. Conversely, wetting the concrete increases the volume of the hardened paste and hence the average distance between the surfaces of the gel.

The second explanation approaches the problem from a viewpoint of internal pore pressure (Bazant and Prat 1988). It is believed that internal pore pressure is developed on the water molecules in the pores in wet concrete due to external loads. Since the migration of water in a pore is not free when adjacent pores are also filled with water and due to capillary actions, the hindered adsorbed water produces a very high disjoining pressure between the contacting cement gels. The pore pressure is responsible to intensity the stress intensities of the micro-crack tips and hence promotes crack propagation under external loads. This reduces the load-resistance of wet concrete, as compared to dry concrete.

To verify these hypotheses and to get an order of magnitude estimate of strength reduction that can be produced by moisture adsorption, the author has performed various mechanical tests that involve the characterization of compressive strength, tensile

strength, and fracture toughness using cylindrical and 3-point bend fracture specimens under 3 different moisture conditioning temperatures. It has been shown that degradation ranges from 20% to over 50%. Conditioning temperature effect does not seem to be significant in all test cases. More details of these material characterizations can be found in Chapter 4 of the thesis.

2.2 Structural Systems

2.2.1 Debonding in FRP/Concrete Systems

A. Definition of Debonding

The term “debonding” can be used to describe a variety of failures in the vicinity of the bond interface where a parent crack propagates parallel to the plane of the interface. For FRP bonded concrete, three materials (FRP, adhesive, and concrete) and two interfaces (FRP/adhesive and adhesive/concrete) are involved. In theory, five distinct failure modes are possible. They are namely, (1) FRP delamination, (2) FRP/adhesive separation, (3) adhesive decohesion, (4) adhesive/concrete separation, and (5) concrete substrate fracture. These five failure modes can broadly be classified as two classes of failure: (a) material decohesion and (b) interface fracture. Failure (1), (3), and (5) are considered material decohesion while failure (2) and (4) are considered interface fracture. Figure 2.2 illustrates each of the possible five debonding scenarios.

B. Experimental Observations

Empirical results have shown that under most circumstances (including loading type, material variations, and retrofit methods), concrete substrate fracture is the predominant mode of failure. For a beam system, concrete debonding is often brittle, can occur with little or no visible warning, and can occur at loads significantly lower than the flexural or shear strength of the retrofit system (Hearing 2000). Delamination of the FRP laminate is also seen from time to time when relatively viscous adhesive is being used. These empirical observations have been reported by a number of research teams who worked at the structural scale (Kaiser 1989, Saadatmanesh and Ehsani 1990, Ritchie et al 1991, Sharif et al 1994, Buyukozturk et al 2002). Besides, a number of attempts have since been made to look at such debonding phenomena at a smaller scale using various

physical models such as the peel and lap shear specimens (Chajes et al 1996, Taljsten 1997, Bizindavyi and Neale 1999, Karbhari et al 1997, Neubauer and Rostasy 1997, Kimpara et al 1999, Nakaba et al 2001, Chen and Teng 2001, Wu et al 2002, Gao et al 2003) and strength and debonding models have been suggested.

C. Possible Causes of Debonding

At the structural level, debonding is often found to initiate from the laminate ends where abrupt discontinuity arise. High concentration of shear and peel stress can be found in the bond line at such locations where shear cracks in concrete are likely to develop. Various methods of anchorages such as anchor bolts, L-shaped plates, and U-anchors, have since been devised with mixed success to prevent debonding from happening (Sharif et al 1994, Garden and Holloway 1998, Khalifa et al 1998, 2000, Smith and Teng 2001, Gunes 2004). Figure 2.3 shows a debonding failure at a soffit of a beam by a sliding mechanism even when double L-shaped plates are applied.

When sufficient and proper end anchorages are deployed, interface debonding would be forced to take place elsewhere, often within the retrofitted span (Hassanen and Raoof 2001). Debonding within the retrofitted span is often initiated from flexural cracks and/or flexural-shear cracks where there are differential crack mouth movements when external load (monotonic or cyclic) is applied to the beam system. Such debonding initiation and propagation has been observed by a number of research teams as early as 1989 (Kaiser 1989, Meier 1992, Neubauer and Rostasy 1997, Hearing 2000, Gunes 2004). Other causes of debonding include but are not limited to imperfect bonding between the laminate and concrete, cyclic loading induced debonding, environmental effects such as thermal cycle induced residual stresses and moisture plasticization of the adhesive material, and vandalism (Hearing 2000). It should also be noted that any presence of flaws might lead to further crack propagation as a vicious cycle. Figure 2.4 illustrates the main causes of interfacial debonding that can often be reproduced in laboratory settings.

D. Debonding Models

Modeling of debonding has been a popular area of interdisciplinary research in the past decade due to the critical importance of debonding failures especially in FRP

retrofitted flexural members. Models proposed have been mostly at the structural scale that predicts the debonding of the entire beam. These models can be generally classified by their approach to the problem as strength approach and fracture approach. While the majority of the models are strength-based, both classes consist of various rigorous analytical formulations as well as relatively simple empirical or semi-empirical methodologies.

Strength Based Models

Strength based models have been developed based on interfacial stresses, concrete tooth models, and bond strength models. By far, the models that are based on the interfacial stress concept are the most complete and thus will be discussed in the herein context. Debonding problems observed during experimental studies have resulted in the research on prediction of interfacial stresses at the FRP/concrete interface. It is now known that interface stresses consist both of a normal and a shear component. Figure 2.5 illustrates the conceptual distributions of interfacial stresses in a FRP retrofitted RC beam without end anchorage. It can be seen that high shear and normal stresses are developed at plate ends and at crack locations. Approximate closed-form models have been developed to predict such stresses, with a majority based on the strain compatibility condition and linear elastic behavior of materials (Taljsten 1997, Malek et al 1998, Smith and Teng 2001).

The following presents a recent and widely used model by Smith and Teng (2001). The analytical closed-form solution assumes linear elastic behavior with deformations due to both axial forces and bending moments of the RC beam as well as the external reinforcement. Shear deformations are being neglected due to their minimal effects. Adhesive layer is assumed to exhibit constant stresses through the thickness. The interface shear stress can be computed from the followings:

$$\tau = m_1 V(x) + m_2 \frac{e^{-\lambda x}}{\lambda} M(x) + \tau^*(x)$$

where x is the distance from plate ends, $V(x)$ and $M(x)$ the applied shear and moment values at the location where the interfacial stress is determined, $\tau^*(x)$ an additional shear stress term that varies with different loading cases, and $m1$, $m2$, and λ are expressions

that consist of material properties and geometric parameters. The interface normal stress can be, on the other hand, computed from the followings:

$$\sigma = e^{-\beta x} [C_1 \cos(\beta x) + C_2 \sin(\beta x)] - n_1 \frac{d\tau(x)}{dx} - n_2 q$$

where C_1 and C_2 contain applied shear and moment information, n_1 , n_2 , and β material properties and geometric parameters.

Having developed the interfacial stress models, a failure criterion is needed to predict the debonding failure load. Early research suggested that debonding failure takes place when the maximum shear and normal stresses reach certain limits (Roberts 1989, Kaiser 1989, Triantafillou and Plevris 1992). Kaiser (1989) has established from experimental testing of CFRP retrofitted beams that the critical interface shear stress that is likely to cause debonding is around 8 MPa. Another approach to suggesting a debonding model (Ziraba et al 1994) is by use of Mohr-Coulomb type criterion, which is given as follows:

$$\tau + \sigma \tan \phi \leq C_a$$

where ϕ is the friction angle and C_a the allowable coefficient of cohesion, both can be determined from parametric finite element studies.

Fracture Based Models

The fracture approach has been used to determine effective bond length in FRP retrofitted members. Recently, a fracture energy based failure model was also developed by Hearing (2000), a prior member of our research group at MIT, to predict debonding initiation and failure of the FRP retrofitted beams. It has been determined that debonding in the concrete substrate, a common failure mode under short-term testing as discussed in an earlier section, is expected to occur under the following critical moment:

$$\frac{M_u}{bd^2 \sqrt{G_f E}} = \left(\frac{3(1-2\alpha\beta)}{\beta(\alpha^3 + 2) - 1.5} \right)^{0.5} \sqrt{\frac{\rho_l}{t_l} \left(\frac{1}{I_1} - \frac{1}{I_2} \right)^{-0.5}}$$

where M_u is the applied critical moment, b and d the width and depth of the beam, G_f and E the fracture energy and modulus of concrete, α the normalized laminate length, β

the position of the loads, ρ_l and t_l the retrofit ratio and thickness of the FRP plate, and \bar{I}_1 and \bar{I}_2 the moment of inertia of the laminated and delaminated sections.

Most recently, Gunes (2004) has proposed a global debonding criterion also based on fracture energy of concrete. It is proposed that debonding of the entire FRP plate would occur when the following is satisfied:

$$\Delta D = \frac{P_{2d}^2}{2K_2} - \frac{P_{1d}^2}{2K_1} = (G_{FII}l_f b_f + \Gamma_{FII}l_a b_a) + W_s^p \geq 0$$

where ΔD is the total energy dissipation in the retrofitted system during the debonding process, P_{2d} and P_{1d} the load values before and after debonding takes place for an arbitrary deflection under the load application points, K_2 and K_1 the stiffnesses of the strengthened and un-strengthened beams, G_{FII} the mode II fracture toughness of concrete, Γ_{FII} the interface fracture energy (between the longitudinal FRP plate and the transverse anchorage reinforcement), $l_f b_f$ the bond area at the FRP/concrete interface, $l_a b_a$ the bond area between the FRP plate and the bond anchorage reinforcement in the transverse direction, and W_s^p the plastic energy dissipation of the rebars inside the concrete during debonding failure.

2.2.2 Environmental Degradation of FRP Bonded Concrete

Research into environmental degradation of FRP bonded concrete is at its infancy and very limited publications can be found up to this point. Almost all studies in this area have been based on accelerated testing of meso-scale specimens (in the cm range), unlike short-term debonding investigations that often involve large-scale beams (in the m range). Specimen types include FRP bonded plain concrete beams, FRP bonded reinforced concrete beams, lap shear specimens, and peel specimens. Most investigations involved characterization of strength parameters such as ultimate strength, stiffness, and deformation (Chajes et al 1995, Karbhari and Engineer 1996, Toutanji and Gomez 1997, Mukhopadhyaya et al 1998, Green et al 2000, Myers et al 2001, Ferrier et al 2001, Tommaso et al 2001) while to the knowledge of the author, only one study (except this current study) involved fracture characterization by means of fracture toughness

parameters (Karbhari et al 1997). With little physical understanding developed so far, modeling of environmental degradation of FRP bonded concrete system is virtually non-existence. Environmental parameters that have been tested usually include the followings: extreme temperature cycles, continuous frozen state, continuous fresh water conditioning, continuous saltwater conditioning, wet/dry cycles using saltwater, freeze/thaw cycles, and UV exposure under sustained load, from which wet/dry cycling is more often tested.

A. Strength Approach Studies

Testing of FRP retrofitted concrete beams (with or without rebars) under wet/dry cycles unanimously registered reduction in flexural stiffness (as indicated from mid-point beam deflection) and ultimate strength after conditioning. Under identical conditioning duration, the degree of stiffness reduction depends largely on the type of FRP being used. In one study (Myers et al 2001), it was experimentally determined that glass FRP bonded specimens lost up to 85% of its flexural stiffness after 20 wet/dry cycles, compared to 55% in the case of carbon FRP bonded specimens. Aramid FRP bonded specimens in the same test series appeared somewhere in between. Ultimate failure load also depreciates at various degrees, depending on the epoxy systems being used. In one study (Toutanji and Gomez 1997), the strength reduction ranged from as little as 3% to as much as 33% after 300 wet/dry cycles. All specimens were found to fail at the FRP/concrete interface. In a study where glass FRP double lap shear specimens were being used (Mukhopadhyaya et al 1998), wet/dry conditioning has resulted in increased shear slip, although it was concluded that the quantification of average shear stress could not effectively demonstrate the damage induced by the exposure.

B. Fracture Approach Studies

Fracture characterization on the durability of glass and carbon FRP bonded concrete against continuous fresh water and synthetic seawater (or salt water) conditioning environments has been performed by means of a peel test, of which the test setup is shown in Figure 2.6 (Karbhari et al 1997).

It has been proposed that this fracture characterization in the peel mode offered the following three distinct advantages over other tests including the pure shear test,

especially that it resembles closely the loading regime and modes of failure that are often encountered under service conditions:

- Bond failure proceeds at a controlled rate
- Peel force provides a direct measure of the work of adhesion
- Failure can be achieved under a mixed mode of loading

It was concluded from the tests that very little effect was found on the short-term exposure to water or seawater on the level of mode I fracture toughness while significant reduction of mode II fracture toughness was observed. A shift in failure mode was also registered for the glass FRP bonded concrete system before and after moisture conditioning. Control specimens exhibited a conventional concrete fracture type of failure while conditioned specimens failed mostly at the epoxy/FRP interface, indicating an adhesive type of failure.

2.3 Theoretical Background of Critical Phenomena

2.3.1 Moisture Diffusion

A. Overview

Diffusion is defined as the process by which matter is transported from one part of a system to another as a result of random molecular motions (Crank 1975). These random molecular motions, in which no molecule has a preferred direction of motion, are however governed by a concentration gradient. There is thus a net movement of these molecules flowing from a higher concentration region to a lower concentration region as a result of the random molecular motions.

Moisture diffusion in solid is a phenomenon where water molecules flow from a moist environment (e.g. a water bath) to a dryer environment (e.g. core of the material). The rate of transfer of water, the diffusing substance, through unit area of a section is proportional to the concentration gradient measured normal to that section, which is expressed by Fick's first law of diffusion:

$$F = -D \frac{\partial C}{\partial x}$$

where F is the rate of transfer per unit area of section (i.e. the amount of water diffusing), C the concentration of water, x the space coordinate measured normal to the section, and

D the diffusion coefficient. The negative sign in the above expression indicates that diffusion takes place in the direction opposite to that of increasing concentration. With respect to time, the rate of diffusion follows Fick's second law of diffusion:

$$\frac{\partial C}{\partial t} = \frac{\partial}{\partial x} \left(D \frac{\partial C}{\partial x} \right)$$

if diffusion is one-dimensional (i.e. concentration gradient is dominant in the x direction). Note here that D may or may not be a constant. In some cases such as diffusion of organic vapors in high-polymer substances, D depends on the concentration of the diffusing substance C . Sometimes, D may also vary with the time during which diffusion has been taking place. Generalizing, Fick's second law can be expressed to describe a full 3-dimensional diffusion process in terms of the nomenclature of vector analysis as:

$$\frac{\partial C}{\partial t} = \text{div}(D \cdot \text{grad}C)$$

B. Types of Diffusion Behavior

Moisture diffusion has been traditionally classified according to the relative rates of diffusion and relaxation (Alfrey et al 1966). The three classes are as follows:

- Case I or Fickian diffusion in which the rate of diffusion is much less than that of relaxation
- Case II diffusion in which diffusion is very rapid compared to the relaxation processes; this is the other extreme as opposed to Case I
- Case III or non-Fickian diffusion in which diffusion occurs at a rate comparable to that of relaxation; this falls somewhere in between Case I and Case II

Case I diffusion is controlled fundamentally by the diffusion coefficient while Case II is controlled by the constant velocity of the advancing diffusion front which makes the innermost limit of penetration of moisture. Case III normally requires two or more parameters to describe the inherent interaction between diffusion and relaxation effects. When the amount of moisture sorption at time t is described by kt^α where K and α are empirical constants that are geometric and material dependent such that:

$$\frac{M_t}{M_s} = kt^\alpha$$

α can be defined in the ranges as follows:

Case I or Fickian	$\alpha = \frac{1}{2}$
Case II	$\alpha \geq 1$
Case III or Non-Fickian	$\alpha \in (\frac{1}{2}, 1)$

Here, M_t represents the mass of water sorbed at time t and M_s the mass sorbed at equilibrium (or saturation). Considering a FRP bonded concrete system, diffusion within the constituent materials often belongs to Case I or Case III. Figure 2.7 illustrates the different types of Case III diffusion compared with Case I behavior.

In most cases, either Fickian or Pseudo-Fickian diffusion is observed. The term Pseudo-Fickian was first used by Rogers (1965) to describe the sorption-desorption curves of the same general shape as in Fickian diffusion, except that the initial linear portion persists for a shorter time. Note here that for ideal Fickian diffusion, the mass uptake curve would exhibit the following characteristics:

- Initial slope is linear
- Linear limit exceeds 60% of the equilibrium mass uptake
- Nonlinear portion of the curve is concave in shape
- Identical mass uptake curves should be generated regardless of coupon thickness

C. Diffusion Coefficient

Diffusion coefficient is defined as the rate at which a diffusion process takes place. A higher diffusion coefficient value corresponds to a faster diffusion process in a given duration. To measure the diffusion coefficient for the material at hand, most researchers assume the diffusion parameter as a constant. When such assumption does not apply to the material in question, a mean value is often obtained. As discussed earlier, the materials we are interested in (FRP, structural adhesive, and concrete) usually exhibit a Fickian or a Pseudo-Fickian diffusion behavior. In such cases, constant diffusion coefficients can be assumed without much loss of accuracy. Measurement of their values experimentally is also much simpler. One method of doing so is by the so-called

gravimetric sorption technique, which involves the generation of the overall moisture uptake curve as shown in Figure 2.8 by submerging a thin sheet of material in a water bath so that 1-dimensional double-sided diffusion takes place.

By solving Fick's second law properly, one could get an approximate relationship that describes the above moisture mass uptake behavior relatively accurately (Crank 1975) as follows:

$$\frac{M_t}{M_s} = \frac{4}{\sqrt{\pi}} \left(\frac{Dt}{h^2} \right)^{0.5}$$

where M_t is the mass of water sorbed at time t , M_s the mass sorbed at equilibrium (or saturation), h the thickness of the material coupon, D the diffusion coefficient. Thus, D can be computed from the initial linear slope of the mass uptake curve. For Pseudo-Fickian diffusion, D can be averaged up to the point of 60% of the initial portion (i.e. $M_t/M_s = 0.6$). Note that M_t/M_s always ranges between 0 and 1.

D. Estimation of Time to Saturation

We can observe from the mass uptake expression that at saturation, the coupon thickness, h , can be correlated to the time to saturation, t_s , as follows:

$$h = 4 \sqrt{\frac{Dt_s}{\pi}}$$

At a fixed moisture sorption temperature, T , the diffusion coefficient of the material remains unchanged. Hence, one can see that time to saturation varies with the square of the coupon thickness. When T is allowed to vary, D will be factored into the rate process as follows (disregarding the complex coupling of simultaneous diffusion of heat and moisture, Crank 1975):

$$t_{s,2} = \left(\frac{D_{T2}}{D_{T1}} \right) \left(\frac{h_2}{h_1} \right)^2 t_{s,1}$$

where D_{T1} and D_{T2} are the diffusion coefficients at temperature T_1 and T_2 for the same material respectively, h_1 and h_2 the respective coupon thickness, $t_{s,1}$ and $t_{s,2}$ the respective time to saturation. Consider that at room temperature, a 6 mm thick concrete, which has a diffusion coefficient of roughly 20×10^{-12} m²/s, saturates in 1 day. The same concrete but

with a thickness of 75 mm, under identical conditioning environment, will take as much as 5 months to saturate, a multiple of 156.

2.3.2 Interface Fracture

A. Overview

Interface fracture is used to describe the fracture phenomena that take place in a layered material system where interfaces exist between adjoining materials. Unlike fracture of a homogeneous isotropic solid, interface fracture in a multi-layer system often presents high order of complexity in terms of stress fields, crack propagation and kinking, as well as edge effects. While load and geometric symmetry usually bring about pure mode fracture in an isotropic solid, elastic mismatch in most cases lead to mixed mode behavior under seemingly symmetric loading and specimen geometry. Analysis of mixed mode behavior can also be extremely tedious and complex, often involving complex variables, integral equations, numerical solutions, and advanced elasticity analyses. Figure 2.9 illustrates such complexity through the expression of stress intensity factor for a compact tension (CT) fracture specimen that consists of a single material versus one with two materials (parameters involved will not be discussed herein). The latter case requires a complex variable definition in which $K = K_I + iK_{II}$, involving both the opening mode and the shearing mode at the crack tip. Despite the difficulty of this subject, interface fracture mechanics is an essential tool to characterize debonding behavior in a layered material system, one of which, of course, is FRP bonded concrete that has been the central theme of this study.

B. Bi-material Elasticity

No matter how many layers are there in a layered material system, an interface can only be formed by two adjoining materials. Bi-material elasticity will thus be first introduced. Consider a bi-material composite that consists of two dissimilar homogeneous isotropic materials that are bonded with continuous traction and displacement fields across the interface as shown in Figure 2.10. The upper layer is defined as material 1 and lower layer material 2. Let E_i , μ_i , and ν_i be the Young's

modulus, shear modulus, and Poisson's ratio respectively for subscript $i = 1, 2$ that correspond to the respective material number.

Dundurs (1969) has observed that a wide class of plane problems of elasticity for bi-materials only depends on two non-dimensional quantities, namely, α and β , as combinations of elastic moduli of the two materials. In the case of plane strain:

$$\alpha = \frac{\bar{E}_1 - \bar{E}_2}{\bar{E}_1 + \bar{E}_2} \quad \text{and} \quad \beta = \frac{1}{2} \frac{\mu_1(1-2\nu_2) - \mu_2(1-2\nu_1)}{\mu_1(1-2\nu_2) + \mu_2(1-2\nu_1)}$$

where $\bar{E} = E/(1-\nu^2)$. α represents the mismatch in tensile modulus while β the mismatch in bulk modulus. α approaches +1 when material 1 is comparatively extremely stiff while -1 when the same layer is extremely compliant. Both α and β vanish when the elastic mismatch is absent. α and β also change signs when the material layers are switched. Figure 2.11 shows the Dundurs parameters of some common material combinations in a FRP bonded concrete system as compared to those in the electronic packaging industry where debonding problems are also considered critical issues. It is clearly seen that the bi-material combinations commonly found in FRP bonded concrete represent some of the most extreme elastic mismatch combinations among the industries.

C. Interface Fracture Energy Release Rate in a Bi-Layer

Interface fracture energy release rate, G , in a bi-layer system is defined as the energy lost by the system (per unit width) due to crack advance. G can be related to material elasticity, elastic mismatch, and the complex stress intensity factors by the following expression:

$$G = \frac{|K|}{E^* \cosh^2(\pi\varepsilon)} = \frac{K_1^2 + K_2^2}{E^*} (1 - \beta^2)$$

where $\frac{1}{E^*} = \frac{1}{2} \left(\frac{1}{E_1} + \frac{1}{E_2} \right)$, $\varepsilon = \frac{1}{2\pi} \ln \left(\frac{1-\beta}{1+\beta} \right)$, and the other parameters as defined above.

Note there that ε is a so-called oscillatory singularity, which brings complications that are not present in the elastic fracture mechanics of homogeneous solids.

Case 1: Interface Crack in a Bi-layer

In a lot of cases, a flawed bi-material system can be modeled as a plain strain infinite bi-layer with an interface crack that is subjected to uniform loading along the edges, as illustrated in Figure 2.12.

Assuming each layer is homogeneous, isotropic, and linear elastic, and that the uncracked interface is perfectly bonded with continuous displacements and tractions, the interface fracture energy release rate has been derived in close form by Hutchinson and Suo (1992) as follows:

$$G = \frac{1}{2E_1} \left(\frac{P_1^2}{h} + 12 \frac{M_1^2}{h^3} \right) + \frac{1}{2E_2} \left(\frac{P_2^2}{H} + 12 \frac{M_2^2}{H^3} - \frac{P_3^2}{Ah} - 12 \frac{M_3^2}{Ih^3} \right)$$

where the dimensionless cross-section A and moment of inertia I are respectively

$$A = \frac{1}{\eta} + \Sigma$$

$$I = \Sigma \left[\left(\Delta - \frac{1}{\eta} \right)^2 - \left(\Delta - \frac{1}{\eta} \right) + \frac{1}{3} \right] + \frac{\Delta}{\eta} \left(\Delta - \frac{1}{\eta} \right) + \frac{1}{3\eta^3}$$

and

$$\Delta = \frac{1 + 2\Sigma\eta + \Sigma\eta^2}{2\eta(1 + \Sigma\eta)}, \quad \Sigma = \frac{1 + \alpha}{1 - \alpha}, \quad \eta = \frac{h}{H}$$

Note here that G represents a steady-state energy release rate, which is independent of the crack length. At this state, the advancing crack tip no longer “feels” the influence of the other end of the crack. Also, G only specifies the magnitude of the near-tip singularity but does not specify any mode mix information. This piece of information can be provided by the complex K , which takes the following form:

$$K = h^{-ie} \left(\frac{1 - \alpha}{1 - \beta^2} \right)^{0.5} \left(\frac{P}{\sqrt{2hU}} - ie^{i\gamma} \frac{M}{\sqrt{2h^3V}} \right) e^{i\omega}$$

where $i = \sqrt{-1}$, and P and M are linear combinations of the edge loads:

$$P = P_1 - C_1 P_3 - C_2 M_3 / h$$

$$M = M_1 - C_3 M_3$$

where C_1, C_2, C_3, U , and V are geometric factors, and ω the shift in phase angle.

Case 2: Substrate Crack in a Bi-layer

A second possible case of cracking in a bi-material system is when a crack is developed in the substrate that is close to and parallel to the interface as shown in Figure 2.13. This type of interface fracture would correspond to the commonly observed concrete delamination in a FRP bonded concrete system.

A similar analysis as in Case 1, which exercises energy arguments and by using the classical beam theory, would yield the following results (Hutchinson and Suo 1992):

$$G = \frac{1}{2E_2} \left(\frac{P_1^2}{A_1 h} + \frac{M_1^2}{I_1 h^3} + \frac{P_2^2}{h(\xi - \xi_1)} + 12 \frac{M_2^2}{h^3(\xi - \xi_1)^3} - \frac{P_3^2}{Ah} - \frac{M_3^2}{Ih^3} \right)$$

where the dimensionless effective cross-section and moment of inertia are given by:

$$A = \xi + \Sigma \quad I = \Sigma \left[(\Delta - \xi)^2 - (\Delta - \xi) + 1/3 \right] + \Delta \xi (\Delta - \xi) + \xi^3 / 3$$

$$A_1 = \xi_1 + \Sigma \quad I_1 = \Sigma \left[(\Delta_1 - \xi_1)^2 - (\Delta_1 - \xi_1) + 1/3 \right] + \Delta_1 \xi_1 (\Delta_1 - \xi_1) + \xi_1^3 / 3$$

where $\Delta = \frac{\xi^2 + 2\xi\Sigma + \Sigma}{2(\xi + \Sigma)}$, $\Delta_1 = \frac{\xi_1^2 + 2\xi_1\Sigma + \Sigma}{2(\xi_1 + \Sigma)}$, $\xi_1 = H_1/h$, and $\xi = H/h$.

Now that the crack is not at the interface, but within the substrate, the stress intensity factors are no longer coupled. K_I and K_{II} can thus be explicitly expressed in the following form:

$$K_I = \frac{P}{\sqrt{2hU}} \cos \omega + \frac{M}{\sqrt{2h^3V}} \sin(\omega + \gamma)$$

$$K_{II} = \frac{P}{\sqrt{2hU}} \sin \omega - \frac{M}{\sqrt{2h^3V}} \cos(\omega + \gamma)$$

where P and M are again linear combinations of the edge loads as defined before; U and V are geometric factors; and ω the shift in phase angle.

D. Crack Kinking

Crack propagation always follow the minimum energy path. In a FRP bonded concrete systems, although the pre-crack (or parent crack) can initially form at a bi-material interface (e.g. epoxy/concrete), subsequent crack propagations do not necessarily follow the direction of the parent crack. In many instances, this parent crack will kink out

of the interface and enter the more fracture prone concrete substrate. The behavior of crack kinking is governed by the relative fracture toughness of the interface over the substrate material. When

$$\frac{\Gamma_i}{\Gamma_s} > \frac{G_i}{G'_{\max}}$$

is satisfied, the crack is likely to kink out of the interface since the interface is relatively tougher than the substrate material (He and Hutchinson 1989, He et al 1991). Here Γ_i is the interface fracture toughness, Γ_s the substrate fracture toughness in mode I, G_i the interface fracture energy release rate (of the parent crack), and G'_{\max} the maximum fracture energy release rate for the kink crack at any putative kink angle. Since G_i is a case of G'_{\max} , the G_i/G'_{\max} is always between 0 and 1. Also, the fracture toughness values are determined experimentally.

2.4 Summary Comments

In this Chapter, a comprehensive literature review is given first regarding the mechanical and durability properties of the FRP composites and adhesive systems that are commonly used in retrofitting concrete structures. In particular, the basic mechanistic effect of moisture on adhesives is discussed, followed by a review of the known adhesion mechanisms that govern the bond properties of a joint. These discussions have laid down the foundation for interpreting the subsequent experimental findings of this work. Also, the readers should be aware of the fact that while tests have been performed on epoxy materials in the aerospace and mechanical engineering industries to study the effect of moisture in the past decades, the results are generally not universally and directly applicable to the debonding problem in the civil engineering structural retrofit context due to a wide variety of epoxy formulations and processing techniques, as well as the different design philosophy and structural requirements, used in the respective industries. Therefore, Chapter 4 of this thesis characterizes the effect of moisture on the structural epoxies that are used to manufacture the bonded system as will be examined in Chapter 5.

The discussion of materials is then followed by a brief review of debonding in FRP retrofitted concrete system, summarizing the experimental and theoretical

advancements regarding the debonding mechanics that is known to the civil engineering community. Although a large amount of work has been performed in the past decade to investigate the short-term behavior of debonding, available knowledge in the long-term behavior and especially the moisture effect on debonding is very limited. Thus, the main focus of the herein research is to generate new scientific knowledge with respect to the moisture effects on the mechanistic behavior and its trends of FRP bonded concrete as an overall joint system, as will be presented in Chapters 5 and 6 respectively. Also, it should be pointed out that strength-based approach has been dominant in prior research studies and fairly limited mechanistic explanation has been offered in light of the debonding phenomenon, which is inherently a fracture problem. As such, this research has adopted a fracture-based approach in order to gain more in-depth understanding into the debonding problem using a newly derived interface fracture model, which will be presented in Chapter 3, as the quantification means and the interface fracture toughness, that can be computed from the model at the critical state, to establish behavioral trends.

Finally, theoretical backgrounds on moisture diffusion and interface fracture, the two important phenomena central to this research, are laid out. Three-dimensional diffusion modeling is a critical simulation activity of this research to link the fracture theories with physical observations of the debonding modes by means of interfacial moisture concentration as well as moisture affected material properties. The simulation is performed by solving Fick's diffusion law, using diffusion coefficients as presented and defined in this chapter that are experimentally determined and tabulated in Chapter 4. The bi-material interface fracture solutions described represent the limiting cases for the tri-material interface fracture models as derived in Chapter 3. The kink criterion is, on the other hand, an important tool for analyzing and interpreting the debonding mechanics detailed in Chapter 6.

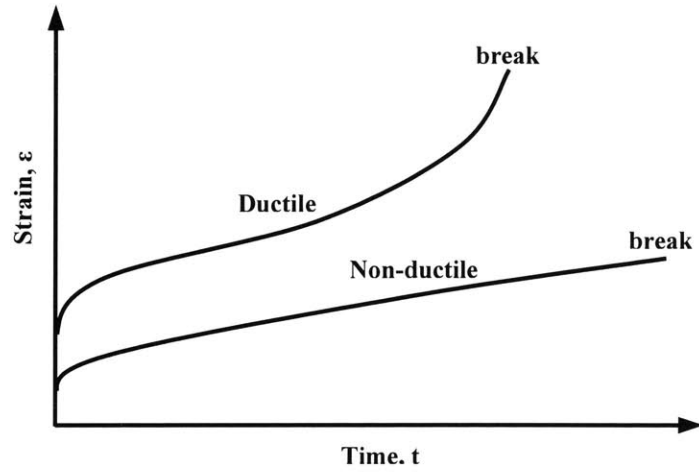


Figure 2.1 Ductile and Non-Ductile Creep Behavior

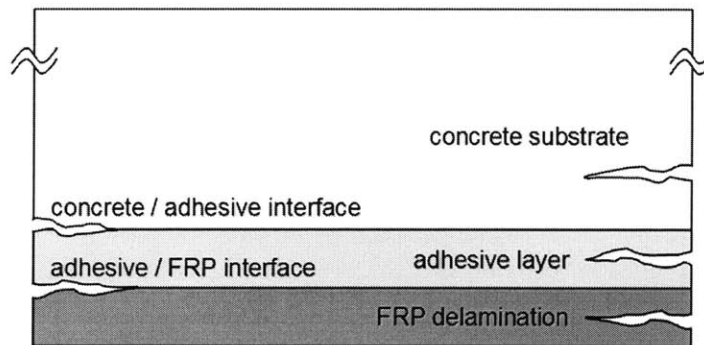


Figure 2.2 Debonding Scenarios in the Vicinity of the Interface

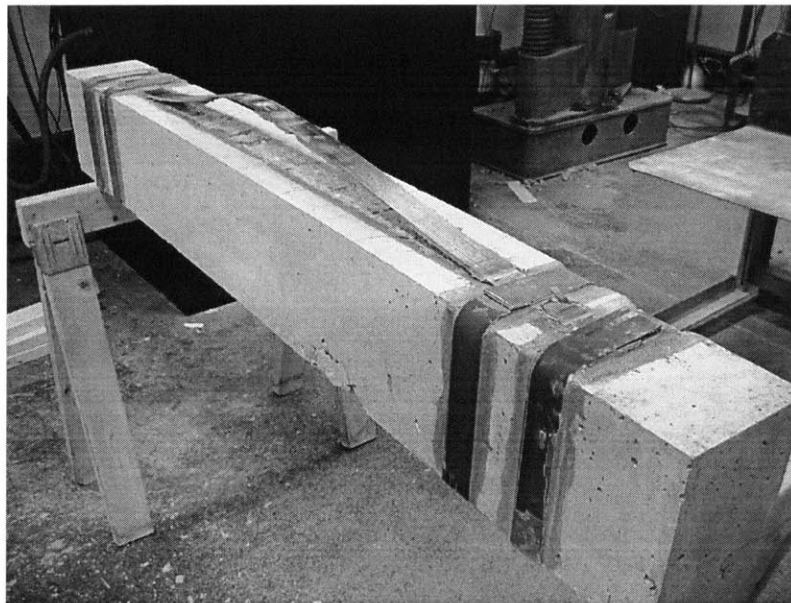
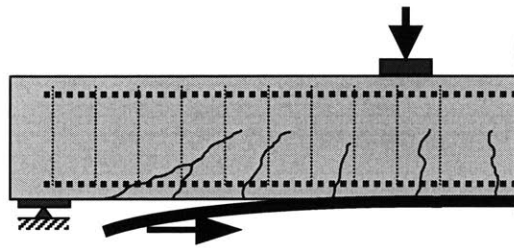
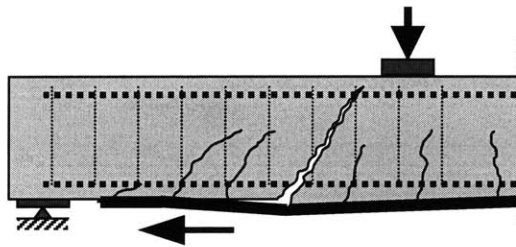


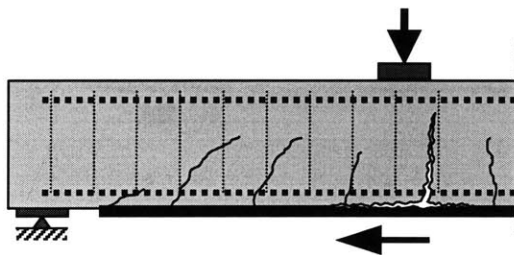
Figure 2.3 Debonding Failure Under End Anchorage (Gunes 2004)



Debonding from laminate end



Debonding from flexural-shear crack



Debonding from flexural crack

Figure 2.4 Common Causes of Debonding

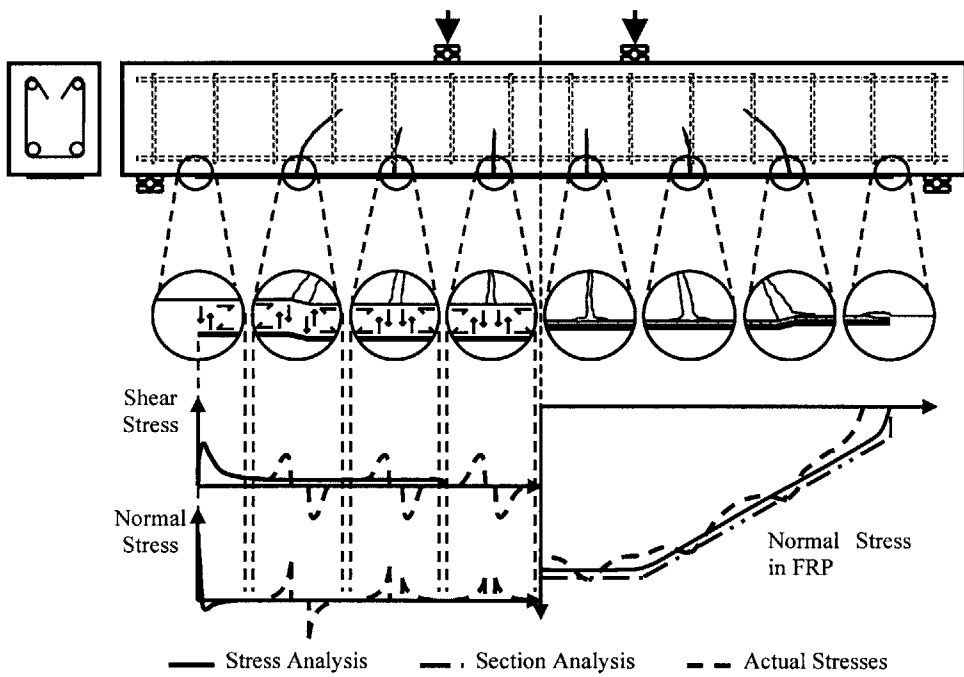


Figure 2.5 Conceptual Illustration of Interfacial Stresses

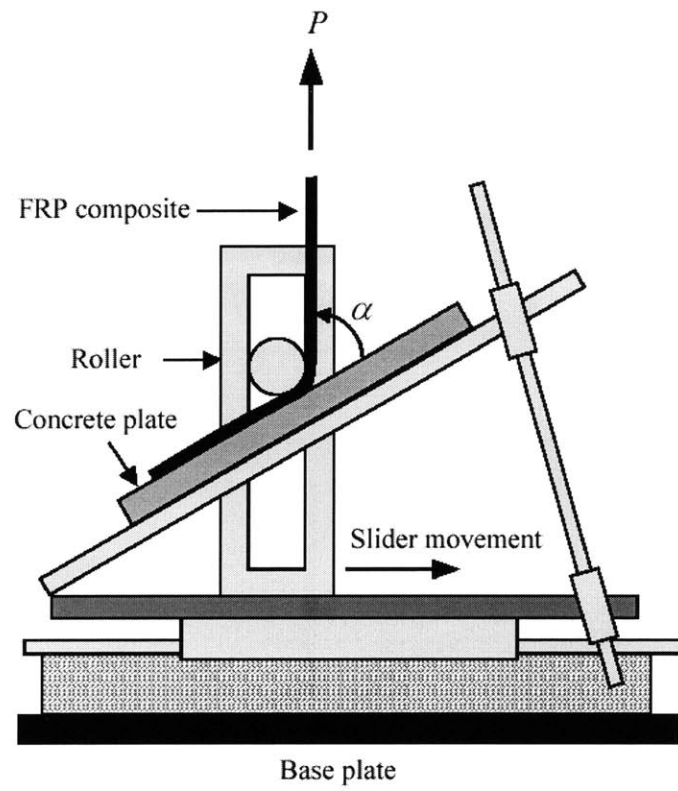


Figure 2.6 Peel Test Setup (Karbhari et al 1996)

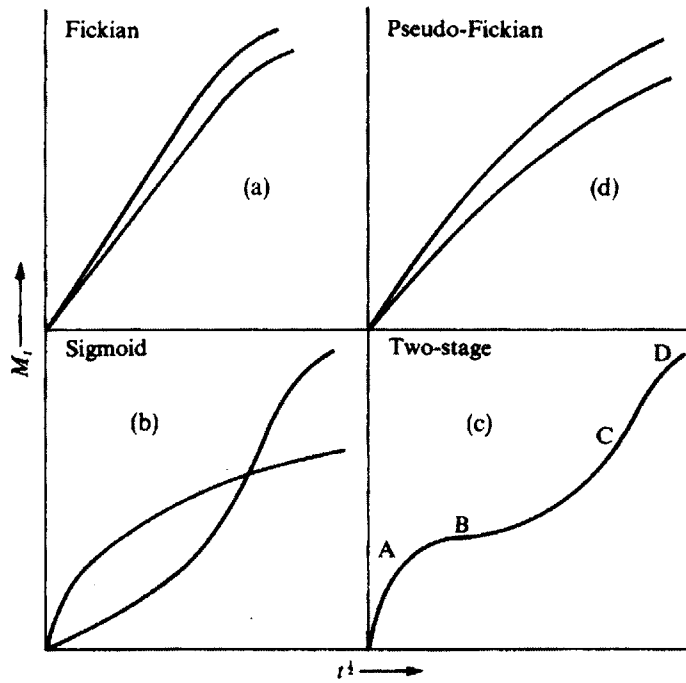


Figure 2.7 Illustration of Case I and Case III Diffusion Behavior (Crank 1975)

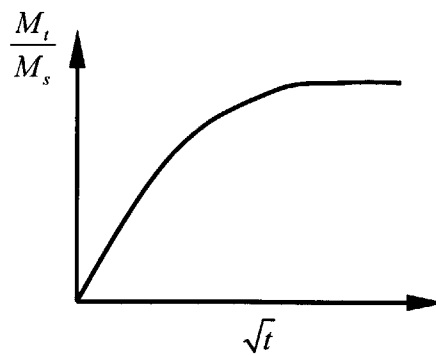
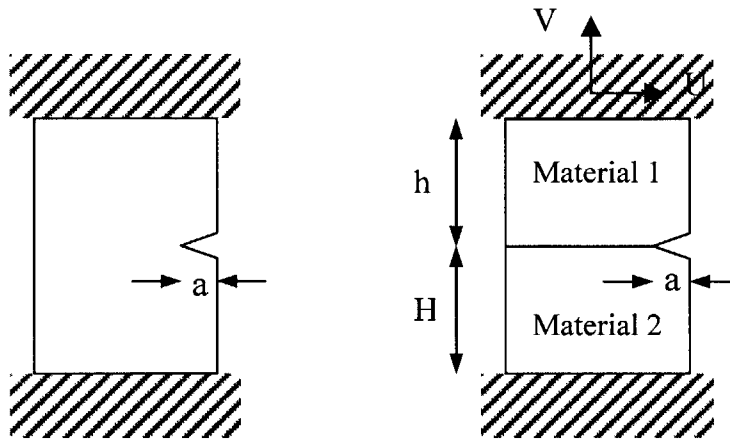


Figure 2.8 Typical Pseudo-Fickian Moisture Uptake Curve



Single material case: $K = y\sigma\sqrt{\pi a}$

Bi-material case:
$$K = h^{-i\epsilon} e^{i\omega} \left(\frac{E_*}{1-\beta^2} \right)^{1/2} \left[\frac{V}{\sqrt{2}} \left(\frac{h}{E_1} + \frac{H}{E_2} \right)^{-1/2} + i \frac{U}{\sqrt{2}} \left(\frac{h}{\mu_1} + \frac{H}{\mu_2} \right)^{-1/2} \right]$$

Figure 2.9 Fracture of Isotropic Material versus Bi-material

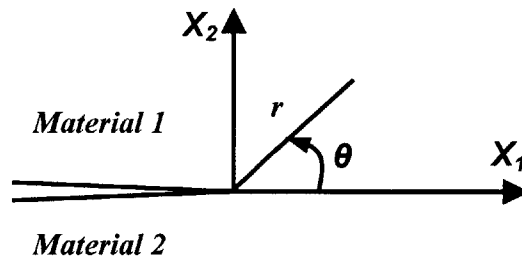


Figure 2.10 Conventions and Geometry for an Interface Crack

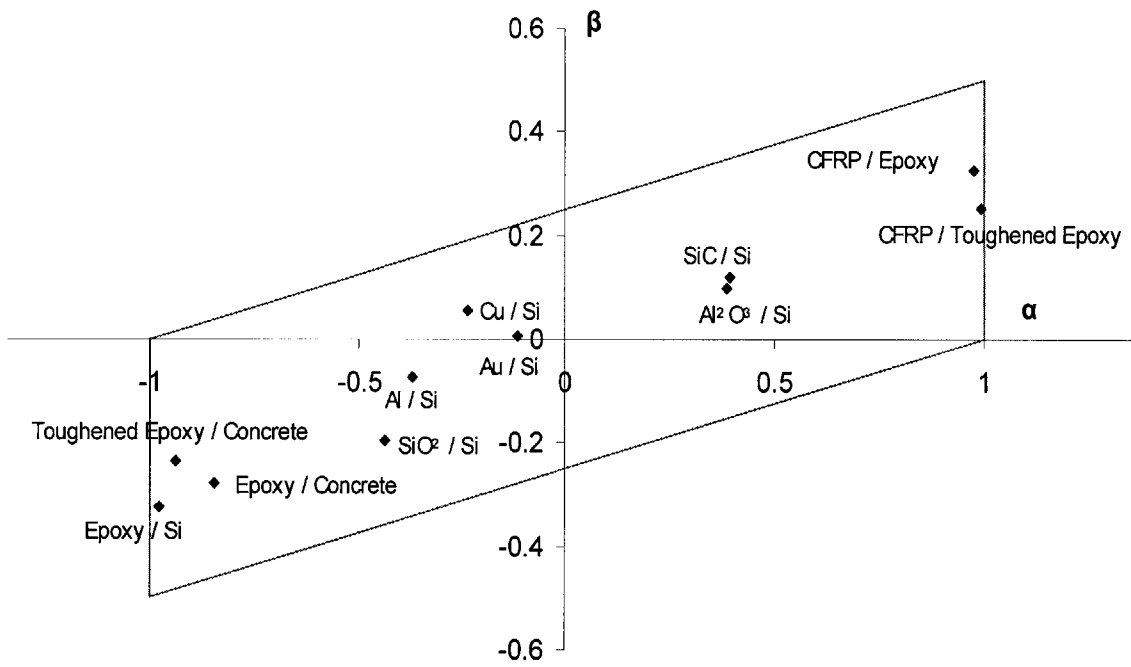


Figure 2.11 Values of Dundurs Parameters for Selected Bi-material Combinations

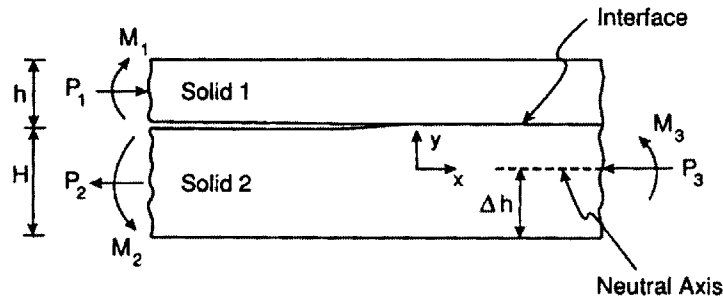


Figure 2.12 Interface Crack in a Bi-Layer (Hutchinson and Suo 1992)

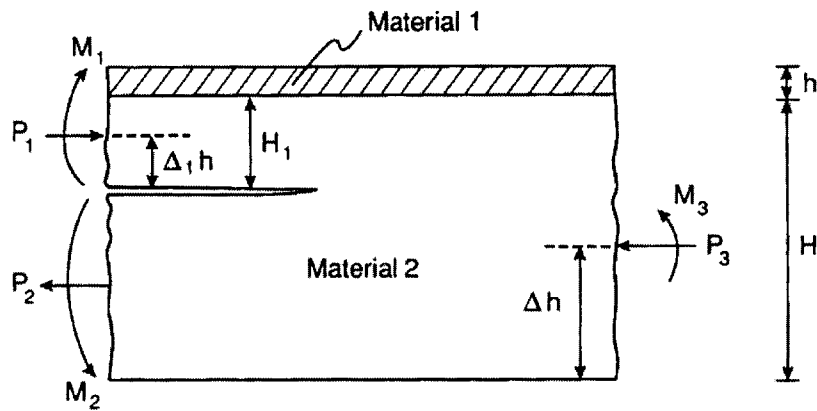


Figure 2.13 Substrate Crack in a Bi-Layer (Hutchinson and Suo 1992)

CHAPTER 3

QUANTIFICATION OF DEBONDING A TRI-LAYER FRACTURE TREATMENT

Debonding resistance of a FRP retrofitted concrete element needs to be properly quantified to facilitate the observation of the effect of moisture on the properties of the bond and its stability. This chapter develops a new tri-layer interface fracture model with fairly general boundary conditions using energy arguments and the classical beam theory. The rationale for adopting the fracture-based approach, as opposed to the more conventional strength-based approach, is first discussed. The need for a new tri-layer model, as opposed to the available bi-layer models, is then justified. Finally, specialized models that are applicable to subsequent fracture tests for transforming test data to interface fracture toughness in the peel and shear modes are presented.

3.1 Strength-Based Approach vs. Fracture-Based Approach

Strength-based characterization has been the dominant approach used by civil engineering researchers in the study of debonding problems in FRP retrofitted RC structures. Models that describe interfacial stress distributions, effective bond length, and

ultimate bond strength in FRP bonded concrete systems in both the structural scale and the mesoscale have been developed in the past decade (Gunes 2004). Modeling of debonding has mostly been based on the concept of interfacial stresses. Approximate closed-form models have been developed to predict such stresses, which contain both a shear and a normal component, with a majority based on the strain compatibility condition and linear elastic material behaviors (Taljsten 1997, Malek et al 1998, Smith and Teng 2001). Various failure criteria, which require the description of interface stresses for the given external loading configuration, have also been proposed to predict the debonding failure load (Roberts 1989, Kaiser 1989, Triantafillou and Plevris 1992, Ziraba et al 1994). While these models have shown some success in predicting the debonding state, they generally suffer from the fact that the models themselves depend on geometric parameters that are often highly system dependent. The debonding characterization is thus not quite transferable from one system to another, even with the use of identical retrofit composites and adhesives.

Fracture-based approach, on the other hand, characterizes debonding by means of an interface fracture toughness parameter, which can be considered a bond property. This bond property and/or behavior remain the same when the bond is subjected to identical interfacial stress states, regardless of the geometric configuration of the retrofitted system. This approach, while relatively new to the civil engineering community, has been successfully implemented to characterize thin-film structures (Hutchinson and Suo 1992), fiber reinforced material interfaces, mortar-aggregate interfacial properties (Trende 1995, Lee and Buyukozturk 1994, Chatterji and Jensen 1992, Diamond et al 1992), as well as dam-soil interaction (Saouma and Morris 1998, Cervenka et al 1998, Chandra and Saouma 2003). Also, the fracture-based approach naturally associates with material systems that contain flaws and cracks, as in the case of FRP debonding where cracks are often already in existence if not subsequently initiated due to further external loading.

In view of its transferability of information and relevance of application context, the fracture-based approach is adopted in this study as a basis for developing the quantification model that describes the debonding behavior in FRP bonded concrete systems.

3.2 Need for a New Tri-Layer Interface Fracture Model

Debonding can be used to describe a variety of failures in the vicinity of the bond interface where a parent crack propagates parallel to the plane of the interface. For FRP bonded concrete, three materials (FRP, adhesive, and concrete) and two interfaces (FRP/adhesive and adhesive/concrete) are involved. Empirical results (Smith and Teng 2001, Gunes 2004) have shown that FRP debonding is a highly complex phenomenon that can involve failure propagation within the concrete substrate, inside the adhesive, and inside the FRP laminate. In certain cases where external degradation agents are involved, interface separation may also be obtained (Karbhari et al 1997). In theory, five distinct failure modes are possible. They are namely, (1) FRP delamination, (2) FRP/adhesive separation, (3) adhesion decohesion, (4) adhesive/concrete separation, and (5) concrete substrate fracture. These five failure modes can broadly be classified as two classes of failure: (a) material decohesion and (b) interface fracture. Failure (1), (3), and (5) are considered material decohesion while failure (2) and (4) are considered interface fracture. Figure 3.1 illustrates each of the possible five debonding scenarios.

These different failure modes are partly attributed to the fact that the adhesive bond line thickness in such retrofitted systems is relatively large, usually in the order of the thickness of the FRP laminate, which is in the mm range. To characterize these different debonding modes, a tri-layer interface fracture model that contains parametrically the material and geometric information of the bonded system, is thus needed. While the conventional bi-layer fracture models (Hutchinson and Suo 1992) is capable of describing other layered systems with negligible bond line thickness such as protective coating, electronic packages, capacitors, and general thin-film/substrate systems, a new tri-layer fracture model needs to be developed to sufficiently describe the FRP debonding problems at hand.

It is, therefore, the objective of this chapter to present the full set of newly derived solutions to five idealized tri-layer debonding models that are subjected to fairly general boundary conditions at the edges, followed by the specialized peel and shear interface fracture models also for the five possible debonding scenarios. The solutions are linear elastic and are derived based on energy arguments and the classical beam theory. These solutions provide a rigorous quantification of the total interface fracture energy release

rate of the bond and represent a partial extension of the well-known and widely used bi-layer fracture energy models that are presented in Hutchinson and Suo (1992). Note here that the derived fracture models describe only the total interface fracture energy without explicit consideration of the mixed-mode stress-intensities at the crack tip. Considerations of such mode-mix behavior (i.e. determination of the opening and shearing mode stress intensities) are instead performed numerically with the use of finite element fracture modeling and interaction integrals, which will be discussed in more detail in Chapter 6 of this thesis.

3.3 Energy Arguments

As discussed earlier, debonding is a highly complex phenomenon. As the parent crack propagates at or near the bond interface, various energy dissipation mechanisms may take place. Some possible mechanisms include the release of elastic strain energy built up in the bond during fracture (i.e. when new fracture surfaces are generated), non-linear elastic, viscoelastic, or plastic behavior of the adhesive bond line depending on the material being used and the service conditions the bond is subjected to, frictional effect at interfaces especially that at the adhesive/concrete interface where mechanical interlocking exists when the concrete surface is roughened for bonding, and microcracking as well as plasticity in the concrete substrate. The total amount of energy dissipated during debonding, D , can thus be expressed as the sum of the work of adhesion, γ_s , that is responsible for generating new surfaces and the other energy dissipative mechanisms, γ_d over the area of debonding, dA :

$$D = \int \gamma_s dA + \int \gamma_d dA$$

For fracture to occur, the energy release, $\int G dA$, should thus be greater than or equal to the total amount of energy dissipated:

$$\int G dA \geq D$$

In the case of fracture under prescribed load, the total potential of the bonded system, Π , is related to the elastic strain energy U and potential energy due to external loads V as follows:

$$\Pi = U - V$$

Consider a linear elastic assumption for first order analysis as in most fracture problems, where at the solution state, $V = 2U$ exactly. Therefore, at fracture

$$d\Pi = -dU$$

Hence,

$$G = -\frac{d\Pi}{dA} = \frac{dU}{dA} = d(U_d)$$

where U_d is the strain energy per unit length per unit width of the bonded system. In other words, for interface fracture to occur at the steady state (Hutchinson 1996), the amount of energy dissipated in creating a new interface crack, dD , should equal the change in elastic strain energy due to cracking (i.e. strain energy release). The fracture energy release rate G is thus the difference between U_d of a cracked body (far behind the crack tip or downstream) and that of an intact body (far ahead the crack tip or upstream), as illustrated in Figure 3.2 for a debonding problem where an interface crack exists between Layer 2 and Layer 3.

$$G = (U_d)_{downstream} - (U_d)_{upstream}$$

As such, G can be computed exactly by evaluating the strain energy per unit width per unit length of the bonded system, which contains a crack in an arbitrary location near the bond interface, using the classical beam theory. The solutions for this tri-layer problem can be algebraically cumbersome and thus non-dimensional area and moment of inertia are carefully chosen for systematic tabulation for use in future analyses as illustrated in the next section.

3.4 Interface Fracture Models and Solutions

In this section, the tri-layer interface fracture energy release rate models (hereafter called G models) are derived in accordance to the energy principles described in the previous section. For a tri-material layered system, there are altogether five possible fracture scenarios, two being interface separation and three material decohesion, as previously presented. Each of the debonding modes is idealized and defined in Figure 3.3 for derivation purposes. Table 3.1 summarizes the interface fracture cases and the corresponding debonding modes in case of a FRP bonded concrete system with respect to the case numbers of the idealized models.

Table 3.1 Summary of G Model Cases

	Interface Fracture Mode	Corresponding Debonding Mode in FRP Bonded Concrete Systems
Case 1	Interface Separation between Layers 1 & 2	FRP/Adhesive Interface Separation
Case 2	Interface Separation between Layers 2 & 3	Adhesive/Concrete Interface Separation
Case 3	Material Decohesion of Layer 1	FRP Delamination
Case 4	Material Decohesion of Layer 2	Adhesive Decohesion
Case 5	Material Decohesion of Layer 3	Concrete Delamination

Each of the five derived G models can be used to compute the interface fracture energy release rate that corresponds to the observed debonding mode from experiments. Thickness for layer 1 (top) through 3 (bottom) is designated h , t , and H respectively.

Assumptions

Derivation of each idealized debonding model assumes that each of the three layers is homogeneous, isotropic, and linearly elastic. The uncracked interfaces are perfectly bonded with continuous displacements and tractions. The tri-material models are all loaded uniformly along the edges with constant forces (in the form of stretching) and moments per unit width at the neutral axis of the respective composite arms. Plain strain condition is assumed, as the bond width is usually 1 – 2 orders of magnitude higher than the bond thickness.

Derivation

All five G models are developed using identical derivation procedures. In what follows, the derivation and solution of the Case 2 G model are first presented, followed by the generalized solution form that applies to all five cases and the tabulated results of the general terms for each case.

As discussed in the last section, the interface fracture energy release rate G can be obtained by computing the difference between the U_a of a cracked body (far behind the crack tip or downstream) and that of an intact body (far ahead the crack tip or upstream), i.e.

$$G = (U_d)_{\text{downstream}} - (U_d)_{\text{upstream}}$$

Thus for Case 2, by referring to Figure 3.2 again:

$$G_{\text{Case2}} = (U_d)_{\text{Arm1}} + (U_d)_{\text{Arm2}} - (U_d)_{\text{Arm3}}$$

Each arm can be treated as a composite beam and the classical beam theory can be used to derive the expression for U_d for each particular arm. U_d is defined as the total elastic strain energy, U , per unit width per unit length of the bond. Hence, when constant load and moment are involved, U_d of a composite arm a can be expressed as follows:

$$U_d = \frac{P_a^2}{2(\overline{EA})_{\text{Arm } a}} + \frac{M_a^2}{2(\overline{EI})_{\text{Arm } a}}$$

where P_a is the constant load (stretch) per unit width acting on the neutral axis of the composite beam, M_a the constant moment per unit width applied about the same neutral axis, $(\overline{EA})_{\text{Arm } a}$ the plain strain axial rigidity of the composite arm, and $(\overline{EI})_{\text{Arm } a}$ the flexural rigidity. The general form of G will thus be as follows:

$$G_{\text{Case2}} = \left(\frac{P_1^2}{2(\overline{EA})_{\text{Arm1}}} + \frac{M_1^2}{2(\overline{EI})_{\text{Arm1}}} \right) + \left(\frac{P_2^2}{2(\overline{EA})_{\text{Arm2}}} + \frac{M_2^2}{2(\overline{EI})_{\text{Arm2}}} \right) - \left(\frac{P_3^2}{2(\overline{EA})_{\text{Arm3}}} + \frac{M_3^2}{2(\overline{EI})_{\text{Arm3}}} \right)$$

Now, the composite rigidities are developed for each arm.

Arm 1

For Arm 1, which is behind the crack tip, the neutral axis of the bi-layer composite beam is defined at a location $h\delta$ above the crack interface, where δ can be derived as follows:

$$\delta = \frac{\Sigma_{12} + 2\Sigma_{12} \frac{\gamma}{\eta} + \left(\frac{\gamma}{\eta} \right)^2}{2 \left(\Sigma_{12} + \frac{\gamma}{\eta} \right)}$$

of which $\Sigma_{ij} = \frac{\overline{E}_i}{E_j}$, $\overline{E}_n = \frac{E_n}{1-\nu_n^2}$ for plain strain

$$\eta = \frac{h}{H}, \quad \gamma = \frac{t}{H}$$

Here, E_n is the elastic modulus of material layer n , ν_n the corresponding Poisson's ratio, i and j the material layer numbers which range from 1 to 3. When the rigidities are derived with respect to the modulus of Layer 3, the dimensionless (normalized with respect to the thickness of layer 1, h) cross-section area $A_{1,2}$ and moment of inertia $I_{1,2}$ are respectively:

$$A_{1,2} = \Sigma_{13} + \Sigma_{23} \frac{\gamma}{\eta}$$

$$I_{1,2} = \Sigma_{13} \left[\left(\frac{\gamma}{\eta} \right)^2 + (1-2\delta) \left(\frac{\gamma}{\eta} \right) + \frac{3(1-2\delta)^2 + 1}{12} \right] +$$

$$\Sigma_{23} \left[\delta \left(\frac{\gamma}{\eta} \right) \left(\delta - \frac{\gamma}{\eta} \right) + \frac{1}{3} \left(\frac{\gamma}{\eta} \right)^3 \right]$$

Arm 2

Arm 2 only consists of Layer 3 and thus the neutral axis coincides with the centerline of the layer, which is $H/2$ from the crack interface. So, the cross-section area $A_{2,2}$ and moment of inertia $I_{2,2}$ are respectively:

$$A_{2,2} = \frac{1}{\eta}$$

$$I_{2,2} = \frac{1}{12\eta^3}$$

Arm 3

Finally for Arm 3, which is far ahead of the crack tip, the tri-layer composite beam has a neutral axis defined at $h\Delta$ above the bottom of the beam, where Δ can be derived as follows:

$$\Delta = \frac{1 + \Sigma_{23}\gamma(2 + \gamma) + \Sigma_{13}\eta(2 + 2\gamma + \eta)}{2\eta(1 + \Sigma_{23}\gamma + \Sigma_{13}\eta)}$$

The dimensionless cross-section area $A_{3,2}$ and moment of inertia $I_{3,2}$ are respectively:

$$A_{3,2} = \Sigma_{13} + \Sigma_{23} \frac{\gamma}{\eta} + \frac{1}{\eta}$$

$$I_{3,2} = \Sigma_{13} \left[\left(\frac{1+\gamma}{\eta} - \Delta \right)^2 + \left(\frac{1+\gamma}{\eta} - \Delta \right) + \frac{1}{3} \right] + \Sigma_{23} \left[\left(\frac{\gamma}{\eta} \right)^3 \left(\frac{1}{\gamma^2} + \frac{1}{\gamma} + \frac{1}{3} \right) + \left(\frac{\gamma}{\eta} \right) \left(\Delta - \frac{2+\gamma}{\eta} \right) \right] + \frac{\Delta}{\eta} \left(\Delta - \frac{1}{\eta} \right) + \frac{1}{3\eta^3}$$

Combining, the interface fracture energy release rate, G , which specifies the total magnitude of the near-tip singularity for a Case 2 debonding, is expressed as follows:

$$G_{Case2} = \frac{1}{2E_3} \left[\frac{P_1^2}{A_{1,2}h} + \frac{M_1^2}{I_{1,2}h^3} + \frac{P_2^2}{A_{2,2}h} + \frac{M_2^2}{I_{2,2}h^3} - \frac{P_3^2}{A_{3,2}h} - \frac{M_3^2}{I_{3,2}h^3} \right]$$

A limiting case of this solution is when layer 2 vanishes (i.e. $t \rightarrow 0$, hence $\gamma \rightarrow 0$). In such case, the above solution converges exactly to the bi-layer solution derived by Hutchinson and Suo (1992) presented earlier in Chapter 2.

Note also that the fracture model is in overall equilibrium when the edge loads and moments are related as follows:

$$P_1 - P_2 - P_3 = 0$$

$$M_1 - M_2 + P_1(h\delta + H - h\Delta) + P_2\left(h\Delta - \frac{H}{2}\right) - M_3 = 0$$

Note here that the signs or directions of the loads and moments do not affect the value of G . However, this is not so when stress intensity factors, which are also expressed as a function of these external loads, are considered (Hutchinson 1996).

Generalized Solutions

The expression of G presented above can take the general form:

$$G_{Case k} = \frac{1}{2E_3} \left[\frac{P_1^2}{A_{1,k}h} + \frac{M_1^2}{I_{1,k}h^3} + \frac{P_2^2}{A_{2,k}h} + \frac{M_2^2}{I_{2,k}h^3} - \frac{P_3^2}{A_{3,k}h} - \frac{M_3^2}{I_{3,k}h^3} \right]$$

where the dimensionless cross-section areas $A_{i,k}$ and moment of inertias $I_{i,k}$ are differently expressed for each debonding fracture scenario due to the different neutral axis position definitions as a result of the specific crack locations. Tables 3.2 through 3.4 summarize

the corresponding $A_{i,k}$ and $I_{i,k}$ for the three composite arms. Thickness, modulus, crack location, and neutral axis parameters are defined as follows:

h = Layer 1 thickness, t = Layer 2 thickness, H = Layer 3 thickness

$$\Sigma_{mn} = \frac{\bar{E}_m}{E_n} \quad \text{where } m, n = 1, 2, 3$$

$$\eta = \frac{h}{H}, \quad \gamma = \frac{t}{H}, \quad \xi = \frac{1}{\eta}, \quad \xi_i = \frac{H_i}{h} \quad \text{where } i = 1, 2, 3$$

$$\alpha = \frac{\Sigma_{23}\gamma(2+\gamma)+1}{2\eta(1+\Sigma_{23}\gamma)}$$

$$\alpha_3 = \frac{(\eta\xi_3)^2 + \Sigma_{23}\gamma(2\eta\xi_3 + \gamma) + \Sigma_{13}\eta(2\eta\xi_3 + 2\gamma + \eta)}{2\eta(\eta\xi_3 + \Sigma_{23}\gamma + \Sigma_{13}\eta)}$$

$$\delta = \frac{\Sigma_{12} + 2\Sigma_{12}\frac{\gamma}{\eta} + \left(\frac{\gamma}{\eta}\right)^2}{2\left(\Sigma_{12} + \frac{\gamma}{\eta}\right)}$$

$$\Delta = \frac{1 + \Sigma_{23}\gamma(2+\gamma) + \Sigma_{13}\eta(2+2\gamma+\eta)}{2\eta(1 + \Sigma_{23}\gamma + \Sigma_{13}\eta)}$$

$$\Delta_2 = \frac{\Sigma_{12}\left(1 + 2\frac{\gamma}{\eta} - 2\xi_2\right) + \left(\frac{\gamma}{\eta} - \xi_2\right)^2}{2\left(\Sigma_{12} + \frac{\gamma}{\eta} - \xi_2\right)}$$

$$\Delta_3 = \frac{1 + \Sigma_{23}\gamma(2+\gamma) + \Sigma_{13}\eta\xi_1(2+2\gamma+\eta\xi_1)}{2\eta(1 + \Sigma_{23}\gamma + \Sigma_{13}\eta\xi_1)}$$

$$\Delta_{33} = \frac{1 + \Sigma_{23}\xi_2\eta(2+\xi_2\eta)}{2\eta(1 + \Sigma_{23}\xi_2\eta)}$$

Table 3.2 Solutions of $A_{I,k}$ and $I_{I,k}$

<i>Case</i>	$A_{I,k}$	$I_{I,k}$
$k = 1$	Σ_{13}	$\frac{\Sigma_{13}}{12}$
$k = 2$	$\Sigma_{13} + \Sigma_{23} \frac{\gamma}{\eta}$	$\Sigma_{13} \left[\left(\frac{\gamma}{\eta} \right)^2 + (1-2\delta) \left(\frac{\gamma}{\eta} \right) + \frac{3(1-2\delta)^2 + 1}{12} \right] + \Sigma_{23} \left[\delta \left(\frac{\gamma}{\eta} \right) \left(\delta - \frac{\gamma}{\eta} \right) + \frac{1}{3} \left(\frac{\gamma}{\eta} \right)^3 \right]$
$k = 3$	$\Sigma_{13} (1 - \xi_1)$	$\Sigma_{13} \frac{(1 - \xi_1)^3}{12}$
$k = 4$	$\Sigma_{13} + \Sigma_{23} \left(\frac{\gamma - \xi_2}{\eta} \right)$	$\Sigma_{13} \left[\left(\frac{\gamma}{\eta} \right)^2 + (1-2\Delta_2 - 2\xi_2) \left(\frac{\gamma}{\eta} \right) + \frac{3(1-2\Delta_2)^2 + 1}{12} + \xi_2^2 - \xi_2 (1-2\Delta_2) \right] + \Sigma_{23} \left[\Delta_2 \left(\frac{\gamma}{\eta} \right) \left(\Delta_2 - \frac{\gamma}{\eta} \right) + \frac{1}{3} \left(\frac{\gamma}{\eta} \right)^3 - \frac{1}{3} \xi_2^3 - \xi_2^2 \left(\Delta_2 - \frac{\gamma}{\eta} \right) - \xi_2 \left(\Delta_2 - \frac{\gamma}{\eta} \right)^2 \right]$
$k = 5$	$\Sigma_{13} + \Sigma_{23} \frac{\gamma}{\eta} + \xi_3$	$\Sigma_{13} \left[\left(\frac{\gamma}{\eta} \right)^2 + (1-2\alpha_3 + 2\xi_3) \left(\frac{\gamma}{\eta} \right) + \xi_3 (1-2\alpha_3 + \xi_3) + \frac{3(1-2\alpha_3)^2 + 1}{12} \right] + \Sigma_{23} \left[\frac{1}{3} \left(\frac{\gamma}{\eta} \right)^3 + (\xi_3 - \alpha_3) \left(\frac{\gamma}{\eta} \right)^2 + (\xi_3 - \alpha_3)^2 \left(\frac{\gamma}{\eta} \right) \right] + \xi_3 \alpha_3 (\alpha_3 - \xi_3) + \frac{1}{3} \xi_3^3$

Table 3.3 Solutions of $A_{2,k}$ and $I_{2,k}$

<i>Case</i>	$A_{2,k}$	$I_{2,k}$
$k=1$	$\Sigma_{23} \frac{\gamma}{\eta} + \xi$	$\Sigma_{23} \left[\frac{1}{3} \left(\frac{\gamma}{\eta} \right)^3 + (\xi - \alpha) \left(\frac{\gamma}{\eta} \right)^2 + (\xi - \alpha)^2 \left(\frac{\gamma}{\eta} \right) \right] + \frac{1}{3} \xi^3 - (\xi - \alpha) \left(\frac{\alpha}{\eta} \right)$
$k=2$	ξ	$\frac{1}{12} \xi^3$
$k=3$	$\Sigma_{13} \xi + \Sigma_{23} \frac{\gamma}{\eta} + \xi$	$\Sigma_{13} \left[\frac{\xi^3}{3} + \xi^2 \left(\frac{\gamma}{\eta} + \xi - \Delta_3 \right) + \xi \left\{ (\xi - \Delta_3)^2 + \frac{\gamma}{\eta} \left(\frac{\gamma}{\eta} - 2\xi - 2\Delta_3 \right) \right\} \right] + \Sigma_{23} \left[\frac{1}{3} \left(\frac{\gamma}{\eta} \right)^3 + (\xi - \Delta_3) \left(\frac{\gamma}{\eta} \right)^2 + (\xi - \Delta_3)^2 \left(\frac{\gamma}{\eta} \right) \right] + \frac{\xi^3}{3} - \Delta_3 \xi (\xi - \Delta_3)$
$k=4$	$\Sigma_{23} \xi + \xi$	$\Sigma_{23} \left[\frac{1}{3} \xi^3 + (\xi - \Delta_{33}) \xi^2 + (\xi - \Delta_{33})^2 \xi \right] + \frac{\xi^3}{3} - (\xi - \Delta_{33}) \xi \Delta_3$
$k=5$	$\xi - \xi_3$	$\frac{(\xi - \xi_3)^3}{12}$

Table 3.4 Solutions of $A_{3,k}$ and $I_{3,k}$

<i>Case</i>	$A_{3,k}$	$I_{3,k}$
$k=1$		
$k=2$		$\Sigma_{13} \left[\left(\frac{1+\gamma}{\eta} - \Delta \right)^2 + \left(\frac{1+\gamma}{\eta} - \Delta \right) + \frac{1}{3} \right] +$
$k=3$	$\Sigma_{13} + \Sigma_{23} \frac{\gamma}{\eta} + \xi$	
$k=4$		$\Sigma_{23} \left[\left(\frac{\gamma}{\eta} \right)^3 \left(\frac{1}{\gamma^2} + \frac{1}{\gamma} + \frac{1}{3} \right) + \left(\frac{\gamma}{\eta} \right) \left(\Delta - \frac{2+\gamma}{\eta} \right) \right] + \frac{\xi^3}{3} + \Delta \xi (\Delta - \xi)$
$k=5$		

3.5 Specialized Solutions for Debonding in Peel & Shear Fracture Specimens

The generality of loading conditions for the models presented earlier makes them applicable to many different classes of problems that involve a tri-layer material structure. For the purpose of the herein study, debonding in FRP-adhesive-concrete systems that are subjected to peel and/or shear loading can be characterized by specializing the general solutions with specific geometric and loading configurations. The peel and shear loading cases represent the two limiting bounds of a typical debonding problem that takes place within the retrofit span, as illustrated in Figure 3.4. Fracture toughness values determined from tests and computed by means of these tri-layer models thus represent the upper and lower property bounds of the bond. Loadings from the specialized peel and shear models are expressed as the equivalent stretch P_i and moment M_i in the general solutions with adjustments made to the actual loading lines and will be illustrated respectively below for each loading configuration for a Case 2 debonding scenario.

3.5.1 Solutions for Debonding under Peel

Figure 3.5 shows a typical peel fracture model where there is a constant peel load applied at the tip of the FRP cantilever, in which the bending moment increases linearly from the load application point to the crack tip, deviating from the assumed constant moment in the general solution presented above. For a given peel load value, the actual U_d stored in the bonded system just before fracture should thus be lower than the computed value if the constant moment assumption is exercised. To more accurately compute the interface fracture energy release rate under peel load, the U_d that accounts for a linearly increasing moment needs to be explicitly derived to replace the associated constant moment term in the general solution.

First, in all realistic cases, thickness of the concrete block is at least two orders of magnitude higher than that of both the FRP laminate and the epoxy layer (i.e. $H \gg h, t$), hence $\eta \rightarrow 0$ and $\gamma \rightarrow 0$. This leads the 3rd, 4th, 5th, and 6th terms in the general solution to vanish. Also, since there is no horizontal stretching (i.e. $P_l = 0$), only the 2nd moment term remains. As discussed above, however, this constant moment term needs to be converted to a varying moment term which can account for the linearly varying moment that ranges from zero at the FRP tip at which the peel load, P , is applied, to $P(l+a)$ at the

crack tip that is length a ahead of the edge of the concrete block. Here, P is defined as the peel load per unit width B , l the FRP cantilever length, and a the pre-crack length. To derive the expression properly, the overall U_d is evaluated over two sections. The first section computes only the U_d accumulated within the FRP cantilever (i.e. $x=0$ to $x=l$) and the second section computes the U_d accumulated over the pre-crack length (i.e. $x=l$ to $x=l+a$). Let $I_{FRP} = h^3/12$ be the moment of inertia of the FRP cantilever, then

$$G_{peel} = \frac{d}{d(l+a)} \left(\int_0^l \frac{(Px)^2}{2E_1 I_{FRP}} dx + \int_l^{l+a} \frac{(Px)^2}{2E_3 I_{1,2} h^3} dx \right)$$

Integrating and differentiating accordingly, the G_{peel} solution associated with a constant peel load becomes:

$$G_{peel} = \frac{N_y^2}{B^2 E_3 h^3} \left(\frac{(l+a)^2 - l^2}{2I_{1,2}} + \frac{6l^2}{\Sigma_{13}} \right)$$

where N_y is defined as the total peel load over the bond width B (i.e. $N_y=PB$) while all the other parameters are as defined before.

3.5.2 Solutions for Debonding under Shear

Figure 3.6 illustrates a typical single lap shear FRP bonded concrete model that is commonly used in the characterization of effective bond length (see discussion in Chapter 5) and interfacial stresses. A constant shear load, N_x , is applied horizontally to the FRP cantilever while a reaction plate pushes against the concrete block. Compared to the loading line as shown in Figure 3.3, a constant bending moment, which comes from the eccentricity of the load, Ψ , exists due to the fact that the actual loading, N_x , is applied to the centerline of FRP laminate instead of the neutral axis of the composite arm. For instance, the eccentricity that appears in Case 2 is:

$$\Psi = t - h\delta + \frac{h}{2}$$

Using the same arguments for thickness differences of the material layers as in the peel case, only the first two terms of the generalized solution remain, i.e.

$$G_{shear} = \frac{1}{2E_3} \left[\frac{P_1^2}{A_{1,2}h} + \frac{M_1^2}{I_{1,2}h^3} \right]$$

Now that $P_1 = \frac{N_x}{B}$ and $M_1 = \frac{N_x \Psi}{B}$, the G_{shear} model can be expressed in the following form:

$$G_{shear} = \frac{N_x^2}{2B^2 E_3} \left(\frac{1}{A_{1,2}h} + \frac{\Psi^2}{I_{1,2}h^3} \right)$$

where all the parameters are as defined before. Eccentricities, Ψ , for all five cases are summarized in Table 3.5 below.

Table 3.5 Eccentricities

<i>Case</i>	Ψ
<i>k = 1</i>	0
<i>k = 2</i>	$h \left(\frac{1}{2} - \delta \right) + t$
<i>k = 3</i>	$\frac{H_1}{2}$
<i>k = 4</i>	$h \left(\frac{1}{2} - \Delta_2 \right) + t - H_2$
<i>k = 5</i>	$h \left(\frac{1}{2} - \alpha_3 \right) + t + H_3$

3.5.3 Solutions for Debonding under Combined Peel and Shear

Due to the linear elastic nature of the solutions, the two limiting cases, namely peel and shear, can be superimposed when the fracture model is subjected to angular loading as shown in Figure 3.7, which reveals similarity of the actual debonding (Figure 3.4). The interface fracture energy release rate solution, $G_{angular}$, can then be expressed as follows:

$$G_{angular} = \frac{(N \cos \theta)^2}{2B^2 \bar{E}_3} \left(\frac{1}{A_{1,2}h} + \frac{\Psi^2}{I_{1,2}h^3} \right) + \frac{(N \sin \theta)^2}{B^2 \bar{E}_3 h^3} \left(\frac{(l+a)^2 - l^2}{2I_{1,2}} + \frac{6l^2}{\Sigma_{13}} \right)$$

where θ is the angle of loading made with respect to the horizontal axis.

From experimentation where the debonding load values are substituted into the fracture models for determining the interface fracture toughness, the critical $G_{angular}$ value should fall somewhere between critical G_{peel} and critical G_{shear} , although the failure envelope with respect to the loading angle, θ , shall depend on the mixed-mode stress states at the crack tip. A better correlation would thus be drawn between the interface fracture toughness (i.e. critical G) and the phase angle, ψ , which is different from the physical loading angle, θ , and the phase angle, ψ , is defined as the relative contribution of the shearing mode over the opening mode at the crack tip in terms of stress intensity factors (Hutchinson and Suo 1992).

3.6 Verification Studies

To verify the derived analytical models, a numerical study by means of the finite element method has been conducted to compare the interface G values. Virtual crack extension and interaction integral methods (Matos et al 1989) have been implemented in the finite element model in order to evaluate G (or equivalently the J integral) independently. Plain strain condition was again assumed due to the same reasoning used in the derivation of the G models. Verification was performed on Case 2 peel and shear fracture models respectively using common material and geometric data of a typical retrofitted joint. The values are summarized in Table 3.6. For the analytical G model, bond width B was set at 25 mm. For both models, bond length was set at 150 mm, and N_x and N_y were respectively 20 kN and 70 N.

Eight-node isoparametric plain strain elements were used throughout the model and a sub-modeling technique (ABAQUS 2004) was used in the crack tip region where the mid-side nodes were moved to the quarter-point positions to force $1/\sqrt{r}$ singularity to occur at the crack tip. A total of eight rings of 256 elements form the crack tip region, which had an overall size of 0.8 mm x 0.8 mm. The G values were evaluated only from the outer four rings, as it is a known property that near-tip computed G values are not

accurate (Matos et al 1989) due to the inherent nature of the mathematical formulation. Figures 3.8 and 3.9 show the deformed meshes of the crack tip region for each respective loading case. More details to this computation method are provided in Chapter 6 where the interface fracture problem is more fully analyzed including the mode-mix characterization. Table 3.7 provides a summary of the values obtained both from the analytical models and from finite element computation. Excellent agreement on the G values has been shown.

Table 3.6 Model Parameters

	<i>Elastic Modulus, GPa</i>	<i>Poisson's Ratio</i>	<i>Thickness, mm</i>
FRP	148.0	0.27	1.28
Epoxy	1.5	0.35	1.00
Concrete	21.8	0.19	37.50

Table 3.7 Result Comparison

	$G_{shear}, kJ/m^2$	$G_{peeb}, kJ/m^2$
Analytical Model	1.5561	0.4401
Finite Element Computation	1.5584	0.4400

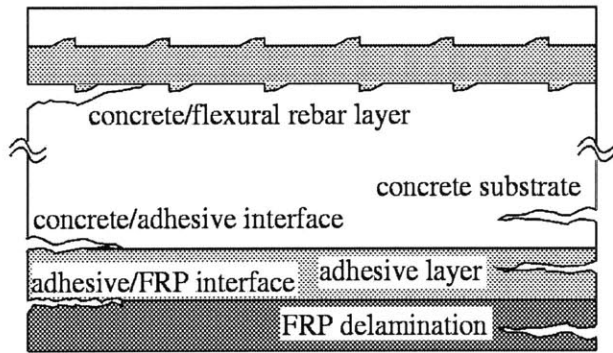


Figure 3.1 Possible Debonding Locations

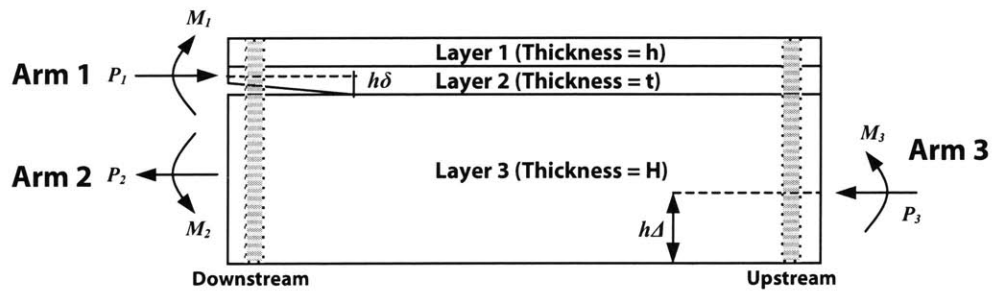


Figure 3.2 Model Idealization and Definition of Debonding Between Layers 2 & 3

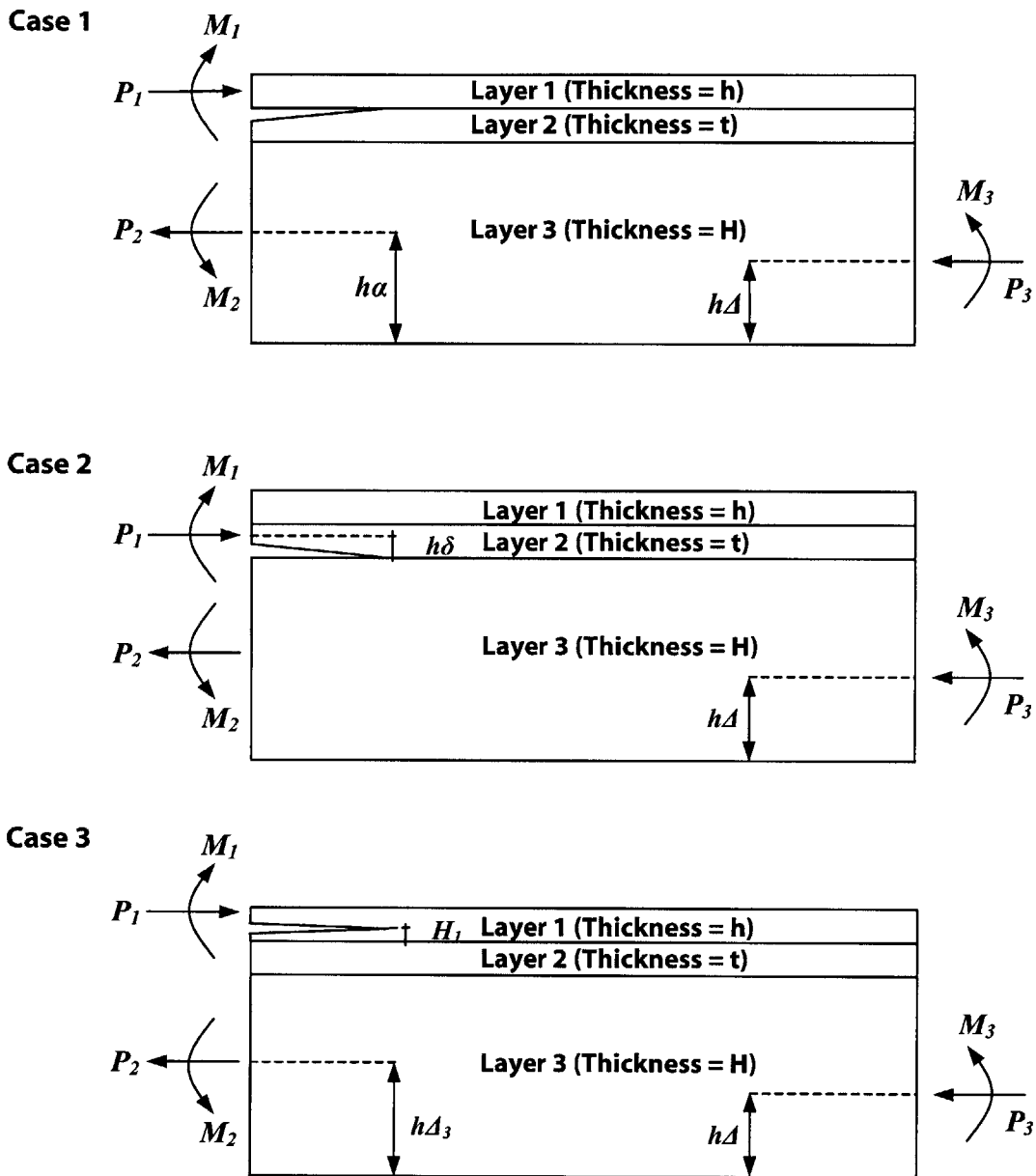


Figure 3.3 Idealization & Definition of All Debonding Scenarios

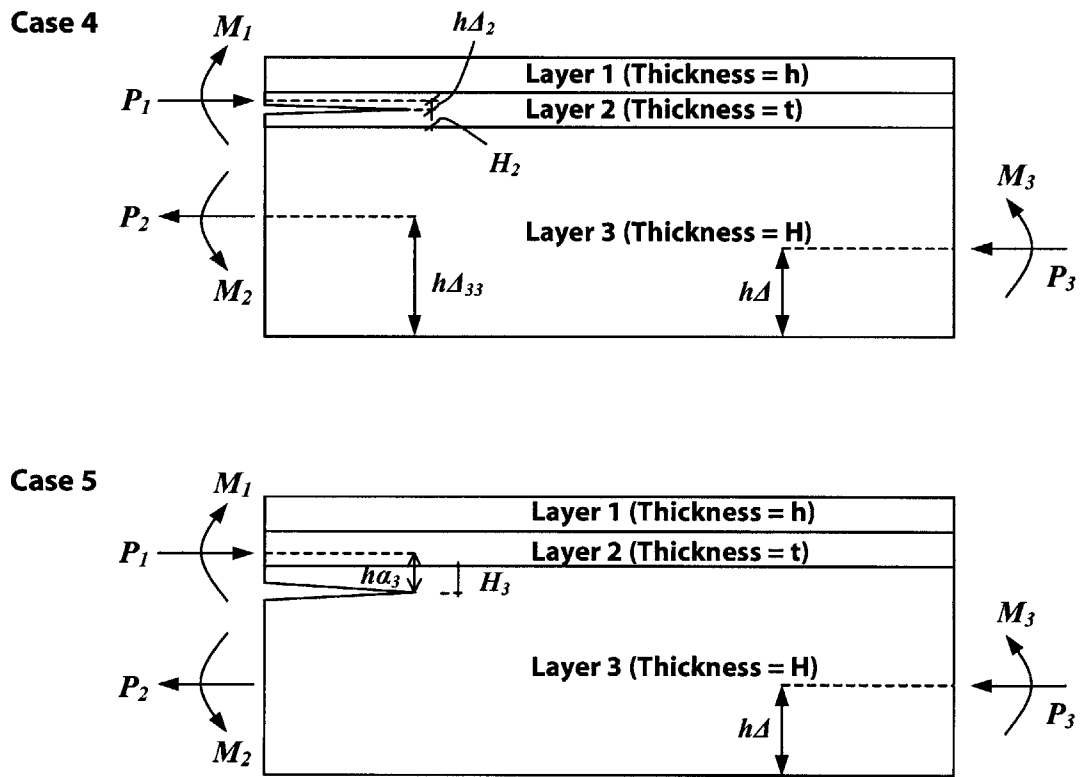


Figure 3.3 (cont) Idealization & Definition of All Debonding Scenarios

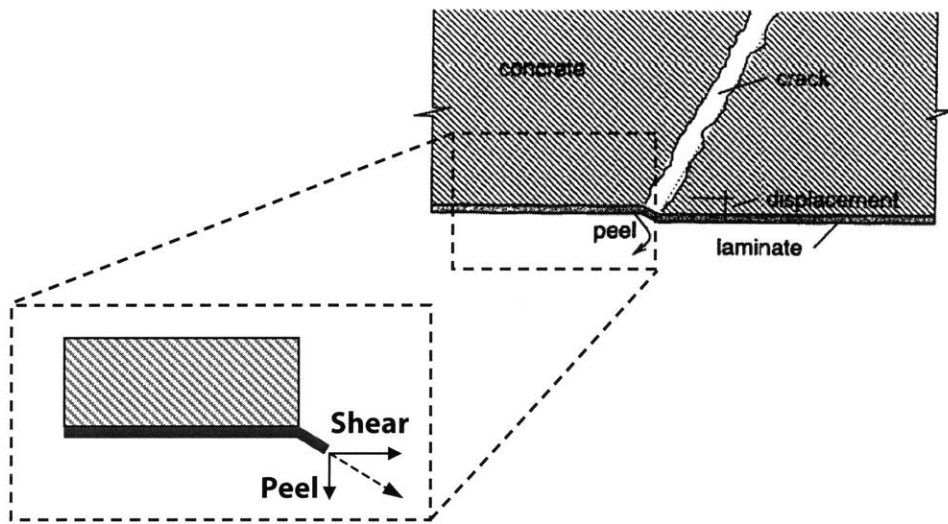


Figure 3.4 Resemblance of Local Debonding Region

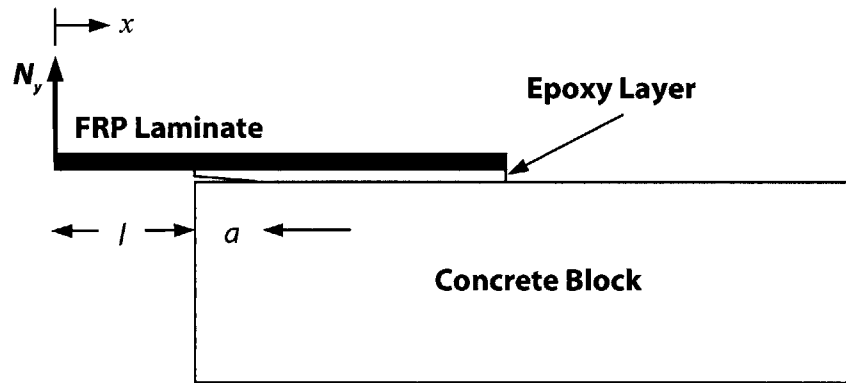


Figure 3.5 Peel Fracture Model

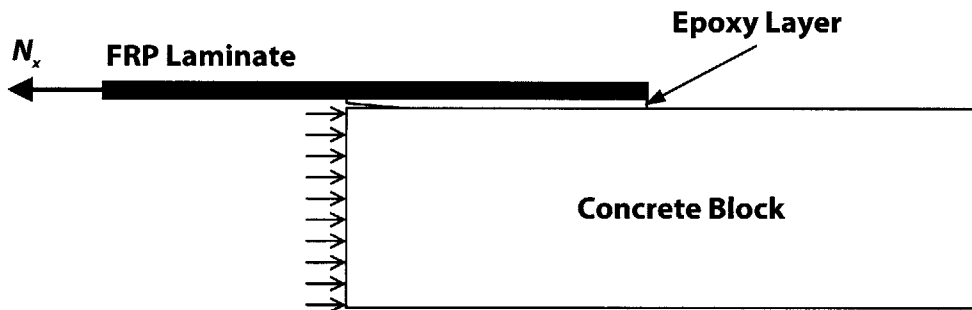


Figure 3.6 Shear Fracture Model

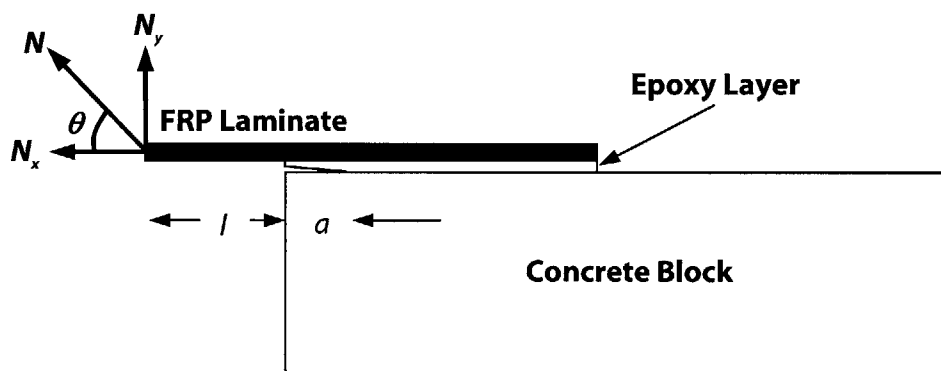


Figure 3.7 Fracture Under Angular Load

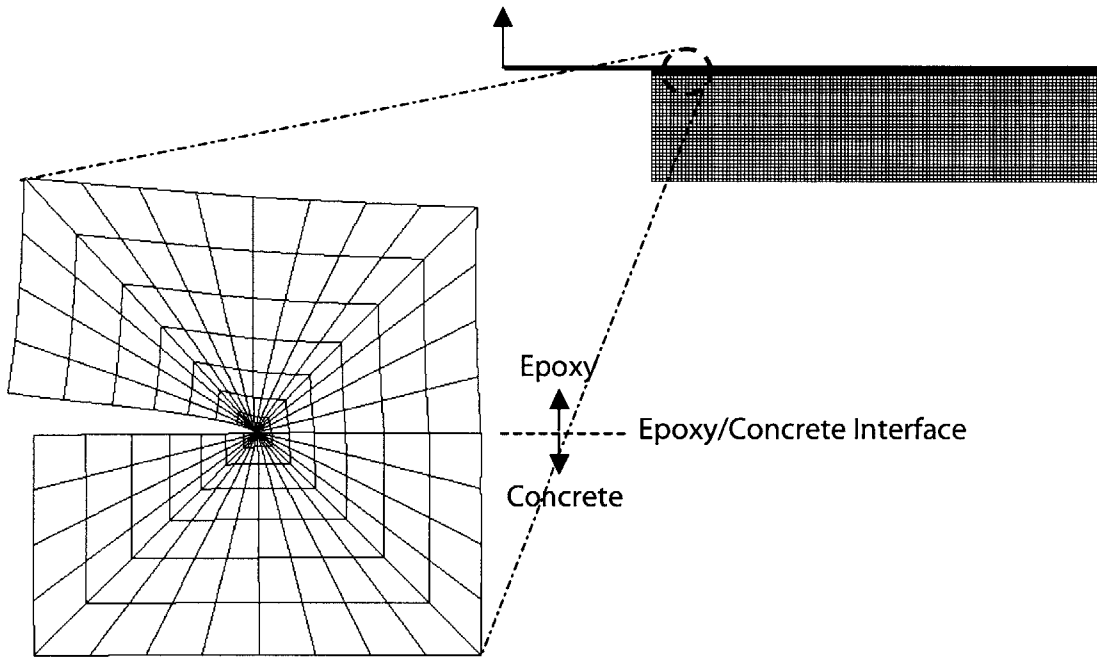


Figure 3.8 Deformed Mesh in the Crack Tip Vicinity of the Peel Model

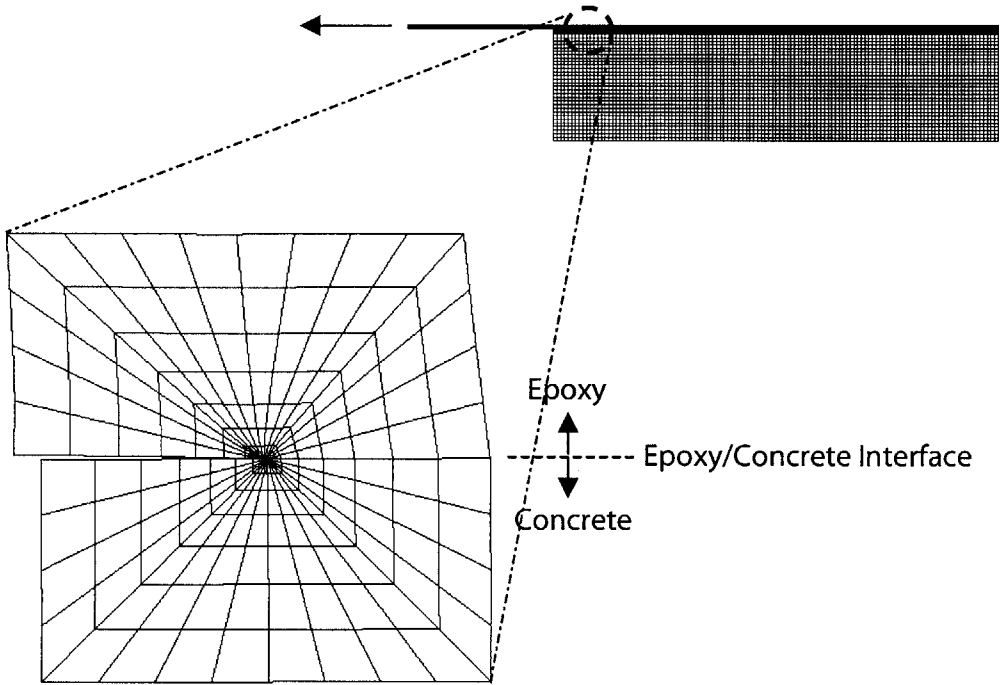


Figure 3.9 Deformed Mesh in the Crack Tip Vicinity of the Shear Model

CHAPTER 4

MATERIAL CHARACTERIZATION & MOISTURE DIFFUSION SIMULATION

To evaluate the interface fracture toughness of a FRP bonded concrete system and its variation under moisture ingress, mechanical properties of the constituent materials as a function of moisture content need to be determined, as shown from the fracture formulations developed in Chapter 3. By conducting moisture diffusion simulation using a three-dimensional finite element model with the geometric configurations of the actual fracture specimen, moisture content in the bond line region can be approximated, hence its mechanical properties estimated. As a basis for subsequent interface fracture analysis, this Chapter presents the results of an extensive material characterization program, which include the determination of diffusion properties, thermal properties, and mechanical properties. Modeling of the three-dimensional diffusion simulation is also presented.

4.1 Material Description

Materials being characterized in this work include a normal grade concrete, one type of carbon FRP (CFRP), and two types of epoxy adhesive systems. These materials

are processed, made, and cured in accordance to available ASTM standards and/or manufacturer stipulations as will be detailed below. The materials discussed herein are identical to those used in the making of peel and shear fracture specimens, which are to be discussed in Chapter 5.

Concrete

The concrete was composed of water, cement, sand and gravel with a mass ratio of 0.5:1.0:2.4:1.6. Aggregates were carefully sieved and remixed to conform to the ASTM C33 grading standard. Maximum gravel size was set at 9.5 mm (3/8") to meet the ASTM C192 requirement of it being three times smaller than the minimum specimen dimension. All aggregates that passed through sieve No.100 were considered too fine and were discarded in order to meet the designed water-cement ratio while maintaining good workability. Fineness modulus of the remixed aggregates was determined to be 2.82. Mixing, casting, and curing procedure fully conformed to the stipulations set forth in ASTM C192. A 28-day curing schedule was followed.

CFRP

CFRP laminates were obtained from a U.S. manufacturer. The laminates were in the form of continuous pultruded prepregged plates that consisted of unidirectional carbon fibers. Fiber volumetric content was 68% according to the manufacturer. Plate thickness was measured at 1.28 mm. These CFRP plates were designed for strengthening concrete, timber, as well as masonry members by bonding onto the structure as external reinforcements. The laminates were fully cured and non-reactive.

Epoxy

Two proprietary epoxy systems obtained from two different U.S. manufacturers were used in this study. Epoxy 1 was a 2-component, 100% solids, moisture-tolerant structural epoxy paste adhesive. Component A represented the epoxy resin while component B the amine hardener. Both components contained crystalline silica (sand) for thixotropy purposes. Mix ratio A:B was 3:1 by weight or volume. Mixing was performed for 3 minutes on a low-speed (400–600 rpm) paddle until uniform in color. The resulting

mix was a light gray paste with good troweling ability. Curing required 7 days in ambient environment.

Epoxy 2 was a two-component, solvent-free, epoxy material designed for use in vertical and overhead applications. According to the manufacturer, component A was an epoxy resin with elastomer additives while component B was an amine hardener. Both components contained fumed silica for thixotropy purposes. Mix ratio A:B was 100:25 by weight or 100:30 by volume. Mixing required a low speed mixer at 400-600 rpm for 5 minutes until components were fully dispersed. The resulting mix was a beige-colored paste with relatively low viscosity compared to Epoxy 1. Curing required 7 days in ambient environment.

4.2 Epoxy Specimen Preparation

All specimens were cast in open Teflon molds that were properly milled to make specimens that meet the respective test standards. Quarter-inch thick aluminum plates were used to rigidly sandwich the Teflon moldings to produce perfectly flat specimens. Teflon was chosen as the mold material for its low surface energy characteristic so that cured epoxy specimens could be easily removed without the use of any mold-release or excessive force that could damage the delicate specimens. Application of mold release was deemed inappropriate in this moisture conditioning study, as residues could form on the surfaces of the cured specimens that might hinder proper moisture diffusion from taking place.

Both epoxies were mixed in accordance to the suggested procedures by the respective manufacturers as described above. Note, however, that these said procedures were intended for practical in-situ mixing, and were not intended to produce a void-free mixture. Although it might seem rational to test void-free specimens for more consistent and repeatable results, it was deemed very challenging of doing so for the viscous ambient-cured epoxies that contained considerable amount of additives. For instance, mixing under vacuum or vacuuming the mixed adhesive has been proved difficult (Lee and Hutchinson 1992) and centrifuging the mixed epoxy would possibly lead to separation of the solid phase (e.g. sand) from the liquid phase (mixed resin). Therefore, both epoxies were mixed as-is with no further attempt to de-void the mixture. Figure 4.1

shows the micrographs at the same scale of both cured Epoxy 1 and Epoxy 2 materials taken from a JEOL 6060 scanning electron microscope. It is clearly seen that Epoxy 1, being a 100% solid formulation, is more porous and brittle, as revealed from the fracture surfaces.

4.3 Conditioning and Test Environments

All material samples were divided into two constant temperature moisture conditioning groups at 23°C and 50°C. Apart from those specimens tested for initial dry properties, all samples were continuously conditioned in water baths providing a 100% RH environment. They were then taken out for weighing and testing in standard laboratory conditions at selected time intervals. Concrete samples were oven dried at 50°C until no weight change could be registered before subjecting them to moisture conditioning. All epoxy specimens were assumed dry initially because the mixing and curing process did not involve water. CFRP samples were only tested for initial properties as a study on the same material by the same research group in collaboration with the INEEL research group (Gunes 2004) has determined that prolonged moisture conditioning has little effect on their properties in the fiber direction, which governs the tensile and flexural responses, due to the fact that carbon fibers are relatively inert to moisture attack, as discussed in Chapter 2.

4.4 Choice of Water for Conditioning

Moisture conditioning can be performed using various types of water baths. In the context of FRP bonded concrete, de-ionized water, salt water, and concrete pore solutions can be the choice. However, a recent independent study (Chin et al 1999) has shown that these different types of water result in little differences in the moisture uptake behavior in epoxy materials that are moisture conditioned at temperatures up to 60°C: (1) diffusion of all three types of water demonstrated a Fickian behavior, (2) diffusion coefficients determined from each type of water within the same temperature group are in good agreements, and (3) saturated moisture mass uptakes are almost identical. Since thermal and mechanical properties of epoxy materials have strong dependency on moisture mass uptake (Nogueira et al 2001) and that the three types of water do not demonstrate

practical differences in moisture uptake both qualitatively and quantitatively, de-ionized water was chosen for conditioning all material samples as a matter of convenience.

4.5 Moisture Sorption Studies – Material Test Program Part 1

Moisture sorption studies were conducted on thin material coupons of concrete, CFRP, and the two epoxies to determine the water-transport properties, in particular, the diffusion coefficients and moisture saturation values (in percentage mass uptake). Ten coupons were tested for each material to provide averaging of the moisture sorption quantification. The aspect ratio (width to thickness) of these samples was so chosen as to resemble a one-dimensional diffusion behavior, as discussed in Chapter 2. The width of the coupons was at least one order of magnitude higher than the thickness. The moisture sorption program is graphically summarized in Figure 4.2.

Concrete coupons with a thickness of 6 mm were carefully cut from the mid sections of 10 randomly selected cylindrical specimens with a 50 mm diameter using a high-speed diamond saw. The thickness of 6 mm was the thinnest possibly achieved with the sawing equipment; attempts were made to produce thinner cuts but had always resulted in apparent flaws within or near the edges. All concrete coupons were closely examined after often dried. Only those free from flaws/cracks and voids were considered valid samples. CFRP coupons were trimmed in square shape from a roll of pultruded prepregated CFRP plate that had a plate width of 50 mm. The CFRP coupons thus had a dimension of 50 mm x 50 mm. Thickness was 1.28 mm as manufactured. Epoxy coupons for both adhesive systems were molded in circular shape with a thickness of 3.2 mm and a diameter of 50 mm as suggested by ASTM D570. Thickness and dimensions were measured using a digital caliper that was accurate up to ± 0.01 mm.

All sorption coupons were first weighed for their dry weights. They were then immersed in constant temperature water baths at 23°C and 50°C respectively to allow continuous moisture sorption to take place. The coupons were taken out for subsequent weighing at selected time intervals. Note that the time intervals between weighing need not be regular in order to generate moisture uptake curves that were used for subsequent computation of diffusion coefficients. Measurements were made on Day 0, 1, 2, 3, 7, 14, 28, 75, 124, 158, and 324 for all moisture coupons. Measurement intervals were shorter

at the beginning to capture the faster moisture uptake behavior. Before each weighing, coupons of the high temperature group were removed from the water baths and first dipped into a water tank at room temperature to suppress surface water desorption due to significant temperature differential between the coupons and the surrounding environment. They were then dried with filter papers, immediately weighed, and returned to the original water baths. All weighing were performed on a AccuLab AL-204 electronic analytical balance that had a precision up to 0.0001g.

4.5.1 Moisture Uptake Behavior

Moisture uptake curves for concrete, CFRP, and the two epoxies are shown respectively in Figures 4.3, 4.4, and 4.5, plotting percentage weight gain M_t versus square root of time. These figures show that mass uptake plots for all materials tested, in general, feature an initial linear region, followed by a region concave to the abscissa, and then by a relatively stable but slower uptake until saturation, resembling the Fickian and pseudo-Fickian behavior as discussed in Chapter 2. In some cases, particularly those associated with high temperature conditioning, the moisture coupons did not saturate (or reached diffusion equilibrium) even after 324 days of continuous exposure in 100% RH environment. As such, normalized plots could not be made accurately on these coupons with respect to the saturated moisture content, M_s , (i.e. M_t/M_s), as illustrated in Figure 2.8. The computation of diffusion coefficients, D , was thus approximately performed, as outlined in Chapter 2, assuming a pseudo-Fickian diffusion behavior. Table 4.1 summarizes the estimated diffusion coefficients, D , and saturated mass uptake, M_s , for the constituent materials.

Table 4.1 Moisture Diffusion Properties

<i>Materials</i>	M_s (%)		D ($\times 10^{-12}$ m ² /s)	
	23°C	50°C	23°C	50°C
Concrete	7.71	7.76	32.4	32.4
CFRP	0.34	0.90	0.68	0.81
Epoxy 1	1.18	2.88	0.18	0.20
Epoxy 2	2.58	5.42	0.23	0.48

It is observed that higher conditioning temperature has generally led to faster moisture diffusion, as indicated from the higher diffusion coefficients and moisture saturation values. The only exception of this phenomenon was that of concrete in which the diffusion behavior did not change with increasing temperature within the tested temperature range. However, initial moisture uptake by the concrete material was much faster than CFRP and epoxies. After only one day of conditioning, the moisture content has already reached 77% of the saturation point. As a result, the moisture uptake curves demonstrated a distinct kinking point beyond which moisture uptake became more gradual. Comparing the shape of the uptake curves with a typical moisture diffusion behavior as discussed in Chapter 2, it could in fact be inferred that the estimated diffusion coefficient for concrete was underestimated as the fastest moisture ingress could have been taken place in the first few hours within Day 1. For the case of CFRP and epoxies, time to saturation tended to be shorter at a lower conditioning temperature. All 50°C CFRP and epoxy moisture coupons did not demonstrate a saturation state even after 324 days of continuous submergence in the water baths. In fact, the linear increasing curve shapes of these coupons suggested high potential of more moisture uptake.

4.5.2 Activation Energy of Moisture Diffusion

From the sorption curves, it is observed that moisture diffusion in epoxy materials is a thermally activated rate process, as higher temperature conditioning had led to more and faster mass uptake at a given time, due probably to the higher probability of the energy of water molecules exceeding the activation barrier set up by the interaction potential from intra-molecular forces during the diffusion process. Such dependence on temperature can be quantified by an Arrhenius relationship as expressed as follows:

$$D = D_0 e^{-\frac{A}{RT}}$$

where D_0 is the pre-exponential coefficient, A the activation energy for moisture diffusion, R the universal gas constant, and T the temperature (on Kelvin scale) at which moisture diffusion takes place. Both D_0 and A can be determined graphically by plotting $\ln D$ versus $1/T$ such that:

$$\ln D = -\frac{A}{R} \left(\frac{1}{T} \right) + \ln D_0$$

The estimated activation energies and the pre-exponential coefficients of the diffusion process in Epoxy 1 and Epoxy 2 are summarized in Table 4.2 as follows:

Table 4.2
Activation Energy Parameters

	A (kJ/mol)	D_0 (m ² /s)
Epoxy 1	3.1	0.63e-12
Epoxy 2	21.7	1.52e-9

This activation energy concept, however, only applies partially to CFRP, as the material comprises of a moisture non-absorbent carbon fiber phase (see Chapter 2 for more detailed discussions on moisture resistant characteristics of carbon fibers) and a moisture absorbent epoxy resin phase. Since the CFRP laminate consists of two distinct material phases and moisture diffusion within the laminate is a complicated phenomenon that consists of moisture transport at fiber/resin interfaces in addition to moisture ingress within the resin, no attempt is made to characterize the activation energy of the moisture diffusion process in this composite material.

Concrete, on the other hand, shows no practical difference in its moisture mass uptake curves under the 2 conditioning temperatures both in terms of its diffusion coefficients and the saturated mass uptake value. Thus, the activation energy for concrete is also not characterized.

4.5.3 Discussions of Diffusion Behavior in Epoxies

From Table 4.1, it is observed that solubility, S , which is defined as the saturated moisture mass uptake per unit volume of the sorption coupon, as reflected in the M_s values, almost doubled in both epoxy systems when temperature was increased from 23°C to 50°C while diffusivity, D , of both materials increased with temperature to varying degrees depending on the epoxy formulation. The increase in Epoxy 1 was fairly insignificant while that in Epoxy 2 was more than doubled. The extent of increase was also reflected in the values of activation energy, in which there was an order of

magnitude difference, although both values fell within the range for most polymers as reported by Loos and Springer (1979).

By definition, the higher activation energy of Epoxy 2 implies a higher energy barrier that needs to be overcome. This might possibly be explained by a higher crosslink density, which is defined as the number of sites chemically joined among adjacent polymer chains (crosslink) per unit volume, in Epoxy 2 and should be reflected in the glass transition temperature, which will be defined and discussed next. However, a higher crosslink density also implies less water uptake at saturation, as there is diminished availability of molecular-sized voids (free volume) in the polymer structure when adjacent polymer chains are brought closer together. Thus, the observed diffusion behavior could not be explained by free-volume arguments alone.

It has been proposed that moisture diffusion consists of two processes – absorption (free water) and adsorption (bound water). Free water occupies the free volume of the epoxy resin while bound water chemically reacts with the hydroxyl groups (–OH) on the polymer chains, which can be found in all epoxy stoichiometry, via hydrogen bonding, hence disrupting the chain and enhancing the chain mobility (Xiao and Shanahan 1998, Vanlandingham et al 1999, Nogueira et al 2001). In other words, the effective crosslink density is reduced when adsorption takes place. The higher solubility observed in Epoxy 2 could thus be due to significant adsorption, which could also possibly explain the dramatic loss of transparency after moisture conditioning, as illustrated in Figure 4.6. The color change was not as profound in the case Epoxy 1.

4.6 Thermal Analysis of Epoxies – Material Test Program Part 2

Dynamic mechanical analysis (DMA) was performed to evaluate the glass transition temperature, T_g , of the epoxies in accordance to ASTM E1640 using a TA Instruments DMA Q800 analyzer. Three-point bend molded epoxy specimens that measured 58 mm x 13 mm x 3.2 mm (length x width x thickness) were tested. A total of 72 three-point bend DMA specimens were tested at 6 time intervals for each epoxy system in each moisture conditioning temperature group. Three identical moisture conditioned specimens of the same type (in terms of materials and conditioning environments) were taken out for testing at each time interval. A DMA cycle involved a

three-point bend loading frequency that was set at 1 Hz to provide oscillatory stress on the specimen with a controlled frequency while at the same time the specimen was subjected to a temperature ramp rate of 1°C/min over the range of 20°C to 100°C. Figure 4.7 shows the schematics of the DMA setup.

In a viscoelastic material such as the polymeric epoxy, stress and strain are out of phase in time due to the time lag generated by the viscous portion of the material. The out-of-phase quantity is known as a phase angle, which is commonly referred to as delta. Tangent delta (hereafter tan-delta), which can be thought of as an index of viscoelasticity, is defined as the modulus ratio of the viscous component over the elastic component. In a perfectly elastic material system, the applied stress and the resulting strain are always in phase. Thus, a small phase angle indicates high elasticity while a large phase angle indicates high viscosity. The modulus response of the epoxy can hence be fully characterized by a complex quantity that consists of an elastic (or storage) modulus component and a viscous (or loss) component. The viscous component signifies the portion of the material that will flow under stress (i.e. creep or stress relaxation). Figure 4.8 shows a typical plot obtained from a DMA test that shows the variations in elastic (storage) modulus, viscous (loss) modulus, and tan-delta.

From the DMA plot, it can be observed that as the storage modulus reduces sharply with increasing temperature, the loss modulus increases accordingly. This signifies the shift of modulus from an elastic state to a viscous state as the temperature the material is subjected to increases. The elastic-viscous shift is referred to as the glass transition and the associated temperature at which this occurs is called the glass transition temperature, T_g . Assigning an exact value to the glass transition has been historically a subject of debate due to the different reasoning in respective applications of the viscoelastic materials. Nevertheless, in applications where load-bearing characteristic of the material is of concern, such as in the case of FRP retrofitting, the glass transition point is usually defined as the onset of a sharp reduction in the storage modulus, as indicated in Figure 4.8. Using this definition, the glass transition temperatures were determined for the two epoxies with increasing moisture content. Tables 4.3 and 4.4 summarize the DMA test results for Epoxy 1 and Epoxy 2 respectively and the data are plotted in Figure 4.9 for better visualization.

Table 4.3 DMA Test Results of Epoxy 1

Epoxy System	Moisture Conditioning Temperature (°C)	M_t (%)	T_g (°C)
Epoxy 1	23	0.0000	52.0
Epoxy 1	23	0.0000	51.8
Epoxy 1	23	0.0003	51.8
Epoxy 1	23	0.0066	49.0
Epoxy 1	23	0.0224	48.6
Epoxy 1	23	0.0771	44.4
Epoxy 1	23	0.0807	44.9
Epoxy 1	23	0.0856	46.3
Epoxy 1	23	0.1093	44.1
Epoxy 1	23	0.1189	45.6
Epoxy 1	23	0.1329	45.0
Epoxy 1	23	0.2395	45.3
Epoxy 1	23	0.3133	44.0
Epoxy 1	23	0.3248	45.3
Epoxy 1	50	0.0689	54.4
Epoxy 1	50	0.0809	54.4
Epoxy 1	50	0.0833	53.4
Epoxy 1	50	0.1537	55.0
Epoxy 1	50	0.2019	50.6
Epoxy 1	50	0.2069	53.3
Epoxy 1	50	0.2486	53.3
Epoxy 1	50	0.2762	52.2
Epoxy 1	50	0.2925	53.1
Epoxy 1	50	0.4429	49.9
Epoxy 1	50	0.4465	51.0
Epoxy 1	50	0.4887	52.2
Epoxy 1	50	0.5242	52.3
Epoxy 1	50	0.6116	52.3
Epoxy 1	50	1.1503	48.0
Epoxy 1	50	1.2195	50.5
Epoxy 1	50	1.2928	48.2

Table 4.4 DMA Test Results of Epoxy 2

Epoxy System	Moisture Conditioning Temperature (°C)	M_t (%)	T_g (°C)
Epoxy 2	23	0.0000	50.4
Epoxy 2	23	0.1302	49.6
Epoxy 2	23	0.1663	50.1
Epoxy 2	23	0.2460	49.0
Epoxy 2	23	0.2523	48.5
Epoxy 2	23	0.2625	49.2
Epoxy 2	23	0.4339	45.0
Epoxy 2	23	0.4469	46.3
Epoxy 2	23	0.5988	45.6
Epoxy 2	23	0.8625	44.1
Epoxy 2	23	0.9159	44.4
Epoxy 2	23	0.9306	44.9
Epoxy 2	23	1.0329	42.3
Epoxy 2	23	1.2200	42.6
Epoxy 2	23	1.2722	43.1
Epoxy 2	50	0.1869	52.4
Epoxy 2	50	0.2500	52.8
Epoxy 2	50	0.2607	53.4
Epoxy 2	50	0.4465	50.9
Epoxy 2	50	0.4700	52.9
Epoxy 2	50	0.4887	51.8
Epoxy 2	50	0.5242	51.2
Epoxy 2	50	0.6116	49.7
Epoxy 2	50	0.7663	48.7
Epoxy 2	50	0.8035	48.0
Epoxy 2	50	1.0400	46.0
Epoxy 2	50	1.1100	45.0
Epoxy 2	50	1.1503	46.6
Epoxy 2	50	1.8900	47.2
Epoxy 2	50	2.1900	47.5
Epoxy 2	50	2.5100	47.8
Epoxy 2	50	2.5700	47.1
Epoxy 2	50	2.6068	46.8

4.6.1 Effect of Moisture on Glass Transition Temperature

As discussed in the last section, hydrogen bonding between the water molecules and the polar hydroxyl groups of the polymer chain will disrupt the crosslink density. It was thus expected that a change in T_g would take place upon moisture conditioning, although the free water would try to hinder chain mobility under external load to some degrees as the free volume is filled. One complication in both epoxy materials was that they were ambient cured, meaning that there was upside potential for further crosslink formation under elevated temperature and hence a higher T_g . For the 50°C moisture conditioned specimens, there existed possible competing mechanisms that came from moisture degradation and high temperature post curing in the water baths.

Figure 4.9 shows the T_g degradation plots against moisture mass uptake of Epoxy 1 and Epoxy 2 respectively. The plots show that T_g of both epoxies degraded with increasing moisture mass uptake. And both epoxy systems had T_g falling between 40°C and 55°C, although that of Epoxy 2 tended to range a bit lower than that of Epoxy 1 at all times regardless of moisture effects. The post-curing effect and the moisture mass uptake acceleration by high temperature conditioning was seen in the up shifting and stretching over a larger range of M_t of the curves. Drop of T_g in the 23°C temperature groups was more dramatic than the 50°C groups, due probably to the lack of T_g enhancing post-curing effect. This enhancement effect arises when more crosslink sites need to be overcome by the hydrogen bonding of the bound water. Nevertheless, T_g degradation behavior seemed to be asymptotic by nature, despite the fact that the asymptotic values were closing in on the rather worrying temperature levels in the mid to low 40s°C for the 23°C conditioned coupons and marginally below 50°C for the 50°C conditioned coupons. This temperature level could practically be reached in a concrete beam soffit.

4.6.2 Effect of Post Curing at Elevated Temperature on Glass Transition Temperature

To confirm the above-mentioned up-shift behavior of the T_g asymptote that was demonstrated in the 50°C groups as compared to the 23°C groups, a comparative

repeatability test was conducted using two identical DMA specimens of Epoxy 1, one being a regular ambient cured sample (called Sample A) while the other one (called Sample B) from the same mixing batch that was post-cured in vacuum for 7 days at 90°C, a temperature level which almost doubled the as cured T_g . Vacuum was used to prevent physical aging at the relatively high temperature.

Both Samples A and B were respectively subjected to a DMA cycle, cooled down, and re-subjected to a second DMA cycle. A total of four curves were thus obtained. By plotting the four curves (storage modulus) on one graph as shown in Figure 4.10, the effect of elevated temperature post-curing is revealed.

It can be noted that, for Sample A, the storage modulus curve shifted to the right after only one DMA cycle, which ramped up to about 80°C from 20°C in 60 minutes (or 1°C/min). For Sample B, on the other hand, both runs yielded almost exactly the same curves, signifying the full curing and hence thermal stability of the epoxy material. The B curve also shifted to the far right, almost doubled the initial T_g of the ambient cured Sample A, greatly relaxing the critical zone of service temperature. This test has thus illustrated the criticality of developing an ambient cured epoxy that could fully crosslink by means of chemical reactions without the aid of heating or of developing an elevated temperature post-curing system for on-site usage.

4.7 Mechanical Property Characterization – Material Test Program Part 3

Mechanical tests were performed on concrete and on both epoxies to determine their properties before and after moisture conditioning. To estimate the interface fracture toughness using the formulations presented in Chapter 3, only the elastic moduli need to be determined. However, it is also beneficial to more extensively characterize their other properties that might increase the overall understanding of the joint behavior and for subsequent interpretation and analysis. As such, the compressive, tensile, and fracture properties of concrete have been characterized. For the two epoxies, both tensile and shear properties are determined. Figure 4.11 illustrates the overall mechanical test program. CFRP was also tested for its initial dry properties in the fiber direction in accordance to ASTM D3039 with displacement control at a rate of 2 mm/min. The elastic

modulus and tensile strength were experimentally determined as 148 GPa and 2.7 MPa respectively.

4.7.1 Concrete Characterization

Concrete is a well-known material and the effect of moisture on their mechanical properties has been investigated by a number of research groups (Bazant and Thonguthai 1978, Bazant and Prat 1988, Ross et al 1996, Neville 1997, Konvalinka 2002). It has generally been observed that mechanical properties degrade with increasing moisture content. In particular, mode I fracture toughness of concrete after fully saturated with moisture and tested under water could reduce by as much as 60% (Bazant and Prat 1988) while the reduction of compressive strength could range from 30% to 40% on 720-day cured concrete, depending on the level of moisture saturation (Konvalinka 2002).

Bazant and Prat (1988) attempted to explain the reduction in fracture toughness from a viewpoint of internal pore pressure. It is believed that internal pore pressure is developed on the water molecules in the pores in wet concrete due to external loads. Since the migration of water in a pore is not free when adjacent pores are also filled with water and due to capillary actions, the hindered adsorbed water produces a very high disjoining pressure between the contacting cement gels. The pore pressure is responsible to intensify the stress intensities of the micro-crack tips and hence promotes crack propagation under external loads. This reduces the load-resistance of wet concrete, as compared to dry concrete.

Konvalinka (2002), on the other hand, approached the degradation problem from a viewpoint of volumetric change of the hardened cement paste. It is believed that drying of concrete decreases the volume of the hardened cement paste, reducing the average distance between the surfaces of the hardened cement gel particles. This reduction naturally leads to increase in secondary bonds between the surfaces, and hence increases the strength of the dry specimens. Conversely, wetting the concrete increases the volume of the hardened paste and hence the average distance between the surfaces of the gel.

To validate these hypotheses on a macroscopic sense as well as to determine the modulus variation with increasing moisture content, compressive tests, splitting tensile tests, and fracture tests have been performed using cylindrical and 3-point bend fracture

specimens in accordance to ASTM C39, ASTM C496, and Bazant's mode 1 concrete fracture test setup (Bazant and Prat 1988). Figure 4.12 shows the schematics of the specimens and test configurations.

Concrete cylinders had a diameter of 50 mm and a height of 100 mm. Fracture beam specimens measured 100 mm x 37.5 mm x 37.5 mm with a through-thickness center notch that was 6.25 mm deep x 1.6 mm wide. Span length of the fracture beams was 93.75 mm, which was 2.5 times the beam thickness. All specimens were continuously moisture conditioned and taken out at selected time intervals for testing in standard laboratory conditions.

Both the compressive and splitting tensile tests were performed on a Baldwin loading frame. Axial strains of the compressive cylinders were measured by means of a pair of clip-on extensometers mounted on opposite sides. Fracture beam tests were, on the other hand, performed on an Instron universal test machine Model 1331 with a loading rate of 0.05 mm/min. Compressive and fracture tests were displacement controlled while tensile tests were load controlled as stipulated in the test standard. Initial properties (both 28-day and oven-dried) are summarized in Table 4.5

Table 4.5 Initial Properties of Concrete

	<i>28-day</i>	<i>Oven-Dried</i>
Compressive Strength (MPa)	29.0	32.4
Elastic Modulus (GPa)	21.8	26.2
Tensile Strength (MPa)	3.9	5.1
Fracture Toughness (MPa \sqrt{m})	0.61	0.82

Figures 4.13, 4.14, and 4.15 plot respectively the variations of compressive properties (strength and modulus), splitting tensile strength, and mode 1 fracture toughness with increasing moisture uptake. Trend lines are also given as a result of regression analysis. Generally speaking, degradation took place in all cases with obvious degradation trends in strength properties. Effect of the different conditioning temperatures, however, does not seem to be significant in all test cases. Strength and fracture toughness reduction ranged from 26% to over 40%, as demonstrated from the

trend lines. These results were inline with the findings obtained by the above named researchers. Modulus degradation, on the other hand, was not as significant, although data scattering seemed to be more substantial, as in the case of compressive strength. The more substantial scattering of data found in compressive tests compared to that in tensile and fracture tests may be explained by the fact that redundant crack paths are available when the concrete material is subjected to compression (such as around the aggregates and through the aggregates) while the crack propagation locus under tension or mode I fracture is relatively clean and clear. Due to data scattering, values of the elastic modulus obtained from the trend lines will be used for the determination of interface fracture toughness.

4.7.2 Epoxy Characterization

A. Tensile Test

Tensile properties were characterized using Type I dumbbell shaped samples, as illustrated in Figure 4.16, in accordance to ASTM D638 with an Instron universal test machine Model 1331 mounted with a 50kN load cell and a pair of self-tightening grips. Crosshead speed was set at 1 mm/min. Strain was measured within the specimen 50 mm gage length using a clip-on Instron extensometer. Initial properties (dry) for both epoxies were determined and summarized in Table 4.6:

Table 4.6 Initial Tensile Properties of Epoxies

	<i>Epoxy 1</i>	<i>Epoxy 2</i>
Tensile Strength (MPa)	21.9	23.0
Tensile Strain at Failure (%)	0.24	3.97
Tensile Modulus (GPa)	4.1	1.5

Tensile strength and stiffness generally degraded with increasing moisture uptake, while elongation at break increased. In the case of Epoxy 2, which was an elastomer-toughened epoxy, the elongation at break was substantial. Figure 4.17 shows the variations of these properties for both Epoxy 1 and Epoxy 2 and Tables 4.7 and 4.8 summarize the tensile properties determined with respect to percentage moisture uptake for Epoxy 1 and Epoxy 2 respectively.

Table 4.7 ASTM D638 Test Results on Tensile Properties of Epoxy 1

Epoxy System	Moisture Conditioning Temperature (°C)	M_t (%)	Tensile Strength (MPa)	Tensile Strain (%)	Tensile Modulus (GPa)
Epoxy 1	23	0.00	23.32	0.28	3.90
Epoxy 1	23	0.00	20.87	0.24	4.17
Epoxy 1	23	0.03	21.07	0.22	4.31
Epoxy 1	23	0.04	21.17	0.23	3.92
Epoxy 1	23	0.05	21.62	0.23	4.26
Epoxy 1	23	0.06	22.44	0.22	4.84
Epoxy 1	23	0.08	22.62	0.26	3.39
Epoxy 1	23	0.22	22.85	0.37	3.52
Epoxy 1	23	0.22	23.16	0.34	3.58
Epoxy 1	23	0.26	23.95	0.37	3.41
Epoxy 1	23	0.32	20.36	0.27	3.72
Epoxy 1	23	0.35	20.23	0.35	3.16
Epoxy 1	50	0.00	22.62	0.26	3.39
Epoxy 1	50	0.03	29.05	0.44	3.48
Epoxy 1	50	0.05	25.25	0.48	2.84
Epoxy 1	50	0.05	24.66	0.45	2.78
Epoxy 1	50	0.07	27.15	0.47	3.15
Epoxy 1	50	0.17	22.05	0.37	3.19
Epoxy 1	50	0.22	20.83	0.40	2.83
Epoxy 1	50	0.23	23.39	0.42	3.33
Epoxy 1	50	0.23	22.82	0.40	3.01
Epoxy 1	50	0.59	17.30	0.29	3.44
Epoxy 1	50	0.67	18.55	0.37	2.61
Epoxy 1	50	0.68	16.62	0.35	2.34
Epoxy 1	50	1.08	16.32	0.47	2.34
Epoxy 1	50	1.08	16.66	0.45	2.52
Epoxy 1	50	1.14	16.72	0.43	2.46

Table 4.8 ASTM D638 Test Results on Tensile Properties of Epoxy 2

Epoxy System	Moisture Conditioning Temperature (°C)	M_t (%)	Tensile Strength (MPa)	Tensile Strain (%)	Tensile Modulus (GPa)
Epoxy 2	23	0.00	23.00	3.83	1.64
Epoxy 2	23	0.01	22.76	3.50	1.41
Epoxy 2	23	0.02	22.92	4.43	1.50
Epoxy 2	23	0.51	20.90	3.77	1.44
Epoxy 2	23	0.56	20.54	3.78	1.39
Epoxy 2	23	0.87	18.84	4.93	1.28
Epoxy 2	23	0.91	18.62	4.96	1.29
Epoxy 2	23	1.41	17.61	7.82	1.48
Epoxy 2	23	1.64	18.28	8.53	1.29
Epoxy 2	23	1.72	17.11	11.64	1.22
Epoxy 2	23	2.14	17.63	13.33	1.30
Epoxy 2	23	2.15	17.9	14.43	1.40
Epoxy 2	50	0.16	24.13	2.88	1.26
Epoxy 2	50	0.17	23.69	2.57	1.32
Epoxy 2	50	0.18	23.33	4.01	1.30
Epoxy 2	50	0.19	24.08	3.56	1.27
Epoxy 2	50	0.21	23.08	3.62	1.25
Epoxy 2	50	1.34	20.99	9.68	1.15
Epoxy 2	50	1.37	20.96	11.04	1.12
Epoxy 2	50	1.97	21.56	8.23	1.17
Epoxy 2	50	2.00	22.09	7.15	1.13
Epoxy 2	50	2.01	21.76	6.11	1.05
Epoxy 2	50	2.57	20.90	8.09	1.09
Epoxy 2	50	2.57	20.75	8.84	1.05
Epoxy 2	50	3.61	20.58	12.01	1.06
Epoxy 2	50	3.63	20.63	13.2	1.01

The results indicate that the absolute degradation for the 50°C group were generally more pronounced than the 23°C group and the range of moisture content involved was much wider. Yet, increase in conditioning temperature seemed to have increased the initial strength and failure strain of both materials while the compliance was also increased. Most of the degradation on strength properties took place during the initial stages of moisture diffusion and then stabilized with increasing moisture content. Modulus degradation, on the other hand, was more steady and generally demonstrated a linear degradation trend up to the tested range of moisture contents.

For Epoxy 1, the decrease in strength and modulus was both close to 40%. Failure was considered brittle, as indicated by the very low failure strain, which was less than 0.5% at all times. The low level of strain was deemed understandable given that Epoxy 1 was mixed with a solid base material that contained sand additives, which naturally acted as stress raisers.

For Epoxy 2, the reduction in strength and modulus was approximately 25% and 30% respectively. As a consequence of the elastomer toughening mechanism, failure strain was an order of magnitude higher than that of Epoxy 1. There was also a 300% increase in strain for the given test period due to substantial mix of crazing (horizontal pattern) and shear banding (angular pattern) developed before the ultimate failure state. Figure 4.18 shows a close up of this phenomenon taken after a tensile test within the gage length area, of which the bottom represented the tensile fracture surface and the top went into the grip. Note that the crazing pattern was developed perpendicular to the loading direction.

B. Shear Test

Shear test of the punch type was used to determine shear strength of the epoxy materials. Tests were carried out following the ASTM D732 specifications. A punching shear tool, which was placed between the platens of the crossheads of the Instron 1331, was specially made in accordance to the standard. Figure 4.19 shows the schematics of this punching shear tool.

Test specimens were in the form of 50 mm diameter disk with a thickness of 3.2 mm. The specimen shape and size were basically identical to those of the epoxy moisture

coupons, except that there was a concentric center cutout of 11 mm in diameter so that the hardened dowel could be properly fastened to perform the punching action. Crosshead speed was maintained at 1.25 mm/min. Tables 4.9 and 4.10 summarizes the test results and Figure 4.20 illustrates the trends of behavioral changes of the punching shear strength with increasing moisture uptake.

Table 4.9 ASTM D732 Test Results on Shear Strength of Epoxy 1

Epoxy System	Moisture Conditioning Temperature (°C)	M_t (%)	Shear Strength (MPa)
Epoxy 1	23	0.00	28.47
Epoxy 1	23	0.00	28.06
Epoxy 1	23	0.01	28.65
Epoxy 1	23	0.02	25.67
Epoxy 1	23	0.03	29.37
Epoxy 1	23	0.03	24.39
Epoxy 1	23	0.03	30.71
Epoxy 1	23	0.04	28.48
Epoxy 1	23	0.04	31.17
Epoxy 1	23	0.06	30.52
Epoxy 1	23	0.08	29.12
Epoxy 1	23	0.08	29.93
Epoxy 1	23	0.15	29.05
Epoxy 1	23	0.16	30.02
Epoxy 1	23	0.20	25.09
Epoxy 1	23	0.21	25.01
Epoxy 1	23	0.22	31.53
Epoxy 1	23	0.22	28.18
Epoxy 1	23	0.23	30.13
Epoxy 1	23	0.24	31.65
Epoxy 1	23	0.37	29.78
Epoxy 1	23	0.43	25.14
Epoxy 1	23	0.47	27.88
Epoxy 1	23	0.49	28.32
Epoxy 1	23	0.54	26.65
Epoxy 1	23	0.55	29.80
Epoxy 1	23	0.59	26.54

Table 4.9 (cont') ASTM D732 Test Results on Shear Strength of Epoxy 1

Epoxy System	Moisture Conditioning Temperature (°C)	M_t (%)	Shear Strength (MPa)
Epoxy 1	50	0.00	34.10
Epoxy 1	50	0.00	32.02
Epoxy 1	50	0.01	34.20
Epoxy 1	50	0.01	34.34
Epoxy 1	50	0.19	31.81
Epoxy 1	50	0.20	34.36
Epoxy 1	50	0.21	34.97
Epoxy 1	50	0.21	35.77
Epoxy 1	50	0.29	33.70
Epoxy 1	50	0.29	34.48
Epoxy 1	50	0.30	27.65
Epoxy 1	50	0.30	32.21
Epoxy 1	50	0.39	31.25
Epoxy 1	50	0.42	30.44
Epoxy 1	50	0.43	29.40
Epoxy 1	50	0.44	28.54
Epoxy 1	50	0.62	28.01
Epoxy 1	50	0.65	27.79
Epoxy 1	50	0.68	26.20
Epoxy 1	50	0.72	26.38
Epoxy 1	50	1.08	24.21
Epoxy 1	50	1.11	22.06
Epoxy 1	50	1.20	24.63
Epoxy 1	50	1.39	23.10
Epoxy 1	50	1.68	22.76
Epoxy 1	50	1.75	29.09
Epoxy 1	50	1.94	26.31

Table 4.10 ASTM D732 Test Results on Shear Strength of Epoxy 2

Epoxy System	Moisture Conditioning Temperature (°C)	M_t (%)	Shear Strength (MPa)
Epoxy 2	23	0.00	25.57
Epoxy 2	23	0.00	26.67
Epoxy 2	23	0.01	28.10
Epoxy 2	23	0.02	26.43
Epoxy 2	23	0.41	27.56
Epoxy 2	23	0.41	25.59
Epoxy 2	23	0.51	26.97
Epoxy 2	23	0.65	25.51
Epoxy 2	23	0.69	26.67
Epoxy 2	23	0.87	30.20
Epoxy 2	23	0.87	32.15
Epoxy 2	23	0.88	31.89
Epoxy 2	23	0.91	32.94
Epoxy 2	23	0.95	29.98
Epoxy 2	23	1.47	32.36
Epoxy 2	23	1.49	30.18
Epoxy 2	23	1.53	30.10
Epoxy 2	23	2.03	31.61
Epoxy 2	23	2.10	33.19
Epoxy 2	23	2.20	30.96

Table 4.10 (cont') ASTM D732 Test Results on Shear Strength of Epoxy 2

Epoxy System	Moisture Conditioning Temperature (°C)	M_t (%)	Shear Strength (MPa)
Epoxy 2	50	0.18	30.61
Epoxy 2	50	0.19	30.77
Epoxy 2	50	0.19	29.06
Epoxy 2	50	0.20	31.29
Epoxy 2	50	1.08	28.29
Epoxy 2	50	1.08	31.73
Epoxy 2	50	1.19	30.14
Epoxy 2	50	1.19	28.21
Epoxy 2	50	1.38	30.85
Epoxy 2	50	1.91	33.85
Epoxy 2	50	1.98	32.98
Epoxy 2	50	2.01	33.41
Epoxy 2	50	2.60	34.53
Epoxy 2	50	2.65	28.38
Epoxy 2	50	2.66	32.60
Epoxy 2	50	3.56	33.61
Epoxy 2	50	3.67	34.65
Epoxy 2	50	3.79	33.06

Epoxy 1 exhibited a degradation behavior very similar to its tensile counterparts. Strength degradation was approximately 13% and 30% for the 23°C and 50°C temperature groups respectively. High temperature post-curing effect was eventually offset by the moisture degradation effect, as the shear strength of the 50°C group dipped below the initial shear strength of ambient-cured samples.

On the contrary, Epoxy 2 exhibited no shear strength degradation. In fact, the trend lines suggested some increase upon moisture sorption. In addition, temperature effect was relatively insignificant beyond 1% moisture mass uptake as the data points of both temperature groups fell in close proximity. These characteristics might have strong correlation with the elastomer additives that toughened the epoxy materials. Comparing the results of Epoxy 1 and Epoxy 2, it can be concluded that punching shear degradation mechanism could be heavily dependent on the epoxy material formulation.

4.8 3-D Moisture Diffusion Simulation

Three-dimensional moisture diffusion simulation was performed to understand and estimate the moisture diffusion behavior in the interfacial bond region, by means of the finite element method. A discretized mathematical model was built using the exact fracture specimen geometry, as will be discussed next in the context of the fracture test program presented as Chapter 5. Diffusion coefficients and solubility that were presented earlier were used as inputs in the computation. Temperature effect was incorporated with the use of the associated set of temperature-dependent diffusion coefficients, without resorting to solving a coupled differential equation that involved both temperature and mass diffusion. This is justifiable due to the fact that moisture diffusion took place at a constant temperature for the problem at hand. In this computational problem, diffusion was only driven by a concentration gradient.

4.8.1 Solution Techniques

The governing equations for mass diffusion were basically an extension of Fick's equations, allowing non-uniform solubility of moisture in the base material and for mass diffusion driven by gradients of temperature and pressure. For the problem at hand, the non-uniformity was not modeled and a Fickian behavior was assumed. The basic solution variable (used as the degree of freedom at the nodes of the mesh) was the “normalized concentration”, expressed as mass concentration of moisture divided by the solubility of the base material. As such, the “normalized concentration” always ranged from 0 to 1. In the herein case where the mesh included dissimilar materials with shared nodes at the interfaces, the normalized concentration was continuous across the interface between the adjoining different materials.

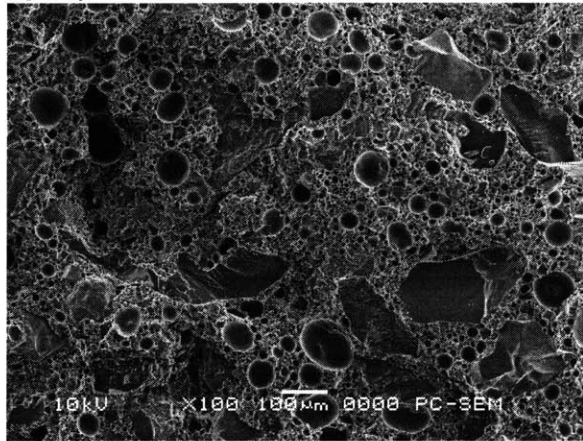
Time integration in the transient diffusion analysis was done with the backward Euler method (also referred to as the modified Crank-Nicholson operator) since this method is unconditionally stable for the linear problem. The moisture migration behavior was simulated with a time marching scheme of which the analysis was complete when the steady state criterion, which was defined as the point in time when all normalized concentrations change at less than the defined threshold rate, has been met.

4.8.2 The Model

Figure 4.21 shows the 3-D finite element model used for the analysis. 3-D solid diffusion elements were used. All interfaces were properly tied. The model was initially dry and was subjected to an instantaneous surface saturation boundary condition, simulating a dry specimen immersed in a water bath. The 1.28 mm CFRP plate and the 1 mm epoxy layer were successfully modeled using one respective layer of diffusion elements. Sufficiency and accuracy has been verified by preliminary modeling of a similarly sized thin plate (2-D) and results compared against analytical solutions (Crank 1975). The concrete block, on the other hand, was modeled using 8 rows of elements in the thickness direction of 37.5 mm. Unlike stress analysis where more elements are usually placed near stress concentration regions, mass diffusion modeling does not have such requirement and diffusion elements can be equally spaced due to the fact that the “applied load” being the normalized moisture concentration is applied all around the model. Such modeling technique will, however, be different when a coupled stress-diffusion analysis is performed.

Figure 4.22 shows the snapshots of the moisture concentration at the epoxy/concrete bond interface at different points in time. The right side is the cropped concrete block while the left side is the edge at which the CFRP cantilever starts. Note the symmetry about the longitudinal axis and asymmetry about the centerline of the bond. The asymmetric arose as a result of faster diffusion of moisture from the left exposed concrete face. On the right side, moisture will tend to migrate into the concrete core before reaching the interface due to the higher diffusion coefficients and solubility, which gave rise to a steeper concentration gradient. Nevertheless, simulation shows that in 8 weeks, the minimum moisture concentration at that interface will have reached about 50% of the equilibrium value. The total bond line will be saturated in about 200 days. Appendix 1 documents the abbreviated input file of this 3-D finite element model.

Epoxy 1



Epoxy 2

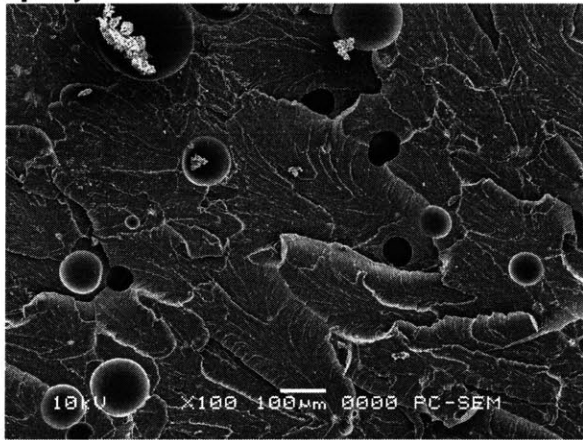


Figure 4.1 Micrographs of Fracture Surfaces of Cured Epoxy 1 and Epoxy 2

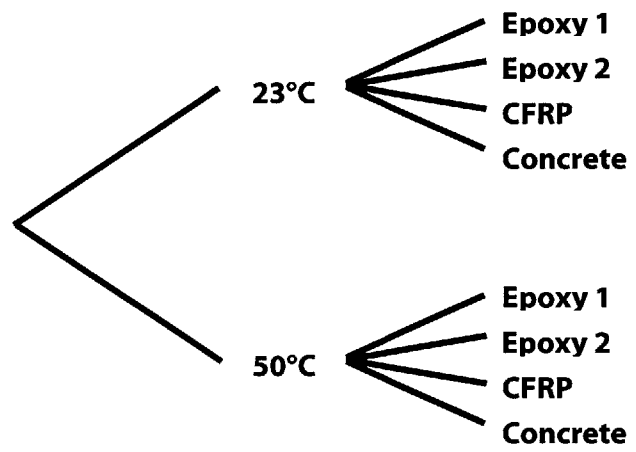


Figure 4.2 Moisture Sorption Test Matrix

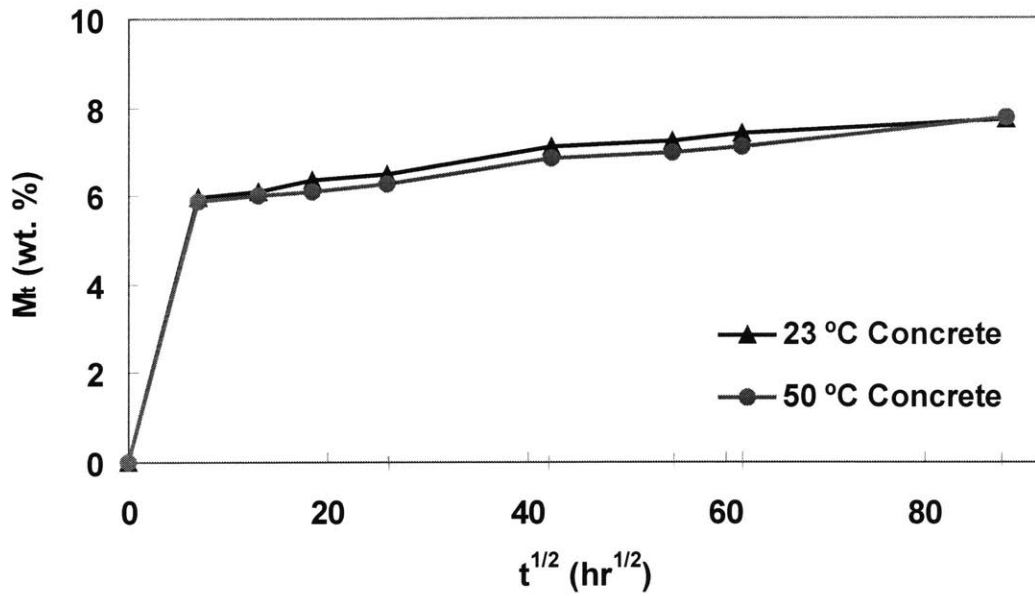


Figure 4.3 Mass Uptake Curves for Concrete

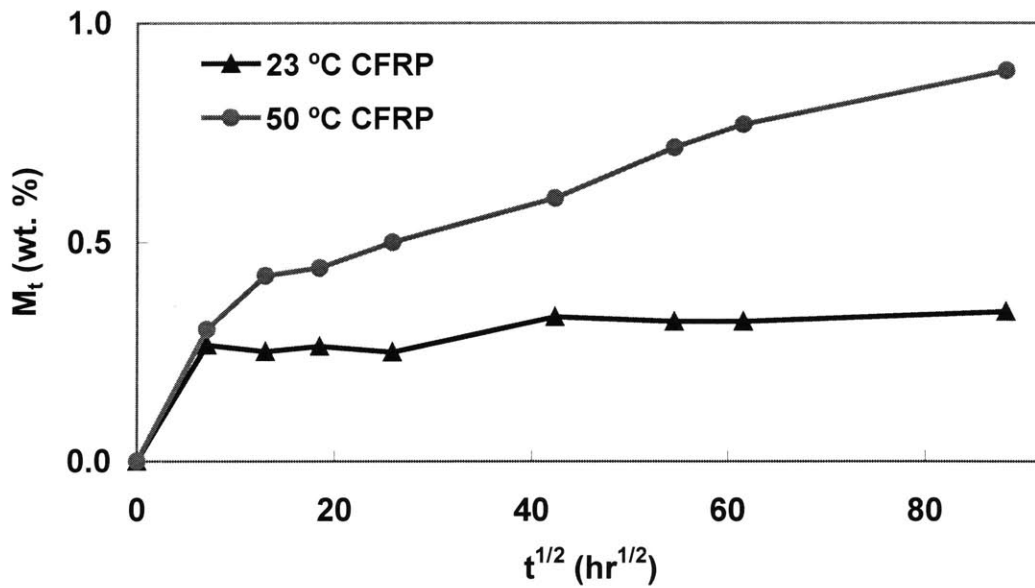


Figure 4.4 Mass Uptake Curves for CFRP

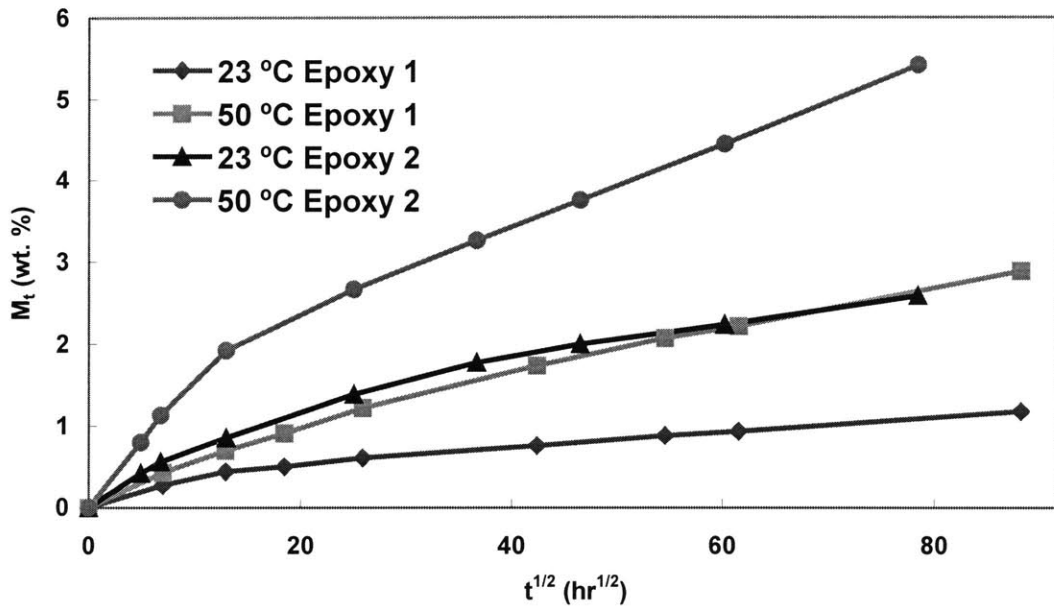


Figure 4.5 Mass Uptake Curves for Epoxy 1 and Epoxy 2

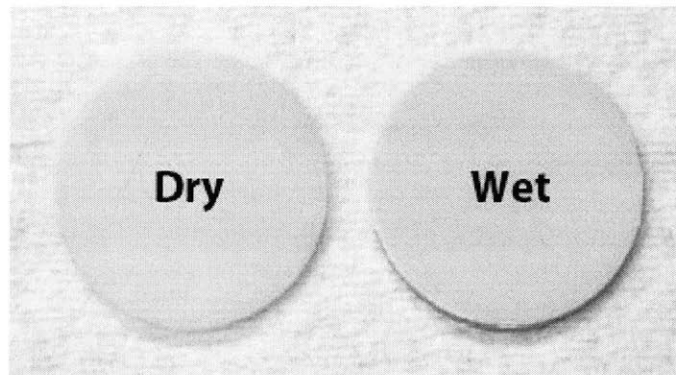


Figure 4.6 Loss of Transparency of Epoxy 2 after Moisture Conditioning

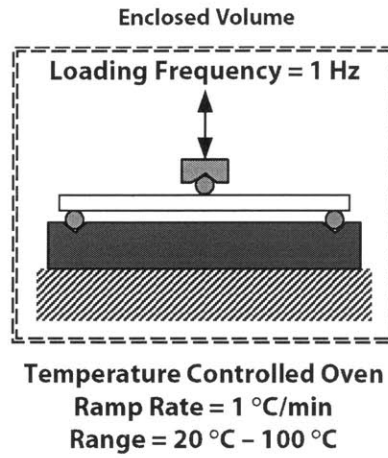


Figure 4.7 DMA 3-Point Bend Test Setup

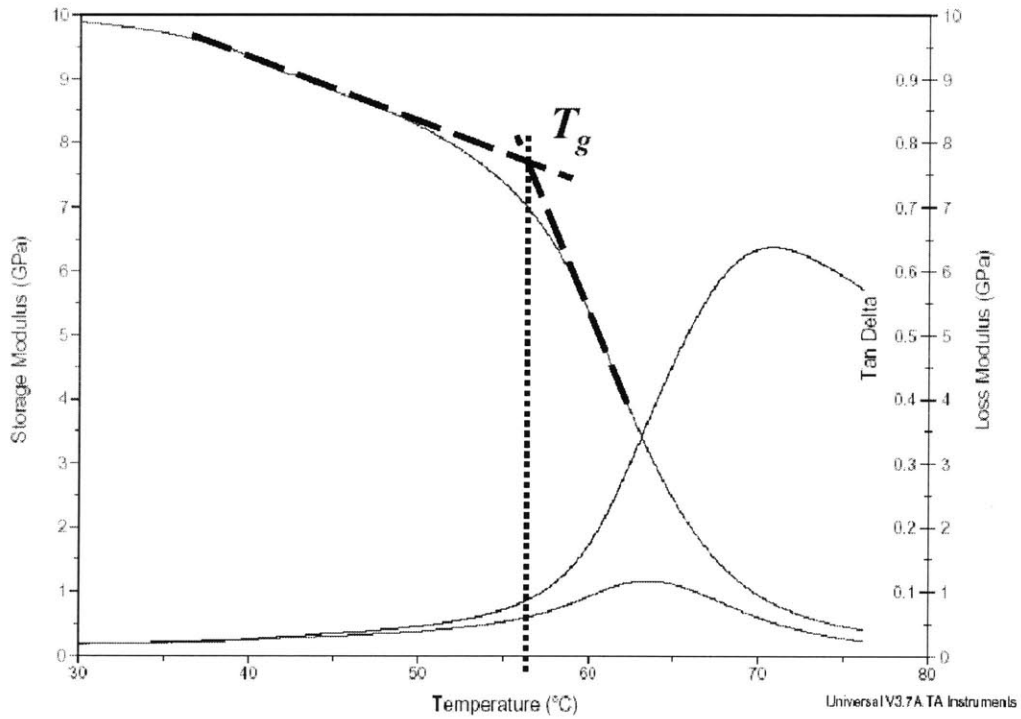


Figure 4.8 Typical Plots from DMA and the Definition of T_g

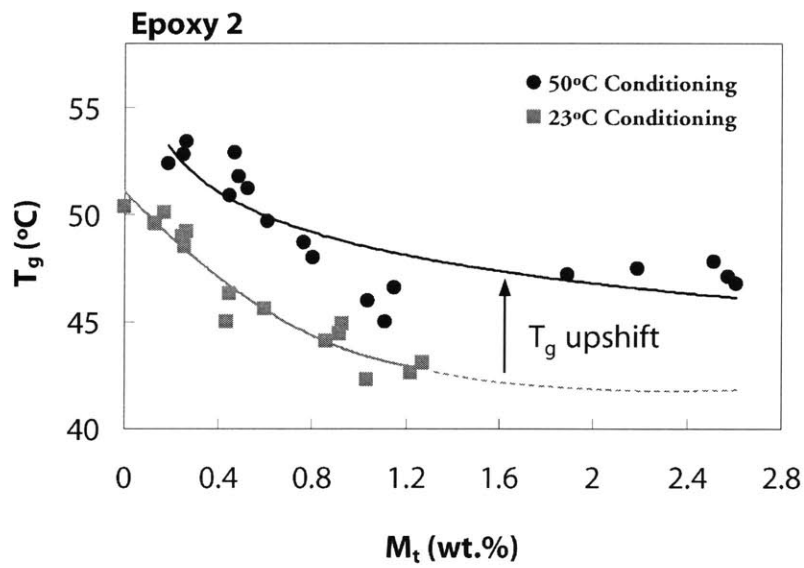
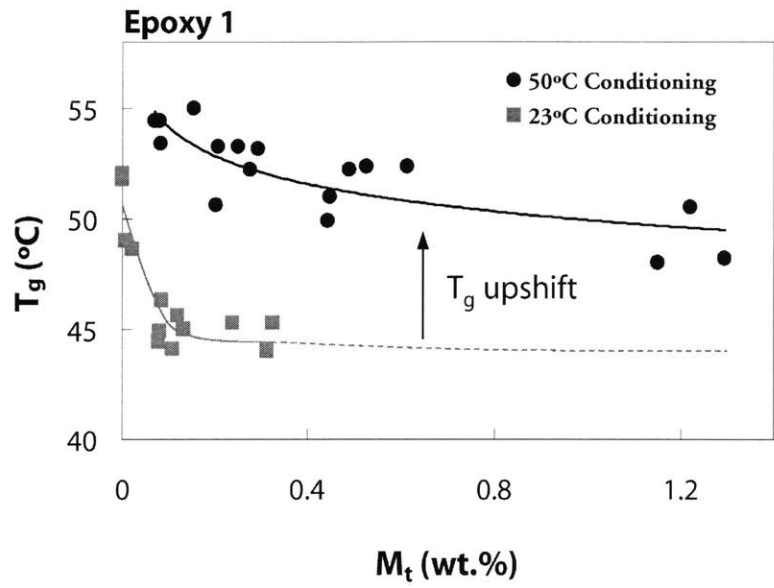


Figure 4.9 T_g versus M_t for Epoxy 1 and Epoxy 2

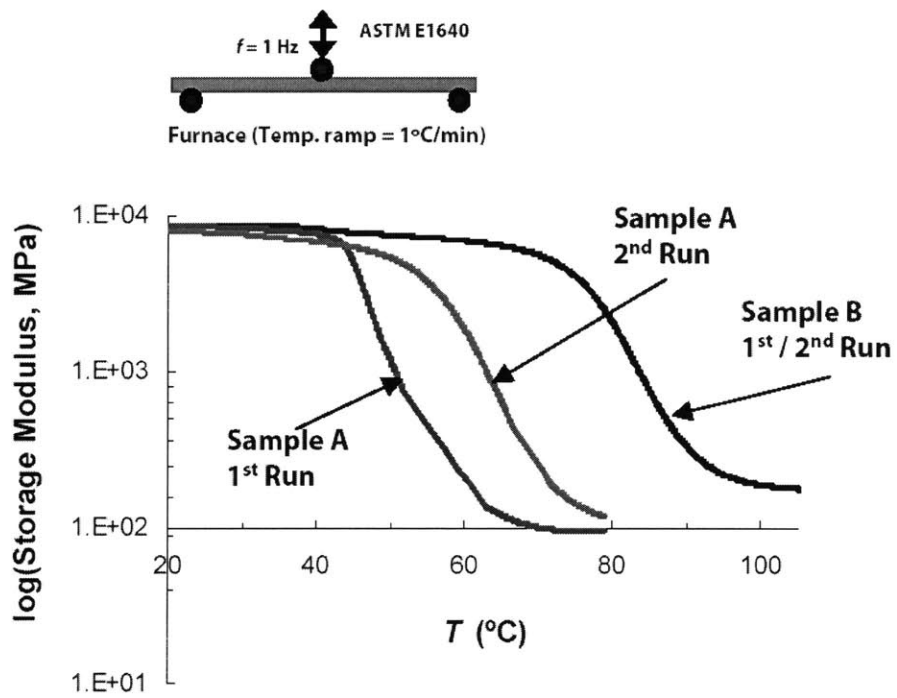


Figure 4.10 Effect of Elevated Temperature Post Curing on Thermal Property Stability of Ambient-Cured Epoxies

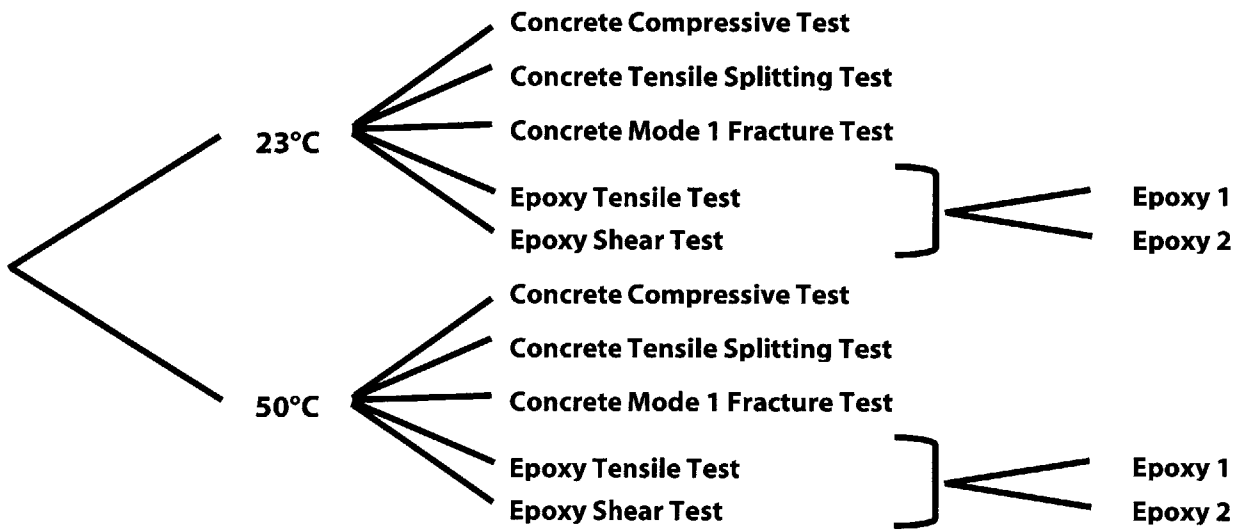
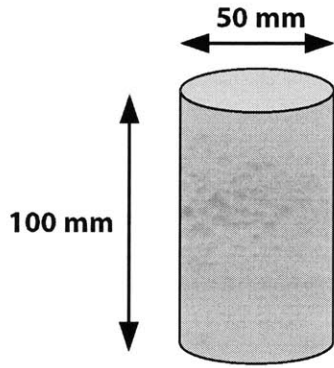
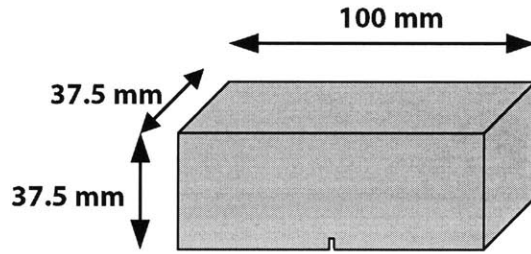


Figure 4.11 Mechanical Test Matrix



Cylindrical Specimen



3-Point Bend Fracture Specimen

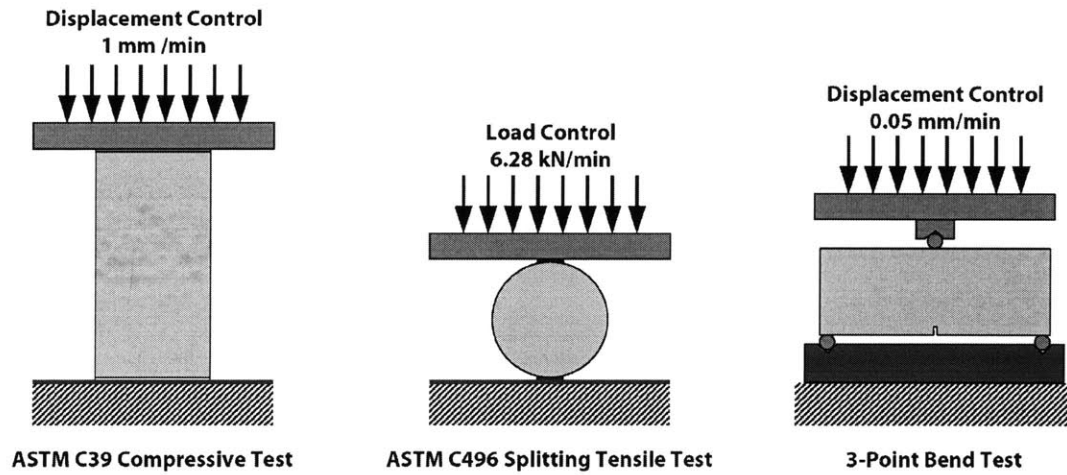


Figure 4.12 Concrete Specimens & Mechanical Test Configurations

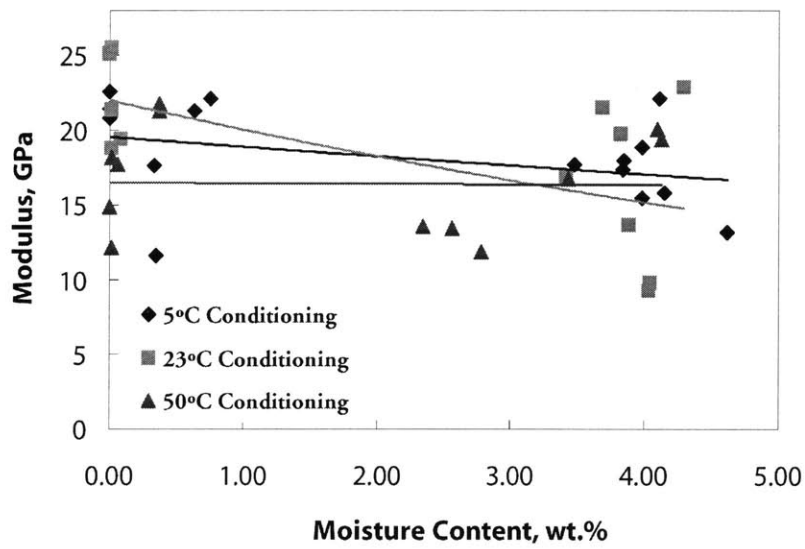
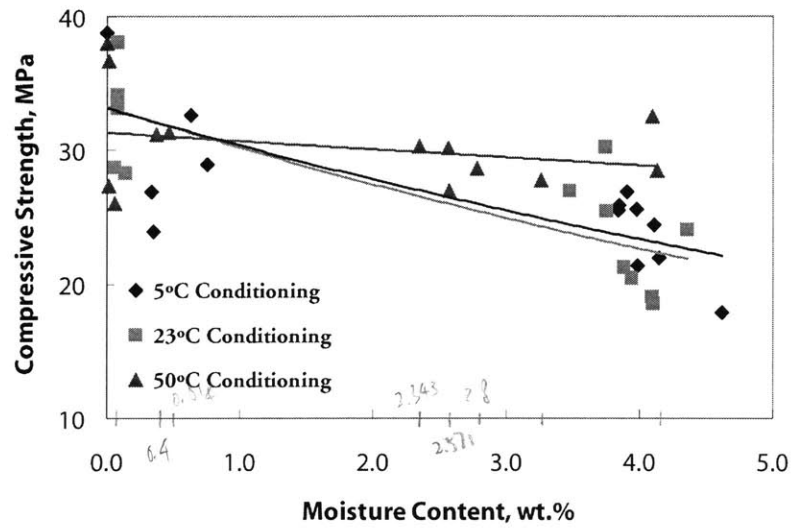


Figure 4.13 Concrete Compressive Properties vs. Moisture Uptake

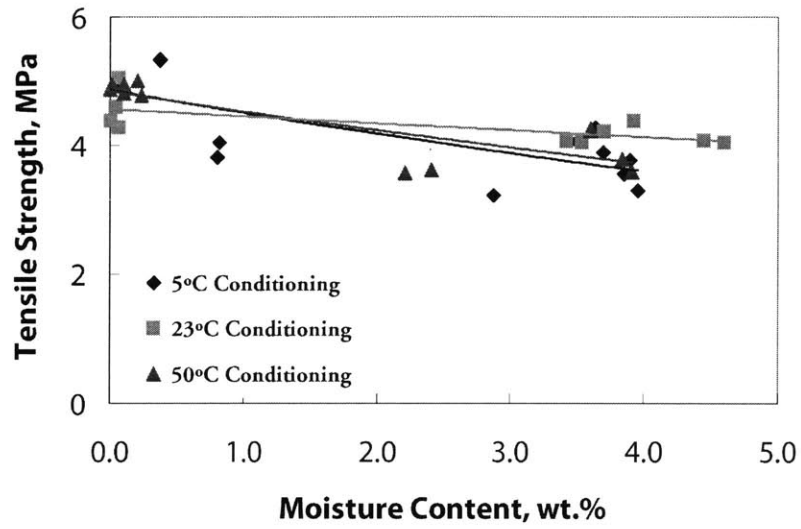


Figure 4.14 Concrete Tensile Strength vs. Moisture Uptake

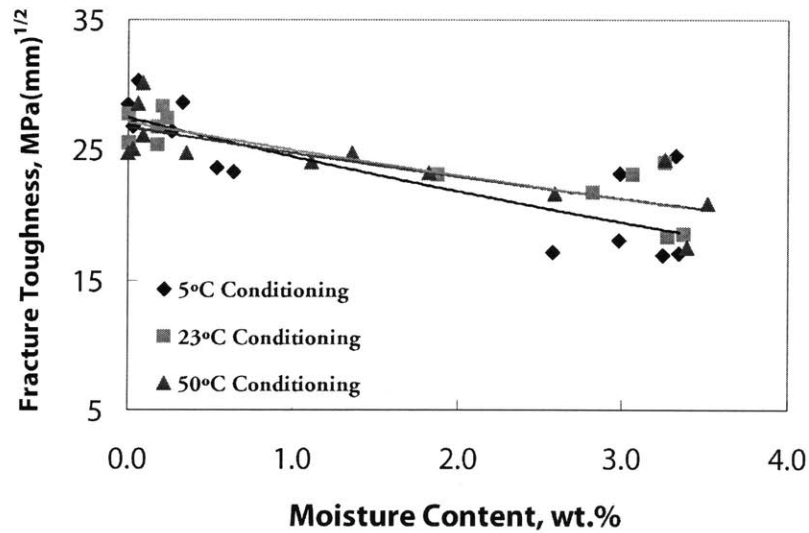


Figure 4.15 Concrete Mode 1 Fracture Toughness vs. Moisture Uptake

Dimensions in mm

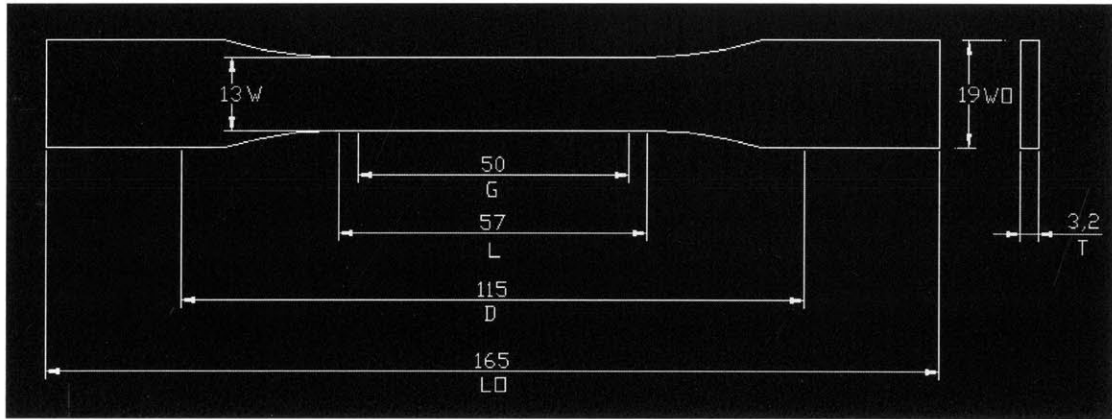


Figure 4.16 ASTM D638 Type 1 Dumbbell Shaped Epoxy Tensile Specimen

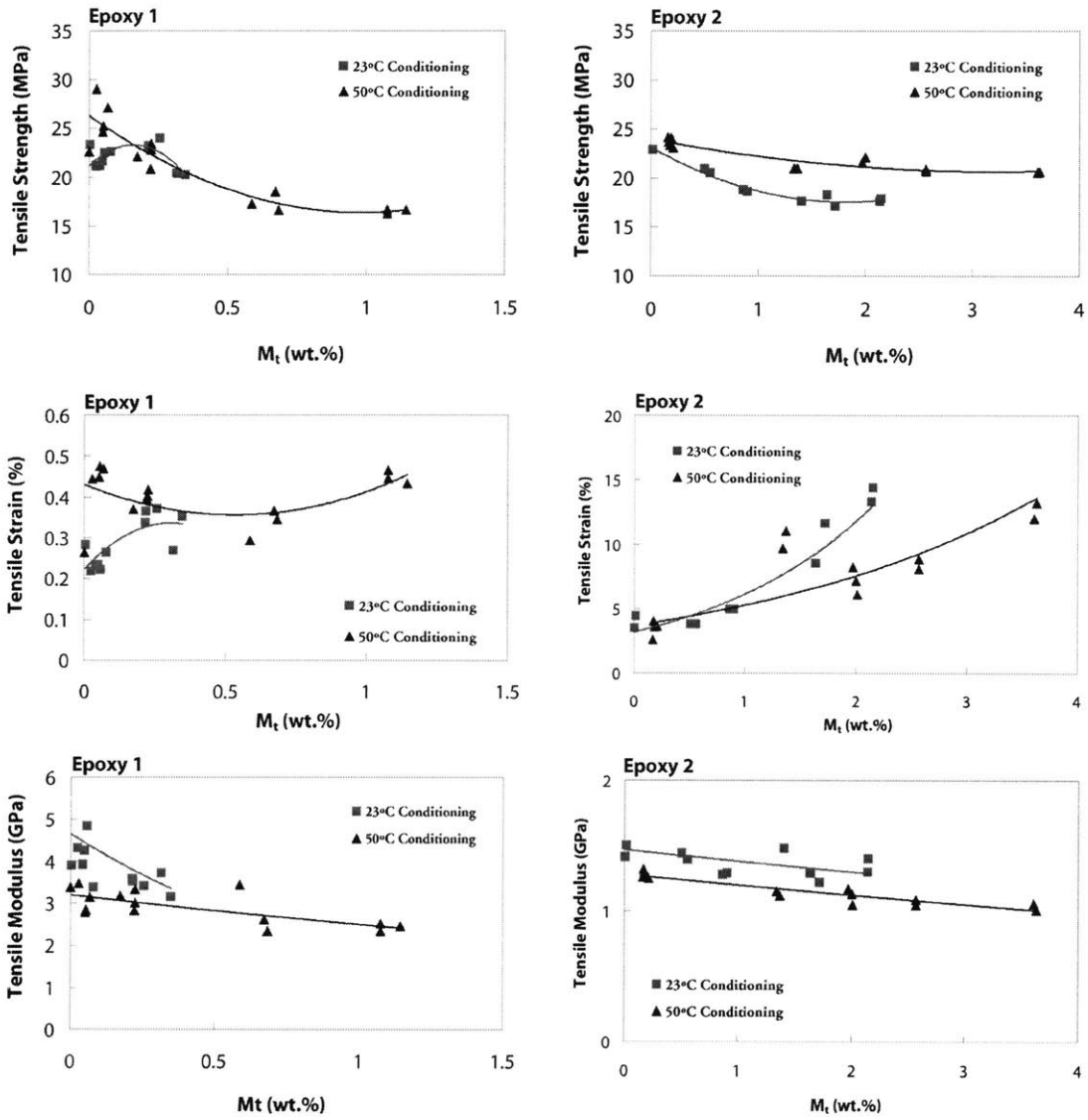


Figure 4.17 Epoxy Tensile Properties vs. Moisture Uptake

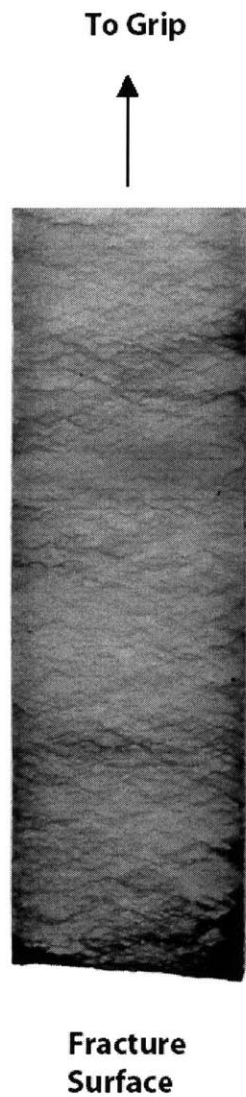


Figure 4.18 Crazing and Shear Banding Developed in the Gage Length of Epoxy 2 Tensile Specimen

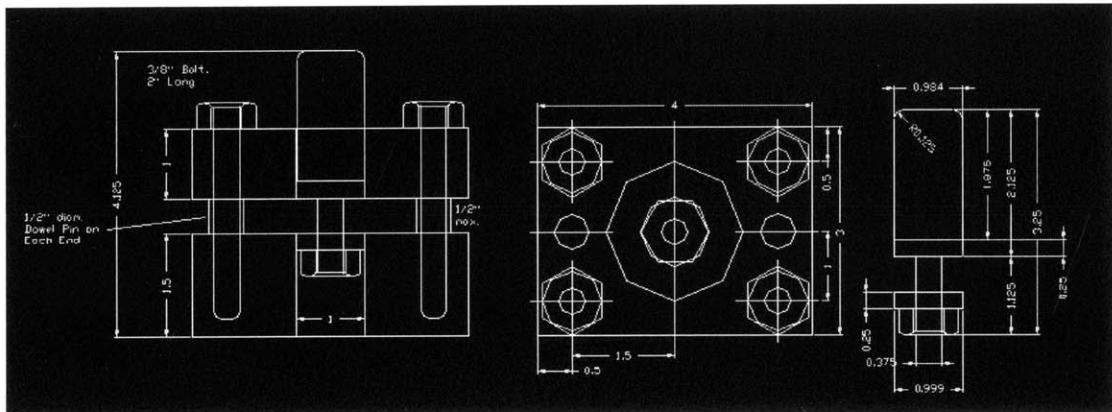


Figure 4.19 ASTM D732 Punching Shear Tool

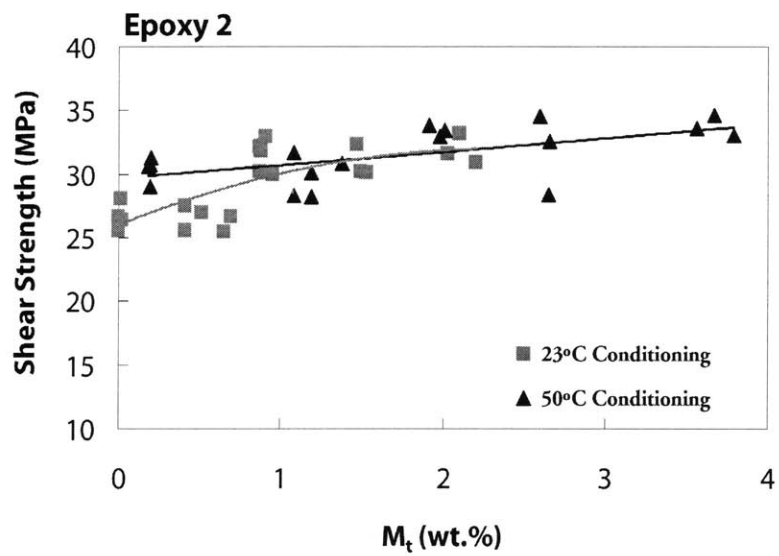
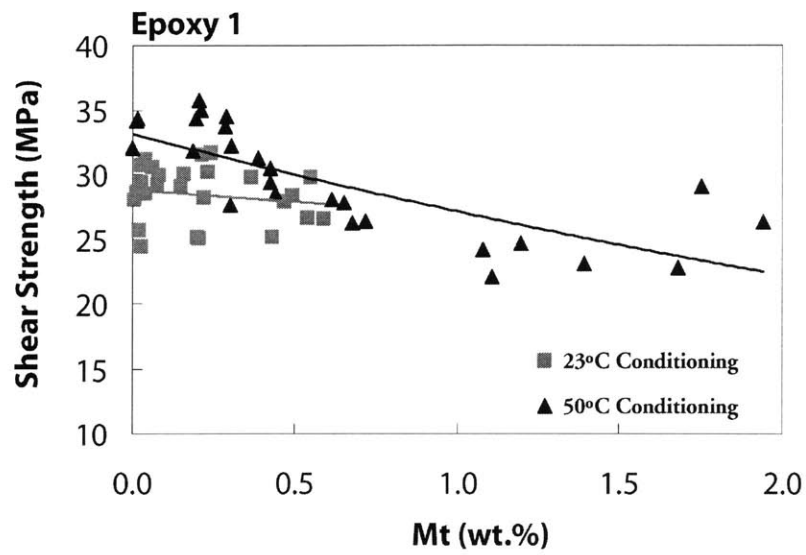
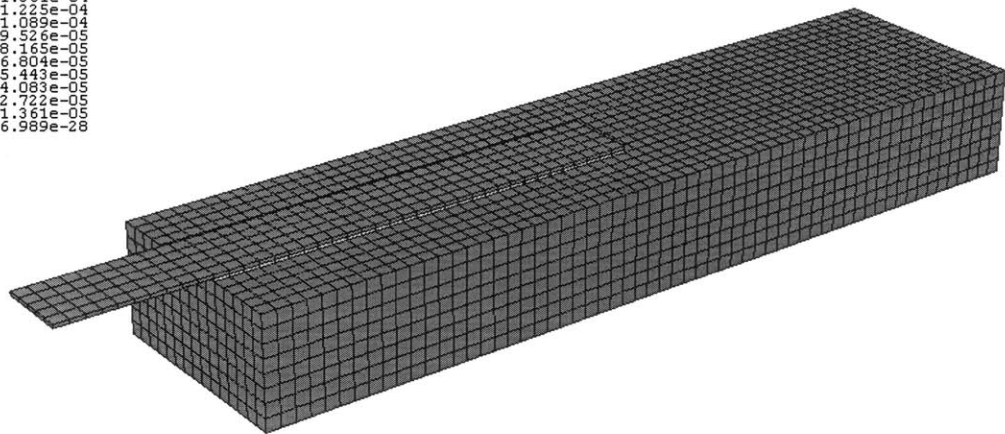


Figure 4.20 Epoxy Shear Strength vs. Moisture Uptake

CONC
(Ave. Crit.: 75%)

+	1.633e-04
+	1.497e-04
+	1.361e-04
+	1.225e-04
+	1.089e-04
+	9.526e-05
+	8.163e-05
+	6.800e-05
+	5.437e-05
+	4.074e-05
+	2.711e-05
+	1.348e-05
+	6.989e-28



ODB: diffusionmodeling.odb ABAQUS/Standard 6.4-1 Mon Jul 19 22:04:10 Eastern Daylight Time 2004

Step: Diffusion, 3Dmoisturediffusion
 Increment 1: Step Time = 1.000
 Primary Var: CONC
 Deformed Var: not set Deformation Scale Factor: not set

Figure 4.21 3D Moisture Diffusion Finite Element Model

CONC
(Ave. Crit.: 75%)

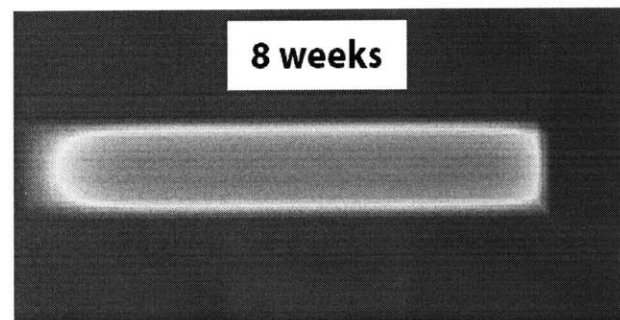
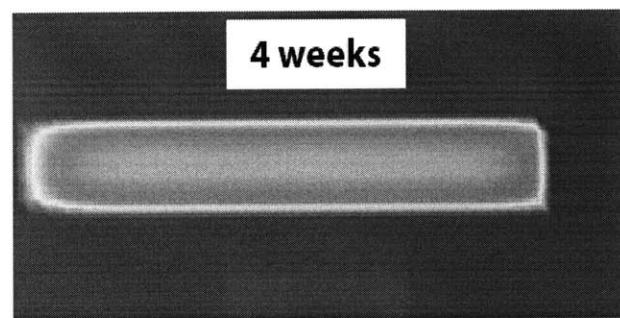
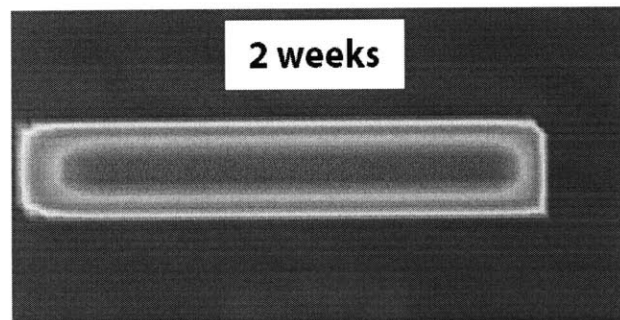
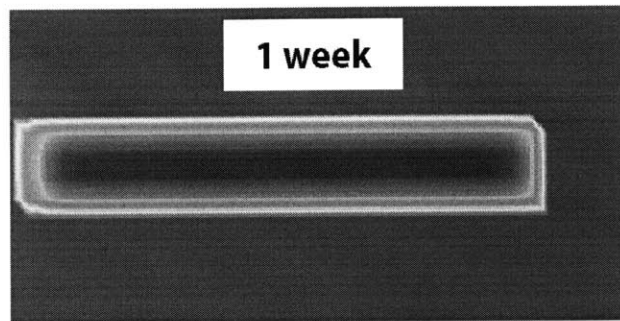
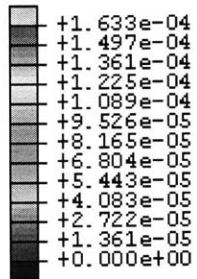


Figure 4.22 Snapshots of Moisture Concentration at the Epoxy/Concrete Interface

CHAPTER 5

INTERFACE FRACTURE TEST PROGRAM PEEL & SHEAR CHARACTERIZATION

The objective of this research is to develop new mechanistic understanding of moisture affected debonding failures in CFRP bonded concrete systems by means of an interface fracture approach. Central to the investigation is the use of interface fracture toughness as the quantification parameter, which is considered a bond property, to analyze, compare, and correlate physical observations of such bonded systems. This chapter details the interface fracture test program which features both peel and shear characterization of moisture conditioned mesoscale FRP bonded concrete models of which the interface fracture toughness are experimentally measured. In what follows, choice of fracture specimen configuration, sample definition and preparation, experimental setup, loading as well as instrumentation, are discussed. Results including debonding modes, load-displacement behavior, and fracture toughness variations are presented and summarized. Findings documented in this chapter form the basis for a synergistic analysis to be performed in the following chapter.

5.1 Selection of Specimen Configurations

As discussed in Chapter 3, peel and shear loadings in the FRP-concrete bond represent two limiting bounds of a typical debonding problem that takes place within the retrofit span. This fracture behavior, in either limiting case, is likely to be a mixed mode problem due to the elastic mismatch of the bonded layers (Hutchinson and Suo 1992). In other words, even when the loading is symmetric or apparently in pure mode (e.g. open or shear), the crack tip region would “feel” both the opening and shearing components simply because the crack lies between (or in close proximity to) two adjoining dissimilar materials. To study such mixed-mode debonding fracture behavior, many interface fracture models have been proposed, including but not limited to the single leg bending (Sundaraman and Davidson 1995), four-point bending (Charalambides et al 1989), edge-notched shear (He et al 1988), and Brazil-nut sandwich (Wang and Suo 1990), as shown in Figure 5.1.

While these models have been rigorously tested and fracture formulations extensively developed, they do not seem to model the debonding problem at hand properly. The bend type specimens are likely to fail prematurely due to concrete cracking, either due to tension or shear, before valid debonding modes can be developed. This is attributed to the fact that concrete is very weak in tension, which is usually five to six times less than the compressive counterpart. Development of concrete cracks will then lead to difficult quantification of the debonding resistance, since the cracking within concrete substrate could contribute significantly in the apparent fracture toughness measured. For the sandwich type specimens, FRP laminates would be sandwiched between two concrete blocks, as shown in Figure 5.2. While this might assimilate well in studying mortar/aggregate interfacial properties (Lee et al 1992), it does not model as well in the case of FRP bonded concrete, since only one side of the FRP laminate is bonded to the concrete substrate while the other side is exposed and unconstrained in most externally retrofitted systems. As a result, Karbhari et al (1996) has developed a peel test setup, as shown before in Figure 2.6, to specifically model FRP debonding. Although this setup may work well with FRP sheet systems, it is deemed unsuitable for use with FRP plates due to their high flexural stiffness. The horizontal slider would move as soon as the FRP plate was fitted into the grip of the loading frame.

Therefore in this study, with considerations of the actual configuration in a retrofitted beam, the peel type fracture and single lap shear fracture specimens are proposed, as shown in Figure 5.3. These two specimen configurations share the commonality of being a layered material system with the FRP exposed on one side that closely resembles the realistic debonding problem at the structural scale. They also retain the realistic bond line features (both width and thickness) at the mesoscale and are relatively easy to setup on an Instron loading frame.

5.2 Specimens

Materials used in making all fracture specimens were identical to those used in the material characterization program as detailed in Chapter 4. Mixing and curing procedures were also as described. To ensure consistency, all concrete was produced from the same batch of mix on the same day, cast upright with the to-be-bonded surface in contact with the mold bottom, and subjected to the same 28-day curing schedule followed by oven drying prior to bonding. Completing drying of the concrete was ensured by no further weight change on 1-day intervals for 3 consecutive days. CFRP plates were trimmed to size from the same roll of material using identical sawing setup for each cut. Epoxy mixing and the bonding procedure were also strictly controlled as discussed before. The following provides a description of the specimen dimensions, followed by some considerations regarding concrete surface preparation and conditioning for bonding as well as the choice of a proper bond length for the shear fracture specimens.

5.2.1 Dimensions

Both peel and shear fracture models were made of identical materials using identical sample preparation procedures as will be described in the following section. Dimensions of the fracture models are shown in Figure 5.4. All models consisted of a 1.28 mm thick CFRP plate bonded to a 37.5 mm thick concrete block with a 1.0 mm thick epoxy bond line. Uniformity of the bond line thickness was controlled by a number of Teflon spacers surrounding the bond. The thickness values resembled that of a real FRP retrofitted concrete bond.

Width of the CFRP plate was 25 mm and so as the width of the bond. Bond length of the peel model was 100 mm while that of the shear model was 150 mm. Rationale for determination of the bond length is discussed in more detail later. The CFRP plate was centered along the longitudinal axis of the concrete block and a 25 mm shoulder was left on either side of the bond to remove edge effects, making the concrete block 75 mm wide in total. Cantilever length of the CFRP for the peel model was 50 mm while that for the shear model was 100 mm so as to provide proper non-slip gripping according to the results of preliminary tests. A 12.5 mm pre-crack was introduced at the epoxy/concrete interface using a 80-micron thick Teflon tape.

5.2.2 Concrete Surface Preparation

Oven-dried concrete blocks were subjected to a bond surface treatment of mechanical abrasion on the cast side that was in contact with the mold during casting by means of a pneumatic needle scaler, as shown in Figure 5.5, because it has been determined (Chajes et al 1996, Toutanji and Ortiz 2001, Lorenzis et al 2001) that mechanical abrasion would result in maximum bond quality over other means such as water jetting, sanding, and grinding. With the mechanical abrasion, it was possible to roughen concrete surfaces to a point that sound aggregates were exposed and loosely held segregated particles removed, providing mechanical interlock with the cured (or hardened) epoxy. After mechanical abrasion, dust and debris was removed from the surface by compressed air and cleaned by methyl ethyl ketone (MEK) to ensure a sound adhesion surface.

5.2.3 Bond Length Determination Using Micro-Strain Profile Analysis

Compared to peel fracture specimens where a typical steady-state debonding length appeared, from preliminary tests, in the low centimeter range that corresponded to a crack-stop propagation pattern under displacement control, shear fracture specimens usually debonded over a rather long bond length in order to reach the same steady-state of asymptotic energy release beyond which the energy release rate becomes independent of the crack length such that the advancing crack front no longer “feels” any influence of

the other end of the crack. As such, a more careful design needs to be performed on the bond length of the shear fracture specimens.

It is known that for bonded joints that are loaded under a shear configuration, the bond stress is not evenly distributed throughout the bond area. Instead, more stress is being taken up by the edge region and the stress decreases exponentially away from the edge, as illustrated from the surface strain variation profile in Figure 5.6. In other words, there exists a bond length beyond which no further increase in bond strength is possible. This length is called the effective transfer length.

The transfer length depends on an array of parameters including but not limited to surface roughness, aggregate size and stiffness, and adhesive stiffness. The value ranges between 40 – 125 mm for CFRP or GFRP bonded concrete in the form of single or double lap shear bonds as reported in the literature (Bizingavyi and Neale 1999; Nakaba 2001; Myers et al 2001). Since transfer length is system dependent, it was thus experimentally determined in this study using identical materials as in the fracture specimens. A series of seven 350-ohm strain gages with a gage length of 6.25mm were mounted on the CFRP plate with a space interval of 30 mm starting from the loaded edge to continuously monitor the micro-tensile strain on the plate surface loaded under apparent pure shear. It has been determined that, for the given bond width, materials, and specimen preparation procedures, the shear transfer length was approximately 150 mm for both epoxy systems beyond which the registered strain was close to zero. The experimentally obtained micro-strain profile, $\varepsilon(x)$, is shown in Figure 5.7 and the measurements compare very well with results from finite element modeling prediction and that from the widely used analytical model (Sierra-Ruiz et al 2002), which has the following form:

$$\varepsilon(x) = \frac{N}{BE_1 h} \frac{\sinh\left(\frac{L-x}{L_0}\right)}{\sinh\left(\frac{L}{L_0}\right)} \quad ; \quad \text{where } L_0 = \sqrt{\frac{E_1 h t}{\mu_2}}$$

Here, L represents the bond length, B the bond width, h the CFRP plate thickness, t the bond line thickness, E_1 the elastic modulus of the plate, μ_2 the shear modulus of the epoxy, and N the shear load. This analytical model was derived from the shear lag theory

and it assumes elasticity. As a result of this analysis, a bond length of 150 mm was thus used in all shear fracture specimens to ensure complete stress transfer to take place.

5.3 Fracture Test Program

All specimens were divided into two main groups for regular and high temperature moisture conditioning respectively at 23 °C and 50 °C. Each group consisted of both peel and shear tests. Half of the specimens for each loading configuration were made with Epoxy 1 while the other half Epoxy 2 (for definitions and description of the epoxies, see Chapter 4). Each specimen subgroup was then conditioned for 0 week, 2 weeks, 4 weeks, and 8 weeks at which time three randomly chosen samples were taken out and mechanically tested to failure in standard laboratory conditions. The selected time intervals were so chosen based on the distinguishable moisture concentration patterns indicated by the results of the 3-D diffusion simulation discussed in Chapter 4. Correspondence of the conditioning duration and the estimated minimum moisture concentration at the epoxy/concrete interface are summarized below in Table 5.1.

Table 5.1 Correspondence of Conditioning Duration & M_t/M_s

Conditioning Duration (weeks)	Estimated Minimum M_t/M_s (%)
0	0
2	16
4	30
8	50

0-week conditioning corresponded to initial dry (defined as 50% RH) testing without any moisture conditioning. Other specimens were conditioned at 100% RH at their respective temperatures. Continuous moisture conditioning represents an accelerated conditioning environment for both temperature groups. Figure 5.8 illustrates the overall fracture test matrix. Altogether 84 specimens were tested (instead of 96 because one subgroup could not be tested due to a 1-week machine maintenance). Figure 5.9 shows part of the specimens under ambient-cure.

High temperature wet conditioning was conducted using a Q-Fog CCT 1100 environmental chamber while room temperature wet conditioning was conducted in water

baths in the laboratory with temperature control. All specimens were placed inside the chamber uniformly spaced to maximize moisture exposure and uniformity. The high temperature conditioning represents a realistic upper bound of service temperature that could be reached in the soffit of a RC structural member (Mays and Hutchinson 1992). These conditioning environments were identical to those used in the material characterization program described earlier.

5.4 Fracture Test Setup

5.4.1 Peel Fracture

Peel fracture tests were performed on an Instron universal test machine Model 1331 using a 2.2 kN (500 lb) load cell under displacement control. Crosshead speed was 2 mm/min. All specimens were tested at standard laboratory condition. High temperature conditioned specimens were removed from the conditioning chambers, wrapped in impermeable plastic wrap to retain moisture, and left for a few hours until the specimens reached the test temperature to prevent moisture desorption driven by temperature differential.

Each peel fracture specimen was rigidly clamped by a specially designed fixture, which was secured to the lower piston of the Instron. Alignment and leveling of the specimen were carefully performed using setscrews that were built into the fixture. The upper load cell was connected with a high carbon steel rod (Grade AISI 1055) designed with a 360° hinge mechanism on both ends to make the vertical peel possible. At all registered load levels, displacement within the rod was considered negligible due to low load. Load, crosshead displacement, and crack length were carefully and continuously monitored until the CFRP plate was entirely peeled off. The complete peel fracture setup is shown in Figure 5.10.

5.4.2 Shear Fracture

Shear fracture tests were carried out in an upright position also in the Instron 1331 using a 50 kN load cell displacement controlled at 1 mm/min. All conditioned specimens were tested at standard laboratory condition. Each shear fracture specimen was rigidly clamped in the specially designed carbon steel fixture (Grade AISI 1018), which was

secured to the lower crosshead. A 12.5 mm thick reaction plate provided the necessary rigidity, after some preliminary testing, to prevent concrete block from any movement during pulling of the CFRP plate. Alignment was carefully adjusted so that the plate line up with the longitudinal axis of the upper self-tightening serrated grip.

A 50 mm grip length was used to ensure no slippage under the range of critical load level. In fact, it has been preliminarily tested that the 25 mm wide CFRP plate exhibited no slippage up to the load cell limit, which was 50 kN, while the critical load level of the shear fracture specimens was less than half of that limit. For dry specimens, 350-ohm strain gages with a 6.25 mm gage length were mounted onto the CFRP plate to monitor the surface strain profiles. Shear slip was measured by a linear variable displacement transducer (LVDT) to monitor the displacement of a 6 mm thick Plexiglass target that was adhered onto the CFRP plate right at the pre-crack tip location. More details regarding the shear slip measurement are given below. The complete shear fracture test setup is shown in Figure 5.11.

Shear Slip Measurement

Shear slip represents the accumulated shear deformation of the thin adhesive layer under shear and there is no easy way to monitor that deformation directly. While various shear-slip models have been proposed that consist of both the loading and unloading curves (Gustafsson 1987; Taljsten 1996; Chen and Teng 2001), shear slip measurements on single lap shear specimens seem to have been tacitly performed and defined. One indirect way to make the measurement is by placing a target on the CFRP plate very close to the crack tip and assume that the CFRP has the same displacement as the adhesive layer at that exact position. By referencing the target with a stationary point, the differential displacement captured represents the shear deformation accumulated up till that point. It should be noted that shear deformation of the adhesive is non-uniform along the bond length due to the exponentially decaying stress as presented in the effective transfer length discussion and thus the measurement is highly sensitive to the target location. A thinner target that results in less area averaging of the shear deformation in the crack tip vicinity would generally yield a more accurate representation of the shear slip.

Preliminary tests have shown that placing the target in different locations in the vicinity of the crack tip could lead to vast difference in shear slip response. When the target was placed just behind the crack-tip, a perfectly linear response that came from the CFRP was obtained. When the target was placed right on the crack-tip, a nonlinear response with an initial linear region was registered. Non-linearity was probably due to plastic yielding of the adhesive layer and possibly arose as well from the mechanical interlock at the interface under high loads. Figure 5.12 illustrates these two different measured responses.

Thus, a 6 mm thin target was placed on every specimen on the CFRP at the crack tip location for shear slip measurement until the critical state. Upon explosive shear fracture at the critical state, the thin target, which was adhered to the CFRP plate, often fell off or became loose as a result of elastic spring back of the CFRP. Hence, the unloading shear slip curves could not be consistently produced and would not be used in any subsequent quantification analysis.

5.5 Results

5.5.1 Failure Modes

A. Peel Fracture Modes

Typical failure modes of Epoxy 1 and Epoxy 2 with and without moisture conditioning are shown in Figures 5.13 and 5.14. Dry Epoxy 1 specimens exhibited failure in the adhesive itself, rendering a cohesive type of failure. The pre-crack, which was placed at the epoxy/concrete interface, kinked upward into the adhesive layer near the CFRP/epoxy interface upon reaching peak load. Crack gradually extended along until complete peel off. A thin layer of epoxy was adhered to the debonded CFRP strip while the bulk of the adhesive layer stayed intact on the concrete block. This phenomenon was observed for both temperature groups, although the high temperature group showed more signs of CFRP delamination intercalated in the epoxy cohesive failure. Failure surfaces felt powdery to the touch and small grains of sand could clearly be seen.

Wet Epoxy 1 specimens, on the other hand, exhibited the distinctive epoxy/concrete interface separation. Only a relatively small amount of loose concrete particles adhered to the debonded plate, which consisted of the CFRP plate and an almost

intact adhesive layer. The matching profile of the bond line was revealed from the adhesive side and the failure surfaces were still damp to the touch. The needle scaler roughened concrete surface was once again revealed. For both temperature groups, failure was observed as a crack-and-halt progressive phenomenon, as opposed to the gradual crack extension behavior observed in the dry case. It was also surprising to see that, although the peel fracture process did not take place all at once for the whole strip, the crack did not kink into the concrete substrate at all during the whole process but remained propagating along the moist epoxy/concrete interface.

For Epoxy 2, a shift in failure mode from material decohesion to interface separation was again observed as in the case of Epoxy 1 after the introduction of moisture. All dry Epoxy 2 specimens failed by concrete delamination. The pre-crack kinked into the concrete substrate near the epoxy/concrete interface on first crack advance and continued to fracture parallel to the interface until complete peel off. A thin layer of concrete was found adhered to the debonded strip, which consisted of an intact adhesive layer.

Failure of wet Epoxy 2 specimens was similar to wet Epoxy 1 specimens. Epoxy/concrete interface separation took place consistently. The imprinted surface profile on the adhesive side was even clearer on Epoxy 2 due to the higher wetting ability of Epoxy 2. Little, if any, concrete debris adhered to the debonded strip. The freshly exposed failure surface was still moist to the touch.

B. Shear Fracture Modes

In all shear fracture failures, debonding took place all at once in a brittle manner, regardless of the epoxy systems. This was so due to the careful design of the bond length which matched exactly with the effective transfer length of the system such that the energy release (fracture driving force) matched exactly with the total fracture resistance of the system over the designed bond length under a displacement-controlled shear loading. Progressive crack propagation within the bond length could not be detected. Cohesive failure took place when dry while interface separation consistently took place when wet. Figures 5.15 and 5.16 show this dramatic change in failure modes for typical Epoxy 1 and Epoxy 2 specimens respectively.

For dry Epoxy 1 specimens, cohesive fracture occurred in the form of CFRP delamination, with some intercalated epoxy decohesion very close to the CFRP/epoxy interface at times.

Compared to the dry Epoxy 1 specimens, moisture conditioned Epoxy 1 specimens experienced a complete shift in failure mode where failure took place at the epoxy/concrete interface with almost no concrete debris adhered to the debonded strip. Sometimes, the parent interface crack would kink upward to the CFRP/epoxy interface toward the end of the interface debonding process.

Dry Epoxy 2 specimens, on the other hand, failed by concrete delamination with a thin layer of concrete debonded just beneath epoxy/concrete interface. Broken aggregates were clearly seen at the fracture surfaces on both sides. Probably as a result of high stress concentration at the edge of the reaction plate, a concrete chunk was often sheared off near that edge vicinity. The crack however quickly propagated upward toward but beneath the epoxy/concrete interface and continued to propagate parallel to that interface in a concrete delamination mode.

Like wet Epoxy 1 specimens, wet Epoxy 2 specimens also failed in a relatively clean epoxy/concrete interface separation mode. A mirror image of the mechanically abraded concrete profile could be clearly seen on the adhesive side and only a small amount of loose particles were adhered to the debonded strip. For both cases, the fractured interface was still damp to the touch and close ups showed that the pre-crack concrete surface was at the same level as the freshly re-exposed concrete surface after debonding, confirming the observation of an interface separation mode. Also, attention should be paid to the intact aggregates and preserved roughened surface profiles. A final observation was that the alignment markings were still very clearly seen.

5.5.2 Load-Displacement Behavior

A. Peel Fracture Behavior

Typical load-displacement curves for peel fracture specimens bonded with Epoxy 1 and Epoxy 2 before and after moisture conditioning are shown in Figures 5.17 and 5.18, respectively. It is observed that a typical load-displacement curve produced by a peel test appeared in a seesaw pattern with decreasing local peak loads as the crack propagated

further. Each local peak represented the onset of crack advance and the sudden drop in load corresponded to the actual crack front propagation. The first peak was always the highest, signifying a larger fracture resistance to overcome, possibly due to mathematically blunter crack that was introduced simply by the edge of a Teflon tape. Subsequent crack fronts should tend to be much sharper as they were naturally evolved, amplifying the crack intensity in the tip vicinity. The only exception to this typical curve shape was from Epoxy 1 dry specimens, which produced a distinctive gradual load reduction, meaning that cracks did not advance in a crack-and-halt manner like all others did, but took place in a gradual extension manner. This behavior was inline with the physical observation of how the crack propagated to final failure where the crack gradually extended along until complete peel off. Unloading and reloading curves that followed instantaneous load drops were, in general, secant lines that radiated from the origin. This is an important observation as it means that peel fracture process was globally linear elastic and the strain energy built up by the peel force just before the onset of crack advance was fully exhausted at crack advance.

B. Shear Fracture Behavior

Figures 5.19 and 5.20 show typical shear-slip curves generated from the single lap shear fracture tests before and after moisture conditioning of Epoxy 1 and Epoxy 2 specimens respectively. Only the loading curve portion up to the critical state is shown. Unloading portion of the curves could not be consistently reproduced due to the difficulty in monitoring the shear slip response beyond peak load at which shear fracture took place in a catastrophic manner, as discussed earlier.

In general, it is observed that dry Epoxy 1 specimens exhibited a more linear behavior as well as lower load and slip at the critical state. The specimens seemed to gain toughness, as shown from the area under curve, after they were moisture conditioned. After high temperature moisture conditioning, some global yielding signature by the flat portion near the peak load region was also observed before fracture or unloading took place. Shear modulus, defined as the slope of the curves, of all specimens were in close range.

Epoxy 2 specimens, on the other hand, showed a contrary response. Dry specimens possessed better shear resistance than wet ones while all shear-slip curves were much more non-linear than those of Epoxy 1 specimens. Nevertheless, the initial portion appeared to be linear up to approximately 50% of the critical load before non-linearity took over. Shear modulus and critical load tended to decrease upon moisture conditioning, regardless of conditioning temperature.

5.5.3 Interface Fracture Toughness

Interface fracture toughness values for both the peel and shear fracture cases are computed by means of the fracture formulations derived in Chapter 3. By inputting the peak loads, and the corresponding degraded elastic properties that are determined from the associated plots in Chapter 4, the interface fracture toughness values can be obtained. The choice of exact formulation for use in each loading case matches with the actual failure mode Case k observed. For instance, when concrete delamination is observed, the Case 5 expressions are used and the thickness of thin layer of concrete measured in order to have an appropriate value for H_3 (see Figure 3.3). The main expressions for both fracture cases are as follows:

Peel Fracture

$$\Gamma_{peel} = \frac{N_{y,\max}^2}{B^2 E_3 h^3} \left(\frac{(l+a)^2 - l^2}{2I_{1,k}} + \frac{6l^2}{\Sigma_{13}} \right)$$

Shear Fracture

$$\Gamma_{shear} = \frac{N_{x,\max}^2}{2B^2 E_3} \left(\frac{1}{A_{1,k} h} + \frac{\Psi^2}{I_{1,k} h^3} \right)$$

Table 5.2 summarizes the numerical values of the basic parameters used in the computation of fracture toughness. Computed values of peel and shear fracture toughness are summarized in Tables 5.3 and 5.4 respectively.

Table 5.2 Basic Parameters Used to Compute Interface Fracture Toughness

Parameter	Notation	Value	Unit
CFRP cantilever length	l	50.00	mm
Pre-crack length	a	12.50	mm
Bond width	B	25.00	mm
CFRP thickness	h	1.28	mm
Epoxy bond line thickness	t	1.00	mm
Concrete block thickness	H	37.50	mm
CFRP Modulus	E_1	148.00	GPa
Epoxy Modulus	E_2	<u>Epoxy 1:</u> $E_{2,23^\circ C} = 4.14e^{-0.9383M_t}$ $E_{2,50^\circ C} = 3.20e^{-0.2463M_t}$ <u>Epoxy 2:</u> $E_{2,23^\circ C} = 1.47e^{-0.0616M_t}$ $E_{2,50^\circ C} = 1.28e^{-0.0656M_t}$	GPa GPa GPa GPa
Concrete Modulus	E_3	$E_3 = 21.98e^{-0.0929M_t}$	GPa
Moisture Content	M_t	<u>Epoxy 1:</u> $M_{t,0 \text{ week},23^\circ C} = 0.00$ $M_{t,0 \text{ week},50^\circ C} = 0.00$ % $M_{t,2 \text{ weeks},23^\circ C} = 0.19$ $M_{t,2 \text{ weeks},50^\circ C} = 0.46$ % $M_{t,4 \text{ weeks},23^\circ C} = 0.35$ $M_{t,4 \text{ weeks},50^\circ C} = 0.86$ % $M_{t,8 \text{ weeks},23^\circ C} = 0.59$ $M_{t,8 \text{ weeks},50^\circ C} = 1.44$ % <u>Epoxy 2:</u> $M_{t,0 \text{ week},23^\circ C} = 0.00$ $M_{t,0 \text{ week},50^\circ C} = 0.00$ % $M_{t,2 \text{ weeks},23^\circ C} = 0.41$ $M_{t,2 \text{ weeks},50^\circ C} = 0.87$ % $M_{t,4 \text{ weeks},23^\circ C} = 0.77$ $M_{t,4 \text{ weeks},50^\circ C} = 1.63$ % $M_{t,8 \text{ weeks},23^\circ C} = 1.29$ $M_{t,8 \text{ weeks},50^\circ C} = 2.71$ % <u>Concrete:</u> $M_{t,0 \text{ week}} = 0$ % $M_{t,2 \text{ weeks}} = 1.25$ % $M_{t,4 \text{ weeks}} = 2.34$ % $M_{t,8 \text{ weeks}} = 3.90$ %	

Table 5.3 Interface Peel Fracture Toughness

Epoxy System	Cond. Temp. (°C)	Cond. Time (weeks)	Γ_{peel} (J/m ²)	Debonding Mode
Epoxy 1	23	0	359	Epoxy Decohesion
Epoxy 1	23	0	344	Epoxy Decohesion
Epoxy 1	23	0	349	Epoxy Decohesion
Epoxy 1	23	4	421	Epo./Con. Interface Sep.
Epoxy 1	23	4	400	Epo./Con. Interface Sep.
Epoxy 1	23	4	443	Epo./Con. Interface Sep.
Epoxy 1	23	8	445	Epo./Con. Interface Sep.
Epoxy 1	23	8	431	Epo./Con. Interface Sep.
Epoxy 1	23	8	412	Epo./Con. Interface Sep.
Epoxy 1	50	0	478	Epoxy Decohesion
Epoxy 1	50	0	539	Epoxy Decohesion
Epoxy 1	50	0	542	Epoxy Decohesion
Epoxy 1	50	2	578	Epo./Con. Interface Sep.
Epoxy 1	50	2	487	Epo./Con. Interface Sep.
Epoxy 1	50	2	552	Epo./Con. Interface Sep.
Epoxy 1	50	4	555	Epo./Con. Interface Sep.
Epoxy 1	50	4	490	Epo./Con. Interface Sep.
Epoxy 1	50	4	424	Epo./Con. Interface Sep.
Epoxy 1	50	8	523	Epo./Con. Interface Sep.
Epoxy 1	50	8	397	Epo./Con. Interface Sep.
Epoxy 1	50	8	568	Epo./Con. Interface Sep.
Epoxy 2	23	0	1011	Concrete Delamination
Epoxy 2	23	0	1034	Concrete Delamination
Epoxy 2	23	0	1028	Concrete Delamination
Epoxy 2	23	4	375	Epo./Con. Interface Sep.
Epoxy 2	23	4	388	Epo./Con. Interface Sep.
Epoxy 2	23	4	406	Epo./Con. Interface Sep.
Epoxy 2	23	8	334	Epo./Con. Interface Sep.
Epoxy 2	23	8	439	Epo./Con. Interface Sep.
Epoxy 2	23	8	377	Epo./Con. Interface Sep.
Epoxy 2	50	0	1284	Concrete Delamination
Epoxy 2	50	0	978	Concrete Delamination
Epoxy 2	50	0	1157	Concrete Delamination
Epoxy 2	50	2	399	Epo./Con. Interface Sep.
Epoxy 2	50	2	423	Epo./Con. Interface Sep.
Epoxy 2	50	2	404	Epo./Con. Interface Sep.
Epoxy 2	50	4	395	Epo./Con. Interface Sep.
Epoxy 2	50	4	430	Epo./Con. Interface Sep.
Epoxy 2	50	4	424	Epo./Con. Interface Sep.
Epoxy 2	50	8	488	Epo./Con. Interface Sep.
Epoxy 2	50	8	386	Epo./Con. Interface Sep.
Epoxy 2	50	8	400	Epo./Con. Interface Sep.

Table 5.4 Interface Shear Fracture Toughness

Epoxy System	Cond. Temp. (°C)	Cond. Time (weeks)	Γ_{shear} (J/m ²)	Debonding Mode
Epoxy 1	23	0	854	Epo. Decoh. / FRP Delam.
Epoxy 1	23	0	969	FRP Delamination
Epoxy 1	23	0	887	Epo. Decoh. / FRP Delam.
Epoxy 1	23	4	2586	Epo./Con. Interface Sep.
Epoxy 1	23	4	1945	Epo./Con. Interface Sep.
Epoxy 1	23	4	2275	Epo./Con. Interface Sep.
Epoxy 1	23	8	1617	Epo./Con. Interface Sep.
Epoxy 1	23	8	2051	Epo./Con. Interface Sep.
Epoxy 1	23	8	2412	Epo./Con. Interface Sep.
Epoxy 1	50	0	2189	FRP Delamination
Epoxy 1	50	0	1820	Epo. Decoh. / FRP Delam.
Epoxy 1	50	0	1967	Epo. Decoh. / FRP Delam.
Epoxy 1	50	2	1663	Epo./Con. Interface Sep.
Epoxy 1	50	2	3672	Epo./Con. Interface Sep.
Epoxy 1	50	2	N/A	Specimen Breakage
Epoxy 1	50	4	1931	Epo./Con. Interface Sep.
Epoxy 1	50	4	2635	Epo./Con. Interface Sep.
Epoxy 1	50	4	2282	Epo./Con. Interface Sep.
Epoxy 1	50	8	1988	Epo./Con. Interface Sep.
Epoxy 1	50	8	1419	Epo./Con. Interface Sep.
Epoxy 1	50	8	2289	Epo./Con. Interface Sep.
Epoxy 2	23	0	3014	Concrete Delamination
Epoxy 2	23	0	2707	Con. Delam. / FRP Delam.
Epoxy 2	23	0	3133	Concrete Delamination
Epoxy 2	23	4	2027	Epo./Con. Interface Sep.
Epoxy 2	23	4	3477	Epo./Con. Interface Sep.
Epoxy 2	23	4	2695	Epo./Con. Interface Sep.
Epoxy 2	23	8	2478	Epo./Con. Interface Sep.
Epoxy 2	23	8	2632	Epo./Con. Interface Sep.
Epoxy 2	23	8	N/A	Specimen Breakage
Epoxy 2	50	0	2701	Concrete Delamination
Epoxy 2	50	0	3304	Concrete Delamination
Epoxy 2	50	0	3091	Concrete Delamination
Epoxy 2	50	2	2399	Epo./Con. Interface Sep.
Epoxy 2	50	2	2092	Epo./Con. Interface Sep.
Epoxy 2	50	2	N/A	Specimen Breakage
Epoxy 2	50	4	1475	Epo./Con. Interface Sep.
Epoxy 2	50	4	1675	Epo./Con. Interface Sep.
Epoxy 2	50	4	1724	Epo./Con. Interface Sep.
Epoxy 2	50	8	1346	Epo./Con. Interface Sep.
Epoxy 2	50	8	1588	Epo./Con. Interface Sep.
Epoxy 2	50	8	1532	Epo./Con. Interface Sep.

A. Peel Fracture Toughness

Average values of peel fracture toughness are graphically summarized in Figures 5.21 and 5.22 respectively for the two epoxies. By examining the plots, it is seen that the peel fracture toughness trends are strongly tied to the first (or absolute) peak loads in the load-displacement curves presented earlier. The higher is the first peak, the higher is the peel fracture toughness. In fact, the linear elastic fracture energy formulation implies this correlation.

For Epoxy 1 specimens, the recorded fracture toughness was steady throughout the moisture conditioning program, despite the fact that failure mode had been shifted from epoxy decohesion to epoxy/concrete interface separation due to the introduction of moisture. This was quite surprising because if the fracture toughness for a epoxy decohesion mode was similar to a epoxy/concrete interface separation mode, one would expect statistically equal amount of observations in each case (either dry or wet). However, this was not the case. So it might be suggesting that before and after moisture ingress, the fracture toughness for both epoxy decohesion and epoxy/concrete interface separation might have changed magnitudes in opposite directions. More in-depth discussion will be provided on this in Chapter 6.

For Epoxy 2 specimens, on the other hand, a phenomenal drop in fracture toughness has been registered when specimens were moisture conditioned for 2 weeks or more. The drop in fracture resistance was more than 60% in both temperature groups. The first-crack fracture toughness then became steady and did not reduce further with time. Note that the dry fracture toughness of Epoxy 2 specimens represented the peel fracture resistance (that nevertheless consisted of both an open and a shear mode as discussed before) of the concrete being used, as the failure modes were unanimously concrete delamination. The high initial (dry) fracture toughness of Epoxy 2 specimens may be suggesting the existence of an extra toughening mechanism such as crazing and shear banding contributed by the rubber particles inside the epoxy layer. Note also that the fracture toughness of all wet specimens were in the same range and the readers should recall that the failure modes for all wet specimens were also identical, regardless of the conditioning temperature and the type of epoxy used. Since epoxy/concrete interface separation took place for wet specimens and that the fracture toughness values were

sharply reduced, it might be suggesting that the constituent materials limits were not fully (or largely) utilized as concrete did not fracture and epoxy did not craze.

B. Shear Fracture Toughness

Average values of shear fracture toughness are summarized graphically in Figures 5.23 and 5.24 respectively. A clear degradation trend can be seen for Epoxy 2 specimens with increasing moisture conditioning while an interesting counter-intuitive phenomenon is shown for Epoxy 1 specimens where the initial (dry) fracture toughness is substantially lower than wet counterparts.

Epoxy 1 specimens exhibited a surge in fracture toughness upon initial moisture contact despite the shift in failure mode from a material decohesion one to an interface separation one. After the surge, fracture toughness steadily decreased with increasing moisture content. This trend was evidenced in both temperature groups, although the surge in the high temperature group was less dramatic, possibly due to a post-curing effect at that high temperature.

For Epoxy 2 specimens, accelerated moisture diffusion, with the aid of elevated temperature, has been able to degrade more than 50% of the original (dry) shear fracture toughness in as short as 8 weeks, although the reduction has slowed down and became more asymptotic starting at the 4-week interval. A similar but slower degradation trend is seen for moisture conditioning without elevated temperature (i.e. 23°C wet). These degradation trends were considered in line with the peel fracture case when factoring in a similar shift in failure modes.

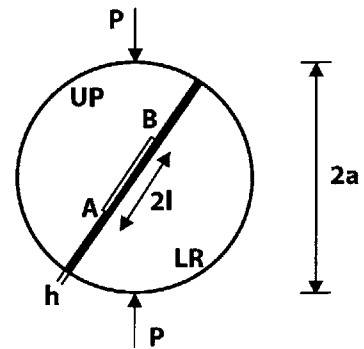
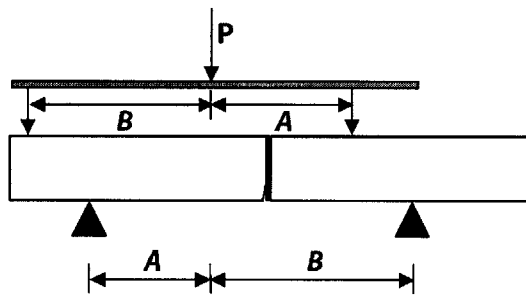
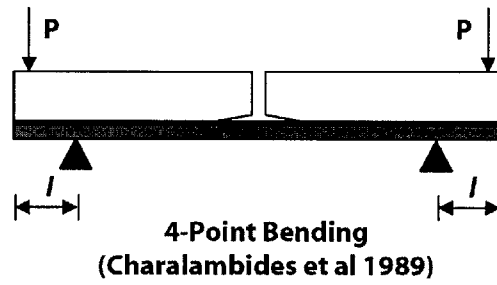
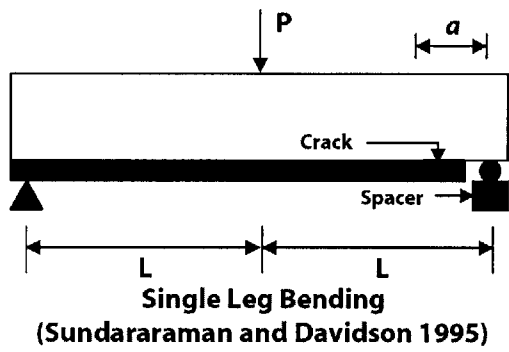


Figure 5.1 Traditional Interface Fracture Specimens

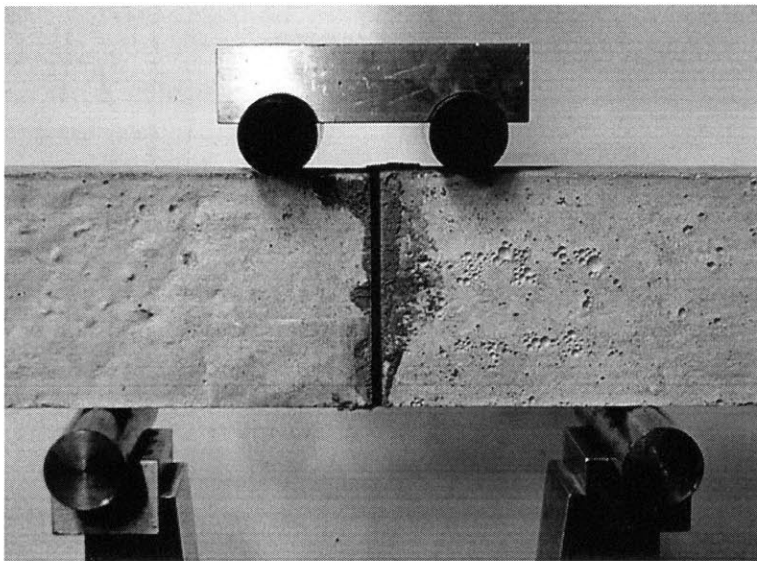
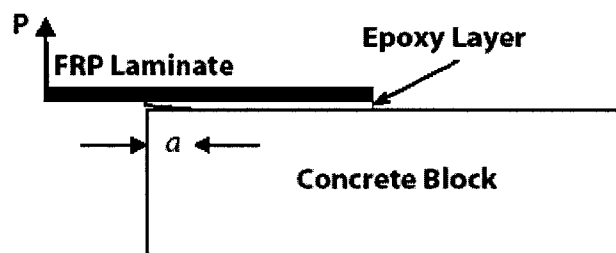


Figure 5.2 Example of a FRP Bonded Concrete Sandwiched Specimen

Peel Fracture



Shear Fracture

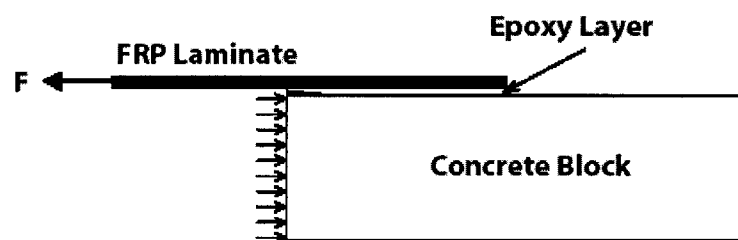


Figure 5.3 Chosen Interface Fracture Specimens

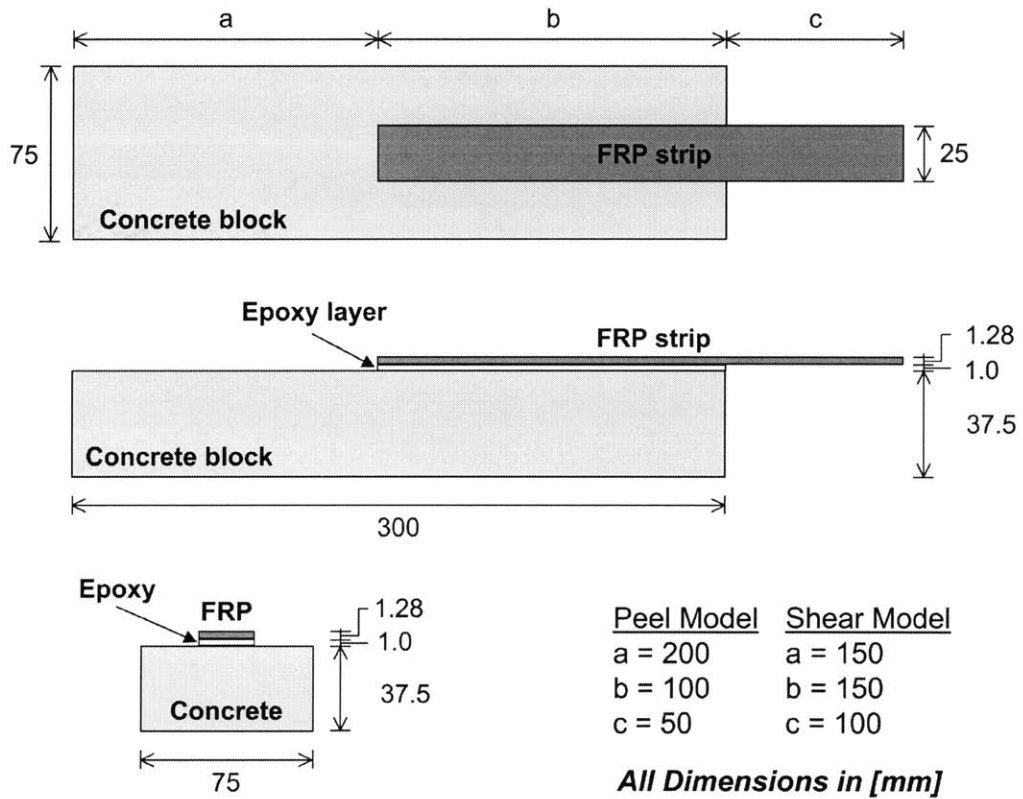


Figure 5.4 Dimensions of Specimens



Figure 5.5 Pneumatic Needle Scaler

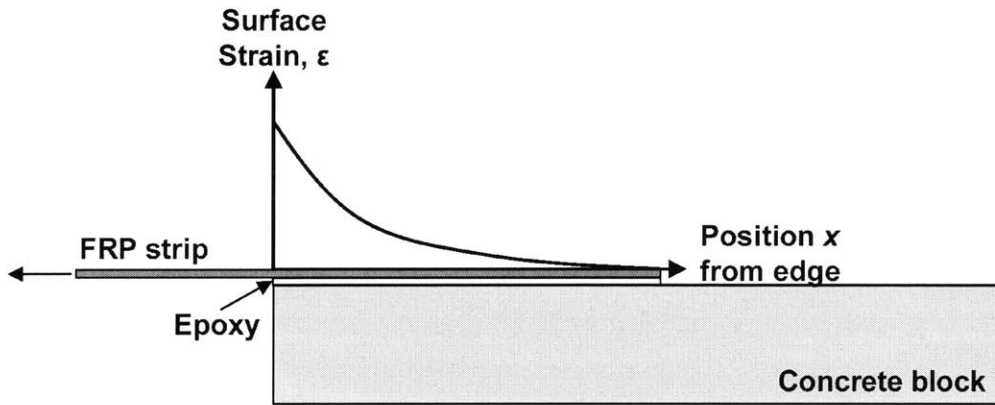


Figure 5.6 Surface Strain Variation Under Shear Load

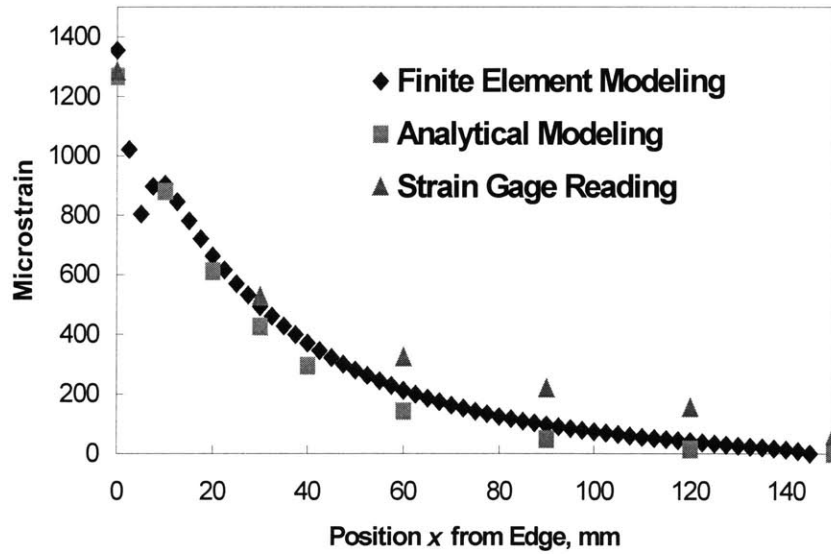


Figure 5.7 Determination of Bond Length for Shear Fracture Specimens Using Micro-Strain Profile Analysis

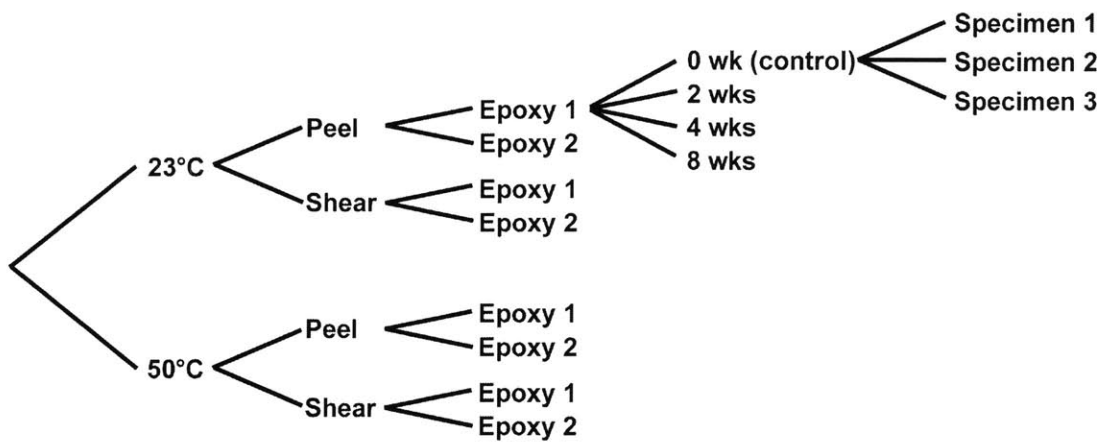


Figure 5.8 Fracture Test Matrix



Figure 5.9 Fracture Specimens under Ambient Cure

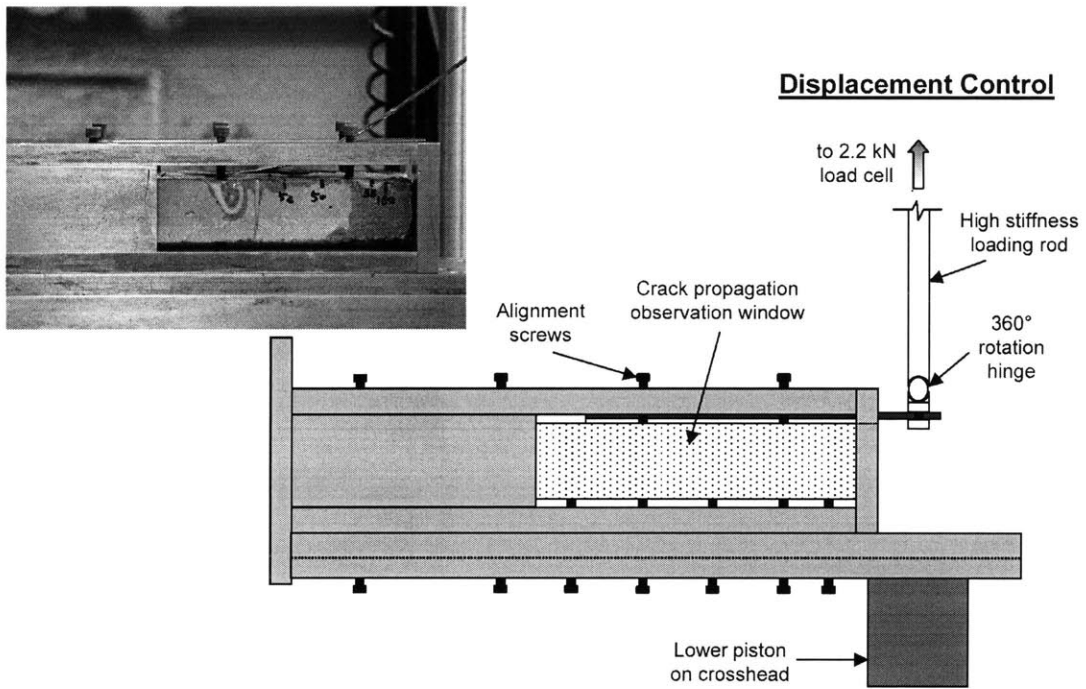


Figure 5.10 Peel Fracture Test Setup

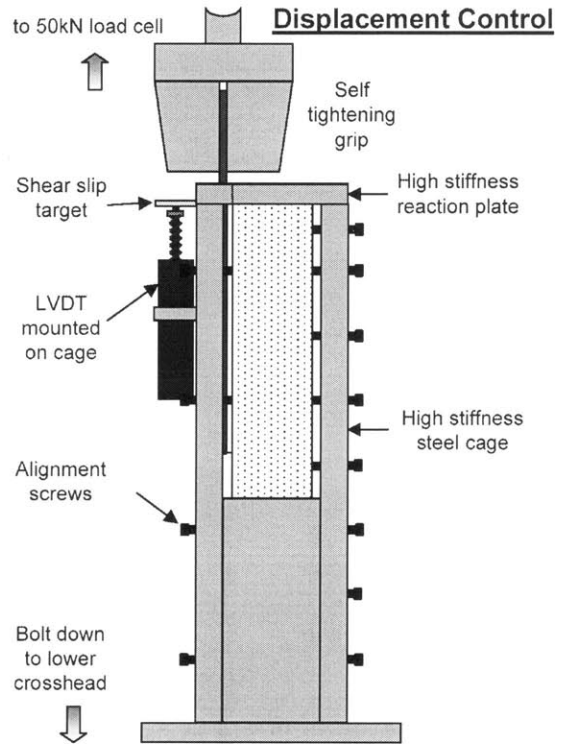
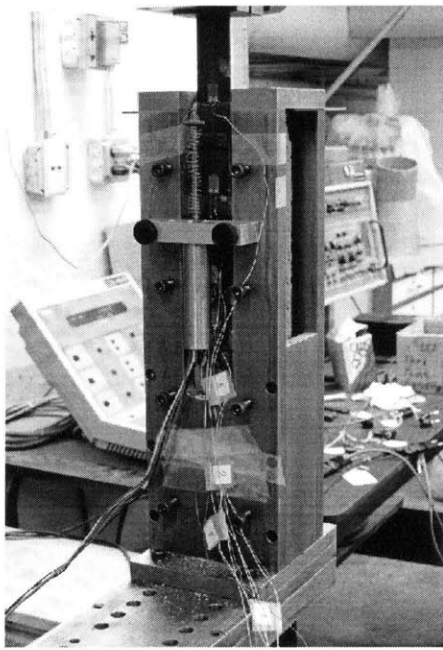


Figure 5.11 Shear Fracture Test Setup

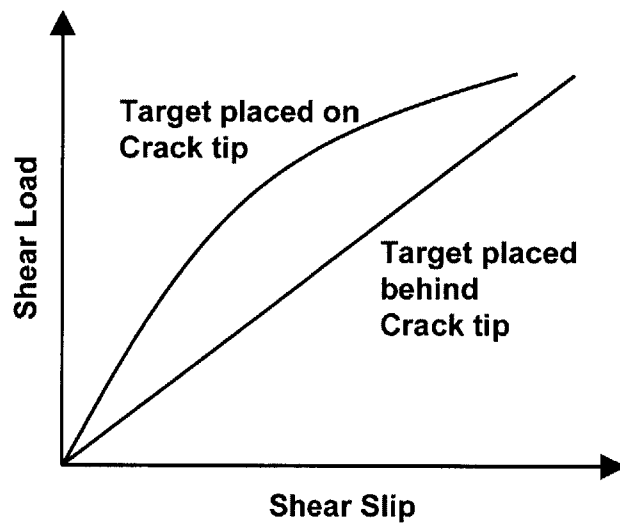


Figure 5.12 Shear Slip Response Due to Different Target Locations

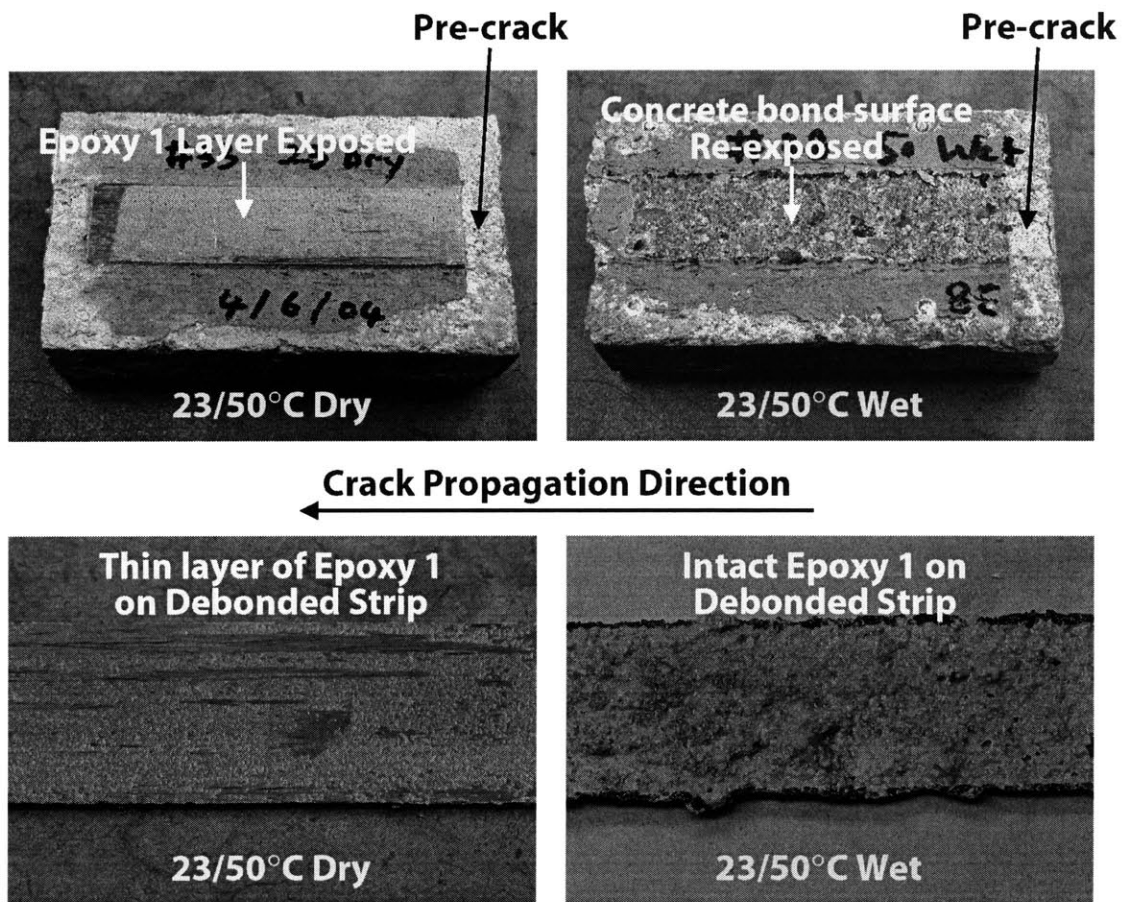


Figure 5.13 Typical Epoxy 1 Peel Fracture Modes

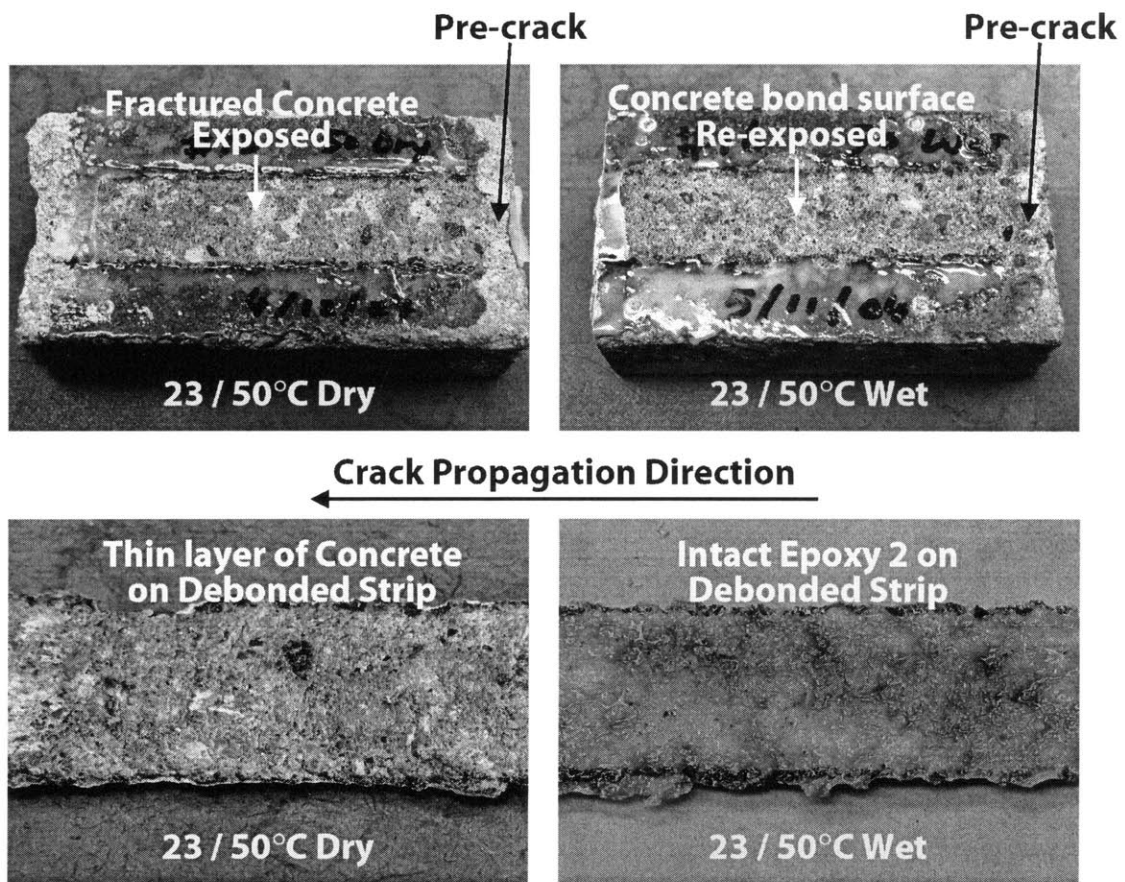


Figure 5.14 Typical Epoxy 2 Peel Fracture Modes

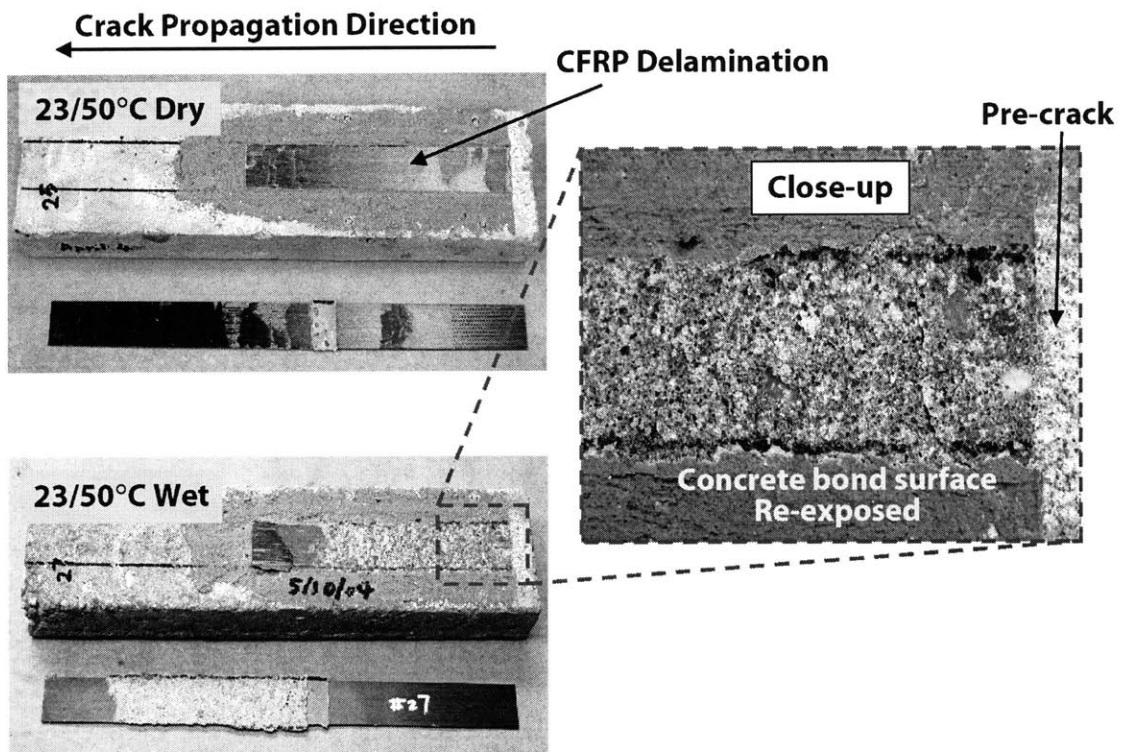


Figure 5.15 Typical Epoxy 1 Shear Fracture Modes

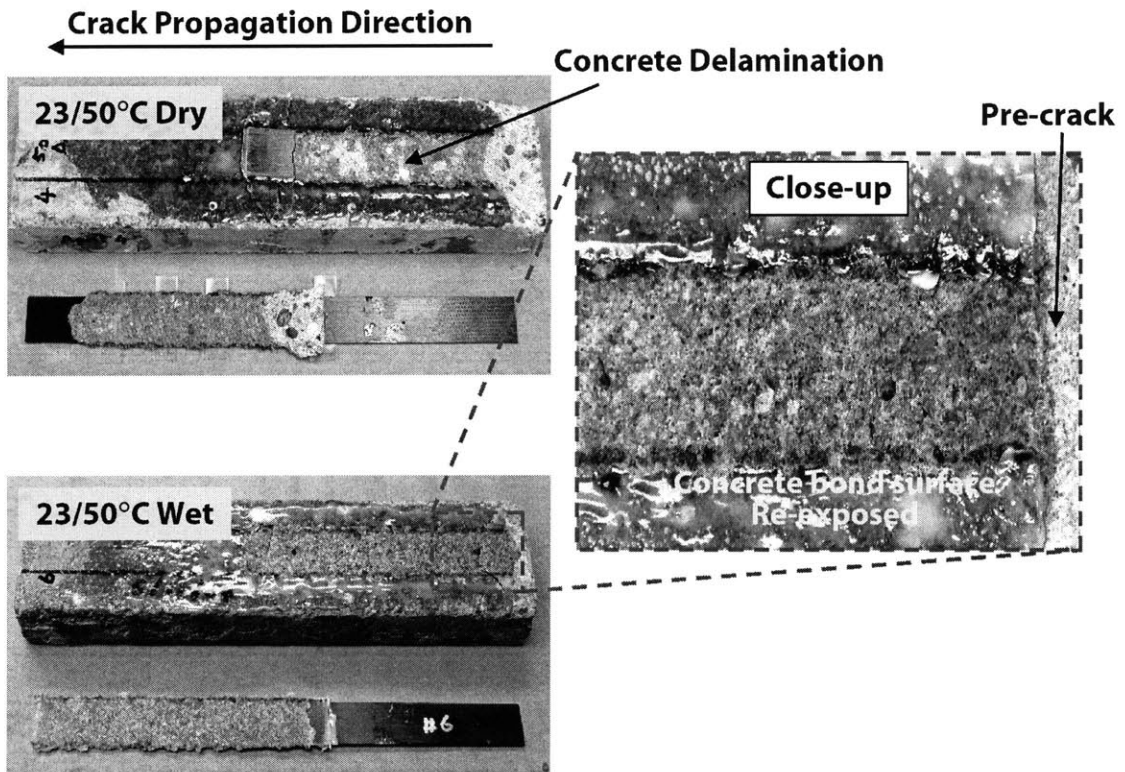


Figure 5.16 Typical Epoxy 2 Shear Fracture Modes

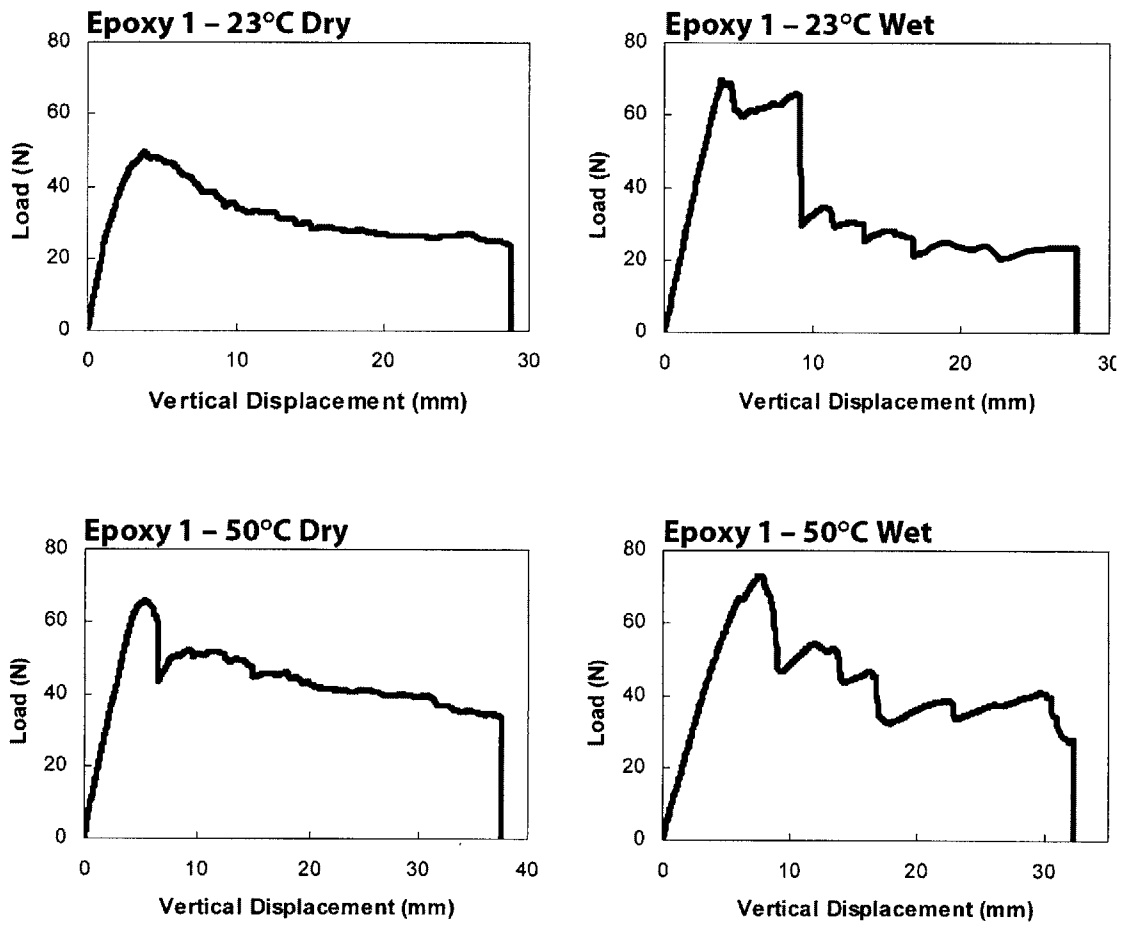


Figure 5.17 Typical Epoxy 1 Load-Deformation Curves under Peel

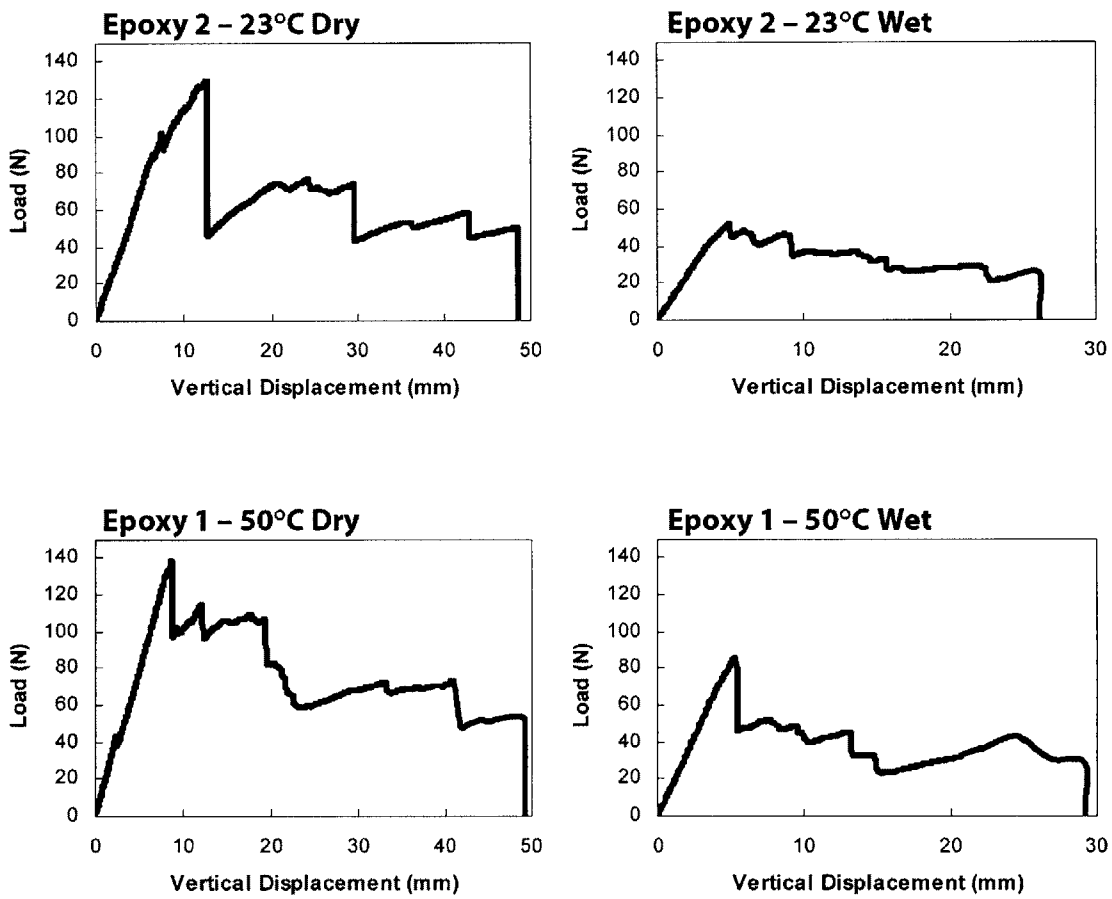


Figure 5.18 Typical Epoxy 2 Load-Deformation Curves under Peel

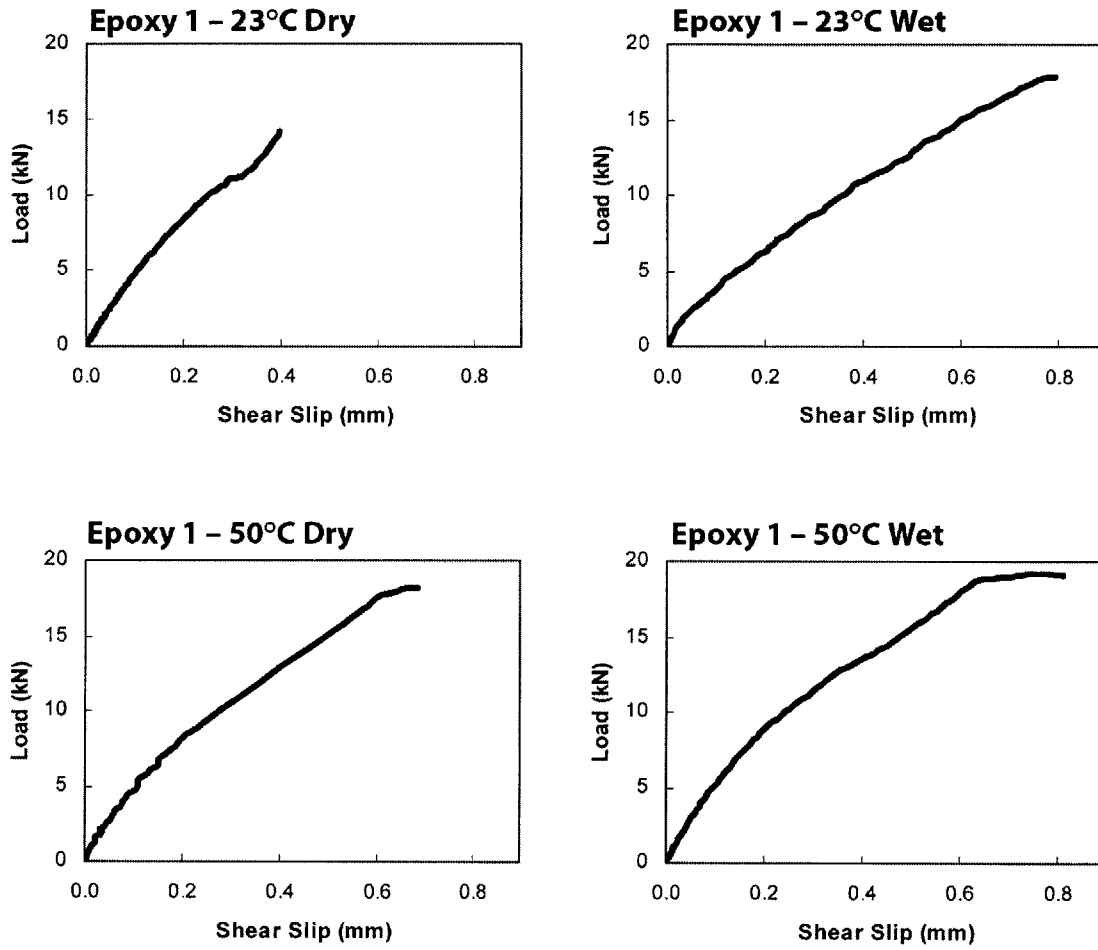


Figure 5.19 Typical Epoxy 1 Load-Deformation Curves under Shear

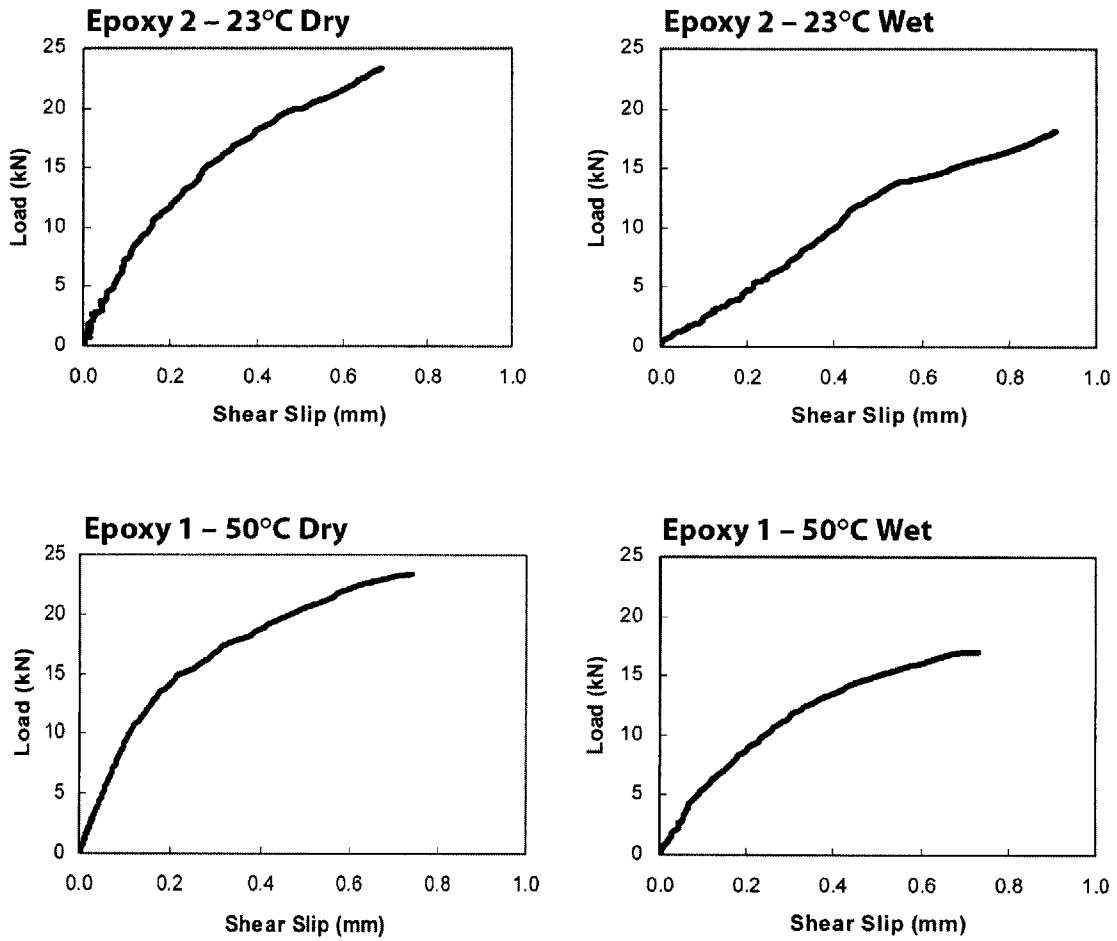


Figure 5.20 Typical Epoxy 2 Load-Deformation Curves under Shear

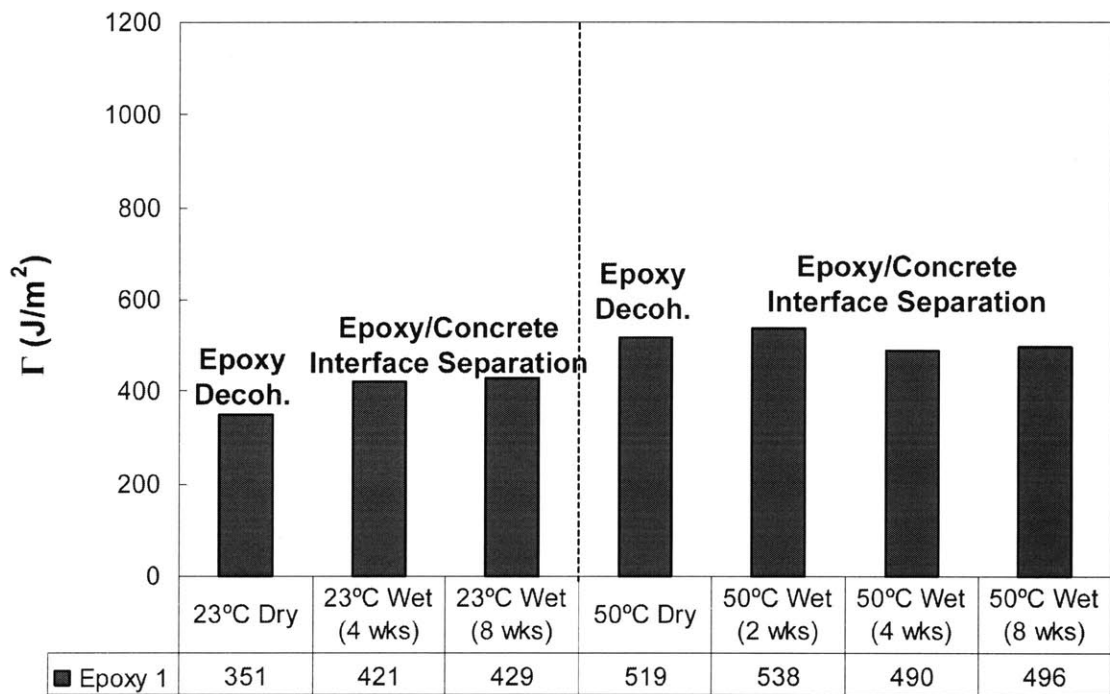


Figure 5.21 Peel Fracture Toughness Variation of Epoxy 1

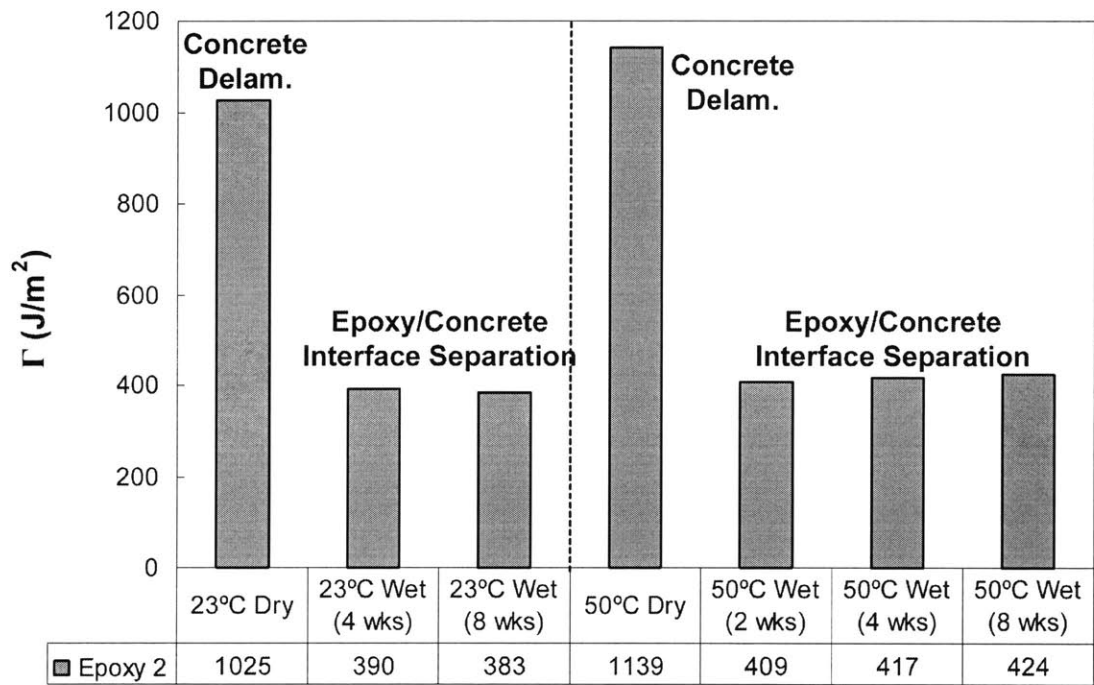


Figure 5.22 Peel Fracture Toughness Variation of Epoxy 2

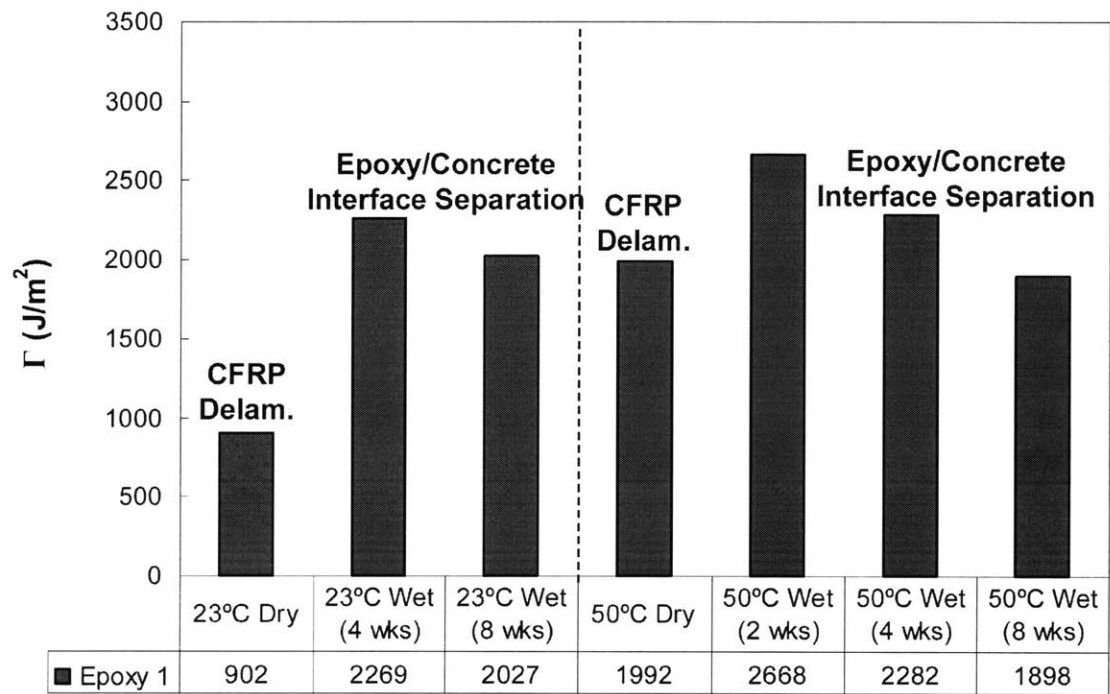


Figure 5.23 Shear Fracture Toughness Variation of Epoxy 1

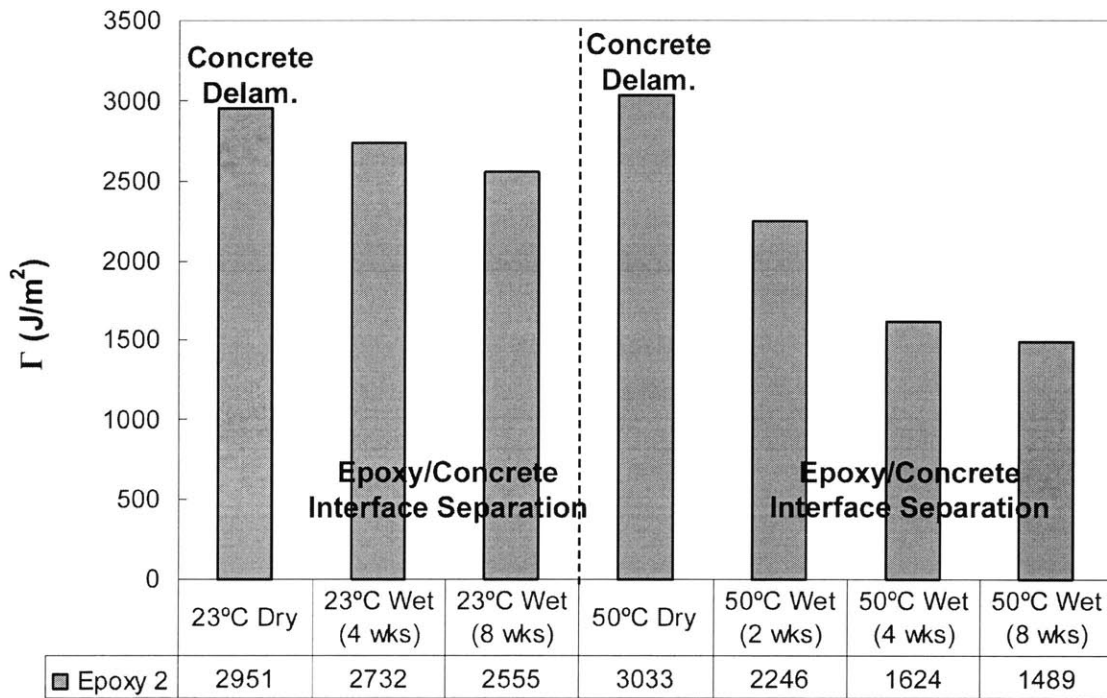


Figure 5.24 Shear Fracture Toughness Variation of Epoxy 2

CHAPTER 6

INTERFACE FRACTURE ANALYSIS OF FRP DEBONDING AFFECTED BY MOISTURE

In the prior chapters, a set of new tri-layer fracture energy models is derived to facilitate the quantification of one of the five possible debonding failures in FRP bonded concrete by computing the interface fracture toughness of mesoscale peel and shear fracture specimens that consisted of real-scale bond lines and are subjected to accelerated moisture conditioning for selected time intervals before mechanically tested to failure. As inputs in the computation, diffusion and mechanical properties of the constituent materials with respect to moisture uptake are physically determined. Three-dimensional moisture diffusion simulations are also performed to estimate the moisture concentration in the interfacial bond region at a given point in time. With the knowledge of the computed toughness values and their trends with respect to increasing moisture ingress, observed debonding modes and their shift behavior from dry to wet, as well as the simulated diffusion behavior and quantification, this chapter analyzes the debonding problem synergistically by combining and correlating with results from finite element

fracture computation, mode-mix characterization, and kink criterion implementation, to develop better understanding of various mechanistic debonding behavior affected by moisture. Discussions are made mainly from an interface fracture mechanics perspective.

6.1 Effect of Moisture on Debonding Resistance

Fracture toughness variation plots presented in Chapter 5 have shown that different epoxy systems could lead to different initial response to moisture ingress, although degradation behavior has generally been observed with prolonged conditioning. This general trend observation is common between the two temperature groups for both epoxies. The following tries to correlate the fracture toughness variations with the results generated from the finite element moisture diffusion simulation as presented in Chapter 4 for both the peel and shear fracture cases.

6.1.1 Effect on Peel Fracture Toughness

Regardless of the mechanism that has led to the initial change (from dry to wet) of fracture toughness, both epoxies exhibited a rather steady toughness variation trend after only 2 weeks of moisture conditioning. This was considered quite surprising because the 3-D diffusion simulation indicated that even after 8 weeks of continuous moisture conditioning at 50°C, diffusion activities in the interfacial region was still very active. In fact, it was predicted that not until after 200 days would the bond line start to saturate. Upon closer examination, two commonalities were found. The first fact is that in all peel fracture cases, regardless of epoxy systems and conditioning duration beyond 2 weeks, epoxy/concrete interface separation was observed consistently as the debonding mode in the region where the first crack advance took place. The second fact is that the moisture concentration in that region, which was usually not more than a few centimeters in length, had a minimum of 50%, as shown in Figure 6.1. When the moisture concentration was less than this value, a different debonding mode was likely to occur. For instance, when it was dry (i.e. 0%), concrete delamination initiated in Epoxy 2 instead. Combination of these facts has led to the thinking of a possible threshold of moisture concentration beyond which no significant further change in mechanism and hence fracture toughness could occur. In the herein case, that threshold seemed to be 50% or

less. This argument, if true, should be supported by further evidence in the case of shear fracture.

In the case of Epoxy 2, the shift in debonding mode from concrete delamination to epoxy/concrete interface separation has revealed the fact that when dry, the epoxy/concrete interface fracture toughness was higher than that for concrete delamination, which was approximately 1000 J/m^2 , although it would be technically difficult to measure the dry interface toughness values. Nevertheless, that value has dropped to close to 400 J/m^2 after moisture concentration has reached 50% or less and thus signified a substantial loss of adhesion between epoxy and concrete as a consequence of moisture ingress, provided that the original epoxy and concrete still remain in the interfacial region without formation of any new interphase material (more discussion on this later using crack kinking arguments).

In the case where Epoxy 1 is involved, the phenomenon was more complex. It was experimentally found that upon introduction of moisture to the specimens, the fracture toughness did not decrease as in the case of Epoxy 2. As a matter of fact, there seemed to be a tendency of slight increase in fracture toughness from dry to wet. This behavior was at first considered counter-intuitive because in the dry case, debonding took place as epoxy decohesion very close to the CFRP/epoxy interface. After getting wet, failure shifted to epoxy/concrete interface, which had a higher toughness values than the dry case, meaning that the interface fracture toughness for epoxy decohesion near the CFRP/epoxy interface has increased, after getting wet, to a level at least higher than that of the wet epoxy/concrete interface. In other words, there existed a material toughening mechanism that has enhanced the toughness of Epoxy 1 with the introduction of moisture. This might be attributed to the plasticization of the epoxy material as a result of increasing moisture content that would generally reduce the strength properties (as seen in material degradation plots presented in Chapter 4) but would on the other hand increase the fracture toughness of the epoxy material itself (Mays and Hutchinson 1992). Within 2 weeks, the epoxy itself might have toughened to a point where the other weaker debonding mode (in this case, epoxy/concrete interface separation) took over. More insights could be gained toward this plasticization effect by analyzing the shear fracture cases in a similar manner. Also, the comparable magnitudes of the fracture toughness

before and after moisture ingress could only be considered coincidental. One should not think that the bond did not degrade at all simply because not much variation in fracture toughness was exhibited before and after moisture ingress (Figure 6.2). In fact, different debonding modes have been observed and degradation has indeed occurred due to the reduction in fracture toughness for the epoxy/concrete interface from dry to wet.

6.1.2 Effect on Shear Fracture Toughness

Shear fracture toughness of all wet peel specimens showed some degradation over time between the 2-week and 8-week test periods. In particular, Epoxy 2 high temperature conditioning group has started to show sign of slowing after 4 weeks. The fracture toughness has degraded by approximately half after 8 weeks. While the proposed asymptotic degradation behavior requires further tests on specimens that are conditioned for longer time, it has been observed from diffusion simulation that the minimum moisture concentration in the shear fracture region, which is also the entire bond region due to the effective transfer length design (see Chapter 5 for definition and discussions), has reached roughly 50% in 8 weeks time, as shown in Figure 6.3. This observation coincides with that of the peel fracture case where the 50% seemed to be the moisture concentration threshold that would produce little further degradation. In the shear fracture case, however, the duration for such asymptotic behavior was much longer because the entire 150 mm bond contributed to the debonding resistance, as opposed to the few centimeters near the edge region in peel fracture. Degradation behavior for Epoxy 1 was, in general, more gradual than that of Epoxy 2.

Considering the dry-wet transition, Epoxy 1 specimens exhibited a sharp increase in toughness after getting wet, as shown in Figure 6.4, with an associated shift in debonding mode from CFRP delamination to epoxy/concrete interface separation. Note that the wet debonding interface separation mode was the same as in peel fracture while the CFRP delamination took place very close to the CFRP/epoxy interface, as if only a layer of fibers was delaminated. This toughness increase behavior deviated from the Epoxy 2 behavior, which was some how expected after studying the peel fracture case. By revisiting the epoxy plasticization arguments developed earlier, one might expect an increase in fracture toughness in the CFRP/epoxy interfacial region with increasing

toughening due to moisture ingress that might in turn enhance the adhesion between the two. As opposed to the epoxy/concrete interface, the CFRP/epoxy interface tended to be more stable due to the low surface free energy of the CFRP (Mays and Hutchinson 1992) so that moisture was less likely to stay in the interface, but rather entered the polymeric structure of the epoxy (either within the bond line or in the matrix of the CFRP plate) to produce the plasticization effect. However, the plasticization argument generally applies to all epoxy materials, but such toughness enhancement effect was not observed in Epoxy 2 fracture specimens at all during the dry-wet transition. This has prompted one to think of the origin of the “moisture-tolerant” description of the proprietary Epoxy 1 system (see Chapter 4 under the section of Material Description) involving a moisture-cure formulation that is commonly found in epoxies used for underwater applications (Argon 2004, Oman 2004). This is somewhat inline with the slight enhancement of tensile properties of Epoxy 1 upon initial moisture conditioning as indicated in the mechanical property variation plots presented in Chapter 4. Nevertheless, these observations have revealed the need for knowing the exact chemical formulation of the epoxy adhesives in studying the moisture effect on FRP debonding problems.

6.2 Effect of Moisture on Locus of Fracture

The locus of fracture for all dry cases stayed within the material layers. The parent pre-crack at the epoxy/concrete interface that was generated by a 80-micron thin Teflon film kinked into the material layers either above or below that interface. For Epoxy 1, kinking occurred at the very tip of the pre-crack and the crack searched upward to the vicinity of the CFRP/epoxy interface region and the crack propagated along that interface until the entire strip was debonded. For Epoxy 2, the parent crack kinked downward into the concrete substrate below the epoxy/concrete interface and subsequent crack propagation stayed close and parallel to that interface, leading to a thin layer of concrete adhered to the debonded strip. The locus of fracture for all wet cases, on the other hand, occurred apparently at the epoxy/concrete interface, staying at the same level as the pre-crack. In other words, no kinking was observed.

To study the shift in crack kinking behavior, the kink criterion (He and Hutchinson 1988) is employed. The kink criterion states that when

$$\frac{\Gamma_i}{\Gamma_s} > \frac{G_i}{G'_{\max}}$$

is satisfied, the parent crack that lies at the interface of two adjoining materials will tend to kink into the substrate in consideration. Here, Γ_i is the interface fracture toughness, Γ_s the substrate fracture toughness in mode I, G_i the interface fracture energy release rate (as computed from the derived G model in Chapter 3), and G'_{\max} the maximum fracture energy release rate for the kink crack at any putative kink angle. Figure 6.5 shows the G_i/G'_{\max} ratio variations for several sets of elastic mismatch (Hutchinson and Suo 1992). One should note that the ratio is less than unity because G_i is always less than G'_{\max} due to the definition of G'_{\max} . In what follows, only Epoxy 2, which produced the more traditional debonding mode, is discussed because of similar considerations and arguments of the kink criterion in both epoxy systems.

6.2.1 Locus of Fracture for Dry Specimens

When dry, Epoxy 2 exhibited a concrete delamination mode of debonding and the corresponding peel and shear fracture toughness values were roughly 1000 J/m² and 3000 J/m² respectively. Since debonding did not occur at the interface, the actual toughness values of the epoxy/concrete interface were higher than those values. Taking the Mode I fracture toughness values of concrete (oven-dried) as presented in Chapter 4, the values can be summarized as follows for assessing the kink criterion:

Table 6.1 Dry Fracture Toughness

	Γ_i (J/m ²)	Γ_s (J/m ²)
Dry Peel Fracture	>1000	~26
Dry Shear Fracture	>3000	~26

Recalling the fact that G_i/G'_{\max} has a value less than unity (see Figure 6.5), it is clearly noted that Γ_i/Γ_s is 1 to 2 orders of magnitude larger for both the peel case and the shear case. The kink criterion thus predicts that the parent pre-crack would kink into the concrete substrate. This prediction is inline with the observed failure mode where

concrete delamination indeed took place in both loading configurations. The examination also suggests that the Mode 1 fracture toughness of Epoxy 2 is higher than 3000 J/m², which is deemed reasonable for an elastomer-toughened epoxy in which substantial crazing can take place, as physically shown in Figure 4.18.

Although the kink criterion is capable of predicting the initial crack propagation tendency, it fails to provide further insight regarding the subsequent crack front behavior. In other words, the kink criterion explains why the pre-crack kinked into the concrete substrate, but it does not indicate why the crack continued to propagate close and parallel to the epoxy/concrete interface, but not continue to penetrate deeper into the supposedly brittle concrete block, resulting in a thin layer of concrete adhered to the debonded strip.

To understand this crack propagation behavior, the stress states around the crack tip region need to be understood. As such, a mode-mix separation analysis has been performed by use of the finite element method and the M-integral analysis as detailed immediately below.

A. Mode Separation Analysis by Finite Element Method (Matos et al 1989)

In order to compute K_I^* (open mode) and K_{II}^* (shear mode) for the interface crack problem where a parent crack lies in between the epoxy and concrete layers, the J -integral is first computed conventionally using the virtual crack extension method, which is represented by the following expression:

$$J = -(\partial U / \partial a)_F \approx -\frac{1}{2} \{u_n\}^T (\partial [S] / \partial a) \{u_n\}$$

Here, U is the potential energy of the bonded material system and the differentiation with respect to parent crack length a is carried out at fixed load. The vector $\{u_n\}$ contains as elements the nodal degrees of freedom for a finite element calculation and $[S]$ is the stiffness matrix for the mesh of elements used to solve the interface crack problem. The crack problem is first solved to obtain the vector $\{u_n\}$. Then a small virtual crack extension is caused in the plane of the crack and a new value of the stiffness computed. The crack can be extended by rigidly moving a core of elements around the tip and distorting only one ring of elements. That is, all elements outside the distorted ring are rigidly held. Consequently, in the core of rigid elements and in the outer rigid area,

$\partial[S]/\partial a = 0$. The computation of the changed stiffness is very limited and the multiplication only involves small vectors and matrices.

After the J is computed, one may proceed to compute K_I^* and K_{II}^* for the interface crack problem respectively. To do this, a special numerical procedure called the M-integral technique is required due to the fact that when evaluating the path integrals, the displacements solution in one material does not satisfy the governing equations in the other, and so the symmetric and anti-symmetric parts are invalid displacements in both materials. As such, Matos et al (1989) have developed a numerical technique that provides adjustments to the displacements fields in order to correctly and accurately obtain the respective stress intensity factors.

With the computed $\{u_n\}$ by the finite element method, add to the displacements by $\{\Delta u_n\}_I$ for a problem in the same geometry for which $K_{II}^* = 0$ and $K_I^* = \Delta K_I^*$. This set of displacements can represent any problem desired (e.g. $\Delta K_I^* = 0.1$) and it should be noted that the field is actually needed only for the nodes associated with the distorted ring of elements. In view of this, the asymptotic crack tip displacements can be used everywhere as a suitable field and they have an expression as follows:

$$\Delta u_I^j = \frac{\Delta K_I^*}{2G_j} \sqrt{\frac{r}{2\pi}} \frac{e^{\pi\varepsilon}}{(1 + e^{2\pi\varepsilon})} \mathbf{f}_I(r, \theta, \varepsilon, \mu_j)$$

where j denotes material 1 or 2 and f_I the function that describes the oscillatory characteristic of the near tip displacement field at the bimaterial interface and will be precisely defined later. The vector $\{\Delta u_n\}_I$ is obtained by evaluating Δu_I^j at the required nodes. With the value of $\partial[S]/\partial a$ already computed earlier for the computation of J , the calculation in $J = -(\partial U/\partial a)_F$ is repeated with the vector $\{u_n\} + \{\Delta u_n\}_I$ instead of $\{u_n\}$ alone. That is:

$$J_{new,I} = J + \Delta_I J \approx -\frac{1}{2} [\{u_n\} + \{\Delta u_n\}_I]^T (\partial[S]/\partial a) [\{u_n\} + \{\Delta u_n\}_I]$$

Computationally,

$$\Delta_I J = -\frac{1}{2} [\{u_n\} + \{\Delta u_n\}_I]^T (\partial[S]/\partial a) [\{u_n\} + \{\Delta u_n\}_I] + \frac{1}{2} \{u_n\}^T (\partial[S]/\partial a) \{u_n\}$$

The result of this calculation, $J + \Delta_I J$, can be shown as:

$$\Delta_I J = \frac{1}{H} (\Delta K_I^{*2} + 2K_I^* \Delta K_I^*)$$

Rearranging,

$$K_I^* = \frac{H \Delta_I J}{2 \Delta K_I^*} - \frac{1}{2} \Delta K_I^*$$

and the 2nd term can be neglected compared to the 1st if ΔK_I^{*2} is small compared to $H \Delta_I J$.

The procedure can then be repeated for an added vector $\{\Delta u_n\}_{II}$ such that $K_I^* = 0$ and $K_{II}^* = \Delta K_{II}^*$ for the evaluation of K_{II}^* . Here, the displacements are such that

$$\Delta \mathbf{u}_{II}^j = \frac{\Delta K_{II}^*}{2G_j} \sqrt{\frac{r}{2\pi}} \frac{e^{\pi\varepsilon}}{(1+e^{2\pi\varepsilon})} \mathbf{f}_{II}(r, \theta, \varepsilon, \mu_j)$$

Then it follows similarly that the new value from $J = -(\partial U / \partial a)_F$ is $J + \Delta_{II} J$ and

$$K_{II}^* = \frac{H \Delta_{II} J}{2 \Delta K_{II}^*} - \frac{1}{2} \Delta K_{II}^*$$

The components of the functions $f_I(r, \theta, \varepsilon, \mu_j)$ and $f_{II}(r, \theta, \varepsilon, \mu_j)$ that introduce the oscillatory characteristic of the near crack tip displacement field are obtained as follows:

$$f_{1I} = D_j + 2\delta_j \sin \theta \sin \Psi$$

$$f_{2I} = -C_j - 2\delta_j \sin \theta \cos \Psi$$

and

$$f_{1II} = -C_j + 2\delta_j \sin \theta \cos \Psi$$

$$f_{2II} = -D_j + 2\delta_j \sin \theta \sin \Psi$$

D_j , C_j , d_j and Ψ are defined as

$$\delta_1 = e^{-(\pi-\theta)\varepsilon} \delta_2 = e^{(\pi+\theta)\varepsilon}$$

$$\Psi = \varepsilon \log r + \frac{\theta}{2}$$

$$D_j = \beta \gamma_j \cos \frac{\theta}{2} + \beta' \gamma_j' \sin \frac{\theta}{2}$$

$$C_j = \beta' \gamma_j \cos \frac{\theta}{2} - \beta \gamma_j' \sin \frac{\theta}{2}$$

$$\beta = \frac{0.5 \cos(\varepsilon \log r) + \varepsilon \sin(\varepsilon \log r)}{0.25 + \varepsilon^2}$$

$$\beta' = \frac{0.5 \sin(\varepsilon \log r) - \varepsilon \cos(\varepsilon \log r)}{0.25 + \varepsilon^2}$$

$$\gamma_j = \mu_j \delta_j - \frac{1}{\delta_j} \gamma_j' = \mu_j \delta_j + \frac{1}{\delta_j}$$

where (r, θ) are the polar coordinates, ε the bimaterial constant and j is the material index.

Hence, K_I^* (open mode) and K_{II}^* (shear mode) for an interface crack problem are computed. Finally, it should be noted that K_I^* and K_{II}^* are related to J and G in the case of linear elasticity as follows:

$$J_{\text{Linear Elastic}} = G = \frac{|K|}{E^* \cosh^2(\pi \varepsilon)} = \frac{K_I^{*2} + K_{II}^{*2}}{E^*} (1 - \beta^2)$$

where $\frac{1}{E^*} = \frac{1}{2} \left(\frac{1}{E_1} + \frac{1}{E_2} \right)$, $\varepsilon = \frac{1}{2\pi} \ln \left(\frac{1 - \beta}{1 + \beta} \right)$, and the other parameters as defined before in Chapter 2 under the discussion of Bimaterial Elasticity.

B. Effect of Negative K_{II}^*

Implementing the described numerical scheme into a Case 2 problem (epoxy/concrete interface separation) using the properties and loading described in Section 3.6, the following is resulted (see Appendix for input files of the finite element models):

Table 6.2 Mode Separation for Case 2

	K_I^* (MPa $\sqrt{\text{mm}}$)	K_{II}^* (MPa $\sqrt{\text{mm}}$)
Peel Fracture	35.58	-13.56
Shear Fracture	23.99	-67.52

It can be observed that even though the models are subjected to “pure mode” loadings in either the peel or shear case, the mixed mode behavior is profound as indicated by the same order K_I^* and K_{II}^* values. Another important observation here is that K_{II}^* is negative. Considering the sign convention of a small element near the epoxy/concrete interface, a negative K_{II}^* value implies crack formation in a fashion that it kinks upward toward the interface, as shown in Figure 6.6. Since K_I^* is positive, indicating an opening mode, the upward kinking is facilitated. In other words, once the crack deviates from the pre-crack location at the epoxy/concrete interface and enters the concrete substrate due to fulfillment of kink criterion as discussed above, the crack will kink back up toward the interface due to the negative K_{II}^* effect. Once that crack tip reaches the interface, the kink criterion is again fulfilled. As a consequence, the crack propagates in a zigzag fashion within the concrete substrate, but tends to stay close to the epoxy/concrete interface due to both the fulfillment of kink criterion and the effect of negative K_{II}^* , resulting in a thin layer of concrete adhering to the debonded strip for all dry cases under both peel and shear fracture configurations.

6.2.2 Locus of Fracture for Wet Specimens

When wet, all specimens exhibited a consistent interface separation mode at the epoxy/concrete interface. Since the epoxy materials had a Mode I fracture toughness in the very high range, as deduced in the last section, crack kinking was unlikely to occur into the epoxy layer. As such, the kink criterion is implemented to assess the potential of kinking into the concrete substrate. Table 6.3 summarizes the measured fracture toughness values, with the Mode I substrate fracture toughness being that of wet concrete, as determined in Chapter 4.

Table 6.3 Wet Fracture Toughness

	Γ_i (J/m ²)	Γ_s (J/m ²)
Wet Peel Fracture	~400	~20
Wet Shear Fracture	~1500	~20

This time, although the interface fracture toughness values were greatly reduced by more than half, the respective Γ_i/Γ_s ratios still indicate orders of magnitude difference compared to G_i/G'_{\max} , which is practically bounded between zero and unity. In other words, the kink criterion predicts that the interface pre-crack to kink into the concrete substrate in both cases, which is contrary to the physical observations of an apparent interface separation without evidence of concrete delamination. Since one may not argue with experimental facts and that the kink criterion is not likely to be violated in steady-state fracture (Hutchinson and Suo 1992), the apparent contradiction might be explained by an interphase layer that is either weaker than concrete (in terms of fracture) or tougher than the interface, as shown in Figure 6.7.

A. Possible Existence of Weak Interphase

With a weak interphase that exists between epoxy and concrete, fulfillment of the kink criterion would lead to the observation of the parent crack kinking out of the interface and enters the interphase layer. Once the crack is inside the interphase, the crack may either continue to propagate toward the interphase/concrete interface or kink back up toward the epoxy/interphase interface due to the negative K_{II}^* effect. Assuming that the interphase is weaker in fracture sense than the underlying concrete, the kink criterion will indicate that the interphase crack will tend to stay within the layer. As a result, the crack propagates within the interphase layer in a zigzag fashion, bounded by the interfaces of the epoxy/interphase and the interphase/concrete. Since this layer could be relatively thin, naked eyes might not be able to detect crack propagations within such a layer and the observers would have believed that an apparent interface separation has taken place.

B. Possible Existence of Tough Interphase

Another possibility would be due to the formation of a tough interphase material as a result of moisture ingress. Should this interphase possess a Mode I fracture toughness in the same order or even higher than that of the epoxy/concrete interface, kinking would not occur, according to the kink criterion. The interface pre-crack would propagate continuously along that interface until complete debonding. Given the fact that Epoxy 2 is a liquid epoxy system that possesses very good wetting ability, the material could have diffused into the adjoining top layer of the porous concrete. As a consequence of moisture ingress, that epoxy/concrete mix could well be toughened by epoxy plasticization, forming an interphase that possesses a fracture toughness value even higher than that of the interface itself.

C. Possible Non-Existence of Interphase

Epoxy 1 specimens, on the other hand, are not likely to have such formation of tough interphase due to the special 100% solids formulation. Wetting ability is particularly poor and diffusion into the top surface layer of concrete forming an interphase is deemed unlikely. As a result, it has prompted one to rationalize the possible non-existence of an interphase altogether. Now that moisture ingress takes place and water can diffuse into the bond line interface, it might be possible for certain condensation to occur between the two solids, namely epoxy and concrete, both of which are porous. Since water has theoretically an infinite fracture toughness value, a layer of water between the epoxy and concrete materials would lead to the non-fulfillment of the kink criterion, hence an interface separation mode, hence satisfying the experimental fact and the kink criterion prediction. In any case, validation of these interphase layer concepts requires further studies that extend into the field of materials science and engineering.

6.3 Plasticity in the Debonding Process

Finally, one would be able to do a first order estimate of the amount of plasticity and 2nd order energy dissipation mechanisms that are involved in the debonding process under both the peel and shear configurations. This can be carried out by comparing the

linear elastic tri-layer interface fracture toughness with the appropriate areas under curves obtained directly from the experiments, from which the fracture toughness values are estimated by:

$$\Gamma = \frac{\Delta A}{B \cdot da}$$

which is the fundamental definition of fracture energy release rate. Here, ΔA represents the area enclosed by the proper sets of loading and unloading curves, B the width of the bond, and da the length of crack advance. Figures 6.8 and 6.9 illustrate the idealization of the load-deformation curves, the respective definition of ΔA (indicated as shaded areas in the idealized plots), and the correlation plots between the method of fracture energy formulation and the method of area.

For the case of peel fracture, excellent correlation is demonstrated, indicating that the peel fracture process is mainly a linear elastic one. In fact, this is demonstrated in the level of loading (in the N range) as well as from the linear shape of the loading curves.

For the case of shear fracture, on the other hand, the linear elastic formulation shows a general underestimation of the fracture toughness. This signifies that more energy dissipation mechanisms exist. Examining the critical load level involved (in the kN range) reveals that the materials limits are in close proximities and hence non-linearity and plasticity can arise. Some of such mechanisms can be due to microcracking of concrete, crazing and shear banding of toughened epoxies, and local plasticity resulted from mechanical interlocks at asperities of the bond.

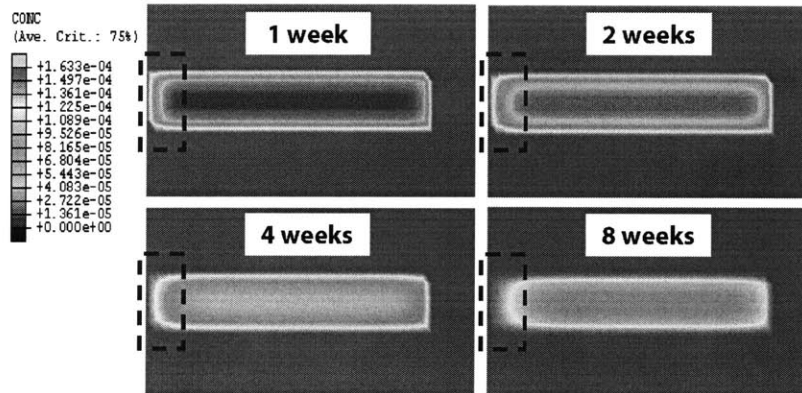
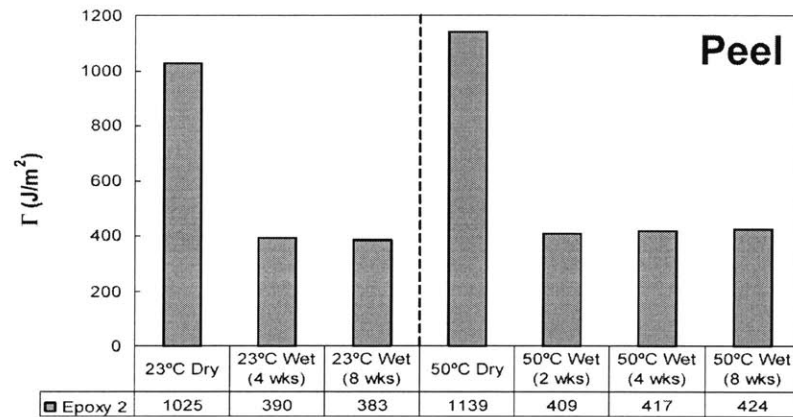


Figure 6.1 Correlation of Moisture Concentration in the Peel Fracture Region

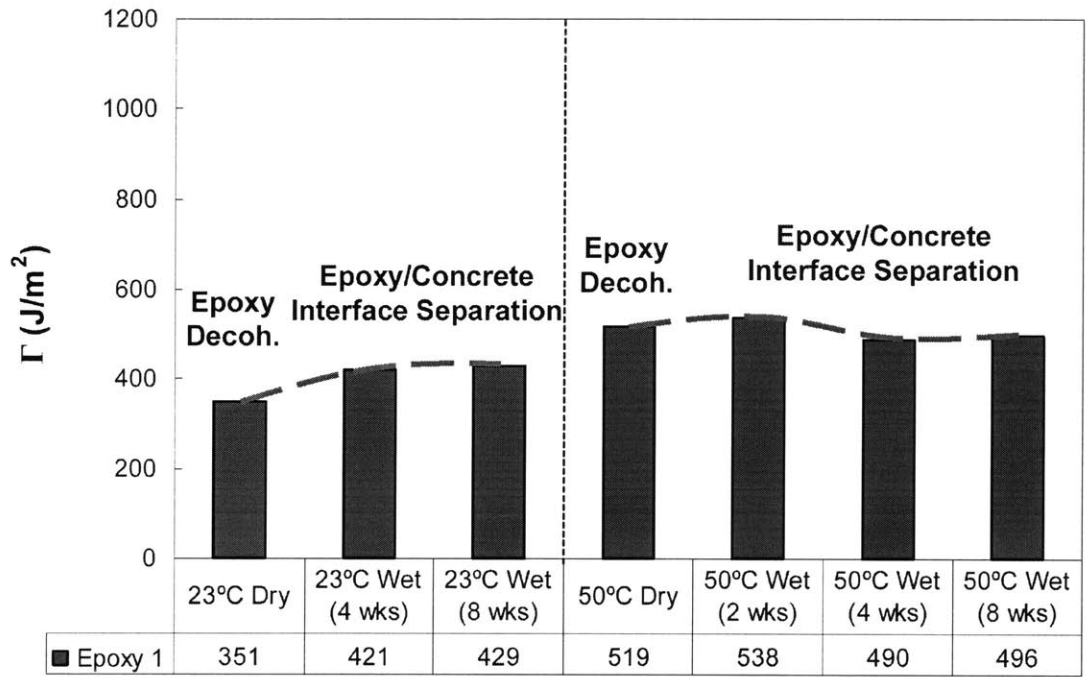


Figure 6.2 Atypical Variation of Epoxy 1 Peel Fracture Toughness

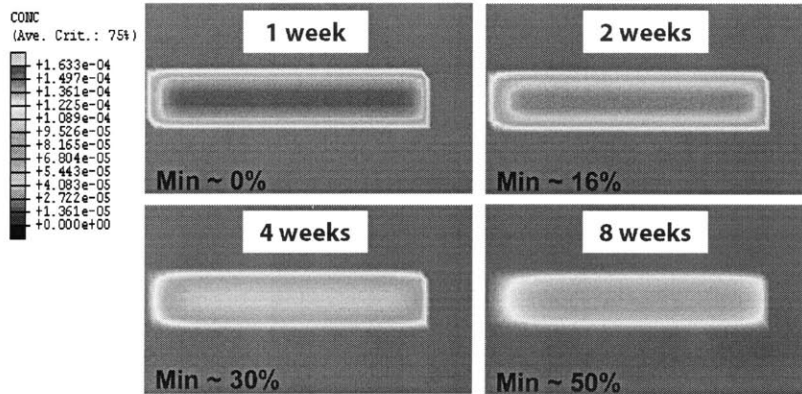
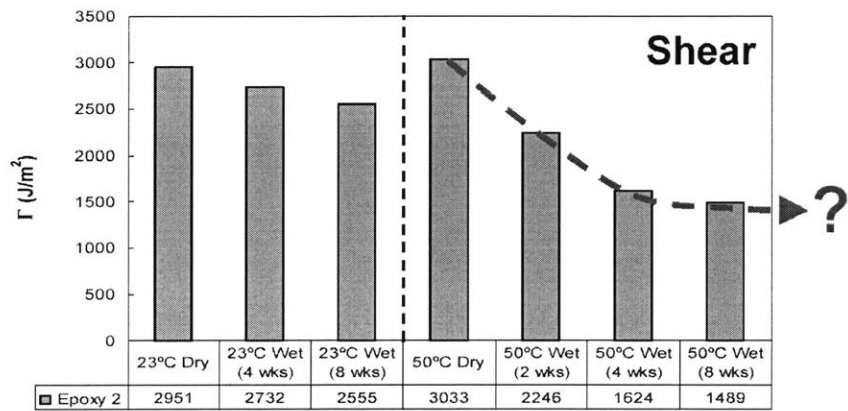


Figure 6.3 Correlation of Moisture Concentration in the Shear Fracture (Bond) Region

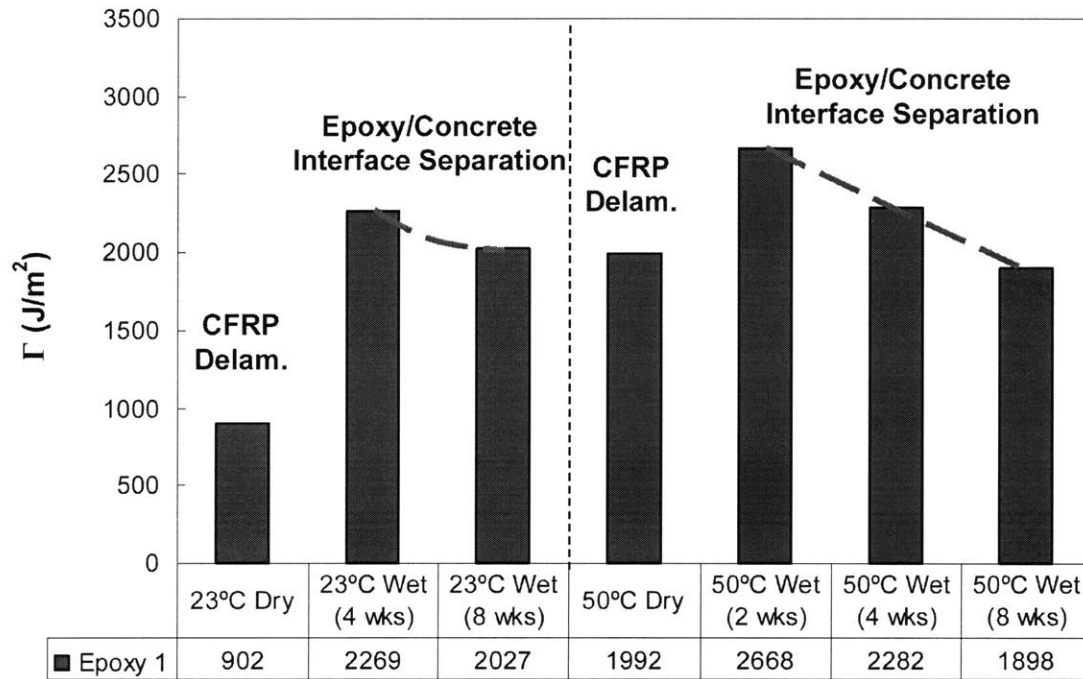


Figure 6.4 Atypical Variation of Epoxy 1 Shear Fracture Toughness

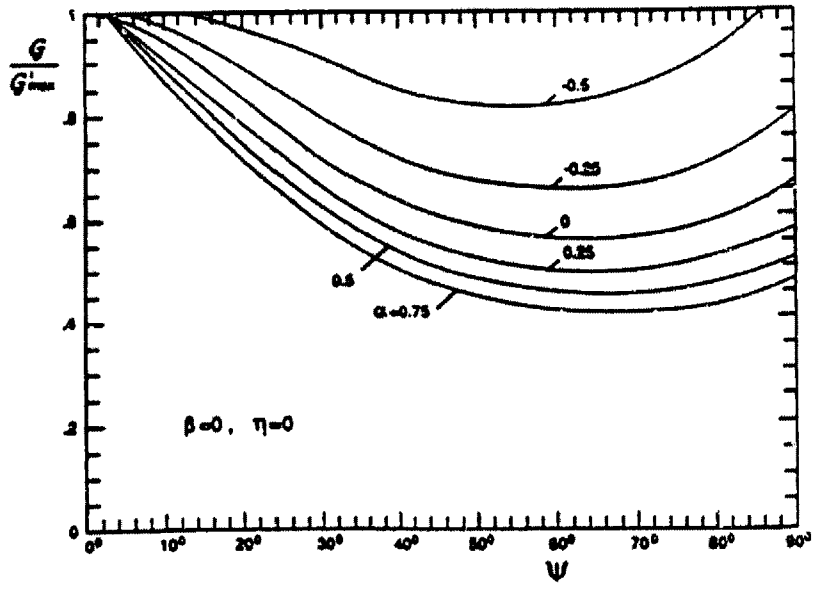


Figure 6.5 Variations of Fracture Energy Release Rate Ratios with Phase Angle (Hutchinson and Suo 1992)

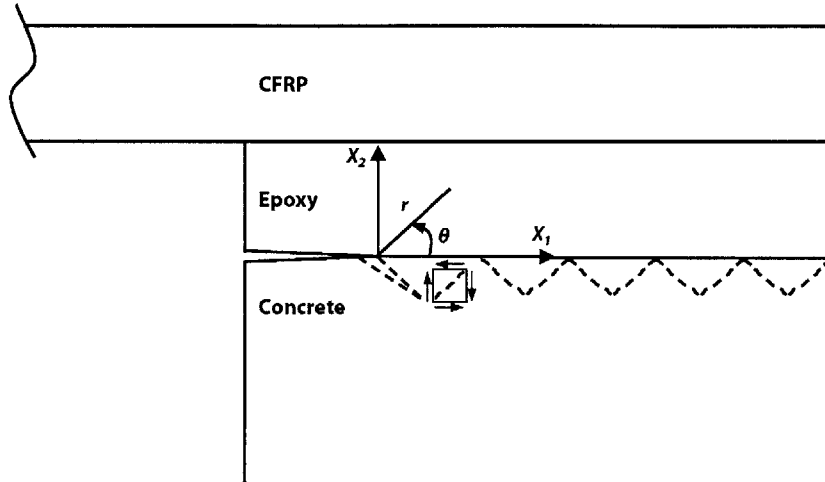


Figure 6.6 Effect of Negative K_{II}^*

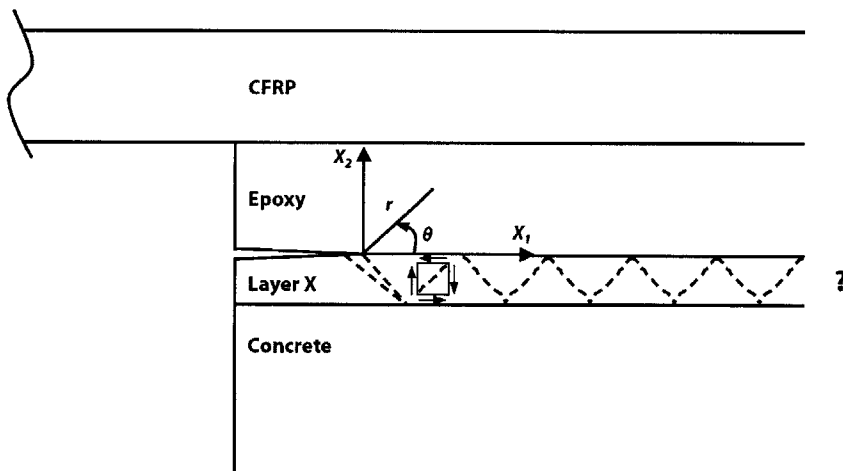


Figure 6.7 Possible Existence of Interphase between Epoxy and Concrete

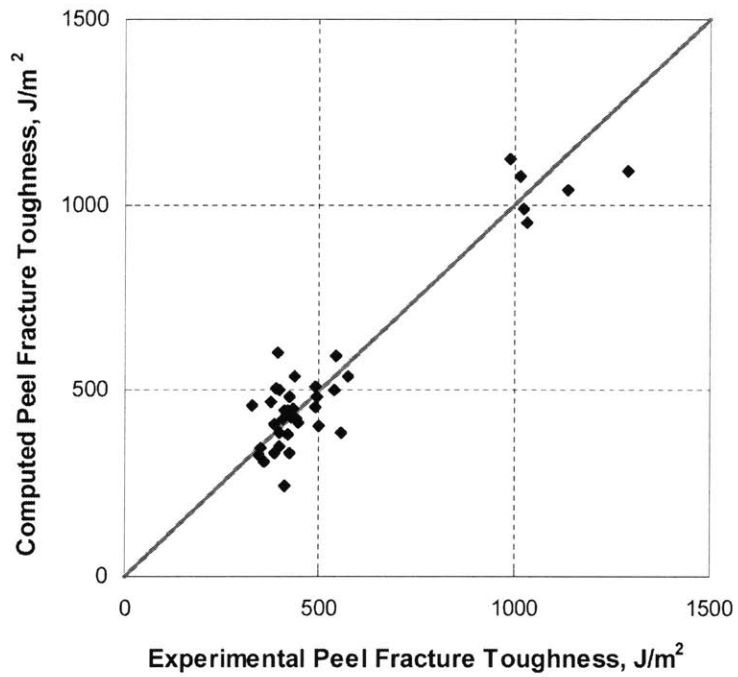
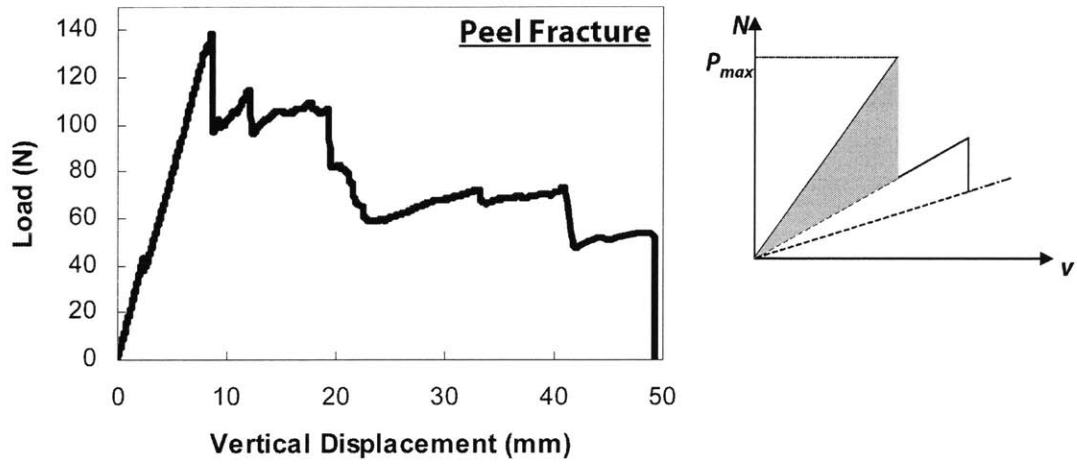


Figure 6.8 Correlation of the Peel G Model

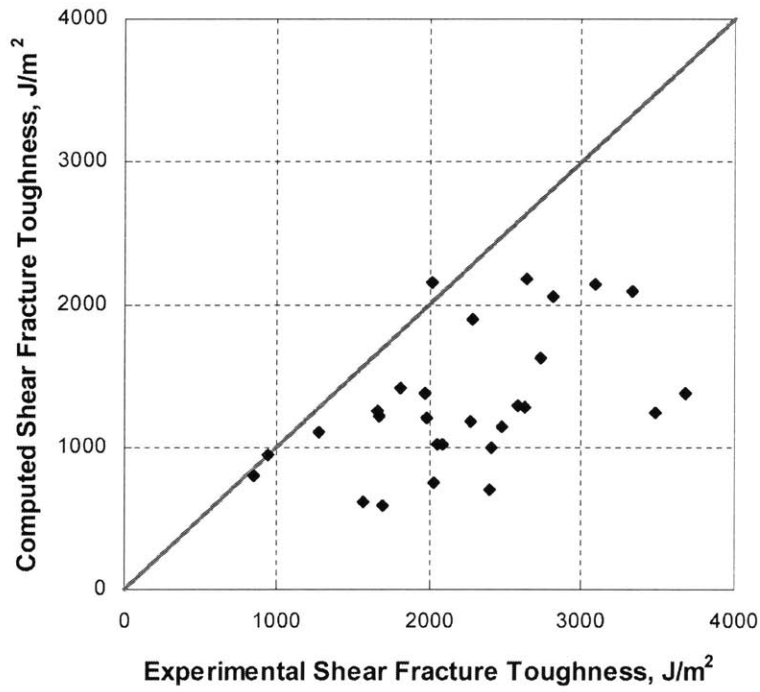
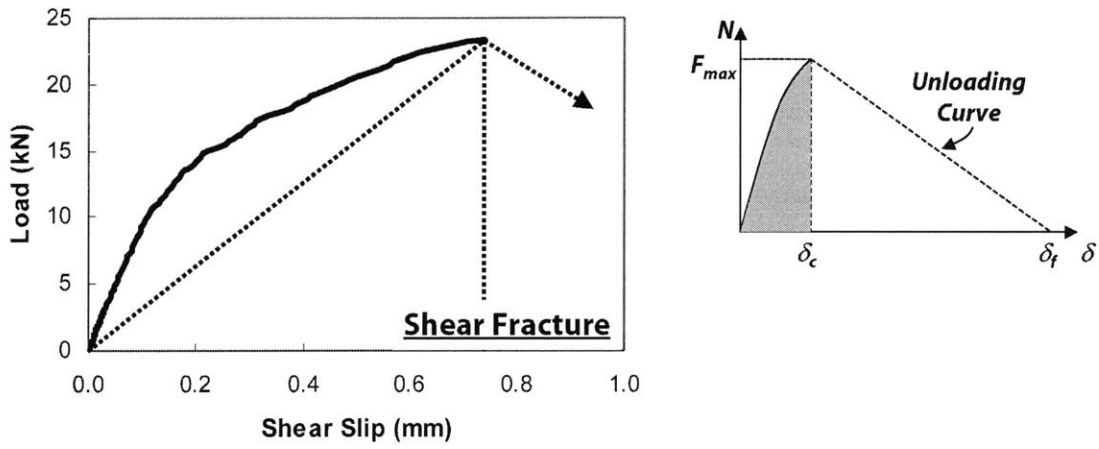


Figure 6.9 Correlation of the Shear G Model

CHAPTER 7

SUMMARY, CONCLUSION, & FUTURE WORK

Bonding of FRP laminates to concrete beams and slabs for flexural strengthening and repair has become a widespread practice in the construction industry in the past decade due to the advantageous mechanical properties, lightness, corrosion resistance, and decreasing cost of the composite materials, especially that of carbon FRP. While short-term mechanical and failure behaviors of such retrofitted systems have been studied and understood to a point that construction specifications were recently made available by ACI and NCHRP, long-term performance and durability issues with respect to the effects of moisture ingress, thermal cycles, freeze-thaw actions, and coupling of environmental and mechanical loading remain largely uncertain and unanswered. Although the advanced composites themselves could be durable against the various degradation effects, the bonded system as a whole would usually possess a lower resistance to the same environments due to the existence of interfaces, property mismatch between adjoining materials, and the presence of discontinuities which give rise to extra

paths of contamination and fracture, additional failure mechanisms, adhesion problems, residual stress development, and stress concentrations.

In particular, little understanding has been developed regarding the effect of moisture on the stability and bond properties of these FRP retrofitted concrete systems that may govern the lifecycle and effectiveness of the retrofit itself. Realistically, moisture could diffuse into the interfacial bond region through the adjoining concrete, existing crack mouths, and around the bond lines. Once moisture is trapped in the region, it could be difficult to recover the dryness due to the nature of the materials and the bond configurations. The retained moisture could then lead to bond deterioration and premature debonding could occur at an even earlier stage as a result of adhesion impedance and possible interphase formation.

The research documented in this dissertation represents an early attempt to develop mechanistic understanding of moisture affected debonding failures in carbon FRP bonded concrete that simulate the possible debonding scenarios from within the retrofit span in a flexurally retrofitted concrete system under moisture attack.

7.1 Research Approach

To achieve the research objective, an interface fracture approach is adopted to examine the moisture affected debonding problem. Central to the investigation is the interface fracture toughness parameter being the quantification parameter that is used to analyze, compare, and correlate the observed behavior. Owing to the inherently thick epoxy bond line, a new tri-layer fracture energy model is developed in order to provide a viable means to describe the five possible debonding scenarios of which two being interface separation and three being material decohesion in a FRP-epoxy-concrete retrofitted system.

Debonding characterization is conducted using mesoscale peel and shear fracture models that are manufactured using real-scale bond lines. These physical models are subjected to accelerated hygro-thermal conditioning to achieve various levels of moisture content in the interfacial bond region. The conditioned samples are then mechanically tested at selected time intervals in standard laboratory conditions so that the change in bond fracture toughness and debonding behavior with respect to time or moisture content

can be captured. Moisture concentration in the bond region for the selected time intervals are assessed by means of 3-D finite element diffusion simulations, of which the required input of diffusion properties (i.e. diffusivity and solubility) for each constituent materials are determined physically by moisture uptake tests. Mechanical property variations of these materials with respect to moisture uptake that correspond to the level of moisture concentration of the bonded system are also determined by ASTM tests in order to properly compute the interface fracture toughness of the bond at the given point in time.

With the experimentally determined fracture toughness values, moisture diffusion information from finite element simulations, and observed debonding failure modes, interface fracture analysis is performed to determine the role of moisture in the debonding process, and to understand the associated mechanistic debonding fracture behavior.

7.2 Summary of Research Results

7.2.1 Tri-Layer Interface Fracture Model Development

FRP debonding has been empirically shown to be a highly complex phenomenon that can involve failure propagation within the concrete substrate, inside the adhesive, FRP delamination, FRP/epoxy interface separation, and epoxy/concrete interface separation, totaling five distinct debonding modes, although the latter two have not been discovered until recently and from this current work. These many different failure modes are partly attributed to the fact that the adhesive bond line thickness is relatively large and such a tri-layer interface fracture model that contains parametrically the material and geometric information of such bonded system is needed.

Using the linear elastic assumption and energy arguments as suggested by Hutchinson (1996), the steady-state total interface fracture energy release rate, G , is obtained by evaluating the difference in strain energy density far behind and far ahead of the crack tip. Due to its steady-state nature, the parameter is independent of the initial crack length. With the use of the classical beam theory, the full set of tri-layer G model solutions are developed for five idealized plain-strain debonding cases, which correspond to the five debonding modes observed empirically. These newly derived models represent an extension of those bi-layer models developed earlier by Hutchinson and Suo (1992)

and they contain fairly general boundary conditions at the edges (i.e. stretching and bending), making them applicable to many different classes of fracture problems that involve a tri-layer material structure.

In particular, the derived models are specialized to describe peel and shear debonding fracture. The specialized fracture models are used to compute the interface fracture toughness of the fracture samples loaded under peel and shear configurations. This computation also represents a conversion of strength data obtained from tests to fracture parameters used for analysis. The specialized models are then verified using the finite element method by comparing the interface G values. Excellent agreements are obtained.

7.2.2 Constituent Material Characterization

Constituent materials are tested for their property variation under the influence of accelerated moisture ingress. Acceleration is facilitated by means of continuous conditioning and elevated temperature. Moisture uptake behavior of each of the three constituent materials is first studied. It is determined that elevated temperature will increase the rate of moisture diffusion, which is represented by the moisture diffusion coefficient. Concrete is found to possess the highest rate of diffusion, followed by CFRP and then epoxy. Solubility (or saturated moisture content) of concrete is close to 8% by weight regardless of conditioning temperature, while that for epoxy and CFRP is respectively 1 - 6% and 0.3 - 0.9%, depending on the temperature at which moisture diffusion takes place.

Thermal analysis through dynamic mechanical analysis (DMA) has shown that the two ambient-cured structural epoxy systems tested possessed an initial glass transition temperature in the low 50s (°C), and can be lowered with increasing moisture intake. In view of the fact that the epoxies are developed for structural applications, the glass transition point is defined by the drop in storage modulus as opposed to some other definitions that are associated with the loss modulus or tan-delta that are used widely in the polymer research community. The asymptotic values for the two epoxies are found to be in the low 40s (°C), which can be practically achieved in a concrete beam soffit. High temperature conditioning, however, can give rise to a post-curing effect, which will raise

the asymptotic glass transition point and compete with the moisture degradation effect. It is also determined from DMA plots that the ambient-cured structural epoxy systems does not possess enough thermal stability simply by ambient curing. Prolonged elevated temperature post-curing is found to be able to remove such instability and a repeatable DMA curve can be produced.

Mechanical tests on moisture conditioned material samples reveal that moisture is generally detrimental to their strength and stiffness, and at times at alarming levels (e.g. 50% reduction). In the case of concrete, fracture toughness is also significantly reduced while for epoxies, plasticization can occur due to wetness, which leads to substantial increase in tensile failure strain, implying a possible increase in fracture toughness.

7.2.3 3-D Moisture Simulation

Three-dimensional moisture diffusion simulation is performed to understand and quantify the moisture diffusion behavior in the interfacial bond region, by means of the finite element method. A discretized mathematical model is built following the fracture specimen geometric configurations. 3-D diffusion elements are used and the solution technique is based on Fick's 2nd Law of Diffusion. Diffusivity and solubility that are experimentally determined in the material characterization program are used as inputs in the finite element computation. Temperature effect is incorporated with the use of the proper set of temperature-dependent diffusion parameters, without resorting to solving the coupled differential equation that involves both temperature and mass diffusion. This is justified by the fact that moisture diffusion takes place at a constant temperature for the problem at hand. In other words, the moisture diffusion process in the specimens is only driven by concentration gradient. The model is initially dry everywhere except the outer surfaces are subjected to an instantaneous wetness that represents a fully saturated condition, simulating the submergence of the specimen into a water bath.

Simulation results show that moisture can migrate from all directions with particularly high rate from the concrete substrate due to its relatively high diffusivity and solubility. Symmetric diffusion is noted about the longitudinal axis of the bond and asymmetry is observed about the centerline of the bond due to uneven amount of moisture diffusing from the exposed concrete faces. Due to significant concentration

gradient between the exposed surfaces and the dry core, moisture tends to migrate into the thicker and high-solubility concrete at the beginning of the diffusion process. In 8 weeks, the minimum moisture concentration at the epoxy/concrete interface will have reached about 50% of the equilibrium value. The entire bond interface will be saturated in about 200 days. Note however that the entire model is not yet saturated due to the fact that the concrete core can continue to absorb moisture even after the bond interface saturation as a consequence of the high solubility of the concrete material, although the diffusion process has slowed down because of the reducing moisture concentration gradient with increasing time.

7.2.4 Interface Fracture Characterization

Interface fracture tests are performed in the peel and shear loading configurations. Results showed that moisture can initially enhance or reduce the fracture toughness of the bond, depending on the epoxy formulation being used. The initial fracture toughness can be accompanied by various debonding modes, ranging from concrete delamination, to epoxy decohesion, to FRP delamination, depending on the epoxy system. Regardless, these failure modes all belong to material decohesion.

With increasing moisture ingress, nevertheless, interface fracture toughness tends to decrease over time and an asymptotic behavior can be achieved. The asymptote is formed in as short as 2 weeks for peel fracture while that for shear fracture appears to be more gradual and does not show sign until after 8 weeks time. The accompanied fracture toughness mode is also shifted from a material decohesion mode to epoxy/concrete interface separation, which has been considered unlikely to occur before, but is consistently observed for the first time in all wet specimens in this research study. 3-D moisture diffusion simulation suggested that the asymptotic behavior is associated with a moisture concentration threshold at the epoxy/concrete interface that is in the proximity of 50% of saturation.

Finite element fracture analysis combined with M-integral implementation have shown that both peel and shear debonding fracture consist of a positive K_I^* (opening mode) and a negative K_{II}^* (shearing mode) component at the crack tip vicinity. The

implication of a negative K_{II}^* on the locus of fracture in dry specimens that involve concrete delamination is that the crack tends to stay close to the fracture interface and will not continuously penetrate into the concrete substrate after the crack kinking criterion is initially satisfied. Once the crack kinks into the concrete substrate away from the epoxy/concrete interface where the pre-crack is introduced, the negative K_{II}^* effect will drive the crack back up to the interface. This continual zigzag locus as the crack advance to complete the debonding will thus produce an apparent parallel crack development, forming a thin layer of concrete adhering to the debonding strip.

In the case of wet specimens, the kink criterion still predicts that concrete delamination will have occurred, which apparently violated the physical observation of the epoxy/concrete interface separation mode. Interface fracture mechanics arguments suggested that this contradiction may be attributed to either an interface weakening or toughening mechanism that is associated with the possible existence of an interphase layer, depending on the epoxy systems being used. Interphase may be formed, for instance, even before any moisture ingress, due to the penetration of the low viscosity epoxy into the porous concrete substrate. Such a pre-existing interphase will undergo changes in fracture toughness as a result of moisture ingress, possibility toughening up due to plasticization effects of the epoxy phase. However, such interphase pre-formation is unlikely for the other highly viscous solid epoxy system and thus any interfacial toughening is improbable. One may be able to explain the epoxy/concrete interface separation phenomenon for such high viscosity epoxy systems by considering the interface moisture condensation as an extra material layer with infinite fracture toughness that existed between the epoxy and the concrete layers. The physical meaning of an infinite fracture toughness of moisture is that the epoxy/concrete pre-crack cannot penetrate through the water layer as the “material” flows to resist fracture within the water layer. Hence, the pre-crack has to continue to develop and propagate along the epoxy/concrete interface until debonding is complete. These aspects, however, need to be further studied by testing and analysis.

7.3 Conclusion

This research has demonstrated that moisture is a detrimental environmental agent that can degrade the integrity of a FRP bonded concrete system as well as the mechanical properties of its constituent materials. Moisture degradation in FRP bonded concrete is found to be a highly complex phenomenon that involves changes in failure loads, debonding modes, and interfacial properties. These changes seem to depend heavily on the type of epoxy used and it is becoming clear that the knowledge of the exact chemical composition of such epoxies is required to develop full understanding of the degradation process and mechanics.

Interface fracture mechanics has proved to be a very useful approach to quantify and analyze the debonding problem, especially in logging the behavioral changes with the use of the interface fracture toughness parameter. Compared to the more popular strength-based approaches, the interface fracture approach quantifies the layered material system with respect to the bond property of a real scale bond line. The bond property is highly transferable and can be used directly in FRP retrofit design using a fracture approach analogous to material property in conventional beam design using a strength approach. With the newly developed tri-layer interface fracture model, the five possible debonding scenarios can be more precisely and accurately described and quantified for the first time.

While material decohesion has been observed in dry specimens, epoxy/concrete interface separation has been observed in wet specimens consistently for the first time. This phenomenon is observed for both peel and shear fracture specimens and is accompanied by a moisture concentration threshold that can be as low as half of the moisture saturation level. Identical observation of failure modes is attributed to the fact both fracture processes consist of a similar mixed-mode stress states, although with different magnitudes for each mode. Within 2 weeks, the degradation asymptote can be reached for peel fracture to occur while in roughly 8 weeks, shear fracture degradation can be maximized. Interface fracture analysis has suggested the possible existence of an interfacial toughening or weakening mechanism as a consequence of moisture diffusion. Interphase formation is found to be possible and warrants further in-depth investigation

for verifications. Using a similar interface fracture analysis, an explanation has been offered the first time to the concrete delamination mechanics behavior.

Before further understanding has been developed regarding how moisture degradation can be mitigated in a FRP bonded concrete system, moisture is to be avoided at all cost in such retrofitted structures that have been designed in accordance to specifications developed based on short-term tests.

7.4 Contributions

As one of the early attempts to characterize the moisture affected debonding behavior of FRP-bonded concrete system under peel and shear fracture loading, the following contributions have been made:

- Devised a robust fracture-based research methodology for quantifying the debonding behavior in a multi-layer retrofitted system
- Developed a new set of fracture energy solutions that can precisely quantify debonding as a tri-layer problem
- Developed new knowledge and data on material deterioration due to moisture and temperature
- Developed new fracture toughness data on debonding due to moisture and temperature
- Discovered a new debonding mode of epoxy/concrete interface separation that can be observed consistently
- Developed new mechanistic understanding of FRP bonded concrete regarding how they fail as a function of moisture uptake by means of interface fracture analysis
- Discovered the physical phenomenon of moisture concentration threshold that would lead to asymptotic degradation of the bond

It is also believed that this thesis research will directly impact professional practice, as the findings have formed the basis for future analysis directions and development of design guidelines.

7.5 Future Work

This research work has developed the foundation, based on interface fracture mechanics, to investigate moisture affected debonding in FRP retrofitted concrete systems with respect to the materials and mechanics understanding of the problem. Now that interface fracture analysis has suggested the possible existence of an interfacial toughening or weakening mechanism as a result of moisture ingress, the first step would be to verify the existence of interphase using several different epoxy systems. To verify the formation of interphase, one might conduct a series of reversibility tests after the specimens are moisture conditioned continuously at selected durations. By recovering the dryness at the interface, any deviation from the initial fracture toughness values would indicate permanent damages done to the interfacial region as a result of new interphase formation due to moisture ingress. However, a full recovery of fracture toughness should not preclude the existence of interphase formation due to the fact that epoxy properties are sometimes reversible upon drying. This, nevertheless, could be studied by performing a scanning electron microscopy analysis by looking at the fracture surface to examine the possible interphase formation.

After understanding has been gained upon the interfacial material changes, moisture cyclic (wet-dry cycles) tests can be performed to examine the accumulative effects of moisture ingress and egress on the debonding mode and resistance of the retrofitted system. The cyclic threshold proximity that would produce the most damage, beyond which the interface fracture toughness values do not further reduce, could also be determined. A cyclic model analogous to the Paris' law in case of fatigue characterization can be developed using fracture toughness in place of crack length. The cyclic moisture conditioning tests represents an extension of the continuous moisture conditioning and subsequent drying beyond one cycle. Duration of each moisture ingress and egress cycle can be determined based on three-dimensional moisture diffusion along with the observation of moisture concentration threshold that produces maximum toughness degradation.

These aforementioned studies could also be coupled with the effect of sustained load to simulate real-life service conditions. Various levels of load that are in the proximity of the asymptotic values determined from the previous tests can be used. Any

crack propagation activity and possible viscoelastic behavior (due to the elevated temperature conditioning) during the coupling can be closely monitored. Intact specimens will then be taken out to test for residual debonding resistance. To model the possible viscoelastic effects, the tri-layer fracture energy model can be extended to cater to viscoelasticity description of the bond line. Viscoelastic fracture consideration could be very critical in the case of FRP retrofitted concrete systems due to the fact that the glass transition temperature of such ambient-cured epoxies is in close proximity of the real-life service temperature. With the viscoelastic fracture model in hand, time-dependence of the debonding process can then be estimated.

Having developed understanding and quantification of the debonding problem under various moisture effects, a correlation study by means of fracture mechanics principles, finite element parametric simulation, and physical validation tests, can be performed to draw links between the debonding observed in fracture tests at the meso-level to the debonding in large-scale FRP retrofitted RC beams under common loading configurations. The thrust of this study is based upon the fact that interface fracture in the form of debonding is a local phenomenon. With identical or similar interfacial stress states in the crack proximity, the debonding response to external load should remain similar regardless of the specimen geometry and size, be it at the mesoscale or the structural scale. By proper modeling of a pre-crack in the finite element retrofitted beam model, the interfacial stress states can be directly correlated with the externally applied load at a range of magnitudes for different loading cases. By determining the interface fracture toughness of a given retrofit bond as a bond property, the debonding initiation load of the retrofitted beam may be estimated from the correlation curves. One might therefore make use of experimentally determined bond properties to design a FRP retrofit beam system against debonding, analogous to making use of material properties to design a beam against ultimate failure strength.

BIBLIOGRAPHY

ACI 440F. (2000), *Guide for the Design and Construction of Externally Bonded FRP Systems for Strengthening Concrete Structures*, ACI Committee 440-F Draft Document, American Concrete Institute, Detroit.

Adamson, M.J. (1980), *J. Mater. Sci.*, 15, 1736.

Aiello, M.A., Frigione, M., and Acierno, D. (2002), “Effects of Environmental Conditions on Performance of Polymeric Adhesives for Restoration of Concrete Structures”, *Journal of Materials in Civil Engineering*, Vol.14, No.2, pp.185-189.

Alfrey, A., Gurnee, E.F., and Lloyd, W.G. (1966), *Journal of Polymer Science*, Vol.C12, pp.249.

Ali, M.S.M., Oehlers, D.J., and Bradford, M.A. (2001), “Shear Peeling of Steel Plates Adhesively Bonded to the Sides of Reinforced Concrete Beams”, *Proceedings of the Institution of Civil Engineers, Structures and Buildings*, Vol.140, pp.249-259.

Allanson, R. Westland Aerospace, private communication.

Amer, M.S., Koczak, M.J., and Schadler, L.S. (1995), *Comp. Interfaces*, 3, 41.

Antoon, M.K. and Koenig, J.L. (1980), *Journal of Macromolecular Science – Reviews of Macromolecular Chemistry*, C19(1), pp.135.

Apicella, A. and Nicolais, L. (1981), *Ind. End. Chem. Prod. Res. Dev.*, 20, 138.

- Apicella, A., Migliaresi, C., Nicolais, L., Iaccarino, L., and Roccotelli, S. (1983), *Composites*, 14, 387.
- Apicella, A., Nicolais, L., and Carfagna, C. (1981), "The Role of the Polymeric Matrix", *Processing and Structural Properties of Composite Materials*, Seferis, J.C. and Nicolais, L., (Editors), Plenum Press, New York.
- Apicella, A., Nicolais, L., and Cataldis, C. (1985), *Adv. Polym. Sci.*, 66, 189.
- Apicella, A., Nicolais, L., Mikols, W.J., and Seferis, J.C. (1984), *Interrelations between processing structure and properties of polymeric materials*, Seferis, J.C. and Theocaris, P.S., (Editors), Elsevier: Amsterdam, pp.629.
- Armstrong, K.B. (1996), "Effect of Absorbed Water in CFRP Composites on Adhesive Bonding", *Int. J. Adhesion and Adhesives*, 16, pp.21-28.
- Asada, T. and Onogi, S. (1963), *J. Colloid, Sci.*, 18, 784.
- Ascione, L. and Feo, L. (2000), "Modeling of Composite/Concrete Interface of RC Beams Strengthened with Composite Laminates", *Composites: Part B*, 31, pp.535-540.
- Ashby, M.F. and Jones, D.R.H. (1980), *Engineering Materials 1 – An Introduction to their Properties and Applications*, Pergamon Press.
- ASTM C192, "Standard Test Method for Making and Curing Concrete Test Specimens in the Laboratory", *ASTM International*.
- ASTM C39, "Standard Test Method for Compressive Strength of Cylindrical Concrete Specimens", *ASTM International*.
- ASTM C496, "Standard Test Method for Splitting Tensile Strength of Cylindrical Concrete Specimens", *ASTM International*.
- ASTM C882, "Standard Test Method for Bond Strength of Epoxy Resin Systems Used with Concrete by Slant Shear", *ASTM International*.
- ASTM D3039, "Standard Test Method for Tensile Properties of Polymer Matrix Composite Materials", *ASTM International*.
- ASTM D570-98. (1998), "Standard Test Method for Water Absorption of Plastics", *ASTM International*.
- ASTM D638-02. (2002) "Standard Test Method for Tensile Properties of Plastics", *ASTM International*.

- ASTM D732-02. (2002) "Standard Test Method for Shear Strength of Plastics by Punch Tool", *ASTM International*.
- ASTM E104-85. (1991), *Annual Book ASTM Stand*, Part 14, pp.85-87.
- ASTM E1640-99. (1999) "Standard Test Method for Assignment of the Glass Transition Temperature by Dynamic Mechanical Analysis", *ASTM International*.
- Baker, A.A. and Jones, R. (Editors). (1988), *Bonded Repair of Aircraft Structures*, Martinus Nijhoff.
- Barbero, E.J. (1998), *Introduction to Composite Materials Design*, Taylor & Francis, Inc.
- Barger, J.D. (2000), Effects of Aging on Bond Between FRP and Concrete, MS Thesis, West Virginia University, Department of Civil Engineering.
- Barral, L., Cano, J., Lopez, J., Lopez-Bueno, I., Nogueira, P., Abad, M.J., Torres, A., Ramirez, C. (2000), *J. Appl. Polym. Sci.*, 77, 2305.
- Barral, L., Cano, J., Lopez, J., Nogueira, P., Abad, M.J., and Ramirez, C. (1997), *J. Therm. Anal.*, 50, 409.
- Barral, L., Cano, J., Lopez, J., Nogueira, P., Ramirez, C., and Abad, M.J. (1998), *J. Therm. Anal.*, 52, 823.
- Barrie, J.A. (1968), *Diffusion in Polymers*, Crank, J. and Park, G.S. (Editors), Academic Press: New York, pp.259.
- Barton, S.J. and Prutchard, G. (1994), *Polym. Adv. Technol.*, 5, 245.
- Bascom, W.D. and Cottingham, R.L. (1976), *J. Adhes.*, 7, 333.
- Bazant, Z.P. and Kaplan, M.F. (1996), *Concrete at High Temperatures – Material Properties and Mathematical Models*, *Concrete Design and Construction Series*, Longman Group Limited.
- Bazant, Z.P. and Prat, P.C. (1988), "Effect of Temperature and Humidity on Fracture Energy of Concrete", *ACI Materials Journal*, Jul-Aug, pp.262-271.
- Bazant, Z.P. (1984), "Size Effect in Blunt Fracture: Concrete, Rock, and Metal", *Journal of Engineering Mechanics*, ASCE, Vol.110, No.4, Apr., pp.518-535.
- Bazant, Z.P. (1985), "Fracture in Concrete and Reinforced Concrete", *Mechanics of Geomaterials: Rocks, Concrete, Soils*, John Wiley & Sons, Chichester, pp.259-304.

- Bazant, Z.P. (1985), "Fracture Mechanics and Strain-Softening of Concrete", Preprints, *U.S.-Japan Seminar on Finite Element Analysis of Reinforced Concrete Structures*, Japan Society for the Promotion of Science, Tokyo, May 1985, pp.71-92.
- Bazant, Z.P. (1987), "Fracture Energy of Heterogeneous Materials and Similitude", Preprints, *International Conference on Fracture of Concrete and Rock* (Houston, June 1987), Society of Experimental Mechanics, Bethel, pp.390-402.
- Bazant, Z.P., Sener, S. and Prat, P.C. (1986), "Size Effect Tests of Torsional Failure of Concrete Beams", *Report No. 86-12/428s*, Center for Concrete and Geomaterials, Northwestern University, Evanston.
- Bazant, Z.P. and Cao, Z. (1987), "Size Effect in Punching Shear Failure of Slabs", *ACI Structural Journal*, Vol.84, No.1, pp.44-53.
- Bazant, Z.P. and Oh, B.H. (1983), "Crack Band Theory for Fracture of Concrete", *Materials and Structures, Research and Testing* (RILEM, Paris), Vol.16, No.93, pp.155-177.
- Bazant, Z.P. and Panula, L. (1978), "Statistical Stability Effects in Concrete Failure", *Proceedings*, ASCE, Vol. 104, EM5, pp.1195-1212.
- Bazant, Z.P. and Pfeiffer, P.A. (1986), "Shear Fracture Tests of Concrete", *Materials and Structures, Research and Testing* (RILEM, Paris), Vol.19, No.110, pp.111-121.
- Bazant, Z.P. and Prat, P.C. (1988), "Effect of Temperature and Humidity on Fracture Energy of Concrete", *ACI Materials Journal*, Title no. 85-M32.
- Bazant, Z.P. and Thonguthai, W. (1978), "Pore Pressure and Drying of Concrete at High Temperature", *Proceedings*, ASCE, Vol.104, EM5, pp.1059-1079.
- Bazant, Z.P. and Kim, J.K. (1984), "Size Effect in Shear Failure of Longitudinally Reinforced Beams", *ACI JOURNAL, Proceedings*, Vol.81, No.5, pp.456-468.
- Bazant, Z.P., Kim, J.K., and Pfeiffer, P.A. (1984), "Determination of Nonlinear Fracture Parameters from Size Effect Tests", NATO Advanced Research Workshop on Application of Fracture Mechanics to Cementitious Composites, Northwestern University, Evanston, pp.143-169.
- Bazant, Z.P., Kim, J.K., and Pfeiffer, P.A. (1986), "Nonlinear Fracture Properties from Size Effect Tests", *Journal of Structural Engineering*, ASCE, Vol.112, No.2, pp.289-307.

- Beck Tan, N., McKnight, S.H., and Palmese, G.R. (1997), Proceedings of the American Chemical Society --- Division of Polymeric Materials: Science and Engineering , Vol.77, pp.640-641.
- Biro, D.A., Pleizier, G., and Deslandes, Y. (1993), *Compos. Sci. Technol.*, 46, 293.
- Bizindavyi, L. and Neale, K.W. (1999), "Transfer Lengths and Bond Strengths for Composites Bonded to Concrete", *Journal of Composites for Construction*, Vol.3, No.4, pp.153-160.
- Bland, D.R. (1960), *The Theory of Linear Viscoelasticity*, Pergamon Press.
- Boerio, F.J. and Hong, P.P. (1990), *Mater. Sci. Eng.*, A126, 245.
- Bond, A. AERE Harwell, private communication.
- Bonniau, P. and Bunsell, A.R. (1981), *J. Compos. Mater.*, 15, 272.
- Bonniau, P. and Bunsell, A.R. (1984), *Environmental Effects on Composite Materials*, Vol. 2, Springer, G.S. (Editor), Technomic Publishing Company, Lancaster, pp.209.
- Bowditch, M.R. (1996), "The Durability of Adhesive Joints in the Presence of Water", *Int. J. Adhesion and Adhesives*, 16, pp.73-79.
- Bowditch, M.R. and Stannard, K.J. (1982), *Composites*, 13, 298.
- Bowditch, M.R., (1996), "The Durability of Adhesive Joints in the Presence of Water", *Int. J. Adhesion and Adhesives*, Vol.16, pp.73-79.
- Bowditch, M.R., Clark, J.D., and Stannard, K.J. (1987), "Adhesion 11", *Elsevier Applied Science*, pp.1.
- Bowditch, M.R., Hiscock, D., and Moth, D.A. (1991), *Int. J. Adhesion Adhes.*, 11(3), pp.163-169.
- Brewer, D., Gasparini, D.A., and Andreani, J. (1990), *J. Struct. Eng.*, 116(5), pp.1180-1198.
- Brewis, D.M., Comyn, J., and Tegg, J.L. (1980), *Int. J. Adhes. Adhes.*, 1, 35.
- Brewis, D.M., Comyn, J., Shalash, R.J.A., and Tegg, J.L. (1980), *Polymer*, 21, pp.357-360.
- Brockmann, W. (1983) *Durability in Structural Adhesives*, Kinloch, A.J. (Editor), Elsevier Applied Science, London, pp.300.
- Broek, D. (1986), *Elementary Engineering Fracture Mechanics*, 4th Edition, Kluwer Academic Publishers.

- Browning, C.E., Husman, G.E., and Whitney, J.M. (1977), *Composite Materials: Testing and Design*, ASTM STP617, Davis Jr., J.G. (Editor), American Society for Testing and Materials, Philadelphia, pp.481-496.
- Buyukozturk O., Gunes O., and Karaca E. (2003), "Progress on Understanding Debonding Problems in Reinforced Concrete and Steel Members Strengthened Using FRP Composites", *Proceedings of the 10th International Conference and Exhibition on Structural Faults and Repair*, Commonwealth Institute, London, UK.
- Buyukozturk, O. and Hearing, B. (1998), "Failure Behavior of Pre-cracked Concrete Beams Retrofitted with FRP," *Journal of Composites for Construction*, Vol.2, No.3, pp.138-144.
- Buyukozturk, O., Gunes, O., and Karaca, E. (2002), "Debonding Problems in FRP Strengthened Beams," *Proceedings of the Seventh U.S. National Conference on Earthquake Engineering*, Boston, MA.
- Calbo L.J. (Editor) (1987), *Handbook of Coatings Additives*, Marcel Dekker Inc.
- Carter, H.G. and Kibler, K.G. (1978), *J. Comp. Mater.*, 12, 118.
- Cervenka, J., Kishen, C. and Saouma, V. (1998), "Mixed Mode Fracture of Cementitious Bimaterial Interfaces; Part I: Experimental Results", *Engineering Fracture Mechanics*, Vol.60, No.1, pp.83-94.
- Cervenka, J., Kishen, C. and Saouma, V. (1998), "Mixed Mode Fracture of Cementitious Bimaterial Interfaces; Part II: Numerical Simulation", *Engineering Fracture Mechanics*, Vol.60, No.1, pp.95-107.
- Chajes, M.J., Thomson, T.A.Jr., and Farschman, A. (1998), "Durability on Concrete Beams Externally Reinforced with Composite Fabrics", *Construction and Building Materials*, Vol.9, pp.141-148.
- Chajes, M.J., Finch, W.W., Januszka, T.F., and Thomson, T.A. (1996), "Bond and Force Transfer of Composite Material Plates Bonded to Concrete," *ACI Structural Journal*, Vol.93, No.2, pp.208-217.
- Chajes, M.J., Januszka, T.F., Mertz, D.R., Thomson T.A.Jr., and Finch, W.W. (1995), "Shear Strengthening of Reinforced Concrete Beams Using Externally Applied Composite Fabrics", *ACI Struct. J.*, 92(3), pp.295-303.

- Chajes, M.J., Thomson, T.A.Jr., Januszka, T.F., and Finch, W.W. (1994), "Flexural Strengthening of Concrete Beams Using Externally Bonded Composite Materials," *Construction and Building Materials*, Vol.8, No.3, pp.191-201.
- Chajes, M.J., Thomson, T.A.Jr., and Farschman, C.A. (1995), "Durability of Concrete Beams Externally Reinforced with Composite Fabrics," *Construction and Building Materials*, Vol.9, No.3, pp.141-148.
- Chandra, K. and Saouma, V. (2003), "Fracture of Rock-Concrete Interfaces: Laboratory Tests and Applications", *ACI Structural Journal*.
- Charalambides, P.G., Lund, J., Evans, A.G., and McMeeking, R.M. (1989), "A Test Specimen for Determining the Fracture Resistance of Bimaterial Interfaces", *Journal of Applied Mechanics*, Vol.56, pp.77-82.
- Chen, J.F. and Teng, J.G. (2001), "Anchorage Strength Models for FRP and Steel Plates Bonded to Concrete", *Journal of Structural Engineering*, Vol.127, No.7, pp.784-791.
- Cherepanov, G.P. (1979), *Mechanics of Brittle Fracture*, McGraw-Hill Book Co., New York, pp.174 and 455.
- Chin, J.W., Nguyen, T., and Aouadi, K. (1997), "Effects of Environmental Exposure on Fiber-Reinforced Plastic (FRP) Materials Used in Construction", *Journal of Composites Technology and Research*, Vol.19, No.4, pp.205-213.
- Chin, J.W., Nguyen, T., and Aouadi, K. (1999), "Sorption and Diffusion of Water, Salt Water, and Concrete Pore Solution in Composite Matrices", *Journal of Applied Polymer Science*, Vol.71, pp.483-492.
- Chin, J.W. and Wightman, J.P., "Composites Bonding", *ASTM STP 1227*, Damico, D.J., Wilkinson, T.L.Jr., and Nicks, S.L.F. (Editors), American Society for Testing and Materials, Philadelphia, PA.
- Chin, J.W., Nguyen, T., and Aouadi, K. (1997), "Effects of Environmental Exposure on Fiber-Reinforced Plastic (FRP) Materials Used in Construction", *Journal of Composites Technology & Research, JCTRER Journal of Composites Technology & Research, JCTRER*, Vol.19, No.4, pp.205-213.
- Christensen, B.J., Mason, T.O., and Jennings, H.M. (1992), *J. Am. Ceram. Soc.*, 75, 939.
- Chung, D.D.L. (1994), *Carbon Fiber Composites*, Butterworth-Heinemann.

- Civil Engineering Research Foundation (2001), *Gap Analysis for Durability of Fiber Reinforced Polymer Composites in Civil Infrastructure*.
- Clarke, J.L. (Editor) (1996), *Structural Design of Polymer Composites*, E&FN Spon.
- Collings, T.A., Harvey, R.J., and Dalziel, A.W. (1993), *Composites*, 24, 625.
- Comyn, J. (1981), *Developments in Adhesives – 2*, Kinloch, A. J. (Editor), Applied Science Publishers, London, Chapter 8.
- Comyn, J. (1985), “Polymer Permeability”, *Elsevier Applied Science*, London, pp.177.
- Comyn, J. (1989), *J. Adhes*, 29, 121.
- Comyn, J.(1982), “Adhesive 6” K.W. Allen (Editor), Applied Science Publishers, London, 1982, pp.159-171.
- Coomarasamy, A. and Goodman, S. (1999), “Investigation of the Durability Characteristics of Fiber Reinforced Plastic (FRP) Materials in Concrete Environment”, *Journal of Thermoplastic Composite Materials*, Vol.12, pp.214-226.
- Cotter, J.L. (1977), “Developments in Adhesives --- 1”, Wake, W.C. (Editor), Elsevier Applied Science, London, pp. 1.
- Cottrell, A.H. (1964), *The Mechanical Properties of Matter*, John Wiley & Sons, New York, pp.430.
- Crank, J. (1975), *The Mathematics of Diffusion*, 2nd Edition, Oxford Science Publications.
- Crank, J. (1983), *Durability of Structural Adhesives*, Kinloch, A.J. (Editor), Applied Science Publishers: New York, pp.84.
- Crank, J. and Park, G.S. (1968), *Diffusion in Polymers*. Academic Press, London.
- Crocombe, A.D. (1997), “Durability Modeling Concepts and Tools for the Cohesive Environmental Degradation of Bonded Structures”, *International Journal of Adhesion and Adhesives*, Vol.17, pp.229-238.
- Crossman, F.W., Mauri, R.E., and Warren, W.J. (1978), *Advanced Composite Materials - - Environmental Effects*, ASTM STP658; Vinson, J.R. (Editor), American Society for Testing and Materials, Philadelphia, pp.205-220.
- Cuthrell, R.E. (1968), *J. Appl. Polym. Sci.*, 12, 1263.
- Dally, J.W. and Riley, W.F. (1991), *Experimental Stress Analysis*, 3rd edition, McGraw Hill Engineering Mechanics Series.

- Day, D.R. (1990), *New Characterization Techniques for Thin Polymer Films*, Tong, H.M. and Nguyen, L.T. (Editors), John Wiley and Sons: New York, 1990, pp.1.
- Dean, S.W., Pugh, E.N., and Ugiansky, G.M. (Editors) (1984), *Environment Sensitive Fracture – Evaluation and Comparison of Test Methods, ASTM STP-821*.
- DeLollis, N.J. (1977), *Nat SAMPE Symp Exhibition*, 22, 673.
- DeNeve, B. and Shanahan, M.E.R. (1993), *Polymer*, 34, 5099.
- Deneve, B. and Shanahan, M.E.R. (1995), *J. Adhesion*, 49, 165.
- DeWilde, W.P. and Shopov, P.J. (1994), *J. Comp. Struct.*, 27, 243.
- Diamant, Y., Marom, G., and Broutman, L.J. (1981), *J. Appl. Polym. Sci.*, 26, 3015.
- Dowling, N.E. (1998), *Mechanical Behavior of Materials*, 2nd Edition, Prentice Hall.
- Drazal, L.T., Rich M.J., and Koenig, M.F. (1985), *J. Adhes.*, 18, 49.
- Dundurs, J. (1969), “Edge-Bonded Dissimilar Orthogonal Elastic Wedges,” *Journal of Applied Mechanics*, Vol.36, pp.650-652.
- Eckold, G. (1994), *Design and Manufacture of Composite Structures*, Woodhead Publishing Limited.
- Ellis, T.S. and Karasz, F.E., (1984), *Polymer*, 25, 664.
- Enns, J.B. and Gillham, J.K. (1983), *J. Appl. Polym. Sci.*, 28, 2567.
- Evans, A.G. and Hutchinson, J.W. (1989), “Effects of Non-Planarity on the Mixed Mode Fracture Resistance of Bimaterial Interfaces,” *Acta Metall.*, Vol.37, No.3, pp.909-916.
- Fernlund, G. and Spelt, J.K. (1994), *Composites Science and Technology*, 50, pp.441-449.
- Fernlund, G., Papini, M., McCammond, D., and Spelt, J.K. (1994), *Composites Science and Technology*, 51, pp.584-600.
- Ferrier, E., Lagarde, G., and Hamelin, P. (2001), “Concrete Beams Reinforced by FRP: The Effect of Temperature on the Adhesive Layer,” *Composites Science and Technology*, Vol.61, pp.425-431.
- Frigione, M., Aiello, M.A., and Acierno, D. (1998), “Adhesives Based on Epoxy Resins Used to Repair Concrete Structures: Analysis of the Bond Between Resin and Concrete,” *Materials Engineering*, Vol.9, No.3-4, pp.225-235.

- Frigione, M., Naddeo, C., and Acierno, D. (2000), "Epoxy Resins Employed in Civil Engineering Applications: Effects of Exposure to Mild Temperatures," *Materials Engineering*, Vol.11, No.1, pp.59-80
- Fukuzawa, K., Numao, T., Wu, Z., Yoshizawa, H., and Mitsui, M. (1997), "Critical strain energy release rate of interface rebonding between carbon fiber sheet and mortar", *Non-Metallic (FRP) Reinforcement for Concrete Structures, Proceedings of the Third International Symposium*, Vol.1, pp.295-302.
- Fyfe Co. LLC (2004) – direct correspondence.
- Gao, B., Kim, J.K., and Leung, C.K.Y. (2003), "Effect of Rubber Modifier on Interlaminar Fracture Toughness of CFRP-Concrete Interface", *Composites Science and Technology*, 63, pp. 883-892.
- Gao, B., Leung, W.H., Cheung, C.M., Kim, J.K., and Leung, C.K.Y. (2003), "Effects of Adhesives Properties on Strengthening of Concrete Beams with Composite Strips", *FRP Composites in Civil Engineering*, Vol.I, pp. 423-432.
- Gao, B., Kim, J.K., and Leung, C.K.Y. (2003), "Effect of Rubber Modifier on Interlaminar Fracture Toughness of CFRP-Concrete Interface", *Composites Science and Technology*, Vol.63, pp.883-892.
- Garden, H.N. and Hollaway, L.C. (1998a), "An Experimental Study of the Failure Modes of Reinforced Concrete Beams Strengthened with Prestressed Carbon Composite Plates," *Composites Part B*, Vol.29, No.4, pp.411-424.
- Garden, H.N. and Hollaway, L.C. (1998b), "An Experimental Study of the Influence of Plate End Anchorage of Carbon Fiber Composite Plates Used to Strengthen Reinforced Concrete Beams," *Composite Structures*, Vol.42, No.2, pp.175-188.
- Gazit, S. (1978), *J. Appl. Polym. Sci.*, 22, 3547.
- Gillespie, T. and Rideal, E. (1956), *J. Colloid Sci.*, 11, 732.
- Gledhill, R.A. and Kinloch, A.J. (1974), *J. Adhes.*, 6, 315
- Gledhill, R.A., Kinloch, A.J., and Shaw, S.J. (1980), *J. Adhes.*, 11, 3.
- Glenhill, R.A., Shaw, S.J., and Tod, D.A. (1990), *Int. J. Adhesion Adhes.*, 10(3), pp.192-198.
- Goland, M. and Reissner, E. (1943), "The Stresses in Cemented Joints", Presented at the annual meeting, New York of The American Society of Mechanical Engineering.

- Green, M.F., Bisby, L.A., Beaudoin, Y., and Labossiere, P. (2000), "Effect of Freeze-Thaw Cycles on the Bond Durability Between FRP Plate Reinforcement and Concrete," *Canadian Journal of Civil Engineering*, Vol.27, pp.949-959.
- Grinsted, R.A. and Koenig, J.L. (1992), *Macromolecules*, 25, 1229.
- Gunes, O. (2004), *A Fracture Based Approach to Understanding Debonding in FRP Bonded Structural Members*, Ph.D. Thesis, Massachusetts Institute of Technology, Cambridge, MA.
- Gupta, V.B., Drzal, L.T., and Rich, M.J. (1985), *J. Appl. Polym. Sci.*, 30, 4467.
- Gustin, M.E. and Yatomi, C. (1979), *J. Comp. Mater.*, 13, 126.
- Hassanen, M.A.H. and Raoof, M. (2001), "Design Against Premature Peeling Failure of RC Beams with Externally Bonded Steel or FRP Plates", *Magazine of Concrete Research*, Vol.53, No.4, pp.251-262.
- Hata, T., Kitazaki, Y., and Saito, T. (1987), *J. Adhesion*, 21, 177.
- Hawkins, G.F., Steckel, G.L., Nokes, J.P., and Bauer, J.L. (2001), *In-Field Monitoring of the Durability of Composite Materials*, The Aerospace Corporation - Aerospace Report No. ATR-2001 (7595)-1.
- He, M.Y. and Hutchinson, J.W. (1989), "Kinking of Crack Out of an Interface," *Journal of Applied Mechanics*, Vol.56, pp.270-278.
- He, M.Y., Bartlett, A., Evans, A.G., and Hutchinson, J.W. (1991), "Kinking of a Crack Out of an Interface: Role of In-Plane Stress," *Journal of American Ceramics Society*, Vol.74, pp.761-771.
- Hearing, B. (2000), *Delamination in Reinforced Concrete Retrofitted with Fiber Reinforced Plastics*, Ph.D. Thesis, Massachusetts Institute of Technology, Cambridge, MA.
- Hillerborg, A., Modeer, M., and Petersson, P.E. (1976), "Analysis of Crack Formation and Crack Growth in Concrete by means of Fracture Mechanics and Finite Elements", *Cement and Concrete Research*, Vol.6, No.6, pp.773-781.
- Hillerborg, A. (1985), "The Theoretical Basis of a Method to Determine the Fracture Energy G_f of Concrete", *Materials and Structures, Research and Testing (RILEM, Paris)*, Vol.18, No.106, pp.291-296.

- Hojo, H., Tsuda, K., Ogasawara, K., and Mishima, K. (1982), *Progr. Sci. Eng. Comp.*, 2, 1017.
- Holmes, B.L. and Dillard, J.G. (1993), *Proc. 16th Ann. Meeting o the Adhesion Soc.*, Williamsburg, VA, pp.152-154.
- Hull, D. and Clyne, T.W. (1996), *An Introduction to composite materials*, 2nd Ed., Cambridge University Press, Cambridge, U.K.
- Hutchinson, A.R. (1996), "Strengthening of the Quinton Bridges with Externally Bonded Steel Plate Reinforcement" in *Bridge Management 3*, Harding, J.E., Parke, G.A.R., and Ryall, M.J. (Editors).
- Hutchinson, A.R. (1986), *Durability of Structural Adhesive Joints*, Ph.D. Thesis, Dundee University, UK.
- Hutchinson, J.W. (1996), *Mechanics of Thin Films and Multilayers*, Lecture Notes: Solid Mechanics, Technical University of Denmark.
- Hutchinson, J.W. and Suo, Z. (1992), "Mixed Mode Cracking in Layered Materials," *Advances in Applied Mechanics*, Vol.29, pp.63-191.
- Illinger, J.L. and Schneider, N.S. (1980), *Polym. Sci.*, 20, 310.
- Jackson, R.S. and Kinloch A.J. (1996), *Proc. 19th Ann. Meeting of the Adhesion Soc.*, Martle Beach, SC, pp.147-151.
- Jackson, S.P. and Weitsman, Y. (1985), *Proceedings of the Fifth International Conference on Composite Materials*, pp.1435-1452.
- Jelinsky, L.W., Dumais, J.J., Cholli, A.L., Ellis, T.S., and Karasz, F.E. (1985), *Macromolecules*, 18, 1091.
- Jirasek, M., Rolshoven, S., and Grassl, P. (2003), "Numerical Modeling of Size Effect on Fracture Energy of Concrete", *CTU Reports, Czech Technical University in Prague*, Vol.7 (1), pp.25-42.
- Johncock, P. and Tudgey, G.F. (1986), *British Polym. J.*, 18, 292.
- Johnson, W.S., Butkus, L.M., and Valentin, R.V. (1998), *Applications of Fracture Mechanics to the Durability of Bonded Composite Joints*, Report No. DOT/FAA/AR-97/56.

- Jones, R., Swamy, R.N., Bloxham, J., and Bouderbalah, A. (1980), "Composite Behavior of Concrete Beams with Epoxy Bonded External Reinforcement", *Int. J. Cement Composites*, 2(2), 91-107.
- Jones, R.H. (Editor) (2001), *Environmental Effects on Engineered Materials*, Marcel Dekker, Inc.
- Jones, R.M. (1999), *Mechanics of Composite Materials*, Taylor & Francis, Inc.
- Kafkalidis, M.S. and Thouless, M.D. (2002), *The Effects of Geometry and Material Properties on the Fracture of Single Lap-Shear Joints, Report April 2002*
- Kaiser, H. P. (1989), *Strengthening of Reinforced Concrete with Epoxy-Bonded Carbon Fibre Plastics*, Doctoral Thesis, Diss. ETH Nr. 8918, ETH Zurich, Switzerland, (in German).
- Kanninen, M.F. and Popelar, C.H. (1985), *Advanced Fracture Mechanics*, Oxford University Press, New York, pp.17-18, 26-30, and 82.
- Karbhari, V.M. and Engineer, M. (1995), "Assessment of Interfacial Fracture Energy between Concrete and Glass Reinforced Composites", *Journal of Materials Science Letters*, 14, pp.1210-1213.
- Karbhari, V.M. and Engineer, M. (1996), "Investigation of Bond between Concrete and Composites: Use of a Peel Test", *Journal of Reinforced Plastics and Composites*, Vol.15, pp.208-227.
- Karbhari, V.M. and Engineer, M. (1996), "Effect of Environmental Exposure on the External Strengthening of Concrete with Composites – Short Term Bond Durability," *Journal of Reinforced Plastics and Composites*, Vol.15, pp.1194-1216.
- Karbhari, V.M. and Zhao L. (1998), "Issues Related to Composite Plating and Environmental Exposure Effects on Composite – Concrete Interface in External Strengthening", *Composite Structure*, Vol.40, Nos.3-4, pp.293-304.
- Karbhari, V.M., Engineer, M., and Eckel II, D.A. (1997), "On The Durability of Composite Rehabilitation Schemes for Concrete: Use of a Peel Test," *Journal of Materials Science*, Vol.32, No.1, pp.147-156.
- Kazuaki, N., Atsushi, Y., and Hiroyuki, H. (1996), "Numerical Approach for Evaluation of Stress Transmissibility of Composite Interface", *Design and Manufacturing of*

- Composites, Proc., Joint Canada-Japan Workshop on Composites*, Hoa, S.V. and Hamada, H. (Editors), Technomic, Lancaster, PA, pp.183-186.
- Keenan, J.D., Seferis, J.C., and Wuilivan, J.T. (1979), *J. Appl. Polym., Sci.*, 24, 2375.
- Kelly, A. (1989), *Concise Encyclopedia of Composite Materials*, Pergamon Press.
- Kelly, A. and Rabotnov, Y.N. (1985), *Handbook of Composites: Volume 1: Strong Fibers*, North-Holland.
- Ketola, W.D. and Grossman, D. (Editors) (1994), *Accelerated and Outdoor Durability Testing of Organic Materials, ASTM Publication code Number (PCN): 04-012020-14, ASTM*.
- Khalifa, A. and Nanni, A. (2000), "Improving Shear Capacity of Existing RC T-Section Beams Using CFRP Composites," *Cement and Concrete Composites*, Vol.22, pp.165-174.
- Khalifa, A., Gold, W.J., Nanni, A., and Aziz, A.M.I. (1998), "Contribution of Externally Bonded FRP to Shear Capacity of RC Flexural Members," *Journal of Composites for Construction*, Vol.2, No.4, pp.195-202.
- Kimpara, I., Kageyama, K., Suzuki, T., Osawa, I., and Yamaguchi, K. (1999), "Characterization of Debonding Energy Release Rate of FRP Sheets Bonded on Mortar and Concrete", *Advanced Composite Materials*, Vol. 8, No. 2, pp. 177-187.
- Kinloch, A.J. (1982), *Journal of Materials Science*, Vol.17, pp.617.
- Kinloch, A.J. (1983), *Durability of Structural Adhesives*, Applied Science Publishers, London.
- Kinloch, A.J. (Editor) (1987), *Adhesion and Adhesives, Science and Technology*, Chapman and Hall, London.
- Kinloch, A.J. (1979), *J. Adhes.*, 10, 193.
- Knott, J.F. (1973), *Fundamentals of Fracture Mechanics*, Butterworths, London, pp.273.
- Kobatake, Y., Kimura, K., and Katsumada, H. (1993), "A Retrofitting Method for Reinforced Concrete Structures Using Carbon Fiber", *Fiber reinforced plastic (FRP) reinforcement for concrete structures: Properties and applications*, A. Nanni, ed., Elsevier Science, Oxford, U.K., pp.435-450.
- Kobayashi, A.S. (Editor) (1993), *Handbook on Experimental Mechanics*, 2nd Edition, VCH Publishers.

- Konvalinka, P. (Editor) (2001), *Czech Technical University (CTU) Reports: Volume 5 – Contributions to Experimental Investigation of Engineering Materials and Structures*, (2-3).
- Konvalinka, P. and Luxemburk, F. (Editors) (2002), *Czech Technical University (CTU) Reports: Volume 6 – Experimental Investigation of Building Materials and Technologies*, (2).
- Konvalinka, P. and Maca, J. (Editors) (2003), *Czech Technical University (CTU) Reports: Volume 7: Contributions to Computational and Experimental Investigation of Engineering Materials and Structures*, (1).
- Konvalinka, P. (2003), “Changes of Material Characteristics of Concrete under the Freeze-Thaw Loading”, *CTU Reports, Czech Technical University in Prague*, Vol.7 (1), pp.17-196.
- Konvalinka, P. (2002), “Effect of Moisture Content of Concrete Specimen on its Stress-Strain Diagram in Compression”, *CTU Reports, Czech Technical University in Prague*, Vol.6 (2), pp.59-66.
- Konvalinka, P. (2001), “Effect of the Testing Arrangement on Compressive Softening of Concrete”, *CTU Reports, Czech Technical University in Prague*, Vol.5 (2-3).
- Konvalinka, P. (2002), “Effect of Moisture Content of Concrete Specimen on its Stress-Strain Diagram in Compression”, *CTU Reports: Experimental Investigation of Building Materials and Technologies*, Konvalinka, P. and Luxemburk, F. (Editors), 2, Vol. 6, pp. 59-66.
- Kreyszig, E. (1993), *Advanced Engineering Mathematics*, 7th Edition, John Wiley and Sons.
- Kuhl, A. (1998), *A Technique to Measure Interfacial Fracture Toughness*, MS Thesis, Georgia Institute of Technology, Department of Mechanical Engineering.
- Labana, S.S., Newman, S., and Chompff, A.J. (1971), *Polymer Networks: Structure and Mechanical Properties*, Chompff, A.J. and Newman, S. (Editors), Plenum: New York, pp.453-475.
- Ladner, M. and Weder, Ch. (1981), *Concrete Structures with Bonded External Reinforcement*, EMPA Dubendorf.

- Lambros, J. (Spring 2002), *Interfacial Fracture Mechanics*, Lecture Notes, University of Illinois.
- Lee, H. (Nov 1963), *Materials Research & Standards*, 910.
- Lee, K.M., Buyukozturk, O., and Oumera, A. (1992), "Fracture Analysis of Mortar-Aggregate Interfaces in Concrete", *ASCE Journal of Engineering Mechanics*, Vol.118, No.10, pp.2031-2047.
- Lee, M.C., Peppas, N.A. (1993), *J. Appl. Polym. Sci.*, 47, 1349.
- Lees, W.A. (1984), *Adhesives in Engineering Design*, The Design Council.
- Lees, D.E. and Hutchinson, A.R. (1992), "Mechanical Characteristics of Some Cold-Cured Structural Adhesives," *International Journal of Adhesion and Adhesives*, Vol.12, No.3, pp.197-205.
- Loh, W.K., Crocombe, A.D., Abdel Wahab, M.M., and Ashcroft, I.A. (2002), "Environmental Degradation of the Interfacial Fracture Energy in an Adhesively Bonded Joint", *Engineering Fracture Mechanics*, Vol.69, pp.2113-2128.
- Loos, S.C. and Springer, G.S. (1979), *J. Comp. Mater.*, 13, 131.
- Lorenzis, L.D., Miller, B., and Nanni, A. (2001). "Bond of Fiber-Reinforced Polymer Laminates to Concrete." *ACI Materials Journal*, Vol.98. No.3, pp.356-364.
- Luoma, G.A. and Rowland, R.D. (1986), *J. Appl. Polym. Sci.*, 32, 5777.
- MacKague, E.L., Reynolds, J.D. Jr., and Halkias, J.E. (1978), *J. Appl. Polym. Sci.*, 22, 1643.
- Maeda, T., Asano, Y., Sato, Y., Ueda, T., and Kakuta, Y. (1997), "A Study on Bond Mechanism of Carbon Fiber Sheet", *Non-metallic (FRP) reinforcement for concrete structures, Proc., 3rd Int. Sympo. (FRPPCS-3)*, Japan Concrete Institute, Sapporo, Japan, 1, pp.279-286.
- Maggana, C. and Pissis, P. (1999), *J. Polym. Sci. B. Polym. Phys.*, 37, 1165.
- Magonov, S., Elings, V., and Whangbo, M.H. (1997), *Surf Sci. Lett.*, 21, 375.
- Malek, A.M., Saadatmanesh, H., and Ehsani, M.R. (1998), "Prediction of Failure Load of R/C Beams Strengthened with FRP Plate Due to Stress Concentration at Plate End," *ACI Structural Journal*, Vol.95, No.2, pp.142-152.
- Mallick, P.K. (1988), *Fiber Reinforced Composites*, Marcel Dekker, Inc., New York.

- Marchand, P. and Holland, O.T. (2003), *Graphics and GUIs with MATLAB*, 3rd Edition, Chapman and Hall / CRC.
- Marom, G. (1975), *Polymer Permeability*, Comyn, J. (Editor), Elsevier: New York, pp.341.
- Marsh, L.L., Lasky, R., Seraphim, D.P., and Springer, G.S. (1984), "Moisture Solubility and Diffusion in Epoxy and Epoxy-Glass Composites", *IBM J. Res. Develop.*, Vol.28, No.6, pp.655-661.
- Marshall, J.M., Marshall, G.P., and Pinzelli, R.F. (1982), *Proceedings of the 37th Annual Conference, Reinforced Plastics/Composites Institute*, The Society of the Plastics Industry, Inc., pp. 9.C/1.
- MathSoft. (1999), *Mathcad User's Guide 2000*.
- Matos, P.P.L., McMeeking, R.M., Charalambides, P.G., and Drory, M.D. (1989), "A Method for Calculating Stress Intensities in Bimaterial Fracture," *International Journal of Fracture*, Vol.40, pp.235-254.
- Mays, G.C. and Hutchinson, A.R. (1992), *Adhesives in Civil Engineering*, Cambridge University Press, UK.
- Mazars, J. and Bazant, Z.P. (Editors) (1989), *Cracking and Damage – Strain Localization and Size Effect*, Elsevier Applied Science.
- McMillan J.C. (1981), *Developments in Adhesives*, Kinloch A.J. (Editor), Applied Science Publishers, pp.243-278.
- Meese, R.G. (Editor) (1974), *Testing of Adhesives – Tappi Monograph Series No.35*.
- Mehta, P.K. and Monteiro, P.J.M. (1992), *Concrete: Structures, Properties and Materials*, 2nd Edition, Prentice Hall.
- Meier, U. (1992), "Strengthening of Structures with Carbon FRP laminates; Research and Applications in Switzerland", *Advanced Composite Materials in Bridges and Structures* (edited by K W Neale and P Labossiere), Canadian Society for Civil Engineering, Montreal, Canada.
- Menard, K.P. (1999), *Dynamic Mechanical Analysis – A Practical Introduction*, CRC Press.
- Mikols, W.J., Seferis, J.C., Appicella, A., and Nicolais, L. (1982), *Polym. Compos.*, 3, 118.

- Military Handbook, *MIL-HDBK-1002/6*, "Aluminum Structures, Composites Structures, Structural Plastics and Fiber-Reinforced Composites", U.S. Department of Defense, Wright-Patterson AFB, OH.
- Military Handbook, *MIL-HDBK-17-1D*, "Polymer Matrix Composites: Volume 1, Guidelines", U.S. Department of Defense, Wright-Patterson AFB, OH.
- Military Handbook, *MIL-HDBK-17-3D*, "Polymer Matrix Composites: Volume 3, Utilization of Data", U.S. Department of Defense, Wright-Patterson AFB, OH.
- Minford, J.D. (1983), "Durability of Structural Adhesives", Kinloch, A.J.(Editor), *Applied Science*, London, pp. 135.
- Misra, S.C., Manson, J.A., and Sperling, L.H. (1978), *Org. Coatings Plast. Chem. Prepr.*, 39, 152.
- Moloney, A.C., Brewis, D.M., Comyn, J., and Cope, B.C. (1981), *Adhesion 5, Elsevier Applied Science*, London, pp. 153.
- Morgan, R.J. and O'Neal, J.E. (1977), *J. Mater. Sci.*, 12, 1966.
- Morii, T. Tanimoto, T., Hainada, H., Maekawa, Z., Hirano, T., and Kiyosumi, K. (1993), *Comp. Sci. Techno*, 49, 209.
- Mouzakis, D.E. and Karger-Kocsis, J. (1998), *J. Appl. Polym. Sci.*, 68, 561.
- Moy, P. and Karasz, F.E. (1980), *Polym. Eng. Sci.*, 20, 315.
- Moylan, C.R., Best, M.E., and Ree, M. (1991), *J. Polymer, Sci. Part. B. Polym. Phys.*, 29, 8.
- Mukhopadhyaya, P., Swamy, R.N., and Lynsdale C.J. (1998), "Influence of Aggressive Exposure Conditions on the Behavior of Adhesive Bonded Concrete – GFRP Joints," *Construction and Building Materials*, Vol.12, pp.427-446.
- Myers, J.J., Murthy, S.S., and Micelli, F. (2001), "Effect of Combined Environmental Cycles on the Bond of FRP Sheets to Concrete," *Proceedings – Composites in Construction, 2001 International Conference*, Porto, Portugal.
- Nakaba K., Kanakubo, T., Furuta, T., and Yoshizawa H. (2001), "Bond Behavior between FRP Laminates and Concrete", *ACI Structural Journal*, Vol.98, No.3, pp.359-367.
- Nakamura, K., Maruno T., and Sasaki S. (1987), *Int. J. Adhesion Adhes.*, 7(2), pp.97-102.

- NCHRP 10-59 (2004), Research Initiative: Construction Specifications for Bonded Repair and Retrofit of Concrete Structures Using FRP Composites, National Cooperative Highway Research Program, US.
- Nelson, W. (1990), *Accelerated Testing – Statistical Models, Test Plans, and Data Analyses*, Wiley Series in Probability and Mathematical Statistics, John Wiley and Sons.
- Neubauer, U. and Rostasy, F.S. “Bond Failure of Concrete Fiber Reinforced Polymer Plates at Inclined Cracks --- Experiments and Fracture Mechanics Models”, *Fiber Reinforced Polymer Reinforcements*, pp.369-381, SP 188-34.
- Neubauer, U. and Rostasy, F. S. (1997), “Design Aspects of Concrete Structures Strengthened with Externally Bonded FRP-Plates,” *Proceedings of the 7th International Conference on Structural Faults and Repair*, Edinburgh, UK, Vol.2, pp.109-118.
- Neubauer, U. and Rostasy, F.S. (1999), “Bond Failure of Concrete Fiber Reinforced Polymer Plates at Inclined Cracks – Experimental and Fracture Mechanics Model” *Proceedings of the Fourth International Symposium: Non-Metallic (FRP) Reinforcement for Concrete Structures*, ACI SP-188, Dolan, D.W., Rizkalla, S.H., and Nanni, A., (Editors) Baltimore, USA, 369-382.
- Neville, A. (1997), *Properties of Concrete*, 4th Edition, Wiley & Sons.
- Nguyen, T., Hubbard, J.B., and Pommersheim, J.M. (1996), *J. Coat Technol.*, 68, 45.
- Nguyen, T., Bentz, D., and Byrd, E. (1995), *J. Coat Technol.*, 67, 37.
- Nogueira, P., Ramírez, C., Torres, A., Abad, M.J., Cano, J., López, J., López-Bueno, I., and Barral, L. (2001), “Effect of Water Sorption on the Structure and Mechanical Properties of an Epoxy Resin System”, *Journal of Applied Polymer Science*, Vol.80, pp.71-80.
- Oehlers, D.J. and Moran, J.P. (1990), “Premature Failure of Externally Plated Reinforced Concrete Beams”, *Journal of Structural Engineering*, Vol.116, No.4, pp.978-995.
- Orman, S. and Kerr, C. (1971), *Aspects of Adhesion*, Alner, D.J.(Editor), University of London Press, pp. 64.
- Owens, D.K. and Wendt, K.C. (1969), *J. Appl. Polym. Sci.*, 13, 1741
- Palmese, G.R. (1992), PhD Thesis, University of Delaware.

- Palmese, G.R. and McCullough, R.L. (1992), *J. Appl. Polym. Sci.*, 46, 1863.
- Palmese, G.R. and McCullough, R.L. (1994), *J. Adhes.*, 44, 29.
- Papini, M., Fernlund, G., and Spelt, J.K. (1994), *Composites Science and Technology*, 40(1), pp.119-132.
- Papini, M., Fernlund, G., and Spelt, J.K., (1994), *Int. J. Adhesion Adhes.*, 14(1), pp.5-13.
- Parker, B.M. (1994), *Composites Bonding, ATSM STP 1227*, pp.68-81.
- Parker, B.M. DRA Farnborough, private communication.
- Peters, S.T. (1998), *Handbook of Composites*, 2nd Edition, Chapman and Hall.
- Pethrick, R.A., Hollins, E.A., McEwan, I., Pollock, E.A., and Hayward, D. (1996), *Polym. Int.*, 39, 275.
- Popovics, S. (1998), *Strength and Related Properties of Concrete – A Quantitative Approach*, John Wiley and Sons.
- Pritchard, G. (Editor) (1999), *Reinforced Plastics Durability*, CRC Press, Woodhead Publishing Limited.
- Reddy, J.N. and Murty A.V.K. (Editors) (1992), *Composite Structures: Testing, Analysis, and Design*, Springer-Verlag Narosa Publishing House.
- Rice, J.R. (1988), “Elastic Fracture Concepts for Interfacial Cracks,” *Journal of Applied Mechanics*, Vol.55, pp.98-103
- Ritchie, P.A., Thomas, D.A., Lu, L.W., and Connely, G.M. (1991), “External Reinforcement of Concrete Beams Using Fiberglass Reinforced Plastics,” *ACI Structural Journal*, Vol.88, No.4, pp.490-500.
- Roberts, T.M. (1989), “Approximate Analysis of Shear and Normal Stress Concentrations in The Adhesive Layer of Plated RC Beams,” *Structural Engineer*, Vol.67, No.12, pp.229-233.
- Rogers, C.E. (1965), *Physics and Chemistry of the Organic Solid State*, Fox, D., Labes, M.M., and Weissberger, A.(Editors) Vol.II, Chap.6, Interscience, NY.
- Ross, C.A., Jerome, D.M., Tedesco, J.W., and Hughes, M.L. (1996), “Moisture and Strain Rate Effects on Concrete Strength,” *ACI Materials Journal*, Vol.93, No.3, pp.293-300.
- Saadatmanesh, H. and Ehsani, M.R. (1990a), “Fiber Composites Can Strengthen Beams,” *Concrete International: Design and Construction*, Vol.12, No.3, pp.65-71.

- Saadatmanesh, H., and Ehsani, M. (1990b), "RC Beams Strengthened With GFRP Plates. I: Experimental Study," *Journal of Structural Engineering*, Vol.117, No.11, pp.3417-3433.
- Saenger, K.L. and Tong H.M. (1991), *Polym. Eng. Sci.*, 31, 432.
- Sanford, W.M. (1987), PhD Thesis, University of Delaware.
- Saouma, V. and Morris, D. (1998), "Application of Fracture Mechanics to Concrete Dams; A Detailed Case Study", *Dam Engineering*, Vol.IX, No.4, pp.321-344.
- Schapery, R.A. and Sun, C.T. (Editors) (2000), *Time Dependent and Nonlinear Effects in Polymers and Composites*, ASTM STP 1357.
- Schlotter, N.E. (1990), *J. Phys. Chem.*, 94, 1692.
- Schott, H. (1992), *J. Macromol. Sci.-Phys.*, B31, 1
- Sellitti, C., Koenig, J.L., and Ishida, H. (1990), *Mater. Sci. Eng.*, A126, 235.
- Selzer, R and Friedrich, K.J. (1995), *J. Mater. Sci.*, 30, 334.
- Shakhmenko, G. and Birsh, J. (1998), "Concrete Mix Design and Optimization", 2nd International Symposium in Civil Engineering, Budapest.
- Sharif, A., Al-Sulaimani, G.J., Basunbul, I. A., Baluch, M. H., and Ghaleb, B. N. (1994), "Strengthening of Initially Loaded Reinforced Concrete Beams Using FRP Plates," *ACI Structural Journal*, Vol.91, No.2, pp.160-168.
- Sharpe, L.H. (1972), *J. Adhes.*, 4, 51.
- Shen, C.H. and Springer, G.S. (1981), *Environment Effects on Composite Materials*, Springer, G.S. (Editor), Technomic, Lancaster, PA, pp.15, 79.
- Shen, C.H. and Springer, G.S. (1976), *J. Comp. Mater.*, 10, 2.
- Shirrell, C.D. (1978), *Advanced Composite Materials --- Environmental Effects*, ASTM STP658, Vinson, J.R. (Editor), American Society for Testing and Materials, Philadelphia, pp.21-42.
- Shook, G.D. (Editor) (1986), *Reinforced Plastics for Commercial Composites: Source Book*, ASM.
- Sika Corporation USA (2004) – direct correspondence.
- Skourlis, T.P. and McCullough, R.L. (1993), *Compos. Sci. Technol.*, 49, 363.
- Skourlis, T.P. and McCullough, R.L. (1993), *Proceedings of the American Society for Composites Eighth Technical Conference*, pp.218-226.

- Skourlis, T.P. (1996), PhD Thesis, University of Delaware.
- Smith, S.T. and Teng, J.G. (2002), "FRP-Strengthened RC Beams I: Review of Debonding Strength Models", *Engineering Structures*, 24, pp.385-395.
- Smith, S.T. and Teng, J.G. (2001), "Interfacial Stresses in Plated Beams," *Engineering Structures*, Vol.23, No.7, pp.857-871.
- Sohn, D.W., Zhou, Q, and Sung, N. (1984), *Proceedings of the 52nd Annual Technical Conference on Plastics Engineering*, Vol.2, pp.2382.
- Spelt, J.K. and Wylde J. (1996), *Proc. 19th Ann. Meeting of the Adhesion Soc.*, Myrtle Beach, SC., pp.18-21.
- Spinks, G.M., Isles N.A., Egan B.J., and Noakes A. (1992), *Materials Forum*, 16, pp.253-257.
- Stastna, J. and De Kee, D. (1995), *Transport Properties in Polymers*, Technomic: Lancaster, pp.121.
- Su, N., Mackie, R.I., and Harvey, W.J. (1992), *Int. J. Adhesion Adhes.*, 12(2), pp.85-93.
- Tada, H, Paris, P.C., and Irwin, G.R. (1973), *The Stress Analysis of Cracks Handbook*, Del Research Corp., Hellertown.
- Taljsten, B. (1997), "Strengthening of Beams by Plate Bonding," *Journal of Materials in Civil Engineering*, Vol. 9, No. 4, pp. 206-211.
- Tetelman, A.S. and McEvily, A.J. (1967), *Fracture of Structural Materials*, John Wiley & Sons, New York, pp.274-276.
- Theocaris, P.S., Kontou, E.A., and Papanicolau, G.C. (1983), *Colloid Polym. Sci.*, 261, 394.
- Thomason, J.L. (1995), *Composites*, 26, 477.
- Thouless, M.D., Hsueh, C.H., and Evans, A.G. (1983), "A Damage Model of Creep Crack Growth in Polycrystals", *Acta Metallurgica*, Vol.31, No.10, pp.1675-1687.
- Tommaso, A.D., Neubauer, U., Pantuso, A., and Rostasy, F.S. (2001), "Behavior of Adhesively Bonded Concrete-CFRP Joints at Low and High Temperature," *Mechanics of Composite Materials*, Vol.37, No.4, pp.327-338.
- Toutanji, H.A. and Gomez, W. (1997), "Durability Characteristics of Concrete Beams Externally Bonded with FRP Composite Sheets," *Cement and Concrete Composites*, Vol.19, pp.351-358.

- Toya M, Aritomi M, and Chosa A. (1997), "Energy Release Rates for an Interface Crack Embedded in a Laminated Beam Subjected to Three-Point Bending", *Journal of Applied Mechanics*, Vol. 64, pp.375-382.
- TPI Composites (2002), direct correspondence.
- Trabocco, Donnellan and Williams. (1988), *Bonded Repair of Aircraft Structures*", Baker, A.A. and Jones, R. (Editors), Martinus Nijhoff, Ch.7.
- Trende, U. (1995), *Interface Fracture Mechanics of High Strength Concrete: Size Effect and Aggregate Roughness*, SM Thesis, Massachusetts Institute of Technology, Department of Civil and Environmental Engineering.
- Triantafillou, T.C. and Plevris, N. (1992), "Strengthening of RC Beams with Epoxy-Bonded Fibre-Composite Materials," *Materials and Structures*, Vol.25, pp.201-211.
- Tsou, A.H. and Peppas, N.A. (1988), *Polym, Mater. Sci. Eng.*, 58, 952.
- Tu, L. and Kruger, D. (1996), "Engineering Properties of Epoxy Resins Used as Concrete Adhesives," *ACI Materials Journal*, Vol.93, No.1, pp.26-35.
- U.S. Army Corp of Engineers (March 1997), *Engineering and Design: Composite Materials for Civil Engineering Structures, ETL 1110-2-548*.
- van Landingham, M.R. (1997), PhD Thesis, University of Delaware.
- van Landingham, M.R., Eduljee, R.F., and Gillespie, JR., J.W. (1999), "Moisture Diffusion in Epoxy Systems", *Journal of Applied Polymer Science*, Vol.71, pp.787-798.
- Venables, J.D. (1984), *J. Mater. Sci.*, 19, 2431
- Vichit-Vadakan W. (1997), *Shear Behavior of Pre-Cracked, Reinforced Concrete Beams Retrofitted with Glass Fiber Reinforced Plastic Sheet*, SM Thesis, Massachusetts Institute of Technology, Department of Civil and Environmental Engineering, 1997
- Volpe Center (2002), direct correspondence.
- Wagner, H.D. and Lustiger, A. (1994), *Composites*, 77(25), pp.613-616.
- Wake, W.C. (1982), *Adhesion and the Formulation of Adhesives*, 2nd Edition, Applied Science Publishers.
- Wang, X. and Gillham, J.K. (1993), *J. Appl. Polym. Sci.*, 47, 425.
- Ward, I.M. and Hadley, D.W. (1993), *An Introduction to the Mechanical Properties of Solid Polymers*, John Wiley and Sons.

- Weeton, J.W., Peters, D.M., and Thomas, K.L. (1987), *Engineers' Guide to Composite Materials*, American Society for Metals.
- Whitney, J.M. and Browning, C.E. (1978), *Advanced Composite Materials --- Environmental Effects*, ASTM STP658; Vinson, J.R. (Editor), American Society for Testing and Materials, Philadelphia, pp.43-61.
- Williams, J.G., (1988), "On the Calculation of Energy Release Rates for Cracked Laminates", *International Journal of Fracture*, 36, pp.101-119.
- Wingfield, J.R.J. (1993), *Int. J. Adhes. Adhes.*, 13, 151.
- Wong, T.C. and Broutman, L.J. (1985), *J. Polym. Eng. Sci.*, 25, 529.
- Woo, M. and Pignott, M. (1987), *J. Comp. Tech. Res.*, 9, 101.
- Wright, W.W. and Adamson, M.J. (1981), *J. Mater. Sci. Composites*, 12, 201.
- Wu, Z., Yuan, H., and Niu, H. (2002), "Stress Transfer and Fracture Propagation in Different Kinds of Adhesive Joints," *Journal of Engineering Mechanics*, Vol.128, No.5, pp.562-573.
- Wylde, J.W. and Spelt, J.K., (1998), "Measurement of Adhesive Joint Fracture Properties as a Function of Environmental Degradation", *International Journal of Adhesion & Adhesives*, Vol.18, pp.237-246.
- Wypych, G. (1995), *Handbook of Material Weathering*, 2nd Edition, ChemTec Publishing.
- Xiao, G.Z. and Shanahan, M.E.R. (1997), *Polym. Sci. Phys. Ed.*, 35, 2659.
- Xiao, G.Z., Delamar, M., and Shanahan, M.E.R. (1997), *J. Appl. Polym. Sci.*, 65, 449.
- Yaseen, M. and Funke, W. (1978), *J. Oil Color Chemists Assoc.*, 61, 284.
- Yuan, H. and Wu, Z. (2000), "Energy Release Rates for Interfacial Crack in Laminated Structures", *Structural Eng./Earthquake Eng.*, JSCE, Vol.17, No.1, pp.1s-13s.
- Zanni-Deffarges, M.P. and Shanahan, M.E.R. (1993), *Int. J. Adhes. Adhes.*, 13(1), 41.
- Zanni-Deffarges, M.P. and Shanahan, M.E.R. (1994), *J. Adhes.*, 45, 245.
- Zanni-Deffarges, M.P. and Shanahan, M.E.R. (1995), "Diffusion of Water into an Epoxy Adhesive: Comparison between Bulk Behavior and Adhesive Joints", *Int. J. Adhesion and Adhesives*, Vol.15, pp.137-142.
- Zewi, I.G., Flashner, F., and Dodiuk, H. (1984), *Int. J. Adhesion Adhes.*, 4(3), pp.137-139.

Ziraba, Y.N., Baluch, M.H., Basunbul, I.A., Sharif, A.M., Azad, A.K., and Al-Sulaimani, G.J. (1994), "Guidelines Toward the Design of Reinforced Concrete Beams with External Plates," *ACI Structural Journal*, Vol.91, No.6, pp.639-646.

APPENDIX

- APPENDIX 1 - FINITE ELEMENT (ABAQUS) INPUT FILE FOR 3-D
MOISTURE DIFFUSION SIMULATION
- APPENDIX 2A - FINITE ELEMENT (ABAQUS) INPUT FILE FOR GLOBAL
PEEL MODELING
- APPENDIX 2B - FINITE ELEMENT (ABAQUS) INPUT FILE FOR GLOBAL
SHEAR MODELING
- APPENDIX 3A - FINITE ELEMENT (ABAQUS) INPUT FILE FOR
COMPUTATION OF J-INTEGRAL AND MODE SEPARATION
UNDER PEEL
- APPENDIX 3B - FINITE ELEMENT (ABAQUS) INPUT FILE FOR
COMPUTATION OF J-INTEGRAL AND MODE SEPARATION
UNDER SHEAR

APPENDIX 1

Finite Element (ABAQUS) Input File for 3-D Moisture Diffusion Simulation

```
*Heading
** Job name: DiffusionModeling Model name: 3DFRPBonedConcrete
*Preprint, echo=NO, model=NO, history=NO, contact=NO
**
** PARTS
**
*Part, name=Concrete
*End Part
*Part, name=EPOXY
*End Part
*Part, name=FRP
*End Part
**
** ASSEMBLY
**
*Assembly, name=Assembly
**
*Instance, name=FRP-1, part=FRP
      198.,      0.,      38.5
*Node
      1,      -50.,      -12.5,      0.
      2,      -50.,      -12.5,      1.28
      3,     -100.,      -12.5,      1.28
      4,     -100.,      -12.5,      0.
      5,      -50.,      12.5,      1.28
...
      488,      75.,      7.5,      0.
      489,      80.,      7.5,      0.
      490,      85.,      7.5,      0.
      491,      90.,      7.5,      0.
      492,      95.,      7.5,      0.
*Element, type=DC3D8
      1, 56, 61, 225, 189, 1, 2, 13, 30
      2, 189, 225, 226, 190, 30, 13, 14, 29
...
199, 179, 124, 123, 180, 375, 491, 492, 376
200, 180, 123, 11, 12, 376, 492, 185, 184
*Nset, nset=FRPinterface
      1, 8, 9, 11, 53, 54, 55, 56, 65, 66, 67, 68, 69, 70, 71, 72
      73, 74, 75, 76, 77, 78, 79, 80, 81, 82, 83, 84, 85, 86, 87, 88
...
467, 468, 469, 470, 471, 472, 473, 474, 475, 476, 477, 478, 479, 480, 481, 482
483, 484, 485, 486, 487, 488, 489, 490, 491, 492
*Elset, elset=FRPinterface, generate
      51, 200, 1
*Nset, nset=FRPtop
      2, 3, 5, 6, 10, 12, 13, 14, 15, 16, 17, 18, 19, 20, 21, 31
      32, 33, 34, 35, 36, 37, 38, 39, 57, 58, 59, 60, 61, 62, 63, 64
...
355, 356, 357, 358, 359, 360, 361, 362, 363, 364, 365, 366, 367, 368, 369, 370
371, 372, 373, 374, 375, 376
*Elset, elset=FRPtop, generate
      1, 200, 1
*Nset, nset=CantileverBottom
```

```

    1, 4, 7, 8, 22, 23, 24, 25, 26, 27, 28, 29, 30, 40, 41, 42
    43, 44, 45, 46, 47, 48, 49, 50, 51, 52, 53, 54, 55, 56, 189, 190
...
207, 208, 209, 210, 211, 212, 213, 214, 215, 216, 217, 218, 219, 220, 221, 222
223, 224
*Elset, elset=CantileverBottom, generate
    1, 50, 1
*Nset, nset=FRPsides
    1, 2, 3, 4, 5, 6, 7, 8, 9, 10, 11, 12, 13, 14, 15, 16
    17, 18, 19, 20, 21, 22, 23, 24, 25, 26, 27, 28, 29, 30, 31, 32
...
169, 170, 171, 172, 173, 174, 175, 176, 177, 178, 179, 180, 181, 182, 183, 184
185, 186, 187, 188
*Elset, elset=FRPsides
    1, 2, 3, 4, 5, 6, 7, 8, 9, 10, 20, 30, 40, 41, 42, 43
    44, 45, 46, 47, 48, 49, 50, 51, 52, 53, 54, 55, 56, 57, 58, 59
...
179, 180, 181, 182, 183, 184, 185, 186, 187, 188, 189, 190, 191, 192, 193, 194
195, 196, 197, 198, 199, 200
** Region: (FRP:Picked)
*Elset, elset=_PickedSet9, internal, generate
    1, 200, 1
** Section: FRP
*Solid Section, elset=_PickedSet9, material=FRP
1.,
*End Instance
**
*Instance, name=EPOXY-1, part=EPOXY
    223., 0., 37.5
*Node
    1, 75., -12.5, 1.
    2, 70., -12.5, 1.
...
    371, -70., 12.5, 0.
    372, -75., 12.5, 0.
*Element, type=DC3D8
    1, 63, 64, 95, 94, 1, 2, 33, 32
    2, 64, 65, 96, 95, 2, 3, 34, 33
...
149, 339, 340, 371, 370, 277, 278, 309, 308
150, 340, 341, 372, 371, 278, 279, 310, 309
*Nset, nset=FRPEpoxyInterface
    1, 2, 3, 4, 5, 6, 7, 8, 9, 10, 11, 12, 13, 14, 15, 16
    17, 18, 19, 20, 21, 22, 23, 24, 25, 26, 27, 28, 29, 30, 31, 63
...
316, 317, 318, 319, 320, 321, 322, 323, 324, 325, 326, 327, 328, 329, 330, 331
332, 333, 334, 335, 336, 337, 338, 339, 340, 341
*Elset, elset=FRPEpoxyInterface, generate
    1, 150, 1
*Nset, nset=EpoxyConcreteInterface
    32, 33, 34, 35, 36, 37, 38, 39, 40, 41, 42, 43, 44, 45, 46, 47
    48, 49, 50, 51, 52, 53, 54, 55, 56, 57, 58, 59, 60, 61, 62, 94
...
347, 348, 349, 350, 351, 352, 353, 354, 355, 356, 357, 358, 359, 360, 361, 362
363, 364, 365, 366, 367, 368, 369, 370, 371, 372
*Elset, elset=EpoxyConcreteInterface, generate
    1, 150, 1

```

```

*Nset, nset=EpoxySides
  1,  2,  3,  4,  5,  6,  7,  8,  9, 10, 11, 12, 13, 14, 15, 16
 17, 18, 19, 20, 21, 22, 23, 24, 25, 26, 27, 28, 29, 30, 31, 32
...

345, 346, 347, 348, 349, 350, 351, 352, 353, 354, 355, 356, 357, 358, 359, 360
361, 362, 363, 364, 365, 366, 367, 368, 369, 370, 371, 372
*Elset, elset=EpoxySides
  1,  2,  3,  4,  5,  6,  7,  8,  9, 10, 11, 12, 13, 14, 15, 16
 17, 18, 19, 20, 21, 22, 23, 24, 25, 26, 27, 28, 29, 30, 31, 60
...

133, 134, 135, 136, 137, 138, 139, 140, 141, 142, 143, 144, 145, 146, 147, 148
149, 150
** Region: (Epoxy:Picked)
*Elset, elset=_PickedSet5, internal, generate
  1, 150, 1
** Section: Epoxy
** Solid Section, elset=_PickedSet5, material=Epoxy
1.,
*End Instance
**
*Instance, name=Concrete-1, part=Concrete
  298., 0., 0.
*Node
  1, -150., 12.5, 37.5
  2, 0., 12.5, 37.5
...

7199, 3245, 3246, 477, 476, 8783, 8784, 3506, 3505
7200, 3246, 442, 19, 477, 8784, 3478, 511, 3506
*Nset, nset=ConcreteBottom
  5,  6,  7,  8, 11, 12, 14, 15, 17, 19, 87, 88, 89, 90,
91, 92
 93, 94, 95, 96, 97, 98, 99, 100, 101, 102, 103, 104, 105, 106,
107, 108
...

3447, 3448, 3449, 3450, 3451, 3452, 3453, 3454, 3455, 3456, 3457, 3458, 3459, 3460,
3461, 3462
3463, 3464, 3465, 3466, 3467, 3468, 3469, 3470, 3471, 3472, 3473, 3474, 3475, 3476,
3477, 3478
*Elset, elset=ConcreteBottom
1051, 1052, 1053, 1054, 1055, 1056, 1057, 1058, 1059, 1060, 1061, 1062, 1063, 1064,
1065, 1066
1067, 1068, 1069, 1070, 1071, 1072, 1073, 1074, 1075, 1076, 1077, 1078, 1079, 1080,
1081, 1082
...

7048, 7056, 7064, 7072, 7080, 7088, 7096, 7104, 7112, 7120, 7128, 7136, 7144, 7152,
7160, 7168
7176, 7184, 7192, 7200
*Nset, nset=ConcreteSides
  1,  3,  4,  6,  7,  8,  9, 11, 13, 14, 15, 16, 17, 18,
19, 20
 54, 55, 56, 57, 58, 59, 60, 61, 62, 63, 64, 65, 66, 67,
68, 69
...

3485, 3486, 3487, 3488, 3489, 3490, 3491, 3492, 3493, 3494, 3495, 3496, 3497, 3498,
3499, 3500
3501, 3502, 3503, 3504, 3505, 3506
*Elset, elset=ConcreteSides
  1, 31, 61, 91, 121, 122, 123, 124, 125, 126, 127, 128, 129, 130,
131, 132

```

```

133, 134, 135, 136, 137, 138, 139, 140, 141, 142, 143, 144, 145, 146,
147, 148
...
7169, 7170, 7171, 7172, 7173, 7174, 7175, 7176, 7177, 7178, 7179, 7180, 7181, 7182,
7183, 7184
7185, 7186, 7187, 7188, 7189, 7190, 7191, 7192, 7193, 7194, 7195, 7196, 7197, 7198,
7199, 7200
*Nset, nset=ConcreteInterface
1, 2, 9, 10, 21, 22, 23, 24, 25, 26, 27, 28, 29, 30,
31, 32
33, 34, 35, 36, 37, 38, 39, 40, 41, 42, 43, 44, 45, 46,
47, 48
...
1299, 1300, 1301, 1302, 1303, 1304, 1305, 1306, 1307, 1308, 1309, 1310, 1311, 1312,
1313, 1314
1315, 1316, 1317, 1318, 1319, 1320, 1321, 1322, 1323, 1324
*Elset, elset=ConcreteInterface, generate
1201, 1350, 1
*Nset, nset=ConcreteTop
1, 2, 3, 4, 9, 10, 13, 16, 18, 20, 21, 22, 23, 24,
25, 26
27, 28, 29, 30, 31, 32, 33, 34, 35, 36, 37, 38, 39, 40,
41, 42
...
3339, 3340, 3341, 3342, 3343, 3344, 3345, 3346, 3347, 3348, 3349, 3350, 3351, 3352,
3353, 3354
3355, 3356, 3357, 3358, 3359, 3360, 3361, 3362
*Elset, elset=ConcreteTop
1, 2, 3, 4, 5, 6, 7, 8, 9, 10, 11, 12, 13, 14,
15, 16
17, 18, 19, 20, 21, 22, 23, 24, 25, 26, 27, 28, 29, 30,
31, 32
...
6961, 6969, 6977, 6985, 6993, 7001, 7009, 7017, 7025, 7033, 7041, 7049, 7057, 7065,
7073, 7081
7089, 7097, 7105, 7113, 7121, 7129, 7137, 7145, 7153, 7161, 7169, 7177, 7185, 7193
** Region: (Concrete:Picked)
*Elset, elset=_PickedSet12, internal, generate
1, 7200, 1
** Section: Concrete
*Solid Section, elset=_PickedSet12, material=Concrete
1.,
*End Instance
*Nset, nset=EpoxyLayer, instance=EPOXY-1, generate
1, 372, 1
*Elset, elset=EpoxyLayer, instance=EPOXY-1, generate
1, 150, 1
*Nset, nset=_PickedSet17, internal, instance=FRP-1, generate
1, 376, 1
*Nset, nset=_PickedSet17, internal, instance=EPOXY-1
1, 2, 3, 4, 5, 6, 7, 8, 9, 10, 11, 12, 13, 14, 15, 16
17, 18, 19, 20, 21, 22, 23, 24, 25, 26, 27, 28, 29, 30, 31, 32
...
353, 354, 355, 356, 357, 358, 359, 360, 361, 362, 363, 364, 365, 366, 367, 368
369, 370, 371, 372
*Nset, nset=_PickedSet17, internal, instance=Concrete-1
1, 2, 3, 4, 5, 6, 7, 8, 9, 10, 11, 12, 13, 14,
15, 16
17, 18, 19, 20, 21, 22, 23, 24, 25, 26, 27, 28, 29, 30,
31, 32

```

```

...
3485, 3486, 3487, 3488, 3489, 3490, 3491, 3492, 3493, 3494, 3495, 3496, 3497, 3498,
3499, 3500
3501, 3502, 3503, 3504, 3505, 3506
*Elset, elset=_PickedSet17, internal, instance=FRP-1, generate
  1, 200, 1
*Elset, elset=_PickedSet17, internal, instance=EPOXY-1
  1, 2, 3, 4, 5, 6, 7, 8, 9, 10, 11, 12, 13, 14, 15, 16
  17, 18, 19, 20, 21, 22, 23, 24, 25, 26, 27, 28, 29, 30, 31, 61
...
91, 121, 122, 123, 124, 125, 126, 127, 128, 129, 130, 131, 132, 133, 134, 135
136, 137, 138, 139, 140, 141, 142, 143, 144, 145, 146, 147, 148, 149, 150
*Elset, elset=_PickedSet17, internal, instance=Concrete-1
  1, 2, 3, 4, 5, 6, 7, 8, 9, 10, 11, 12, 13, 14,
15, 16
  17, 18, 19, 20, 21, 22, 23, 24, 25, 26, 27, 28, 29, 30,
31, 32
...
7182, 7183, 7184, 7185, 7186, 7187, 7188, 7189, 7190, 7191, 7192, 7193, 7194, 7195,
7196, 7197
7198, 7199, 7200
*Elset, elset=_PickedSurf11_S4, internal, instance=FRP-1, generate
  51, 200, 1
*Surface, type=ELEMENT, name=_PickedSurf11, internal
  _PickedSurf11_S4, S4
*Elset, elset=_PickedSurf12_S3, internal, instance=EPOXY-1, generate
  1, 150, 1
*Surface, type=ELEMENT, name=_PickedSurf12, internal
  _PickedSurf12_S3, S3
*Elset, elset=_PickedSurf13_S5, internal, instance=EPOXY-1, generate
  1, 150, 1
*Surface, type=ELEMENT, name=_PickedSurf13, internal
  _PickedSurf13_S5, S5
*Elset, elset=_PickedSurf14_S2, internal, instance=Concrete-1, generate
  1201, 1350, 1
*Surface, type=ELEMENT, name=_PickedSurf14, internal
  _PickedSurf14_S2, S2
** Constraint: EpoxyConcreteInterface
*Tie, name=EpoxyConcreteInterface, adjust=yes
  _PickedSurf14, _PickedSurf13
** Constraint: FRPEpoxyInterface
*Tie, name=FRPEpoxyInterface, adjust=yes
  _PickedSurf12, _PickedSurf11
*End Assembly
**
*PHYSICAL CONSTANTS, ABSOLUTE ZERO=0
** MATERIALS
**
*Material, name=Concrete
*Diffusivity
  3e-05,0.
*Solubility
  0.0001633,
*Material, name=Epoxy
*Diffusivity
  5e-07,0.
*Solubility
  4.562e-05,
*Material, name=FRP
*Diffusivity, law=FICK
  8e-07,0.
*Solubility
  1.622e-05,
** -----
**
** STEP: Diffusion

```

```
**
*Step, name=Diffusion, inc=2500
3Dmoisturediffusion
*Mass Diffusion, end=SS, dcmax=0.3
1., ,1.0, 7200., 1e-10
**
** BOUNDARY CONDITIONS
**
** Name: MoistureConditioning Type: Mass concentration
*Boundary
_PickedSet17, 11, 11, 1.
**
** OUTPUT REQUESTS
**
*Restart, write, frequency=1
**
** FIELD OUTPUT: Data
**
*Output, field, frequency=1
*Node Output
NNC,
*Element Output
CONC,
*Element Output, elset=EpoxyLayer
ESOL
**
** HISTORY OUTPUT: H-Output-1
**
*Output, history, variable=PRESELECT
*El Print, ELSET=EPOXYLAYER, freq=20, TOTALS=YES
ESOL
*Node Print, freq=999999
*End Step
```

APPENDIX 2A

Finite Element (ABAQUS) Input File for Global Peel Modeling

This file is used to simulate the global behavior of a Case 2 model under peel load.

```
*****
**          INPUT FILE WRITTEN BY CHING AU          **
**                LAST UPDATE: 6.24.2004          **
**  FILE NAME: J-INTEGRALGLOBALMODELPEELCASE2.INP  **
*****
**
*HEADING
J-INTEGRAL COMPUTATION OF FRP BONDED CONCRETE
CASE2: INTERFACE CRACK BETWEEN EPOXY AND CONCRETE
**PREPRINT, ECHO=NO, MODEL=NO, HISTORY=NO
**
*****
** NODE GENERATION **
*****
** -----
** CONCRETE BLOCK
** -----
*NODE, NSET=CONCRETELOWERLEFT
1, -12.5, -37.5
*NODE, NSET=OFFSET1LOWER
41, 12.5, -37.5
*NODE, NSET=CONCRETELOWERRIGHT
241, 137.5, -37.5
*NODE, NSET=REACTIONPLATEEDGE
9641, -12.5, -12.5
*NODE, NSET=OFFSET1UPPER
9681, 12.5, -12.5
*NODE, NSET=PROJECTION1
9881, 137.5, -12.5
*NFILL, NSET=CONCRETELEFT1
**, BIAS=1.5
CONCRETELOWERLEFT, REACTIONPLATEEDGE, 40, 241
*NFILL, NSET=OFFSET1
**, BIAS=1.5
OFFSET1LOWER, OFFSET1UPPER, 40, 241
*NFILL, NSET=CONCRETERIGHT1
**, BIAS=1.5
CONCRETELOWERRIGHT, PROJECTION1, 40, 241
*NFILL, NSET=CONCRETEAREA-I
CONCRETELEFT1, OFFSET1, 40, 1
*NFILL, NSET=CONCRETEAREA-II
**, BIAS=0.9
OFFSET1, CONCRETERIGHT1, 200, 1
**
*NODE, NSET=DUMMY1
14461, -12.5, -1.0
*NODE, NSET=OFFSET2UPPER
14501, 12.5, -1.0
*NODE, NSET=PROJECTION2
14701, 137.5, -1.0
*NFILL, NSET=CONCRETELEFT2
**, BIAS=1.50
REACTIONPLATEEDGE, DUMMY1, 20, 241
*NFILL, NSET=OFFSET2
**, BIAS=1.50
OFFSET1UPPER, OFFSET2UPPER, 20, 241
*NFILL, NSET=CONCRETERIGHT2
**, BIAS=1.50
PROJECTION1, PROJECTION2, 20, 241
*NFILL, NSET=CONCRETEAREA-III
CONCRETELEFT2, OFFSET2, 40, 1
```

```

*NFILL, NSET=CONCRETEAREA-IV
**, BIAS=0.9
OFFSET2, CONCRETERIGHT2, 200, 1
**
*NODE, NSET=CONCRETEUPPERLEFT
16389, -12.5, 0.0
*NODE, NSET=CRACKTIPLOWER
16409, 0.0, 0.0
*NODE, NSET=OFFSET3UPPER
16429, 12.5, 0.0
*NODE, NSET=CONCRETEUPPERRIGHT
16629, 137.5, 0.0
*NFILL, NSET=CONCRETELEFT3
DUMMY1, CONCRETEUPPERLEFT, 8, 241
*NFILL, NSET=OFFSET3
OFFSET2UPPER, OFFSET3UPPER, 8, 241
*NFILL, NSET=CONCRETERIGHT3
PROJECTION2, CONCRETEUPPERRIGHT, 8, 241
*NFILL, NSET=CONCRETEAREA-V
CONCRETELEFT3, OFFSET3, 40, 1
*NFILL, NSET=CONCRETEAREA-VI
**, BIAS=0.9
OFFSET3, CONCRETERIGHT3, 200, 1
**
*NSET, NSET=CONCRETEINTERFACE, GENERATE
16409, 16629, 1
**
** -----
** EPOXY LAYER
** -----
*NODE, NSET=EPOXYLOWERLEFT
20000, -12.5, 0.0
*NODE, NSET=EPOXYLOWERRIGHT
20240, 137.5, 0.0
*NODE, NSET=EPOXYUPPERLEFT
21928, -12.5, 1.0
*NODE, NSET=EPOXYUPPERRIGHT
22168, 137.5, 1.0
*NODE, NSET=CRACKTIPUPPER
20020, 0.0, 0.0
*NODE, NSET=EPOXYOFFSETLOWER
20040, 12.5, 0.0
*NODE, NSET=EPOXYOFFSETUPPER
21968, 12.5, 1.0
*NFILL, NSET=EPOXYLEFT
EPOXYLOWERLEFT, EPOXYUPPERLEFT, 8, 241
*NFILL, NSET=EPOXYOFFSET
EPOXYOFFSETLOWER, EPOXYOFFSETUPPER, 8, 241
*NFILL, NSET=EPOXYRIGHT
EPOXYLOWERRIGHT, EPOXYUPPERRIGHT, 8, 241
*NFILL, NSET=EPOXYAREA-I
EPOXYLEFT, EPOXYOFFSET, 40, 1
*NFILL, NSET=EPOXYAREA-II
**, BIAS=0.9
EPOXYOFFSET, EPOXYRIGHT, 200, 1
**
*NSET, NSET=EPOXYINTERFACELOWER, GENERATE
20020, 20240, 1
*NSET, NSET=EPOXYINTERFACEUPPER, GENERATE
21928, 22168, 1
**
** -----
** FRP LAYER
** -----
*NODE, NSET=FRPLOWERLEFT
30000, -62.5, 1.0
*NODE, NSET=FRPLOWERRIGHT
30320, 137.5, 1.0
*NODE, NSET=FRPUPPERLEFT
33210, -62.5, 2.28
*NODE, NSET=FRPUPPERRIGHT

```

```

33530, 137.5, 2.28
*NODE, NSET=FRPINTERFACESTARTLOWER
30080, -12.5, 1.0
*NODE, NSET=FRPINTERFACESTARTUPPER
33290, -12.5, 2.28
*NODE, NSET=FRPOFFSET1LOWER
30120, 12.5, 1.0
*NODE, NSET=FRPOFFSET1UPPER
33330, 12.5, 2.28
*NFILL, NSET=FRPLEFT
FRPLOWERLEFT, FRPUPPERLEFT, 10, 321
*NFILL, NSET=FRPINTERFACESTART
FRPINTERFACESTARTLOWER, FRPINTERFACESTARTUPPER, 10, 321
*NFILL, NSET=FRPOFFSET1
FRPOFFSET1LOWER, FRPOFFSET1UPPER, 10, 321
*NFILL, NSET=FRPRIGHT
FRPLOWERRIGHT, FRPUPPERRIGHT, 10, 321
*NFILL, NSET=CANTILEVER
FRPLEFT, FRPINTERFACESTART, 80, 1
*NFILL, NSET=FRPAREA-I
FRPINTERFACESTART, FRPOFFSET1, 40, 1
*NFILL, NSET=FRPAREA-II
**, BIAS=0.9
FRPOFFSET1, FRPRIGHT, 200, 1
**
*NSET, NSET=FRPINTERFACE, GENERATE
30080, 30320, 1
**
*****
** INTERFACE NODE CONNECTION **
*****
* MPC
TIE, FRPINTERFACE, EPOXYINTERFACEUPPER
* MPC
TIE, EPOXYINTERFACELOWER, CONCRETEINTERFACE
**
**
*****
** ELEMENT GENERATION **
*****
** -----
** CONCRETE BLOCKS - A TOTAL OF 4080 ELEMENTS
** -----
* ELEMENT, TYPE=CPE8, ELSET=CONCRETEELEMENT
1, 1,3,485,483, 2,244,484,242
* ELGEN, ELSET=CONCRETEELEMENT
1, 120, 2, 1, 34, 482, 120
**
** -----
** EPOXY LAYER - A TOTAL OF 480 ELEMENTS
** -----
* ELEMENT, TYPE=CPE8, ELSET=EPOXYELEMENT
20000, 20000,20002,20484,20482, 20001,20243,20483,20241
* ELGEN, ELSET=EPOXYELEMENT
20000, 120, 2, 1, 4, 482, 120
**
** -----
** FRP LAYER - A TOTAL OF 1600 ELEMENTS
** -----
* ELEMENT, TYPE=CPE8, ELSET=FRPELEMENT
30000, 30000,30002,30644,30642, 30001,30323,30643,30321
* ELGEN, ELSET=FRPELEMENT
30000, 160, 2, 1, 5, 642, 160
**
**
*****
** MATERIAL ASSIGNMENT **
*****
** -----
** CONCRETE

```

```

** -----
*SOLID SECTION, MATERIAL=CONCRETE, ELSET=CONCRETEELEMENT
*MATERIAL, NAME=CONCRETE
*ELASTIC
21.8E3, 0.19
**
** -----
** EPOXY
** -----
*SOLID SECTION, MATERIAL=EPOXY, ELSET=EPOXYELEMENT
*MATERIAL, NAME=EPOXY
*ELASTIC
1.5E3, 0.35
**
** ---
** FRP
** ---
*SOLID SECTION, MATERIAL=FRP, ELSET=FRPELEMENT
*MATERIAL, NAME=FRP
*ELASTIC
148.0E3, 0.27
**
**
*****
** BOUNDARY CONDITIONS **
*****
*NSET, NSET=CONCRETEBOTTOM, GENERATE
1, 241, 1
*NSET, NSET=REACTIONPLATE, GENERATE
1, 9641, 241
*NSET, NSET=CONCRETERIGHTWALL, GENERATE
241, 16629, 241
*NSET, NSET=SHEARINGROLLERS, GENERATE
30000, 30080, 1
33210, 33330, 1
*NSET, NSET=FRPPEELPOINT
33210
*ELSET, ELSET=FRPSHEARINGEDGE, GENERATE
30000, 30644, 161
**
**
*BOUNDARY
CONCRETEBOTTOM, ENCASTRE
REACTIONPLATE, ENCASTRE
CONCRETERIGHTWALL, ENCASTRE
**
** ROLLER CONDITION SHALL BE REMOVED IN PEEL FRACTURE MODELING **
** SHEARINGROLLERS, 2, 2, 0.0
**
*****
** STEP - LOADING **
*****
*STEP
*STATIC
**
** FOR SHEAR LOAD OF 20KN
**DLOAD
**FRPSHEARINGEDGE, P4, -625.0
**
** FOR PEEL LOAD OF 70N
*CLOAD
FRPPEELPOINT, 2, 2.8
*EL PRINT
S,E
*NODE PRINT
U
*EL FILE
S,E
*NODE FILE
U
*END STEP

```

APPENDIX 2B

Finite Element (ABAQUS) Input File for Global Shear Modeling

This file is used to simulate the global behavior of a Case 2 model under shear load.

```
*****
**          INPUT FILE WRITTEN BY CHING AU          **
**                LAST UPDATE: 6.24.2004          **
**  FILE NAME: J-INTEGRALGLOBALMODELSHEARCASE2.INP  **
*****
**
*HEADING
J-INTEGRAL COMPUTATION OF FRP BONDED CONCRETE
CASE2: INTERFACE CRACK BETWEEN EPOXY AND CONCRETE
**PREPRINT, ECHO=NO, MODEL=NO, HISTORY=NO
**
*****
** NODE GENERATION **
*****
** -----
** CONCRETE BLOCK
** -----
*NODE, NSET=CONCRETELOWERLEFT
1, -12.5, -37.5
*NODE, NSET=OFFSET1LOWER
41, 12.5, -37.5
*NODE, NSET=CONCRETELOWERRIGHT
241, 137.5, -37.5
*NODE, NSET=REACTIONPLATEEDGE
9641, -12.5, -12.5
*NODE, NSET=OFFSET1UPPER
9681, 12.5, -12.5
*NODE, NSET=PROJECTION1
9881, 137.5, -12.5
*NFill, NSET=CONCRETELEFT1
**, BIAS=1.5
CONCRETELOWERLEFT, REACTIONPLATEEDGE, 40, 241
*NFill, NSET=OFFSET1
**, BIAS=1.5
OFFSET1LOWER, OFFSET1UPPER, 40, 241
*NFill, NSET=CONCRETERIGHT1
**, BIAS=1.5
CONCRETELOWERRIGHT, PROJECTION1, 40, 241
*NFill, NSET=CONCRETEAREA-I
CONCRETELEFT1, OFFSET1, 40, 1
*NFill, NSET=CONCRETEAREA-II
**, BIAS=0.9
OFFSET1, CONCRETERIGHT1, 200, 1
**
*NODE, NSET=DUMMY1
14461, -12.5, -1.0
*NODE, NSET=OFFSET2UPPER
14501, 12.5, -1.0
*NODE, NSET=PROJECTION2
14701, 137.5, -1.0
*NFill, NSET=CONCRETELEFT2
**, BIAS=1.50
REACTIONPLATEEDGE, DUMMY1, 20, 241
*NFill, NSET=OFFSET2
**, BIAS=1.50
OFFSET1UPPER, OFFSET2UPPER, 20, 241
*NFill, NSET=CONCRETERIGHT2
**, BIAS=1.50
PROJECTION1, PROJECTION2, 20, 241
*NFill, NSET=CONCRETEAREA-III
CONCRETELEFT2, OFFSET2, 40, 1
```

```

*NFILL, NSET=CONCRETEAREA-IV
**, BIAS=0.9
OFFSET2, CONCRETERIGHT2, 200, 1
**
*NODE, NSET=CONCRETEUPPERLEFT
16389, -12.5, 0.0
*NODE, NSET=CRACKTIPLOWER
16409, 0.0, 0.0
*NODE, NSET=OFFSET3UPPER
16429, 12.5, 0.0
*NODE, NSET=CONCRETEUPPERRIGHT
16629, 137.5, 0.0
*NFILL, NSET=CONCRETELEFT3
DUMMY1, CONCRETEUPPERLEFT, 8, 241
*NFILL, NSET=OFFSET3
OFFSET2UPPER, OFFSET3UPPER, 8, 241
*NFILL, NSET=CONCRETERIGHT3
PROJECTION2, CONCRETEUPPERRIGHT, 8, 241
*NFILL, NSET=CONCRETEAREA-V
CONCRETELEFT3, OFFSET3, 40, 1
*NFILL, NSET=CONCRETEAREA-VI
**, BIAS=0.9
OFFSET3, CONCRETERIGHT3, 200, 1
**
*NSET, NSET=CONCRETEINTERFACE, GENERATE
16409, 16629, 1
**
** -----
** EPOXY LAYER
** -----
*NODE, NSET=EPOXYLOWERLEFT
20000, -12.5, 0.0
*NODE, NSET=EPOXYLOWERRIGHT
20240, 137.5, 0.0
*NODE, NSET=EPOXYUPPERLEFT
21928, -12.5, 1.0
*NODE, NSET=EPOXYUPPERRIGHT
22168, 137.5, 1.0
*NODE, NSET=CRACKTIPUPPER
20020, 0.0, 0.0
*NODE, NSET=EPOXYOFFSETLOWER
20040, 12.5, 0.0
*NODE, NSET=EPOXYOFFSETUPPER
21968, 12.5, 1.0
*NFILL, NSET=EPOXYLEFT
EPOXYLOWERLEFT, EPOXYUPPERLEFT, 8, 241
*NFILL, NSET=EPOXYOFFSET
EPOXYOFFSETLOWER, EPOXYOFFSETUPPER, 8, 241
*NFILL, NSET=EPOXYRIGHT
EPOXYLOWERRIGHT, EPOXYUPPERRIGHT, 8, 241
*NFILL, NSET=EPOXYAREA-I
EPOXYLEFT, EPOXYOFFSET, 40, 1
*NFILL, NSET=EPOXYAREA-II
**, BIAS=0.9
EPOXYOFFSET, EPOXYRIGHT, 200, 1
**
*NSET, NSET=EPOXYINTERFACELOWER, GENERATE
20020, 20240, 1
*NSET, NSET=EPOXYINTERFACEUPPER, GENERATE
21928, 22168, 1
**
** -----
** FRP LAYER
** -----
*NODE, NSET=FRPLOWERLEFT
30000, -62.5, 1.0
*NODE, NSET=FRPLOWERRIGHT
30320, 137.5, 1.0
*NODE, NSET=FRPUPPERLEFT
33210, -62.5, 2.28
*NODE, NSET=FRPUPPERRIGHT

```

```

33530, 137.5, 2.28
*NODE, NSET=FRPINTERFACESTARTLOWER
30080, -12.5, 1.0
*NODE, NSET=FRPINTERFACESTARTUPPER
33290, -12.5, 2.28
*NODE, NSET=FRPOFFSET1LOWER
30120, 12.5, 1.0
*NODE, NSET=FRPOFFSET1UPPER
33330, 12.5, 2.28
*NFILL, NSET=FRPLEFT
FRPLOWERLEFT, FRPUPPERLEFT, 10, 321
*NFILL, NSET=FRPINTERFACESTART
FRPINTERFACESTARTLOWER, FRPINTERFACESTARTUPPER, 10, 321
*NFILL, NSET=FRPOFFSET1
FRPOFFSET1LOWER, FRPOFFSET1UPPER, 10, 321
*NFILL, NSET=FRPRIGHT
FRPLOWERRIGHT, FRPUPPERRIGHT, 10, 321
*NFILL, NSET=CANTILEVER
FRPLEFT, FRPINTERFACESTART, 80, 1
*NFILL, NSET=FRPAREA-I
FRPINTERFACESTART, FRPOFFSET1, 40, 1
*NFILL, NSET=FRPAREA-II
**, BIAS=0.9
FRPOFFSET1, FRPRIGHT, 200, 1
**
*NSET, NSET=FRPINTERFACE, GENERATE
30080, 30320, 1
**
*****
** INTERFACE NODE CONNECTION **
*****
*MPC
TIE, FRPINTERFACE, EPOXYINTERFACEUPPER
*MPC
TIE, EPOXYINTERFACELOWER, CONCRETEINTERFACE
**
**
*****
** ELEMENT GENERATION **
*****
** -----
** CONCRETE BLOCKS - A TOTAL OF 4080 ELEMENTS
** -----
*ELEMENT, TYPE=CPE8, ELSET=CONCRETEELEMENT
1, 1,3,485,483, 2,244,484,242
*ELGEN, ELSET=CONCRETEELEMENT
1, 120, 2, 1, 34, 482, 120
**
** -----
** EPOXY LAYER - A TOTAL OF 480 ELEMENTS
** -----
*ELEMENT, TYPE=CPE8, ELSET=EPOXYELEMENT
20000, 20000,20002,20484,20482, 20001,20243,20483,20241
*ELGEN, ELSET=EPOXYELEMENT
20000, 120, 2, 1, 4, 482, 120
**
** -----
** FRP LAYER - A TOTAL OF 1600 ELEMENTS
** -----
*ELEMENT, TYPE=CPE8, ELSET=FRPELEMENT
30000, 30000,30002,30644,30642, 30001,30323,30643,30321
*ELGEN, ELSET=FRPELEMENT
30000, 160, 2, 1, 5, 642, 160
**
**
*****
** MATERIAL ASSIGNMENT **
*****
** -----
** CONCRETE

```

```

** -----
*SOLID SECTION, MATERIAL=CONCRETE, ELSET=CONCRETEELEMENT
*MATERIAL, NAME=CONCRETE
*ELASTIC
21.8E3, 0.19
**
** -----
** EPOXY
** -----
*SOLID SECTION, MATERIAL=EPOXY, ELSET=EPOXYELEMENT
*MATERIAL, NAME=EPOXY
*ELASTIC
1.5E3, 0.35
**
** ---
** FRP
** ---
*SOLID SECTION, MATERIAL=FRP, ELSET=FRPELEMENT
*MATERIAL, NAME=FRP
*ELASTIC
148.0E3, 0.27
**
**
*****
** BOUNDARY CONDITIONS **
*****
*NSET, NSET=CONCRETEBOTTOM, GENERATE
1, 241, 1
*NSET, NSET=REACTIONPLATE, GENERATE
1, 16389, 241
*NSET, NSET=CONCRETERIGHTWALL, GENERATE
241, 16629, 241
*NSET, NSET=SHEARINGROLLERS, GENERATE
30000, 30080, 1
33210, 33330, 1
*NSET, NSET=FRPPEELPOINT
33210
*ELSET, ELSET=FRPSHEARINGEDGE, GENERATE
30000, 30644, 161
**
**
*BOUNDARY
CONCRETEBOTTOM, ENCASTRE
REACTIONPLATE, ENCASTRE
CONCRETERIGHTWALL, ENCASTRE
**
** ROLLER CONDITION SHALL BE REMOVED IN PEEL FRACTURE MODELING **
SHEARINGROLLERS, 2, 2, 0.0
**
*****
** STEP - LOADING **
*****
*STEP
*STATIC
**
** FOR SHEAR LOAD OF 20KN
*DLOAD
FRPSHEARINGEDGE, P4, -625.0
**
** FOR PEEL LOAD OF 70N
**CLOAD
** FRPPEELPOINT, 2, 2.8
*EL PRINT
S,E
*NODE PRINT
U
*EL FILE
S,E
*NODE FILE
U
*END STEP

```

APPENDIX 3A

Finite Element (ABAQUS) Input File for Computation of *J*-Integral and Mode Separation under Peel

This file is a sub model to compute *J*-integral of a Case 2 model under peel load.

```
*****
**          INPUT FILE WRITTEN BY CHING AU          **
**          LAST UPDATE: 6.28.2004                 **
**          FILE NAME: J-INTEGRALSUBMODELPEELCASE2.INP **
*****
**
*HEADING
J-INTEGRAL COMPUTATION OF FRP BONDED CONCRETE
SUBMODEL COMPUTATION AROUND THE CRACK TIP
CASE2: INTERFACE CRACK BETWEEN EPOXY AND CONCRETE
**PREPRINT, ECHO=NO, MODEL=NO, HISTORY=NO
**
*****
**NODE GENERATION **
*****
** -----
** BOTH EPOXY & CONCRETE LAYERS
** -----
*NODE, NSET=CORNERS
1, 0.0, 0.0
17, -0.8, 0.0001
153, -0.8, 0.8
425, 0.8, 0.8
561, 0.8, 0.0
697, 0.8, -0.8
969, -0.8, -0.8
1105, -0.8, -0.0001
1089, 0.0, 0.0
*NGEN, NSET=TIP
1, 1089, 17
*NGEN, NSET=OUTER
17, 153, 17
153, 425, 17
425, 561, 17
561, 697, 17
697, 969, 17
969, 1105, 17
*NFILL, SINGULAR=1
TIP, OUTER, 16, 1
**
*****
** ELEMENT GENERATION **
*****
*ELEMENT, TYPE=CPE8, ELSET=J-ELEMENTS
1, 3,1,35,37, 2,18,36,20
*ELGEN, ELSET=J-ELEMENTS
1, 8, 2, 1, 32, 34, 8
*ELSET, ELSET=EPOXYELEMENT, GENERATE
1, 121, 8
2, 122, 8
3, 123, 8
4, 124, 8
5, 125, 8
6, 126, 8
7, 127, 8
8, 128, 8
*ELSET, ELSET=CONCRETEELEMENT, GENERATE
129, 249, 8
130, 250, 8
```

```

131, 251, 8
132, 252, 8
133, 253, 8
134, 254, 8
135, 255, 8
136, 256, 8
**
*****
** MATERIAL ASSIGNMENT **
*****
** -----
** EPOXY
** -----
*SOLID SECTION, MATERIAL=EPOXY, ELSET=EPOXYELEMENT
*MATERIAL, NAME=EPOXY
*ELASTIC
1.5E3, 0.35
**
** -----
** CONCRETE
** -----
*SOLID SECTION, MATERIAL=CONCRETE, ELSET=CONCRETEELEMENT
*MATERIAL, NAME=CONCRETE
*ELASTIC
21.8E3, 0.19
**
*****
** SUBMODEL ACTIVATION **
*****
*SUBMODEL
OUTER
**
*STEP
*STATIC
1.0,1.0
*BOUNDARY, SUBMODEL, STEP=1
OUTER, 1, 2
**
*****
** J AND K COMPUTATION **
*****
*CONTOUR INTEGRAL, CONTOURS=8, OUTPUT=BOTH, TYPE=J
TIP, 1.0, 0.0
*CONTOUR INTEGRAL, CONTOURS=8, OUTPUT=BOTH, TYPE=K FACTORS
TIP, 1.0, 0.0
**
*****
** OUTPUT RESULTS OTHER THAN J & K **
*****
**EL PRINT
**S, E
**EL FILE
**S, E
**NODE PRINT
**U
**NODE FILE
**U
**
*END STEP

```

APPENDIX 3B

Finite Element (ABAQUS) Input File for Computation of *J*-Integral and Mode Separation under Shear

This file is a sub model to compute *J*-integral of a Case 2 model under shear load.

```
*****
**          INPUT FILE WRITTEN BY CHING AU          **
**          LAST UPDATE: 6.28.2004                 **
**          FILE NAME: J-INTEGRALSUBMODELSHEARCASE2.INP **
*****
**
*HEADING
J-INTEGRAL COMPUTATION OF FRP BONDED CONCRETE
SUBMODEL COMPUTATION AROUND THE CRACK TIP
CASE2: INTERFACE CRACK BETWEEN EPOXY AND CONCRETE
**PREPRINT, ECHO=NO, MODEL=NO, HISTORY=NO
**
*****
**NODE GENERATION **
*****
** -----
** BOTH EPOXY & CONCRETE LAYERS
** -----
*NODE, NSET=CORNERS
1, 0.0, 0.0
17, -0.8, 0.0001
153, -0.8, 0.8
425, 0.8, 0.8
561, 0.8, 0.0
697, 0.8, -0.8
969, -0.8, -0.8
1105, -0.8, -0.0001
1089, 0.0, 0.0
*NGEN, NSET=TIP
1, 1089, 17
*NGEN, NSET=OUTER
17, 153, 17
153, 425, 17
425, 561, 17
561, 697, 17
697, 969, 17
969, 1105, 17
*NFILL, SINGULAR=1, NSET=J-DOMAIN
TIP, OUTER, 16, 1
**
*****
** ELEMENT GENERATION **
*****
*ELEMENT, TYPE=CPE8, ELSET=J-ELEMENTS
1, 3,1,35,37, 2,18,36,20
*ELGEN, ELSET=J-ELEMENTS
1, 8, 2, 1, 32, 34, 8
*ELSET, ELSET=EPOXYELEMENT, GENERATE
1, 121, 8
2, 122, 8
3, 123, 8
4, 124, 8
5, 125, 8
6, 126, 8
7, 127, 8
8, 128, 8
*ELSET, ELSET=CONCRETEELEMENT, GENERATE
129, 249, 8
```

```

130, 250, 8
131, 251, 8
132, 252, 8
133, 253, 8
134, 254, 8
135, 255, 8
136, 256, 8
**
*****
** MATERIAL ASSIGNMENT **
*****
** -----
** EPOXY
** -----
*SOLID SECTION, MATERIAL=EPOXY, ELSET=EPOXYELEMENT
*MATERIAL, NAME=EPOXY
*ELASTIC
1.5E3, 0.35
**
** -----
** CONCRETE
** -----
*SOLID SECTION, MATERIAL=CONCRETE, ELSET=CONCRETEELEMENT
*MATERIAL, NAME=CONCRETE
*ELASTIC
21.8E3, 0.19
**
*****
** SUBMODEL ACTIVATION **
*****
*SUBMODEL
OUTER
**
*STEP
*STATIC
1.0,1.0
*BOUNDARY, SUBMODEL, STEP=1
OUTER, 1, 2
**OR NEED 1 - 6 DOF? IT IS A 2D ANALYSIS ANYWAY
**
*****
** J AND K COMPUTATION **
*****
*CONTOUR INTEGRAL, CONTOURS=8, OUTPUT=BOTH, TYPE=J
TIP, 1.0, 0.0
*CONTOUR INTEGRAL, CONTOURS=8, OUTPUT=BOTH, TYPE=K FACTORS
TIP, 1.0, 0.0
**
*****
** OUTPUT RESULTS OTHER THAN J & K **
*****
**EL PRINT
**S, E
**EL FILE
**S, E
**NODE PRINT
**U
**NODE FILE
**U
**
*END STEP

```